

Further developments of radio-noble gas
groundwater dating – assessment of ^{39}Ar and ^{37}Ar
underground production, and development of a
new ^{85}Kr sampling technique

Inaugural Dissertation

of the Faculty of Science,
University of Bern

presented by

Stéphanie L. Musy

from Belmont-Broye (FR)

Supervisors of the doctoral thesis:

Dr. Roland Purtschert

Prof. Dr. Markus Leuenberger

Climate and Environmental Physics

Physics Institute

Further developments of radio-noble gas groundwater dating – assessment of ^{39}Ar and ^{37}Ar underground production, and development of a new ^{85}Kr sampling technique

Inaugural Dissertation

of the Faculty of Science,
University Bern

presented by

Stéphanie L. Musy

from Belmont-Broye (FR)

Supervisors of the doctoral thesis:

Dr. Roland Purtschert

Prof. Dr. Markus Leuenberger

Climate and Environmental Physics
Physics Institute

Accepted by the Faculty of Science.

Bern, 4.11.2022

The Dean:

Prof. Dr. Marco Herwegh

This work is licensed under a Creative Commons “Attribution
4.0 International” license.



Plain summary

Groundwater supplies billions of people with freshwater for domestic, agricultural, energy, and industrial purposes. Understanding its recharge rates, flow paths, and residence times is essential for protecting the resource in terms of quantity and quality and implementing management policies that ensure equitable and sustainable access to clean water. In this context, assessing the age of the water allows for a better understanding of the water cycle at all scales. Dating methods using radioactive noble gas isotopes rely on the accumulation and/or decay from a known atmospheric activity, which dissolves in the recharge. The focus of this thesis is the application of these dating methods for the radioactive isotopes of argon (^{39}Ar and ^{37}Ar) and krypton (^{85}Kr).

Subsurface production of radioactive isotopes is an inherent problem associated with these methods. Taking this phenomenon into account is essential to avoid biasing the ages concluded from the dissolved activities towards young values. For the methods based on argon-39 (^{39}Ar) and argon-37 (^{37}Ar), some processes are now clearly understood and documented. This is the case of the interactions with neutrons originating from cosmic rays or from the naturally present radioactivity in rocks. In contrast, reactions involving muons, which are different cosmogenic particles, are documented for other applications but have never been considered in the context of groundwater dating methods.

In this thesis, the significant impact of muon-induced reactions on ^{39}Ar and ^{37}Ar activities could be demonstrated for the first time. The activities measured in aquifers in Denmark could be compared with those theoretically produced by the documented and/or the newly-assessed muon processes. For this purpose, a methodical review of all nuclear processes involved in the production of radioargon in the underground was required. In addition, the emanation, which is the transfer process for the atoms produced in the rock to the pore space, was assessed by irradiation experiments in a particle accelerator. These results were then combined with information on depth-dependent recharge residence time to compute the activities accumulating during the infiltration of a water particle. Finally, using numerical modeling tools, the significance of subsurface production processes was extrapolated to a broader context. The simulation of various recharge scenarios allowed a better understanding of the situations where groundwater production is susceptible to induce significant age biases.

In parallel, the use of ^{37}Ar as an indicator of surface water-groundwater interactions was investigated in a pumping experiment in an alluvial aquifer in Emmental (CH). The combination of multiple tracers, such as ^{222}Rn and ^4He , allowed to distinguish the mixing fraction and the travel time of the freshly infiltrated river water from the regional component.

^{85}Kr is a tracer commonly used to date young (< 50 years) groundwater. Conventionally, its sampling is associated with logistical and practical challenges, such as disruption of the age stratigraphy in the well and preferential drainage of permeable aquifer fractions. As part of this thesis, a new *in-situ* sampling method was developed for the ^{85}Kr . The latter consists of small quasi-passive samplers placed directly in the well, thus avoiding the need to pump water to the surface. Thereby, the fieldwork is facilitated, and the accessibility of this dating method is improved. This new technique has been tested and validated in a porous aquifer of the Swiss Plateau and in wells located in the fractured context of the St. Lawrence Lowlands in Canada.

Résumé

Les eaux souterraines alimentent des milliards de personnes en eau douce à des fins domestiques, agricoles, énergétiques et industrielles. La compréhension des taux de recharge, des écoulements et des temps de résidence est essentielle afin de protéger la ressource en termes de quantité et de qualité. Celle-ci permet également la mise en œuvre des politiques de gestion qui garantissent un accès équitable et durable à une eau propre. Dans ce contexte, la détermination de l'âge de l'eau fait partie d'une meilleure compréhension du cycle des eaux souterraines à toute échelle. Les méthodes de datation utilisant les isotopes de gaz nobles radioactifs reposent sur l'accumulation et/ou la désintégration de ces derniers. Une activité atmosphérique connue se dissout dans l'eau de pluie qui se recharge dans les aquifères et est donc isolée de sa source. L'axe central de cette thèse est l'application de ces méthodes de datation avec les isotopes radioactifs de l'argon ainsi que du krypton.

La production souterraine des isotopes radioactifs est un problème inhérent à ces méthodes. La prise en compte de ce phénomène est essentielle afin que les âges conclus à partir des activités dissoutes ne soient pas biaisés vers des valeurs jeunes. Pour les méthodes basées sur l'argon-39 (^{39}Ar) et l'argon-37 (^{37}Ar), certains processus sont à ce jour bien compris et répertoriés. C'est le cas des interactions avec les neutrons qui proviennent soit directement des rayons cosmiques, soit de la radioactivité naturellement présente dans les roches. En revanche, les réactions impliquant des muons, qui sont d'autres particules cosmiques, sont documentées pour d'autres applications mais n'ont jamais été considérées dans le cadre des méthodes de datation de l'eau souterraine.

Dans cette thèse, l'impact significatif des réactions associées aux muons sur les activités d' ^{39}Ar et ^{37}Ar a pu être démontré pour la première fois. Les activités mesurées dans des aquifères au Danemark ont pu être comparées aux activités théoriquement produites par les processus répertoriés et/ou les "nouveaux" processus liés aux muons. Pour ce faire, il était nécessaire de méthodiquement réviser tous les processus nucléaires impliqués dans la production de radioargon dans le souterrain. De plus, l'émanation, qui est le processus de transfert des atomes produits dans la roche vers l'espace poreux, a été appréhendée par des expériences d'irradiation à l'aide d'un accélérateur de particules. Ces résultats ont été ensuite combinés à des informations sur le temps de résidence de la recharge en fonction de la profondeur afin de calculer les activités qui s'accumulent au cours de l'infiltration d'une particule d'eau.

Enfin, l'importance des processus de production souterraine a été extrapolée à un contexte plus large à l'aide d'outils de modélisation numérique. Ces derniers ont permis de simuler divers scénarios de recharge afin de mieux comprendre dans quel cas de figure la production souterraine est susceptible de créer des biais d'âge significatifs. Parallèlement, l'utilisation de l' ^{37}Ar comme indicateur des interactions entre les eaux de surface et les eaux souterraines a été étudiée dans le cadre d'un essai de pompage dans un aquifère alluvial en Emmental (CH). La combinaison de multiples traceurs, tels que le radon-222 (^{222}Rn) et l'hélium-4 (^4He), ont permis de distinguer la fraction, ainsi que le temps de résidence de l'eau provenant de la rivière, par rapport à la composante régionale.

Le krypton-85 (^{85}Kr) est un traceur communément utilisé pour dater les eaux souterraines jeunes (< 50 ans). Conventionnellement, son échantillonnage est associé à des défis logistiques et pratiques, tels que la perturbation de la stratigraphie d'âge dans le puits et le drainage préférentiel des fractions perméables de l'aquifère. Dans le cadre de cette thèse, une nouvelle méthode d'échantillonnage *in situ* a été développée pour le ^{85}Kr . Cette dernière consiste en des petits échantillonneurs quasi-passifs placés directement dans le puits, et permettent donc d'éviter le pompage l'eau vers la surface. Ainsi, le travail de terrain est grandement facilité, et l'accessibilité à cette méthode de datation est améliorée. Cette nouvelle technique a été testée et validée dans un aquifère poreux du Plateau Suisse, ainsi que dans des puits situés dans le contexte fracturé des Basses Terres du St-Laurent, au Canada.

Acknowledgements

None of this work would have been done without the help and support of a lot of people. I would like to express my deepest gratitude to ...

- ... **Dr. Roland Purtschert** for supervising me with unwavering support and guidance; for the countless "quick 10 min meetings" that turned into hours of discussions and the too many draft reviews; for teaching me the mechanics of fieldwork and how there's nothing that can't be fixed (provided you own a Leatherman of course); for all the connections and opportunities; and for always having your door and mind open for questions and discussions of wild ideas.
- ... **Prof. Dr. Markus Leuenberger** for supervising my thesis and for your support each time it was needed.
- ... **Prof. Dr. Reika Yokochi** for examining this thesis, for the constructive and fruitful discussions about science, and your caring advice about non-science.
- ... **Prof. Dr. Saverio Braccini, Dr. Pierluigi Casolaro, and Gaia Dellepiane** for the enjoyable collaboration, for your precious help with the Cyclotron and the neutron flux quantification, and for your kindness in all circumstances.
- ... **Prof. Dr. Philip Bunner, Prof. Dr. Daniel Hunkeler, Dr. Hugo Delottier, Morgan Peel, Laurent Marguet, and Roberto Costa** for the compelling exchanges; for the support with the model and in the field; and for always making me feel welcome at CHYN.
- ... **Prof. Dr. Rolf Kipfer, and Dr. Andrea Popp** for the fruitful collaboration in Emmental, for your support in the field, and for always bringing relevant insight into the discussions.
- ... **Prof. Dr. Florent Barbecot and Dr. Guillaume Meyzonnat** for the supervision and cooperation, but also for welcoming me to Montreal and making me feel at home at 6000 km from home.
- ... **Dr. Klaus Hinsby and Dr. Lars Trolldborg** for your support in Copenhagen, in the field, and with the DK-Model; for always being helpful whatever demand we had.
- ... **Dr. Sophie Guillon** for your help with the numerical models, and your precious time spent on the Hytec verification.

- ... **Rüdiger Schanda, Kurt Grossenbacher, Samuel Mareending, Remo Walther, and Christoph Reinhard** for the technical support in the field and the lab; for your infinite patience with my clumsiness and your perseverance with my German.
- ... **Doris Rätz, Bettina Schüpbach, and Dr. Gunnar Jansen** for always having a solution and a smile for me, no matter what question I bothered you with.

Special thanks should also go to...

- ... **Dr. Tito Arosio, Chantal Zeppenfeld, and Dr. Loïc Schmidely** for the exchanges and for the refreshing outdoor times, whether it involved skis, bikes, or quickdraws.
- ... **Dr. Lucas Silva, Florian Krauss, and Jeemijn Scheen** for your kindness, your little attention, and the deep discussions.
- ... **Markus Grimmer, Vasileios Mandrakis, Lison Soussaintjean, Camilla Jensen, Geunwoo Lee, Imogen Gabriel, Dr. Daniel Baggenstos and Stephan Raiss** for the compassionate support, for adopting me in the "cool kids" group, and for all the good laughs. The journey would not have been the same without you guys
- ... **Eric Humphrey, Gus Wulsin, Arnaud Ruegg, Dr. Reza Sohrabi, Valentin Dall'Alba, Alexis Neven, Sebastien Giroud, and Capucine Marion** for the compelling science exchanges and the forever memories together.

And last but not least...

- ... **Laurence Fischer, Aude Schmid, Emilie Sammali, Clément Brügger, Loric Bovard, and Marc Wehrli** for being the best friends I could possibly ask for; for always being around and blindly believing in me although still wondering what I was actually doing during four years; for the too many glasses of wine, and the lifelong memories that come with them.
- ... **My parents and brother** for giving me the privilege of always choosing my path, for teaching me the meaning of the word "family," and for your forever and unconditional support in any form and situation.
- ... **Marc Andenmatten** for keeping up with grumpy me and loving me a little bit harder each time I was not really lovable; for all the discussions about differential equations; for your understanding and rock-solid support for the late night and early mornings; and for believing in me far more than I ever did.

Contents

Summary	i
Résumé	iii
Acknowledgements	v
1 General Introduction	1
1.1 Structure of the thesis	3
1.2 Groundwater Dating	6
1.3 Environmental tracers	9
References	12
I ^{39}Ar and ^{37}Ar Underground Production	15
2 Introduction : radioargon isotopes	17
2.1 ^{39}Ar and ^{37}Ar applications	17
2.2 Radioargon Sampling and Measurement	20
2.3 Goals and structure of this part	22
References	23
3 Radioargon underground production rates	27
3.1 Introduction: particle fluxes in the atmosphere and underground	27
3.1.1 Cosmogenic particles	27
3.1.1.1 Hadronic component	29
3.1.1.2 Muonic component	30
3.1.2 In-situ Neutrons	35
3.1.2.1 Neutrons from natural rock radioactivity	35
3.1.2.2 Muon-induced neutrons	37
3.2 Radioargon (^{39}Ar and ^{37}Ar) production rates	38
3.2.1 Overview	38
3.2.2 Muon capture reactions	41
3.2.3 Reactions with neutrons	45
3.2.3.1 Argon production cross sections	45

3.2.3.2	Neutron production rates	45
3.2.3.3	Neutron fluxes and energy spectra	51
3.2.4	Total radioargon production rate profiles	53
3.2.4.1	$^{37}\text{Ar}/^{39}\text{Ar}$ ratios	55
3.3	Uncertainties	57
3.3.1	Uncertainties on the muon-capture reaction	57
3.3.2	Uncertainties on the production with neutrons	57
3.3.2.1	Uncertainties on the neutron production rates	58
3.3.2.2	Uncertainties on the neutron energy spectra	60
3.3.3	Total uncertainty on the production rate	62
3.4	Conclusions and outlooks	64
	References	66
4	Determining emanation fractions for ^{39}Ar and ^{37}Ar through irradiation experiments	71
4.1	Introduction	71
4.2	[Article]Quantification of ^{37}Ar emanation fractions from irradiated natural rock samples and field applications	72
4.3	Quantification of ^{39}Ar emanation fractions: preliminary results	87
4.4	Discussion: from the laboratory experiments to the field scale applications . .	90
4.5	Conclusions and outlooks	93
	References	94
5	Field application: Dating groundwater with ^{39}Ar - Underground production in the Danish shallow aquifer system	95
5.1	Introduction	95
5.2	Climatic, geological, and hydrogeological settings of the study area	96
5.3	Material and methods	97
5.3.1	Tracer Data	97
5.3.2	Groundwater Model	101
5.3.3	Emanation fractions	102
5.4	Results	103
5.4.1	Residence time and vertical velocities distributions	103
5.4.2	Activity concentration profiles	105
5.5	Discussion	108
5.6	Conclusions and outlooks	109
	References	111
6	Simulations: Using numerical modeling to constrain the importance of radioargon underground production	113
6.1	Introduction	113

6.2	Material and methods	114
6.2.1	Groundwater models	114
6.2.1.1	Hydrogeosphere	114
6.2.1.2	Hytec	116
6.2.2	Recharge scenarios	116
6.3	Results and discussion	117
6.3.1	Verification with Hytec	117
6.3.2	^{39}Ar , ^{37}Ar and mean age simulations	118
6.3.3	Importance of radioargon underground production	121
6.3.4	^{39}Ar groundwater dating clock	124
6.4	Conclusions and outlooks	125
	References	127
7	Field application: Using ^{37}Ar to trace Surface water - Groundwater interactions in an alluvial aquifer	129
7.1	Introduction	129
7.1.1	Principles of using ^4He , ^{222}Rn and ^{37}Ar for the assessment of SW-GW interactions	130
7.2	[Article]A Framework for Untangling Transient Groundwater Mixing and Travel Times	133
7.3	^{37}Ar as an indicator of SW-GW interactions	151
7.3.1	Background secular equilibrium profile	151
7.3.2	Infiltrating river water fraction and activity concentration	153
7.3.2.1	Background piezometer A41	156
7.3.3	Effect of the variation of the forcing parameters on ^{37}Ar activities	156
7.3.3.1	Monitoring piezometers P48- P52 - RB1	156
7.3.3.2	Pumping well VB2	157
7.4	Conclusions and outlooks	158
	References	160
8	Conclusions : lessons learned and outlooks about ^{39}Ar and ^{37}Ar underground production	163
II	Development of a new sampling method for ^{85}Kr	167
9	Introduction: ^{85}Kr as a tracer for groundwater dating	169
	References	171
10	[Article]In-situ sampling for ^{85}Kr groundwater dating	173

Appendix	A1
A.1 ^{39}Ar underground production in the context of groundwater dating: importance of muon-induced processes	A1
A.2 Radioargon production calculations for typical rock compositions	A2
A.3 Neutron energy spectra simulations data	A6
A.4 Tracer database Denmark	A16
A.5 [Article]Explicit simulation of environmental gas tracers with integrated surface and subsurface hydrological models	A22
References	A35
 Declaration of consent	 I

Chapter 1

General Introduction

Groundwater is a universal water source for agricultural, energy, industrial, and urban purposes. Due to population growth and the impacts of climate change on the hydrological cycle, it will become even more important in the coming decades. Presently, groundwater is the largest component of freshwater accessible for human use. It accounts for 0.7 % of all water on Earth or 95 % of accessible freshwater and provides more than 50 % of domestic and irrigation water used worldwide. In arid and semi-arid regions, as well as in rural areas, the fraction of fresh water derived from groundwater reaches 80 - 100 %. The overall trend around the globe is a decrease in groundwater levels due to withdrawals exceeding natural recharge. Water supply and food production may become unsustainable in the future if fossil and non-renewable groundwaters are used to increase food production. This motivated the United Nations' Millennium Development Goal (MDG), ratified in 1999 by 180 countries, "to the stop unsustainable exploitation of water resource by developing water management strategies at the regional, national and local levels..." (IAEA, 2013; Shiklomanov and Rodda, 2004).

Knowledge about groundwater bodies on a local scale is required for water officials to ensure adequate and long-term access to the available water resource. To adopt effective policies and share limited-access resources, it is crucial to understand the recharge rates, flow paths, and residence times of water sources (IAEA, 2013). Intensifying efforts to understand groundwater cycles at all scales have allowed over 2.6 billion people to gain access to improved sources of drinking water since 1990. This brought the proportion of the population using "improved drinking water sources" from 76 % in 1990 to 91 % in 2015. Among them, 1.9 billion (58 %) gained access to piped drinking water on premises. If globally, the situation seems to improve in terms of water availability, these statistics are hiding important disparities between regions and within countries. Currently, water scarcity still affects more than 40 % of people around the world (United Nations, 2015). Besides the challenge of water quantity, pressure on groundwater quality also dramatically increased in the past decades. Since 1950, increasing content of contaminants such as nitrates and pesticides have been found in groundwaters globally. Pollution plumes from point sources in urban and industrial areas are also increasingly occurring.

In the context of emergent anthropogenic contaminants, it is particularly important to evaluate the proportion of young water exploited (i.e. recharged in the last decades) since this fraction is very susceptible to emerging pollutant contamination. This is also the groundwater that is quickly renewed and thus the most available. In this paradoxical context, a sustainable equilibrium is required to preserve the quality, as well as the quantity, of this resource. Studies of groundwater age and movement are routinely carried out using isotope tracers, covering a range of periods from a few days to millions of years (Lu et al., 2014). Age information, mostly provided by radionuclides, is critical for validating conceptual flow models, calibrating numerical flow models, and predicting the fate of pollutants in groundwater systems and aquifers (Torgersen et al., 2013).

1.1 Structure of the thesis

This thesis is centered on the applications of radioargon (^{39}Ar and ^{37}Ar) and ^{85}Kr methods for groundwater dating purposes. Constraining groundwater ages is essential for protecting the resource in terms of quantity and quality, as well as implementing management policies that ensure equitable and sustainable access to clean water. **Chapter 1** aims to be a **general introduction** about the definitions and concepts of groundwater age, the common issues inherent to the mixable nature of water, and the existing methods to quantify the residence times. When dealing with radioactive tracers, underground production is a recurring topic. **Part I** of this thesis (Chapters 2 - 8) focuses on the mechanisms of **underground production processes for ^{39}Ar and ^{37}Ar** . **Part II** (Chapters 9 - 10) addresses a common challenge associated with radioactive noble gases isotopes: the logistically demanding sampling methods, which are linked with the relatively large volume of water required to reach the analytical minimum. In particular, the **development of a new sampling method for ^{85}Kr** aims to facilitate access to this method.

Chapter 2 is an **introduction to radioargon isotopes** describing their nuclear characteristics, dating principles, as well as the sampling and measurements methods for both ^{39}Ar and ^{37}Ar . This section sheds light on the state of the art for the underground production processes. Currently, only the processes involving the natural rock radioactivity and the primary cosmogenic neutrons were assumed to make a significant contribution to radioargon subsurface concentrations in the context of groundwater dating. While muon-induced reactions have been documented for other domains, they have not been considered in this context.

Accurate quantification of **radioargon underground production rates** in rocks is fundamental for assessing the importance of subsurface production processes on groundwater activities. **Chapter 3** is compiling the existing approaches and data for the calculation of ^{39}Ar and ^{37}Ar depth-dependent production rates. The reaction channels with cosmogenic muons and with the secondary neutrons they induce are considered for the first time for depth ranges relevant for groundwater dating applications. The elemental chemical composition measured in three rock formations, which compose the Danish shallow aquifer system, were used in the calculations. Previous simplifying assumptions about the flux and energy spectra of neutrons in the subsurface could be avoided by considering recent particle physics simulations for realistic aquifer conditions. The overall uncertainty of the calculations could be estimated with Monte Carlo iterations to maximal values of 66 - 75 %.

The emanation fractions link the activities produced in the rocks and those effectively measured in the porous space. Therefore, understanding this process is crucial for predicting the dissolved activities originating from subsurface production. A new methodology has been developed in the frame of this thesis in order to **determine the emanation fractions of ^{39}Ar and ^{37}Ar through irradiation experiments (Chapter 4)**. Rock samples ranging between 1 μm and a few cm were irradiated with neutrons in a routinely operated medical cyclotron. The neutron flux and energy were experimentally measured thanks to an innovative neutron spectrometer. The produced activity was calculated and compared with the escaped activities to determine emanation fractions. For ^{37}Ar , values between 0.02 and 6 %, with consistent patterns and reproducible results were obtained. The recoil emanation fraction was increased by soil weathering and the presence of water. Measuring the activities emanated over time provided the first evidence of the diffusive nature of emanation. For radioactive isotopes, this process determines the activity that prevails in the drainable pore space. Moreover, a heating experiment with CaCO_3 allowed the literature values for diffusion parameters and activation energies to be verified and confirmed that solid-phase diffusion emanation is negligible at room temperature for ^{37}Ar . Finally, a proof of principle for ^{39}Ar emanation determination with higher energy neutrons was successfully carried out, allowing the conclusion of emanation fractions in the range of 0.1 to 1 %.

In **Chapter 5**, the production rates and emanation fractions assessed in the two previous chapters were used in a **field application about groundwater dating with ^{39}Ar in the context of the Danish shallow aquifer system**. The local distribution of residence times with depth was constrained by particle tracking simulations. The dissolved activities resulting from subsurface production were calculated using these recharge scenarios and a 1D analytical flow model. For the first time, the importance of muon-induced production processes for ^{39}Ar and ^{37}Ar groundwater activities was unequivocally demonstrated. Data collected during multiple field campaigns and carefully measured by LLC at the University of Bern support these findings. The residence times inferred from ^{39}Ar in-growth rates could be further constrained by ^{85}Kr and $^3\text{H}/^3\text{He}$ ages.

Chapter 6 covers the extrapolation and generalization of the conclusions from the case study in Denmark to other systems and hydrogeological situations. We propose to **use numerical modeling to constrain the importance of underground production** in a variety of recharge scenarios. For this purpose, a synthetic model was set up in an integrated surface and subsurface hydrological model (HydroGeoSphere). Production rate profiles were implemented in the model, and simulations were run for diverse recharge scenarios. The modeling procedure was furthermore verified by repeating the simulations with another code (Hytec). Subsurface production was demonstrated to have a minor effect in the situation where the water recharges in an unconfined porous aquifer. In contrast, recharge in a fully confined

aquifer, where the infiltration is impeded at shallow depth (<50 m) results in significant age biases. Numerical methods proved to be an appropriate tool for further constraining the critical scenarios for underground production.

Chapter 7 aims to use ^{37}Ar to trace surface water - groundwater interactions in alluvial aquifers. This is the continuation of previous efforts to use this method in the Emmental catchment in Switzerland. New ^{37}Ar samples were collected in the frame of a large-scale pumping experiment together with ^4He and ^{222}Rn . Transient mixing ratios and travels times were unraveled using the combined and continuous monitoring of ^4He and ^{222}Rn . Currently, this framework does not fully integrate the newly sampled ^{37}Ar data. In this section, we discuss their unique ability to provide depth-integrated information about percolation patterns.

Chapter 8 summarizes the lessons learned from ^{39}Ar and ^{37}Ar underground production and provides an overview of the issues at stake.

^{85}Kr applications as a tracer for groundwater dating are introduced in **Chapter 9**. This short section presents the nuclear characteristics and measurement methods with LLC and Atom Trap Trace Analysis (ATTA) for krypton isotopes. There are several challenges associated with conventional sampling, disrupting well stratigraphy and preferential drainage from permeable aquifer fractions. In this context, the passive samplers developed for **in-situ sampling for ^{85}Kr groundwater dating** **Chapter 10** are providing a practical solution, which facilitates field work while minimizing the disturbance of the groundwater system. This method was tested in combination with conventional sampling, as well as passive and active $^3\text{H}/^3\text{He}$ sampling in a porous aquifer in Switzerland. The ages inferred from the different tracers are in agreement with each other, and consistent with the expected age stratigraphy for a porous unconfined aquifer. With the different methods, different information can be collected on the dynamics and age of waters from different compartments of an aquifer with varying conductivities.

1.2 Groundwater Dating

Age of Groundwater

The concept of "age" is unambiguous and intuitively understood by every human. Its application to natural systems inherently assumes a finite volume of material or atoms with a defined initiation time (e.g. ^{14}C dating for a tree). However, groundwater is by nature mobile and mixable, and thus defining the term "age" in this context is not trivial. A bunch of water molecules that infiltrate together may be kilometers away from the location where the sample is taken, allowing time for a wide range of dispersion and diffusion processes (Suckow, 2014). Moreover, water molecules exchange their hydrogen atoms with each other within picoseconds, (Starr et al., 1999) and therefore, even at the smallest scale, the raindrop and the sampled molecules are not the same.

Idealized Age

One way to address this issue is by imagining an infinitesimally small water parcel, which is not influenced by any mixing, dispersion, or diffusion processes, and that is attributed to a flow path and travel time from the groundwater surface to the point of sampling (Suckow, 2014). Thus, the "idealized groundwater age" ΔT is defined as the time elapsed between the infiltration (i.e. the entering into the saturated zone) and the sampling at a specific point (x, y, z) , presumably located at a distance ΔS downstream in the groundwater system [Figure 1.1a, Torgersen et al. (2013)]. Although it is not very realistic, this concept serves as the legal basis for delimiting the protection zones around pumping facilities for drinking water. In Switzerland, for example, the so-called "S2 zone" is defined (among other criteria) by the distance allowing for a groundwater residence of 10 days or more (OEaux, 1998).

Mean residence time

The mean residence time is approached by considering the mass balance in and out of a finite volume. This concept is the basis for the finite differences groundwater flow and transport models, which discretize the system in a large number of these control volumes, and iteratively solve the mass balance equation for them. The water movement being driven by gradient and entropy, the transport path of one molecule of water differs from the mean path obtained by averaging all the molecules in and out of the volume. Consequently, water molecules reside for differing periods in any finite-sized sample of groundwater. Even in 1-D, at the smaller- and short- sampling scale, groundwater is composed of water molecules that have undergone individual transport and mixing reactions, along which dispersive processes alter any idealized groundwater age to a frequency distribution. Additionally, finite sampling volumes and transverse dispersion mix pathways of different lengths from possibly

different recharge entryways when considering the 2-D and 3-D (Figure 1.1b and 1.1c). This leads to potentially asymmetric and very wide age distributions. Therefore, a water sample at a specific location should not be characterized by a single value of "age" but rather a frequency distribution of ages (Torgersen et al., 2013; Suckow, 2014). Considering a central tendency, although it's tempting, is almost always misleading. Transverse dispersion from less permeable aquifer areas (aquitard) also mixes older water, resulting in asymmetric tails for the frequency distribution of groundwater ages (Figure 1.1d).

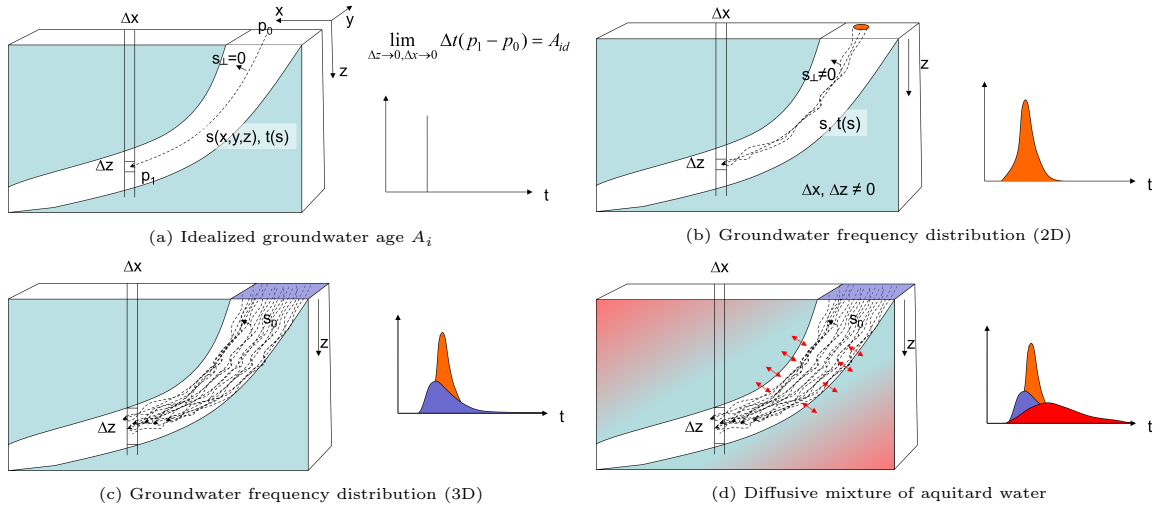


Figure 1.1: Groundwater age concept [modified from Torgersen et al. (2013)]

Theoretically, mean residence times can be calculated based on fluid mass transport physics: based on Darcy's law, travel times and velocity distribution can be calculated from the water table to any point in the system, assuming that the permeability and the hydraulic gradient are precisely known. However, the heterogeneity inherently associated with the underground hydrogeological systems at multiple scales can not realistically be captured by this method. Therefore, we must rely on inferences derived from the concentration of chemical or isotopic tracers measured in a water sample (Bethke and Johnson, 2008).

Tracers are either isotopes of the water molecule or substances that are transported in a similar way as the water molecules. They allow for a quantitative conclusion about natural systems' behavior. An ideal tracer follows the processes like transport, mixing, and chemical reactions undergone by water molecules. However, "similar to" is not "exactly as": sometimes tracers might be retarded degraded, or subject to different net transport directions due to concentration gradients and diffusion. It is, therefore, important to distinguish between tracer and groundwater ages. In principle, groundwater residence times can always be converted to tracer concentrations, whereas the inverse does not necessarily result in a unique solution. For this reason, multiple tracers are commonly used for groundwater studies (Suckow, 2014; Torgersen et al., 2013; Lu et al., 2014).

Mixing Models

The discrepancy between the concept of age as a time difference attributed to an infinitesimal small water parcel, the residence time distribution, and the real-world samples can be solved with mathematical models. Residence time distributions are linked with measurable tracer concentrations (flowing in and out of a given volume) with a convolution integral [Eq. 1.1, Małoszewski and Zuber (1982)]. Because these models integrate all system properties into a few parameters, they are called "Lumped Parameter Models" (LPM) (Suckow, 2014). In this mathematical representation, the "age" is equivalent to the idealized age, which is the difference between the input time t' and the sampling time t . The model is, however, considering the frequency distribution of all the ages in the defined volume $g(t-t')$. For a radioactive tracer, the term $\exp(-\lambda(t-t'))$ accounts for radioactive decay.

$$C_{out} = \int_{-\infty}^t C_{in}(t') \cdot g(t-t') \cdot \exp(-\lambda(t-t')) dt' \quad (1.1)$$

LPM are able to compute the *mean residence time* (MRT) of a sample, which is a weighted average of all idealized ages. LPM can then assess the residence time distributions by minimizing the difference (least square fitting) between the tracer concentrations inferred from the MRT and measurements (Suckow, 2014). By combining multiple tracers with knowledge of hydrogeology, it is often possible to gain a better understanding (at least qualitatively) of the relationship between tracer model ages and groundwater ages in a location (Torgersen et al., 2013).

1.3 Environmental tracers

Environmental tracers are natural or anthropogenic compounds or isotopes widely distributed in the near-surface environment of the Earth. Variations in their abundance can then be used to determine pathways and timescales of environmental processes (Cook and Böhlke, 2000). They are typically broadly distributed with a relatively weak signal contrarily to compounds deliberately introduced to the environment at high concentrations for local experiments. Tracer methods are subdivided into three categories (Bethke and Johnson, 2008):

1. Asymptotic decay methods: based on the radioactive decay of nuclides isolated from their atmospheric source once they infiltrate.
E.g. ^{14}C (Loosli and Oeschger, 1980; Plummer and Glynn, 2013; Fontes and Garnier, 1979; Seltzer et al., 2021), ^{39}Ar (Loosli et al., 1989; Purtschert, 2008; Yokochi et al., 2012; Mace et al., 2017), ^{36}Cl (Corcho Alvarado, 2005; Alfimov and Ivy-Ochs, 2009)
2. Linear accumulation methods: stable nuclides that are produced in the underground and accumulate in flowing groundwater.
E.g. ^4H (Torgersen, 2010; Solomon et al., 1996; Kipfer et al., 2002), ^{222}Rn (Cecil and Green, 2000; Peel et al., 2022; Popp et al., 2021) and ^{40}Ar (Yokochi et al., 2012)
3. History matching methods: radionuclides, or anthropogenic chemical compounds released into the atmosphere since industrial times, whose atmospheric activity is known.
E.g. ^{85}Kr (Musy et al., 2021; Smethie Jr et al., 1992), CFC (Cook and Böhlke, 2000; Plummer and Cook, 2006), SF_6 (Darling et al., 2012)

Radioactive Noble Gases

Groundwater dating methods using radioactive noble gases are based on their asymptotic radioactive decay. For isotopes like ^{39}Ar or ^{81}Kr , nuclear reactions with cosmic rays in the atmosphere results in a constant input concentration (Purtschert et al., 2013, 2021; Loosli, 1983). In addition, during the past ~ 70 years, human activities have released several chemical and isotopic substances into the atmosphere (Figure 1.2). The monitoring of their atmospheric concentrations provides an ideal input function for tracers like ^3H ($t_{1/2} = 12.3$ yrs) and ^{85}Kr ($t_{1/2} = 10.8$ yrs). ^3H was introduced into the atmosphere by nuclear weapon testing, mostly between 1954 and 1964 (Bethke and Johnson, 2008). The decreasing ^3H atmospheric concentration resulted in almost no concentration gradient over the last 10 years. This is overcome by considering its accumulating daughter product ^3He (Gilmore et al., 2021). Therefore, the $^3\text{H}/^3\text{He}$ age does not require knowledge of the atmospheric input curve. ^{85}Kr is released during reprocessing of spent fuel rods from nuclear reactors (Bollhöfer et al., 2018).

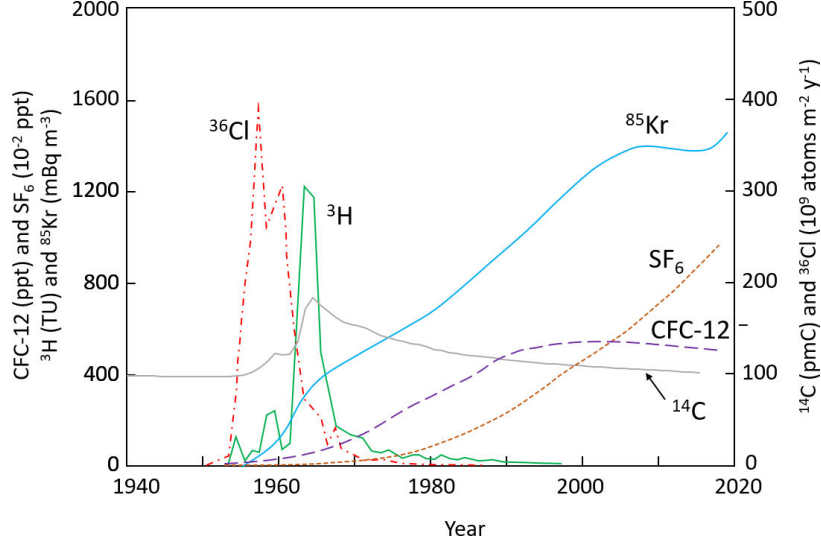


Figure 1.2: Atmospheric concentrations (annual average) of some environmental tracers used as event markers for groundwater dating (Cook, 2020)

Dissolved in precipitations, the radioactive isotopes enter the subsurface and are subsequently isolated from their source. The radioactive decay is then, in the ideal case, the only process changing the tracer concentration in the subsurface. In this case, the apparent tracer age can be calculated from the activity concentration sampled C and the input activity concentration C_0 , with λ being the radioactive decay constant (Eq. 1.2).

$$t = \frac{\ln(\frac{C}{C_0})}{-\lambda} \quad (1.2)$$

Noble gases (Ar, Kr) are preferred tracers despite the high analytical requirements because of the absence of geochemical reactions. In contrast, chemical reactive tracers are often easier to measure, but they are susceptible to dissolution or degradation processes, which are difficult to quantify [e.g. ^{14}C , Seltzer et al. (2021); Fontes and Garnier (1979)]. The tracer input function and its decay rate in the subsurface define the applicable dating range (Figure 1.3). Sometimes, multiple tracers apply to the same time range, allowing for a broader choice or verification between methods [e.g. $^3\text{H}/^3\text{He}$ and ^{85}Kr , Musy et al. (2021)]. Other tracers are closing gaps between methods. For instance, ^{37}Ar is the only tracer usable between ^{222}Rn and $^3\text{H}/^3\text{He}$, and ^{39}Ar closes the gap between ^{85}Kr , and ^{14}C .

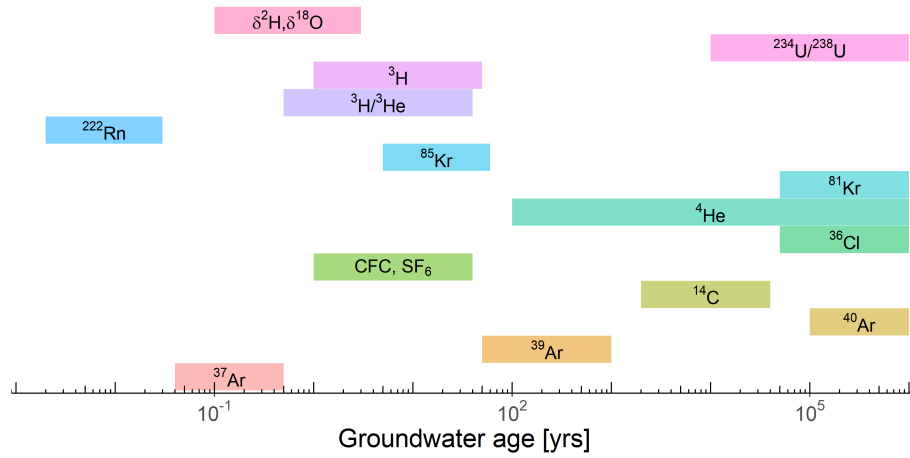


Figure 1.3: The timescale for the application of the principal environmental tracers [Modified from Suckow (2014), and Aggarwal (2013)].

In most cases, the production of radioactive noble gases in the underground is assumed to be negligible. However, early studies have already suggested that this is not always accurate. During her Ph.D., Prof. Dr. Fabryka-Martin was the first one to compile a large number of radionuclide equilibrium concentration calculations for a variety of rock compositions (Fabryka-Martin, 1988). The remarkable accuracy of her calculations, especially given the state of the art at the time, makes her a pioneer whose work is still the main reference for any underground production calculation in present days. The highly over-modern ^{39}Ar , ^{37}Ar and ^{85}Kr activities measured in the Stripa groundwaters in Sweden (Loosli et al., 1989) constitute the first unequivocal demonstration of radionuclides underground production. Since then, the advents in the dating methods with radionoble gases have resulted in an increasing number of case studies where more and more evidence of subsurface production could be observed. If these processes are not correctly accounted for, the groundwater residence times inferred from the radionuclide activities are underestimating the real age of the water. The conclusion of ages biased toward young values can have important consequences for resource management and recharge rate assessments. For this reason, a solid understanding of the processes responsible for radioactive noble gas underground production, as well as their sound quantification is needed.

References

- Aggarwal, P. K. (2013). *Introduction to Isotope methods for dating old groundwater*.
- Alfimov, V. and Ivy-Ochs, S. (2009). How well do we understand production of ^{36}Cl in limestone and dolomite? *Quaternary Geochronology*, 4(6):462–474.
- Bethke, C. M. and Johnson, T. M. (2008). Groundwater Age and Groundwater Age Dating. *Annual Review of Earth and Planetary Sciences*, 36(1):121–152.
- Bollhöfer, A., Schlosser, C., Schmid, S., Konrad, M., and Purtscher, R. (2018). Krypton-85 concentration in air in Central Europe and indications for groundwater dating.
- Cecil, L. D. and Green, J. R. (2000). Radon-222. In Cook, P. G. and Herczeg, A. L., editors, *Environmental Tracers in Subsurface Hydrology*, pages 175–194. Springer US, Boston, MA.
- Cook, P. (2020). *Introduction to Isotopes and Environmental Tracers as Indicators of Groundwater Flow*.
- Cook, P. G. and Böhlke, J.-K. (2000). Determining timescales for groundwater flow and solutes transport. In *Environmental Tracers in Subsurface Hydrology*, pages 1–30. Cook Peter G., Herczeg Andrew L., CSIRO Land and Water, Glen Osmond, Australia, springer science+business media, llc edition.
- Corcho Alvarado, J. A. (2005). *Multiple environmental tracer approaches to resolve the age structure of groundwater in European aquifers*. PhD thesis, Universität Bern.
- Darling, W., Gooddy, D., MacDonald, A., and Morris, B. (2012). The practicalities of using CFCs and SF6 for groundwater dating and tracing. *Applied Geochemistry*, 27(9):1688–1697.
- Fabryka-Martin, J. (1988). *Production of radionuclides in the earth and their hydrogeologic significance, with emphasis on chlorine-36 and iodine-129*. PhD Thesis, University of Arizona, Tucson.
- Fontes, J.-C. and Garnier, J.-M. (1979). Determination of the initial ^{14}C activity of the total dissolved carbon: A review of the existing models and a new approach. *Water Resources Research*, 15(2):399–413.
_eprint: <https://onlinelibrary.wiley.com/doi/pdf/10.1029/WR015i002p00399>.
- Gilmore, T., Cherry, M., Gastmans, D., Humphrey, E., and Solomon, D. (2021). The $^3\text{H}/^3\text{He}$ Groundwater Age-Dating Method And Applications. *Derbyana*, 42.
- IAEA (2013). *Isotope Methods for Dating Old Groundwater*. Non-serial Publications. INTERNATIONAL ATOMIC ENERGY AGENCY, Vienna.
- Kipfer, R., Aeschbach, W., Peeters, F., and Stute, M. (2002). Noble Gases in Lakes and Ground Waters. *First publ. in: Reviews in Mineralogy and Geochemistry 47 (2002), pp. 615-700*, 47.
- Loosli, H. (1983). A dating method with ^{39}Ar . *Earth and Planetary Science Letters*, 63(1):51–62.
- Loosli, H., Lehmann, B., and Balderer, W. (1989). Argon-39, argon-37 and krypton-85 isotopes in Stripa groundwaters. *Geochimica et Cosmochimica Acta*, 53(8):1825–1829.
- Loosli, H. H. and Oeschger, H. (1980). Use of ^{39}Ar and ^{14}C for groundwater dating.
- Lu, Z. T., Schlosser, P., Smethie, W. M., Sturchio, N. C., Fischer, T. P., Kennedy, B. M., Purtschert, R., Severinghaus, J. P., Solomon, D. K., Tanhua, T., and Yokochi, R. (2014). Tracer applications of noble gas radionuclides in the geosciences. *Earth-Science Reviews*, 138:196–214.

- Mace, E., Aalseth, C., Brandenberger, J., Day, A., Hoppe, E., Humble, P., Keillor, M., Kulongoski, J., Overman, C., Panisko, M., Seifert, A., White, S., Wilcox Freeburg, E., and Williams, R. (2017). Methods for using argon-39 to age-date groundwater using ultra-low-background proportional counting. *Applied Radiation and Isotopes*, 126:9–12.
- Małoszewski, P. and Zuber, A. (1982). Determining the turnover time of groundwater systems with the aid of environmental tracers. *Journal of Hydrology*, 57(3-4):207–231.
- Musy, S., Meyzonnat, G., Barbecot, F., Hunkeler, D., Sültenfuss, J., Solomon, D. K., and Purtschert, R. (2021). In-situ sampling for krypton-85 groundwater dating. *Journal of Hydrology X*, 11:100075.
- OEaux (1998). Ordinance on water protection (Ordonnance sur la protection des eaux) - Swiss federal council.
- Peel, M., Kipfer, R., Hunkeler, D., and Brunner, P. (2022). Variable ^{222}Rn emanation rates in an alluvial aquifer: Limits on using ^{222}Rn as a tracer of surface water – Groundwater interactions. *Chemical Geology*, 599:120829.
- Plummer, L. N. and Cook, P. G. (2006). Principles of Chlorofluorocarbons dating. In *Use of Chlorofluorocarbons in hydrogeology*, pages 17–29. I.A.E.A, Vienna.
- Plummer, L. N. and Glynn, P. (2013). Radiocarbon Dating in Groundwater systems. In *Isotope methods for dating old groundwater*, pages 91–124. Vienna, i.a.e.a library edition. OCLC: 844871473.
- Popp, A. L., Pardo-Álvarez, , Schilling, O. S., Scheidegger, A., Musy, S., Peel, M., Brunner, P., Purtschert, R., Hunkeler, D., and Kipfer, R. (2021). A Framework for Untangling Transient Groundwater Mixing and Travel Times. *Water Resources Research*, 57(4):e2020WR028362. _eprint: <https://onlinelibrary.wiley.com/doi/pdf/10.1029/2020WR028362>.
- Purtschert, R. (2008). Timescales and tracers. *Natural groundwater quality*, pages 91–108.
- Purtschert, R., Yokochi, R., Jiang, W., Lu, Z.-T., Mueller, P., Zappala, J., Van Heerden, E., Cason, E., Lau, M., Kieft, T., Gerber, C., Brennwald, M., and Onstott, T. (2021). Underground production of ^{81}Kr detected in subsurface fluids. *Geochimica et Cosmochimica Acta*, 295:65–79.
- Purtschert, R., Yokochi, R., and Sturchio, N. C. (2013). Krypton-81 dating of old groundwater. In *Isotope methods for dating old groundwater*, pages 91–124. Vienna, i.a.e.a library edition. OCLC: 844871473.
- Seltzer, A. M., Bekaert, D. V., Barry, P. H., Durkin, K. E., Mace, E. K., Aalseth, C. E., Zappala, J. C., Mueller, P., Jurgens, B., and Kulongoski, J. T. (2021). Groundwater residence time estimates obscured by anthropogenic carbonate. *Science Advances*, 7(17):eabf3503. Publisher: American Association for the Advancement of Science.
- Shiklomanov, I. A. and Rodda, J. C. (2004). World water resources at the beginning of the twenty-first century. *UNESCO*, 41(07):41–4063–41–4063.
- Smethie Jr, W. M., Solomon, D. K., Schiff, S. L., and Mathieu, G. G. (1992). Tracing groundwater flow in the Borden aquifer using krypton-85. *Journal of Hydrology*, 130(1-4):279–297.
- Solomon, D. K., Hunt, A., and Poreda, R. J. (1996). Source of radiogenic helium 4 in shallow aquifers: Implications for dating young groundwater. *Water Resources Research*, 32(6):1805–1813.
- Starr, F. W., Nielsen, J. K., and Stanley, H. E. (1999). Fast and slow dynamics of hydrogen bonds in liquid water. *Physical Review Letters*, 82(11):2294.

- Suckow, A. (2014). The age of groundwater – Definitions, models and why we do not need this term. *Applied Geochemistry*, 50:222–230.
- Torgersen, T. (2010). Continental degassing flux of 4He and its variability. *Geochemistry, Geophysics, Geosystems*, 11(6):n/a–n/a.
- Torgersen, T., Purtschert, R., Phillips, F. M., Plummer, N., Sanford, W. E., and Suckow, A. (2013). Defining groundwater age. pages 21–32.
- United Nations, U. (2015). *The Millennium Development Goals Report 2015*. Number 15-04513 in The Millennium Development Goals Report. United Nations, New York.
- Yokochi, R., Sturchio, N. C., and Purtschert, R. (2012). Determination of crustal fluid residence times using nucleogenic ^{39}Ar . *Geochimica et Cosmochimica Acta*, 88:19–26.

Part I

^{39}Ar and ^{37}Ar Underground Production

Chapter 2

Introduction : radioargon isotopes

Argon has three stable (^{36}Ar , ^{38}Ar and ^{40}Ar) and more than twenty unstable isotopes. ^{40}Ar is produced in K-bearing minerals by the decay of ^{40}K ($t_{1/2} = 1.248$ Gyr) and constitutes 99.6 % of the argon abundance on Earth (Yokochi et al., 2012). Among the radioactive isotopes, ^{37}Ar and ^{39}Ar are especially of interest in hydrology for their tracer applications (Lal and Peters, 1962).

2.1 ^{39}Ar and ^{37}Ar applications

Argon-39

^{39}Ar ($t_{1/2} = 269$ yrs) is naturally produced in the upper atmosphere by cosmic ray induced spallation and neutron activation of stable ^{40}Ar (reaction channel: $^{40}\text{Ar}(n, 2n)^{39}\text{Ar}$), and decays to ^{39}K by β^- decay. The long residence time of ^{39}Ar in the atmosphere damps its production rate fluctuations and results in a constant concentration (Smith, 1989). The atmospheric mass ratio at steady-state is $8.0 (\pm 0.6) \times 10^{-16}$ (Benetti et al., 2007), which corresponds to a specific activity of $1 \text{ Bq kg}_{\text{air}}^{-1}$ (Mei et al., 2010) or $0.104 \text{ dpm L}_{\text{Ar}}^{-1}$ (Loosli et al., 1989; Loosli and Oeschger, 1968).

The atmospheric argon dissolves in rainwater, infiltrates, and is subsequently isolated from its source. From this point on, ^{39}Ar radioactive decay acts like a chronometer for hydrological reservoirs such as glacial ice, groundwater, and seawater (Lehmann and Purtschert, 1997). ^{39}Ar activities are commonly expressed relative to the atmospheric activity: in % modern. The 100 % modern ^{39}Ar activity in the infiltrating rainwater corresponds to $7.76 \text{ atoms cm}_{\text{W}}^{-3}$ (assuming a temperature $T = 10$ °C during the dissolution). The analytical limit is reached when ^{39}Ar decays to <1 % modern (Yokochi et al., 2012). Thus, in the absence of underground production, the range for ^{39}Ar dating is 50 to 1000 years, where no other reliable dating method exists [Figure 1.3; Ritterbusch et al. (2014)].

ⁱdpm $\text{L}_{\text{Ar}}^{-1}$ is decay per minute, per liter of argon

In opposition to the idea of a strict radioactive decay chronometer, ^{39}Ar activities larger than atmospheric isotopic abundances have been observed in groundwater studies for many decades (Loosli et al., 1989; Andrews et al., 1986). Consequently, significant underground production in the aquifer rock and transfer to the fluid phase must exist. Until recently, these activities were attributed solely to neutron activation reactions of potassium ($^{39}\text{K}(\text{n}, \text{p})^{39}\text{Ar}$) with neutrons from the hadronic component of cosmic raysⁱⁱ, as well as neutrons from natural radioactivity in the rock [natural U and Th decay chains; Fabryka-Martin (1988); Andrews et al. (1989); Šrámek et al. (2017)]. Production with primary cosmogenic neutrons is only significant in the first few meters of soil, where the water typically doesn't reside long and is thus typically neglected for groundwater dating applications. Muons are penetrating cosmogenic secondary particles whose contribution to nuclides and neutrons production rates up kilometers of water equivalent (km.w.e) in the underground is documented in a large body of literature (Malgin and Ryazhskaya, 2008; Kneißl et al., 2019; Aglietta et al., 1999; Mei and Hime, 2006; Malgin, 2017; Kneißl et al., 2019; Braucher et al., 2003; Alfimov and Ivy-Ochs, 2009). These particles were recently identified as significant contributors for ^{39}Ar production (reaction channel: $^{39}\text{K}(\mu^-, \gamma)^{39}\text{Ar}$) in the context of Dark Matter research (Mei and Hime, 2006). However, their importance for shallower groundwater dating applications was never recognized until now.

While insufficient consideration of underground production can create obstacles to groundwater dating, Yokochi et al. (2012) proposed a method using subsurface production as a tool. The chronological applications of ^{39}Ar could be extended by combining it with the radiogenic stable ^{40}Ar : ^{39}Ar reaches a production-decay equilibrium while ^{40}Ar accumulates over time. Consequently, $^{39}\text{Ar}/^{40}\text{Ar}$ ratio decreases with increasing groundwater residence time.

Argon-37

^{37}Ar [$t_{1/2} = 34.95 \pm 0.08$ days; Renne and Norman (2001)] is also naturally produced in the atmosphere by neutron capture on stable ^{40}Ar (reaction channel: $^{40}\text{Ar}(\text{n}, 4\text{n})^{37}\text{Ar}$) and decays to ^{37}Cl by electron capture (EC). Owing to its short half-life and in contrast to ^{39}Ar , ^{37}Ar atmospheric activity is expected to closely follow the variations of the cosmic ray neutron flux time and geographical location (Smith, 1989). In addition, stratospheric vertical transport, emanation from soils, and proximity of anthropogenic sources (emission from power plants) are also influencing the background ^{37}Ar atmospheric activities. In the low troposphere, the ^{37}Ar activity was measured between 0.5–10 mBq m_{air}⁻³ (Purtschert et al., 2017). In the following, we assume the value of 1.2 mBq m_{air}⁻³. As a result, the activity concentration in the infiltrating rainwater is 2×10^{-4} atoms cm_w⁻³.

ⁱⁱIn following, these neutrons are also denoted as "primary cosmogenic neutrons," in opposition with muon-induced neutrons.

In the underground, ^{37}Ar is produced by neutron activation of calcium atoms ($^{40}\text{Ca}(n, \alpha)^{37}\text{Ar}$) and muon capture reactions on potassium ($^{39}\text{K}(\mu^-, 2n)^{37}\text{Ar}$). Riedmann and Purtschert (2011) showed that naturally occurring activities follow an exponentially decreasing depth-dependant profile, peaking at 1 - 2 m below surface up to values of $100 \text{ mBq m}_{\text{air}}^{-3}$. These two orders of magnitude of difference between the atmospheric and underground natural ^{37}Ar activity concentrations make it a very interesting tool for studying surface water - groundwater (SW-GW) interactions. The infiltrating water contains virtually no ^{37}Ar activity. Therefore, the activity sampled at a given depth encloses information about the residence time and percolation depths of the freshly recharged fraction. Among other accumulating tracers, ^{37}Ar closes the gap in timescales of applications between ^{222}Rn and $^3\text{H}/^3\text{He}$ (Schilling et al., 2017; Loosli et al., 2000; Riedmann and Purtschert, 2011).

Additionally, ^{37}Ar is a fission and activation product produced during a clandestine underground nuclear weapon test. It is, therefore, of particular interest when conducting an On-Site Inspection (OSI) to verify the Comprehensive Nuclear-Test-Ban Treaty (CTBT). The latter bans all nuclear test explosions for civilian and military purposes and was adopted by the United Nations General Assembly in 1996. Following an underground nuclear explosion (UNE), radioactive noble gases, and more specifically, ^{37}Ar , $^{131\text{m}}\text{Xe}$, and ^{133}Xe are likely to escape the test chamber. They might be transported to surface within periods from weeks to years by barometric pumping (Johnson et al., 2015; Carrigan et al., 1996; Carrigan and Sun, 2014). The activities produced near the cavities are up to eight orders of magnitude higher than the atmospheric background ($80 - 280 \text{ MBq m}_{\text{air}}^{-3}$ for a 27-kt nuclear test Smith (1971)). The activity transported from a fractured 1 kt detonation to surface gas was modeled in the order of $6 \text{ Bq m}_{\text{air}}^{-3}$ (Carrigan et al., 1996). This is only one order of magnitude higher than the natural activities concluded by Riedmann and Purtschert (2011), highlighting the importance of quantifying the potential background sources for radioargon to be used as a nuclear weapon signature (Johnson et al., 2015; Guillon et al., 2016).

Similarly to ^{39}Ar , the above-mentioned applications only consider the ^{37}Ar production with neutron interactions, even though production processes related to muons were already reported in early literature (Spannagel and Fireman, 1972). ^{39}Ar and ^{37}Ar are therefore produced by very similar reactions and, apart from their half-lives, have identical behavior characteristics. These properties are under-exploited in the current state of the art of their applications. This thesis aims to provide a first framework for combined utilization.

2.2 Radioargon Sampling and Measurement

Measuring ^{39}Ar and ^{37}Ar activity concentrations at natural levels with Low-Level Counting (LLC) methods requires volumes of about $500 \text{ mL}_{\text{STP}}^{\text{iii}}$ of argon (Purtschert et al., 2013; Yokochi et al., 2012). Assuming air equilibrated Water (AEW) at 10°C and a 50 % overall degassing and separation efficiency, a total volume of 2 - 3 tonnes of water must be degassed in the field. In presence of high CH_4 or CO_2 concentrations, for instance, in geothermal systems, even larger volumes of water are required to obtain sufficient quantities of argon (Yokochi et al., 2012). For this purpose, a degassing device was developed by the CEP (Climate and Environmental Physics department) at the University of Bern (Figure 2.1). In this gas extraction system, phase separation over semi-permeable membranes allows the dissolved gases to diffuse from the liquid water to the gas-filled pores through a hydrophobic membrane (therefore preventing the liquid water from passing through the pore). The gas phase in contact with the membrane is maintained at a pressure P1 between 20 - 150 mb, depending on the performance of the pump system and the water and gas fluxes. The extracted gas is compressed (P2) in pre-evacuated sampling containers (alloy cylinders) to be transported to the University of Bern (Purtschert et al., 2013).

The separation of noble gases from the gas mixture sampled at the LLC laboratory is performed by successive steps involving molecular sieves, a gas chromatography separation system, Ti-furnace, and cold traps (Riedmann, 2011; Purtschert et al., 2013). The activity measurements are realized in the underground laboratory of the University of Bern, located at a depth of 35 m below the surface and providing a cosmic ray background reduction by a factor of ~ 10 . The laboratory walls were constructed utilizing a special concrete selected for its low radioactivity content to minimize the γ -ray flux within the lab. Lead shields were built using lead from ancient shipwrecks with very low intrinsic activity. The proportional counters ($V = 16 - 100 \text{ cm}^3$) are built in high-conductivity O_2 -free Cu. They are typically filled with 10 - 22 bars of pure argon and 6 % of CH_4 (as quenching gas). Each counter is placed in a larger proportional detector acting as an anti-coincidence counter. The counting events are detected as a function of the β -decay energy and compared with the spectra of standards and background gas. The energy spectrum is recorded by a 7-bit Multi-Channel Analyzer (MCA) with a linear energy range of 0 - 35 keV (Loosli, 1983; Purtschert et al., 2013). ^{39}Ar β -decays to the ground level of ^{39}K with decay energy of 565 keV, resulting in a continuous spectrum for the β -particle. ^{37}Ar decays to ^{37}Cl by electron capture (EC). Most of the time, a K-Shell electron is emitted with an average energy of 2.8 keV (McIntyre et al., 2017).

ⁱⁱⁱ Standard temperature and pressure (STP) : 25°C and 1 bar

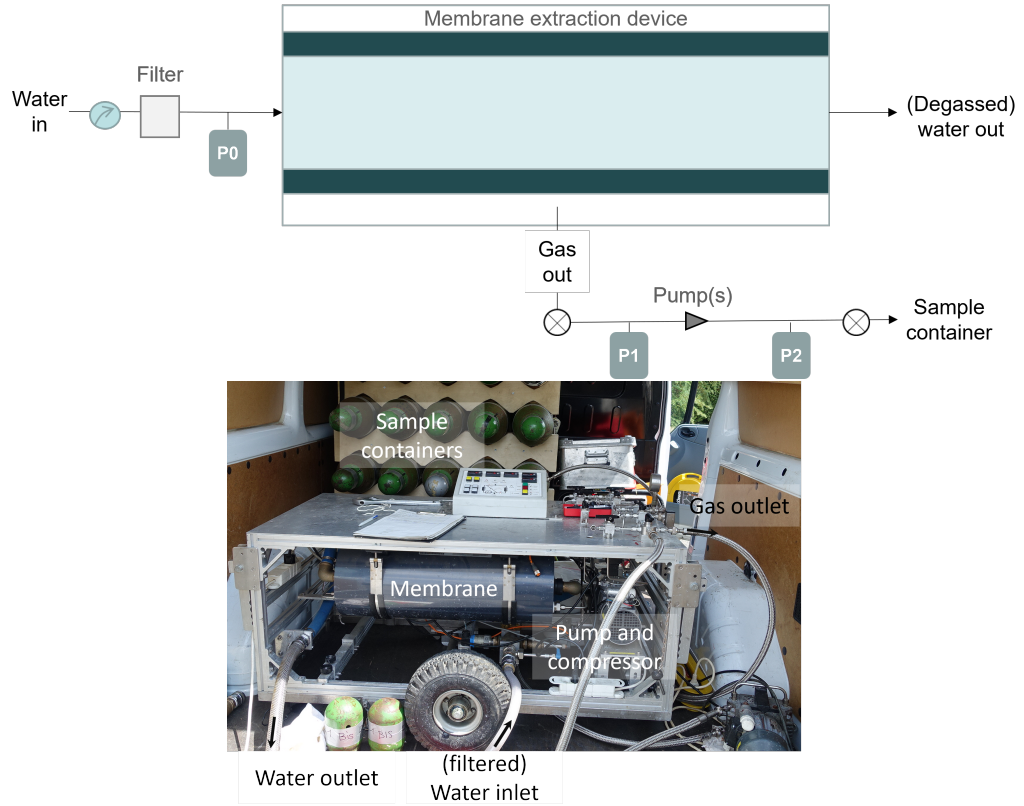


Figure 2.1: Gas extraction system with semi-permeable membranes [modified from Purtschert et al. (2013)]

The radioargon specific activity is calculated from the total net count rate P [Bq] and the known volume of Argon V_{Ar} [cm^3_{Ar}], which can then be converted to mBq m_{Air}^{-3} assuming an argon concentration of 1 % in air. Since the low energy ^{37}Ar decay peak overlaps with the underlying continuous ^{39}Ar spectra, ^{39}Ar is typically the main background source for ^{37}Ar in natural samples (Riedmann and Purtschert, 2011; McIntyre et al., 2017).

2.3 Goals and structure of this part

The first part of this thesis focuses on radioargon underground production processes and their implications. The following factors determine the concentrations of radioactive nuclides underground: (i) Source - the production rate, determined by the natural distribution of the elements and particle fluxes; (ii) Decay - the rate of radionuclide loss that constrains the equilibrium concentrations; (iii) Emanation - the transfer process from the site of production to the pore space where it can be transported, collected and measured; (iv) Transport - the advective and/or diffusive fluid movement in the pore space that influences the equilibrium concentration (Lowrey, 2013).

Chapter 3 is an extensive literature review of all significant subsurface production processes for ^{39}Ar and ^{37}Ar . For the first time, muon capture and muon-induced neutrons are quantified in the depth range relevant for groundwater dating applications. Chapter 4 addresses the quantification of emanation fractions and the importance of recoil versus diffusion processes as a function of the scale considered. In Chapter 5, the production profiles and results from the emanation experiments from the two previous Chapters are used to elucidate over-modern ^{39}Ar activities measured in a field site located in Denmark, in combination with a large-scale national hydrological model. This project highlights the relevance of the newly assessed muon-induced processes for ^{39}Ar and opens the way to the broader investigation of their importance in other recharge contexts. This question is approached with numerical modeling tools in Chapter 6. Chapters 3, 5, and 6 are composing the material for a near-future publication, for which an abstract is found in Appendix A.1. Finally, Chapter 7 presents a field application where ^{37}Ar is used for a SW-GW interaction study in the frame of a large-scale pumping experiment in a major wellfield used for drinking water production in Switzerland.

References

- Aglietta, M., Alyea, E., Antonioli, P., Badino, G., Bari, G., Basile, M., Berezhinsky, V., Bersani, F., Bertaina, M., Bertoni, R., Bruni, G., Romeo, G., Castagnoli, C., Castellina, A., Chiavassa, A., Chinellato, J., Cifarelli, L., Cindolo, F., Contin, A., and Zichichi, A. (1999). Measurement of the neutron flux produced by cosmic ray muons with LVD at Gran Sasso.
- Alfimov, V. and Ivy-Ochs, S. (2009). How well do we understand production of ^{36}Cl in limestone and dolomite? *Quaternary Geochronology*, 4(6):462–474.
- Andrews, J., Davis, S., Fabryka-Martin, J., Fontes, J.-C., Lehmann, B., Loosli, H., Michelot, J.-L., Moser, H., Smith, B., and Wolf, M. (1989). The in situ production of radioisotopes in rock matrices with particular reference to the Stripa granite. *Geochimica et Cosmochimica Acta*, 53(8):1803–1815.
- Andrews, J., Fontes, J.-C., Michelot, J.-L., and Elmore, D. (1986). In-situ neutron flux, ^{36}Cl production and groundwater evolution in Crystalline rocks at Stripa, Sweden. *Earth and Planetary Science Letters*, 77.
- Benetti, P., Calaprice, F., Calligarich, E., Cambiaghi, M., Carbonara, F., Cavanna, F., Cocco, A. G., Di Pompeo, F., Ferrari, N., Fiorillo, G., Galbiati, C., Grandi, L., Mangano, G., Montanari, C., Pandola, L., Rappoldi, A., Raselli, G. L., Roncadelli, M., Rossella, M., Rubbia, C., Santorelli, R., Szec, A. M., Vignoli, C., and Zhao, Y. (2007). Measurement of the specific activity of ^{39}Ar in natural argon. *Nuclear Instruments and Methods in Physics Research Section A: Accelerators, Spectrometers, Detectors and Associated Equipment*, 574(1):83–88.
- Braucher, R., Brown, E. T., Bourlès, D. L., and Colin, F. (2003). In situ produced ^{10}Be measurements at great depths: implications for production rates by fast muons. *Earth and Planetary Science Letters*, 211(3):251–258.
- Carrigan, C. R., Heinle, R. A., Hudson, G. B., Nitao, J. J., and Zucca, J. J. (1996). Trace gas emissions on geological faults as indicators of underground nuclear testing. *Nature*, 382(6591):528–531.
- Carrigan, C. R. and Sun, Y. (2014). Detection of Noble Gas Radionuclides from an Underground Nuclear Explosion During a CTBT On-Site Inspection. *Pure and Applied Geophysics*, 171(3-5):717–734.
- Fabryka-Martin, J. (1988). *Production of radionuclides in the earth and their hydrogeologic significance, with emphasis on chlorine-36 and iodine-129*. PhD Thesis, University of Arizona, Tucson.
- Guillon, S., Sun, Y., Purtschert, R., Raghoo, L., Pili, E., and Carrigan, C. R. (2016). Alteration of natural ^{37}Ar activity concentration in the subsurface by gas transport and water infiltration. *Journal of Environmental Radioactivity*, 155-156:89–96.
- Johnson, C., Armstrong, H., Wilson, W. H., and Biegalski, S. R. (2015). Examination of radioargon production by cosmic neutron interactions. *Journal of Environmental Radioactivity*, 140:123–129.
- Kneißl, R., Caldwell, A., Du, Q., Empl, A., Gooch, C., Liu, X., Majorovits, B., Palermo, M., and Schulz, O. (2019). Muon-induced neutrons in lead and copper at shallow depth. *Astroparticle Physics*, 111:87–99.
- Lal, D. and Peters, B. (1962). Cosmic ray produced isotopes and their application to problems in geophysics. *Progress in Elementary Particle and Cosmic Ray Physics*, 6:1–74. Publisher: Amsterdam.
- Lehmann, B. and Purtschert, R. (1997). Radioisotope dynamics — the origin and fate of nuclides in groundwater. *Applied Geochemistry*, 12(6):727–738.

- Loosli, H. (1983). A dating method with ^{39}Ar . *Earth and Planetary Science Letters*, 63(1):51–62.
- Loosli, H., Lehmann, B., and Balderer, W. (1989). Argon-39, argon-37 and krypton-85 isotopes in Stripa groundwaters. *Geochimica et Cosmochimica Acta*, 53(8):1825–1829.
- Loosli, H. H., Lehmann, B. E., and Smethie, W. M. (2000). Noble gas radioisotopes : ^{37}Ar , ^{85}Kr , ^{39}Ar , ^{81}Kr . In *Environmental Tracers in Subsurface Hydrology*. Cook Peter G., Herczeg Andrew L., CSIRO Land and Water, Glen Osmond, Australia, springer science+business media, llc edition.
- Loosli, H. H. and Oeschger, H. (1968). Detection of ^{39}Ar in atmospheric Argon. page 8.
- Lowrey, J. D. (2013). Subsurface radioactive gas transport and release studies using the UTEX model. Accepted: 2013-10-15T20:18:40Z.
- Malgin, A. S. (2017). Phenomenology of muon-induced neutron yield. *Physical Review C*, 96(1):014605.
- Malgin, A. S. and Ryazhskaya, O. G. (2008). Neutrons from muons underground. *Physics of Atomic Nuclei*, 71(10):1769–1781.
- McIntyre, J. I., Aalseth, C. E., Alexander, T. R., Back, H. O., Bellgraph, B. J., Bowyer, T. W., Chipman, V., Cooper, M. W., Day, A. R., Drellack, S., Foxe, M. P., Fritz, B. G., Hayes, J. C., Humble, P., Keillor, M. E., Kirkham, R. R., Krogstad, E. J., Lowrey, J. D., Mace, E. K., Mayer, M. F., Milbrath, B. D., Misner, A., Morley, S. M., Panisko, M. E., Olsen, K. B., Ripplinger, M. D., Seifert, A., and Suarez, R. (2017). Measurements of Argon-39 at the U20az underground nuclear explosion site. *Journal of Environmental Radioactivity*, 178-179:28–35.
- Mei, D.-M. and Hime, A. (2006). Muon-induced background study for underground laboratories. *Physical Review D*, 73(5).
- Mei, D.-M., Yin, Z.-B., Spaans, J., Koppang, M., Hime, A., Keller, C., and Gehman, V. M. (2010). Prediction of underground argon content for dark matter experiments. *Physical Review C*, 81(5).
- Purtschert, R., Kalinowski, M. B., Bourguin, P., Wieslander, E., Blanchard, X., Riedmann, R., Raghoo, L., Kuśmierczyk-Michulec, J. T., Gheddou, A., and Schlosser, C. (2017). *Ar-37, Be-7 and Xe-133 in the Atmosphere*. CTBTO Expert’s Collection (1998-2021). CTBTO Preparatory Commission, Vienna, Austria. Meeting Name: Science and Technology Conference (2017: Vienna, Austria).
- Purtschert, R., Yokochi, R., and Sturchio, N. C. (2013). Krypton-81 dating of old groundwater. In *Isotope methods for dating old groundwater*, pages 91–124. Vienna, i.a.e.a library edition. OCLC: 844871473.
- Renne, P. R. and Norman, E. B. (2001). Determination of the half-life of ^{37}Ar by mass spectrometry. *Physical Review C*, 63(4):047302.
- Riedmann, R. A. (2011). *Separation of Argon from atmospheric air and Measurement of ^{37}Ar for CTBT purposes*. PhD Thesis, Universität Bern, Bern.
- Riedmann, R. A. and Purtschert, R. (2011). Natural ^{37}Ar Concentrations in Soil Air: Implications for Monitoring Underground Nuclear Explosions. *Environmental Science & Technology*, 45(20):8656–8664.
- Ritterbusch, F., Ebser, S., Welte, J., Reichel, T., Kersting, A., Purtschert, R., Aeschbach-Hertig, W., and Oberthaler, M. K. (2014). Groundwater dating with Atom Trap Trace Analysis of Argon-39. *Geophysical Research Letters*, 41(19):6758–6764.

- Schilling, O. S., Gerber, C., Partington, D. J., Purtschert, R., Brennwald, M. S., Kipfer, R., Hunkeler, D., and Brunner, P. (2017). Advancing Physically-Based Flow Simulations of Alluvial Systems Through Atmospheric Noble Gases and the Novel Argon-37 Tracer Method: Integrating tracers with models. *Water Resources Research*, 53(12).
- Smith, B. (1989). *Naturally occurring nuclear reactions in rock formations and groundwaters*. PhD thesis, University of Bath.
- Smith, J. (1971). Project Gasbuggy: gas quality analysis and evaluation program tabulation of radiochemical and chemical analytical results. Technical Report UCRL-50635(Rev.2); PNE-G-44(Rev.2), California Univ., Livermore. Lawrence Radiation Lab.
- Spannagel, G. and Fireman, E. L. (1972). Stopping rate of negative cosmic-ray muons near sea level. *Journal of Geophysical Research*, 77(28):5351–5359.
- Yokochi, R., Sturchio, N. C., and Purtschert, R. (2012). Determination of crustal fluid residence times using nucleogenic ^{39}Ar . *Geochimica et Cosmochimica Acta*, 88:19–26.
- Šrámek, O., Stevens, L., McDonough, W. F., Mukhopadhyay, S., and Peterson, R. (2017). Subterranean production of neutrons, argon-39 and neon-21 : Rates and uncertainties. *Geochimica et Cosmochimica Acta*, 196:370–387.

Chapter 3

Radioargon underground production rates

3.1 Introduction: particle fluxes in the atmosphere and underground

3.1.1 Cosmogenic particles

The earth's atmosphere is constantly hit by an intense flux of energetic particles accelerated at astrophysical sources. These *primary cosmic rays* originate either from galactic (Galactic Cosmic Rays, GCR) or solar (Solar Cosmic Rays, SCR) sources and are chiefly composed of high energy ($1 - 10^{10}$ GeV) protons, alphas (α), and some heavier particles (Cecchini and Spurio, 2012; Gosse and Phillips, 2001; Palermo, 2016). The primary particles interact with the atoms and nuclei in the atmosphere, resulting in a cascade of particles and reactions: the so-called electromagnetic and hadronic showers, along which energy is lost to the atmosphere. These cascades compose the *secondary cosmic rays*, which are formed by hadrons: baryons (p^+ and n) and mesons (K and π), as well as leptons (e^- , e^+ , μ , ν), and γ -rays (Riedmann and Purtschert, 2011; Garrison, 2014; Palermo, 2016). The cosmic ray fluxes in the atmosphere can therefore be subdivided into three distinct components :

- (i) hadronic: π , K , p^+ and n , which constitute the core of the cascade for energetic events
- (ii) soft: e^- , e^+ , and high energy γ -photons, originating from electromagnetic showers
- (iii) hard: μ resulting mainly from the decay of charged π , and to a minor extent, from K and charmed particles (Riedmann, 2011; Grieder, 2001)

On average, each incident particle generates five successive showers. The total particle flux increases while penetrating in the atmosphere and peaks around 80 to 90 g cm^{-2} [i.e. ~ 20 km; Pfozter Maximum, Allkofer and Grieder (1984)]. Below this altitude, the particle flux decreases due to energy losses and absorption reactions. The secondaries also acquire a transverse momentum resulting in a lateral flux spread (Cecchini and Spurio, 2012).

Attenuation Length As they propagate through the atmosphere and underground, long-lived unstable particles are subject to competition between interaction and decay. Particle lifetime, kinetic energy, and density of the local medium all play major roles in determining which process is likely to occur (Cecchini and Spurio, 2012). The attenuation length is the physical quantity that describes the interaction propensity of a flux of particles with the nuclei of the atoms that constitute the medium and, therefore, its altitude- or depth-dependency. The flux J at a depth h bellow a mass-shielding (in g cm^{-2}) is described by Eq. 3.1, where J_0 is the flux at the surface of the shielding-mass considered, and Λ [g cm^{-2}] is the attenuation length.

$$J = J_0 \cdot \exp -\frac{h}{\Lambda} \quad (3.1)$$

Travel distances are conventionally expressed in equivalent water depth (m.w.e) terms or g cm^{-2} because nuclear particles are attenuated according to the total mass of matter traversed ($1 \text{ m.w.e} = 100 \text{ g cm}^{-2}$). As a result, it is possible to express reaction rates independent of the density of the rock or media.

Most of the secondary particles are absorbed before reaching the Earth's surface, producing for instance cosmogenic radionuclides as ^{14}C in the process, leaving a residual component of weakly interacting particles reaching the air-ground interface. Particles with very low mass, such as ν , can pass through the entire earth without interacting (Smith, 1989; Gosse and Phillips, 2001). n and p^+ undergo strong nuclear interactions and are quickly attenuated in the subsurface. Since they do not undergo strong interactions, muons sit somewhere in the middle and can penetrate through solid rock for a few kilometers (Garrison, 2014).

Cutoff Rigidity The geomagnetic field also influences the probability of cosmic particles reaching Earth's surface, as it deflects low momentum primary cosmic particles back into space (Grieder, 2001). The geomagnetic cutoff rigidity refers to the minimum momentum per unit charge (magnetic rigidity) for an incident particle to reach a particular location on the earth's surface (Gordon et al., 2004). The cutoff rigidity P [GV] is described by the momentum to charge ratio of a particle:

$$P = \frac{p \cdot c}{e} \quad (3.2)$$

where p [$\text{GeV } c^{-1}$] is the momentum of the particle, c is the velocity of light, and e is the particle charge (Dunai, 2000). The cutoff values range from less than 1 GV near the geomagnetic poles to about 16 GV near the equator (Cecchini and Spurio, 2012).

Scaling Factors In the atmosphere, cosmic ray particle flux intensities vary with altitude, location in the geomagnetic field (i.e. latitude), and solar magnetic activity (Gordon et al., 2004). The reference for the cosmogenic fluxes is a horizontal surface at high latitude and sea level (SLHL) with a mid-solar modulation. Any deviation from the standard reference situation is quantitatively addressed by scaling factors (Gosse and Phillips, 2001; Alfimov and Ivy-Ochs, 2009; Dunai, 2000). For instance, cosmic ray intensity is reduced by a factor of ~ 2 at the equator compared to high latitudes (Riedmann, 2011).

3.1.1.1 Hadronic component

In the atmosphere and underground, the high-energy secondary neutrons (≥ 50 MeV) interact with the individual nucleons in nuclei from their environment (Figure 3.1), resulting in the production of nuclides and numerous secondary particles by spallation reactions (Kelley, 2004; Riedmann, 2011). In the energy range of 1 - 5 MeV, spallation reactions are not possible anymore, and neutrons lose their remaining energy by elastic scattering. They pass through the epithermal energy range (0.1 MeV - 0.5 eV) up to the thermal energies (0.025 eV). Eventually, these neutrons are absorbed by the atoms in the medium, resulting in nuclide production (Gosse and Phillips, 2001).

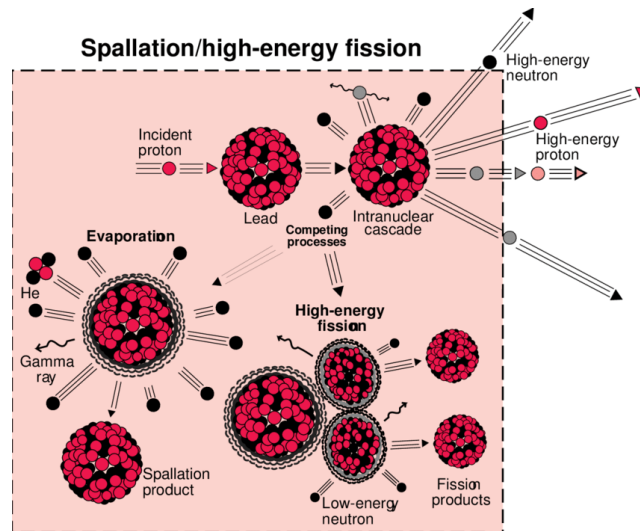


Figure 3.1: Spallation reaction: intranuclear cascade followed by an evaporation-fission stage (Kelley, 2004)

Gordon et al. (2004) measured the neutron energy spectrum and flux on a concrete roof in Yorktown Heights, New York (Figure 3.2). At the earth's surface, the neutron energy spectrum is composed of three peaks. The thermal peak (below 1 eV) reflects neutron thermalization through the atmosphere and back-scattering from the earth. The evaporation peak (~ 1 -2 MeV) has the structure from resonances in the nitrogen and oxygen of the atmosphere and the material surrounding the measurement (concrete roof) (Gordon et al., 2004). The high energy peak (~ 100 MeV) varies by about 30 % daily, with a clear increase on the

high solar activity days (Nakamura et al., 2005). The shape of this neutron spectrum agrees with the one from (Kowatari et al., 2007) in Hokkaido (Japan) at 430 m.a.s.l, supporting the authors' conclusion that neutron energy spectrum shape is independent of altitude.

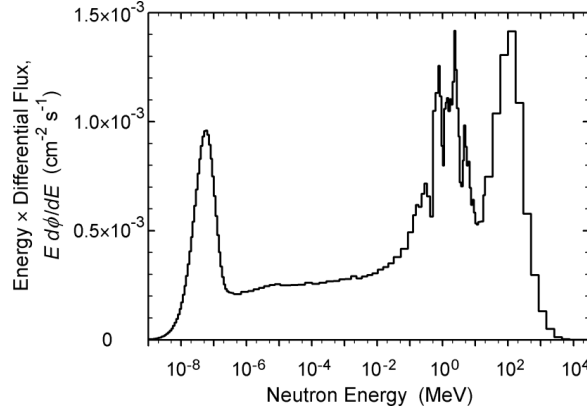


Figure 3.2: Neutron spectrum measured on the roof of the IBM T.J Watson Research Center in Yorktown Heights (U.S.A) measured by (Gordon et al., 2004). The spectrum is represented by the neutron flux (neutron energy E_n , times the fluence rate energy distribution $\partial\phi/\partial E_n$ [also called the differential flux]) versus the energy E_n [MeV]. The energy-integrated neutron flux is $0.0134 \text{ cm}^2 \text{ s}^{-1}$.

In the atmosphere, the neutron attenuation length is in the range of $\Lambda_{n,a} = 160 - 212 \text{ g cm}^{-2}$ (Gordon et al., 2004; Fabryka-Martin, 1988; Riedmann, 2011). Therefore, the atmospheric neutron flux varies by about a factor of 15 between sea level and 3500 m altitude. In comparison, the variation with the latitude is a factor of 2 - 3 between the equator and the poles. Solar modulation induces a smaller variation of 7 - 25 % decrease from maximum to minimum (Gordon et al., 2004). The attenuation length Λ_n for fast neutrons in standard rock is between 140 and 160 g cm^{-2} (Fabryka-Martin, 1988; Stone et al., 1996; Gosse and Phillips, 2001).

3.1.1.2 Muonic component

The free π^\pm and K^\pm mesons in the secondary particle showers can either interact with nuclei in the atmosphere or decay into muons. Eq.3.3 and 3.4 shows the most important decay channels and their respective branching ratios (Cecchini and Spurio, 2012). Muons are charged elementary leptons with about 200 times the rest mass of an electron. They interact with the electromagnetic force, the weak force, and gravity. The reduced interaction probability of these particles (compared to hadrons) makes them the most abundant secondary cosmic ray charged particles at the surface of the earth (Esch, 2001; Niedermann, 2002; Riedmann, 2011; Cecchini and Spurio, 2012). On average, $100 \mu \text{ m}^{-2} \text{ s}^{-1}$ reach the sea level at high latitude with a mean energy of about 4 GeV (Nakamura and Group, 2010). Although they penetrate through significant thickness in most materials, muons can be detected by exploiting the fact that they are charged particles. Hence, they can cause certain materials to scintillate.

$$\pi^\pm \rightarrow \mu^\pm + \nu_\mu \quad (\sim 100\%) \quad (3.3)$$

$$K^\pm \rightarrow \mu^\pm + \nu_\mu \quad (\sim 63.5\%) \quad (3.4)$$

Muons have a half-life of $2.2 \mu\text{s}$ and can only reach the Earth's surface owing to relativistic time dilation (Niedermann, 2002). The dominant spontaneous muon decay processes are described by Eq. 3.5 and 3.6 for their negative, resp. the positive forms (Stone et al., 1998; Garrison, 2014).

$$\mu^- \rightarrow e^- + \bar{\nu}_e + \nu_\mu \quad (3.5)$$

$$\mu^+ \rightarrow e^+ + \nu_e + \bar{\nu}_\mu \quad (3.6)$$

Muon fluxes underground have been extensively studied in recent decades because of the background they induce in deep laboratories ($>1 \text{ km.w.e}$) for rare processes research. This includes the domains of particle, nuclear, and cosmic-ray physics, like for example, low-energy neutrino oscillation and weakly interacting massive particles (WIMP) for Dark Matter detection experiments (Aglietta et al., 1995; Berger et al., 1989; Mei and Hime, 2006; Mei et al., 2010; Wang et al., 2001). At shallow depths ($0 - 100 \text{ m.w.e}$), muons are of interest for geomorphic applications: they induce the production of nuclides underground, which are used to determine surface exposure ages and erosion rates (Alfimov and Ivy-Ochs, 2009; Heisinger et al., 2002b; Stone et al., 1998; Schaller et al., 2002, 2004). In addition, cosmogenic muons are directly ionizing particles, which can also be used for imaging and tomography applications (Ludwig et al., 2019). For example, they were used to look for hidden chambers in pyramids (Morishima et al., 2017), hollow spaces inside volcanos (Oláh et al., 2018), image the damaged reactor cores of Fukushima (Borozdin et al., 2012), or monitor stored CO_2 in geological reservoirs (Klinger et al., 2015).

The underground vertical cosmic-ray muon flux $\phi_{\mu,V} [\text{cm}^{-2} \text{s}^{-1} \text{sr}^{-1}]$ was approximated by semi-empirical parametrizations by many authors (Aglietta et al., 1995; Barbouti and Rastin, 1983; Berger et al., 1989; Bogdanova et al., 2006; Cassidy et al., 1973; Fabryka-Martin, 1988; Heisinger et al., 2002b; Mei and Hime, 2006; Miyake, 1963). Figure 3.3 is a compilation of depth-sensitivity relations (DSR) of vertical muon flux $\phi_{\mu,V}$ for depth ranging from the surface to 100 km.w.e . Generally, a good agreement is observed between 100 and 1000 m.w.e , which is not surprising since this is the range of interest for deep laboratories.

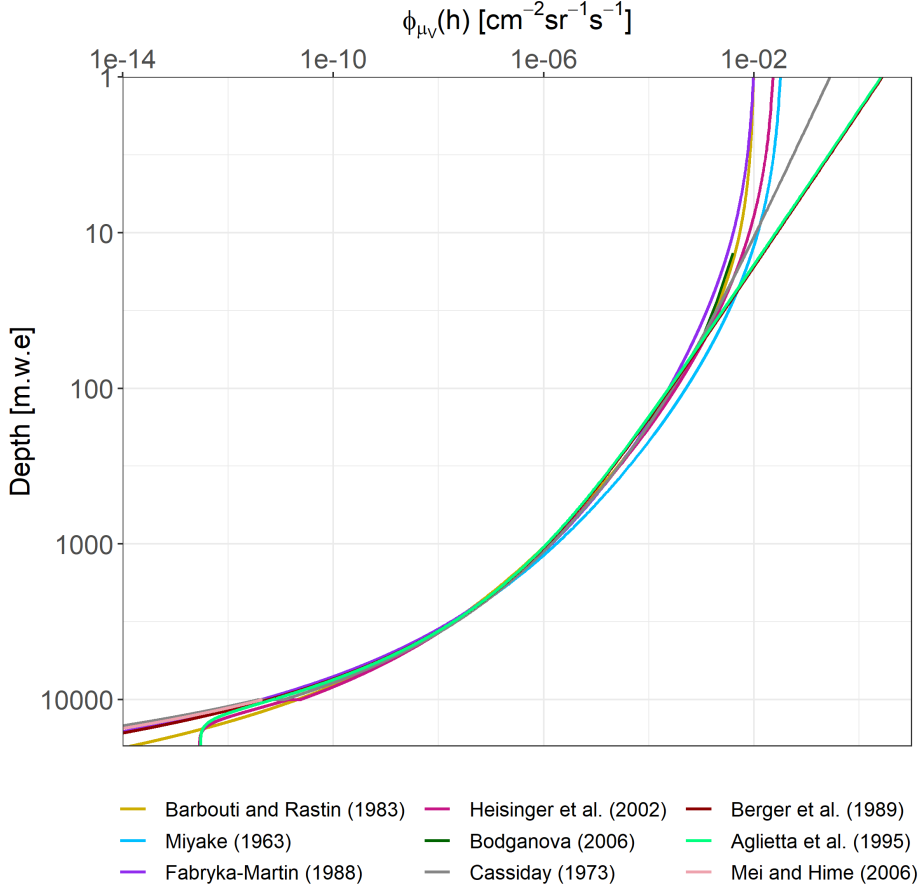


Figure 3.3: Vertical muon intensity $\phi_{\mu,V}$ for depths ranges between surface and 10 km.w.e. The curves are limited to the depth range targetted by their parametrizations

Miyake (1963) was the first to propose the parametrization for lithosphere depth $h < 2000$ m.w.e (Eq. 3.7, Figure 3.4a). Although this is very early literature, the correctness of this estimation was verified by many authors until recent times (Fabryka-Martin, 1988; Alfimov and Ivy-Ochs, 2009; Heisinger et al., 2002b; Grieger et al., 2020).

$$\phi_{\mu,V}(h) = \frac{258.5}{(h + 210) \cdot ([h + 10]^{1.66} + 75)} \cdot \exp(-5.5 \times 10^{-4} \cdot h) \quad (3.7)$$

The angular distribution of incident muons is described by the cosine exponent, $n(h)$ (Eq. 3.8). This empirical factor depends on the muon momentum and depth (Eq. 3.9) (Stone et al., 1996). Experimental measurements with the REGARD muon telescope at 140 m.w.e support these angular- and depth-dependencies (Ludwig et al., 2019). Muons with low energies have a strongly collimated, near vertical flux, gradually changing to a distribution near the horizon for higher energies. This effect occurs because π traveling on inclined trajectories in the low-density upper atmosphere are more likely to decay into energetic muons than to interact with atmospheric nuclei. Conversely, π traveling vertically

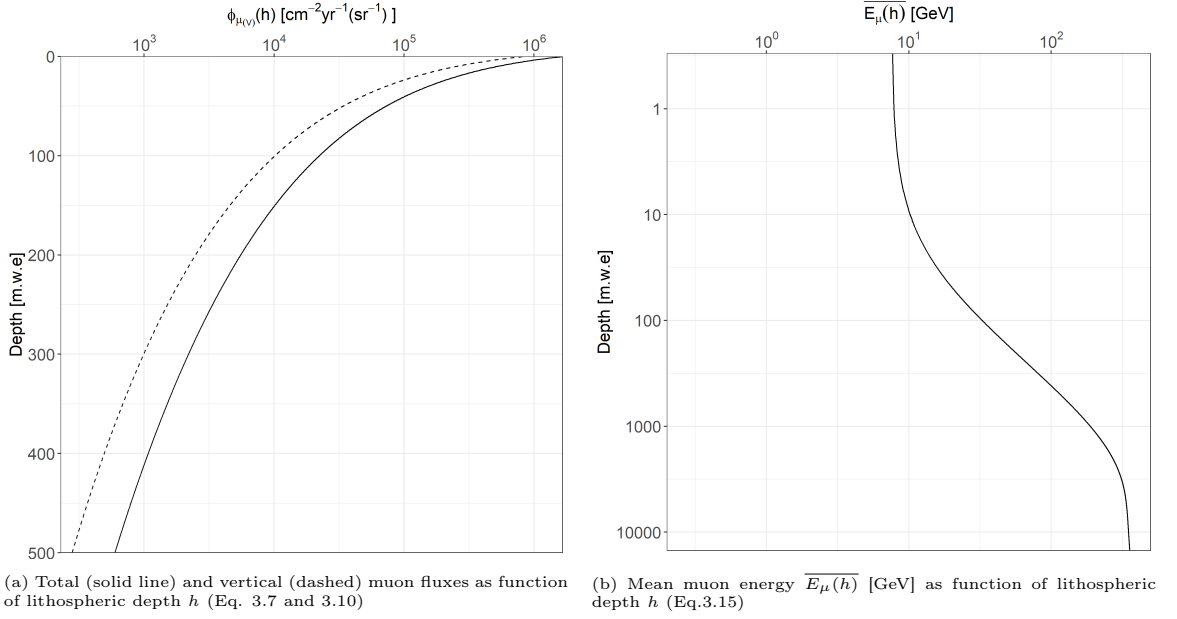


Figure 3.4: Muon flux and mean energy as a function of depth (Heisinger et al., 2002a)

penetrate dense regions of the atmosphere, where interaction probability is greater, and decay chances are smaller (Stone et al., 1998). The angular distribution for higher muon energies is therefore broader. Since the flux in depth is sustained by high-energy muons arriving at shallow angles, the total muon flux has a longer attenuation length than its vertical component.

The total muon flux ϕ_{μ} [$\text{cm}^{-2}\text{s}^{-1}$] is calculated by integrating $\phi_{\mu,V}$ over the zenith angular distribution [Eq. 3.10, Figure 3.4a; Heisinger et al. (2002a)]. The distribution over the azimuth angle is regarded as uniform (Bogdanova et al., 2006).

$$\phi_{\mu}(h, \theta) = \phi_{\mu,V}(h) \cdot \cos^{n(h)} \cdot \theta \quad (3.8)$$

$$n(h) = 3.21 - 0.297 \cdot \ln(h + 42) + 1.21 \times 10^{-3} \cdot h \quad (3.9)$$

$$\phi_{\mu}(h) = \int_{2\pi} \phi(h, \theta) \partial\Omega = \frac{2\pi}{n(h) + 1} \phi_{\mu,V}(h) \quad (3.10)$$

The negative fraction of the total muon flux is described by Eq. 3.11, where $K_{\mu}(E_{\mu})$ is the ratio of positive to negative muons, which theoretically depends on the muon energy E_{μ} . However, for energies $E_{\mu} > 4$ GeV, $K_{\mu} = 1.268$ is considered as constant (Charalambus, 1970; Heisinger et al., 2002b). The total negative muon flux $\phi_{\mu-}(h)$ [$\text{cm}^{-2}\text{s}^{-1}$] is described by Eq. 3.12.

$$f_{\mu^-}(h) = \frac{1}{K_{\mu} + 1} \approx \frac{1}{1 + 1.268} = 0.44 \quad (3.11)$$

$$\phi_{\mu^-}(h) = f_{\mu^-}(h) \cdot \phi_{\mu}(h) \quad (3.12)$$

Mean muon energy In the underground, muons, like all charged particles, lose their energy when they travel through matter. The two main loss mechanisms are ionization (electromagnetic interaction) at low energies and radiative processes for $E_{\mu} > 50$ GeV (photonuclear interactions, e^+e^- (direct) pair production and bremsstrahlung) (Groom et al., 2001; Garrison, 2014). In the shallow - intermediate depth range, muons have energies ≤ 50 GeV, and they are slowed down mainly by ionization. The energy loss is described by Eq. 3.13, in which the so-called “stopping power” dE_{μ}/dx is the average amount of energy lost by a particle when it penetrates a unit length of material. a [$\text{GeV hg}^{-1} \text{cm}^2$] is the energy loss due to ionization and depends on Z/A . b [$\text{hg}^{-1} \text{cm}^2$] is the sum of fractional radiation losses, which depends on Z^2/A . For depths up to 300 m of standard rock, Lechmann et al. (2018) demonstrated that the rock composition induces variations of a maximum of 2.5 % in the particle flux. These parameters also depend on the kinetic energy of the incident particle in some way. The values for standard rocks and muon energies in the range around 30 GeV are $a = 0.227 \text{ GeV hg}^{-1} \text{cm}^2$ and $b = 2.44 \times 10^{-4} \text{ hg}^{-1} \text{cm}^2$ (Gaisser et al., 1996; Groom et al., 2001; Cecchini and Spurio, 2012).

$$\frac{dE_{\mu}}{dx} = a(E) + b(E)E_{\mu} \quad (3.13)$$

The energy $E_{\mu,0}$ of a muon at sea level, which will have the energy E_{μ} at a depth h (under the angle θ) is:

$$E_{\mu,0}(\theta, h) = (E_{\mu} + \frac{a}{b}) \cdot \exp(\frac{h \cdot b}{\cos\theta}) - \frac{a}{b} \quad (3.14)$$

Heisinger et al. (2002b) uses Eq. 3.14 in combination with the differential muon spectrum at sea level $D(E_{\mu,0}, \Theta)$ from Judge and Nash (1965) to calculate the differential muon energy spectra $D(E_{\mu}, \Theta, h)$. The mean total muon energy $\overline{E_{\mu}(h)}$ is approximated as a function of lithospheric depth h (Eq. 3.15, Figure 3.4b). At sea level, $\overline{E_{\mu}(0)} = 7.6$ GeV. It's interesting to note that even if muons lose energy as they penetrate the underground, the mean muon energy increases with depth, up to a maximal value of 350 GeV (at $\sim 10^4$ m.w.e). The muon energy spectrum peaks at low energies at the surface, and therefore, low-energy muons are stopped as the flux passes through the underground, resulting in a higher average energy.

$$\overline{E_{\mu}(h)} = 7.6 + 321.7 \cdot (1 - \exp(-8.059 \times 10^{-4} \cdot h)) + 50.7 \cdot (1 - \exp(-5.05 \times 10^{-5} \cdot h)) \quad (3.15)$$

Stopping Rate As negative muons slow down in the media due to their energy loss, they eventually stop and are captured by the nuclei composing their environment. The stopping rate of negative muons $R_{\mu-}(h)$ [$\text{g}^{-1}\text{yr}^{-1}$] is calculated from the derivative of the total negative muon flux $\phi_{\mu-}(h)$ as proposed by Heisinger et al. (2002b):

$$R_{\mu-}(h) \approx f_{\mu-}(h) \cdot \frac{d}{dh}(\phi_V(h) \cdot \frac{2\pi}{n(h)+1}) \quad (3.16)$$

For practical applications, Eq. 3.16 can be approximated by an exponential depth-dependence:

$$R_{\mu-}(h) = R_{\mu-}(0) \cdot \exp\left(-\frac{h}{\Lambda_{\mu-}}\right) \quad (3.17)$$

with $R_{\mu-}(0) = 190 \text{ g}^{-1}\text{yr}^{-1}$ being the rate of stopping muons at sea level and high latitude [SLHL, Heisinger et al. (2002a)]. The absorption mean free path for stopped negative muons $\Lambda_{\mu-}$ [hg cm^{-2}] depends on the muon energy. Since energy varies with depth, the shape of the muon stopping rate profile also fluctuates (Alfimov and Ivy-Ochs, 2009). To account for this effect, Schaller et al. (2004) proposes an approximation of the $R_{\mu-}(h)$ depth-dependence by k exponents with attenuation coefficients $\Lambda_{k,\mu-}$ [hg cm^{-2}] and relative intensities $p_{k,\mu}$ [–] (Table 3.1) based on the local muon rate from the code of Balco et al. (2008). This results in the approximation of the muon stopping rate for SLHL as a function of lithospheric depth h in Eq. 3.18 (Figure 3.5). The weighted average $\Lambda_{\mu-} = 16.5 \text{ hg cm}^{-2}$ corresponds to a mean free path one order of magnitude larger than the one for the nucleonic component of cosmic ray in the underground ($\Lambda_{n,f} = 160 \text{ g cm}^{-2}$).

$$R_{\mu-}(h) = R_{\mu-}(0) \cdot \sum_k p_{k,\mu} \cdot \exp\left(-\frac{h}{\Lambda_{k,\mu-}}\right) \quad (3.18)$$

Table 3.1: Exponent coefficients for the depth-dependency of the muon stopping rate at SLHL (Eq. 3.18)(Schaller et al., 2004)

$\mathbf{p_{k,\mu}}$	$\mathbf{\Lambda_{k,\mu-}}$
0.845	1030
-0.05	160
0.2050	3000

3.1.2 In-situ Neutrons

3.1.2.1 Neutrons from natural rock radioactivity

The decay of U and Th naturally present in rocks produces α particles, which can travel for about 25 μm in rock while losing their energy by inelastic scattering on atomic electrons and elastic scattering on nuclei. Eventually, α particles either stop and form ^4He atoms by ionizing the material around them, or interact with the nucleus of an atom. This capture process happens under the condition that the particle has enough energy to overcome

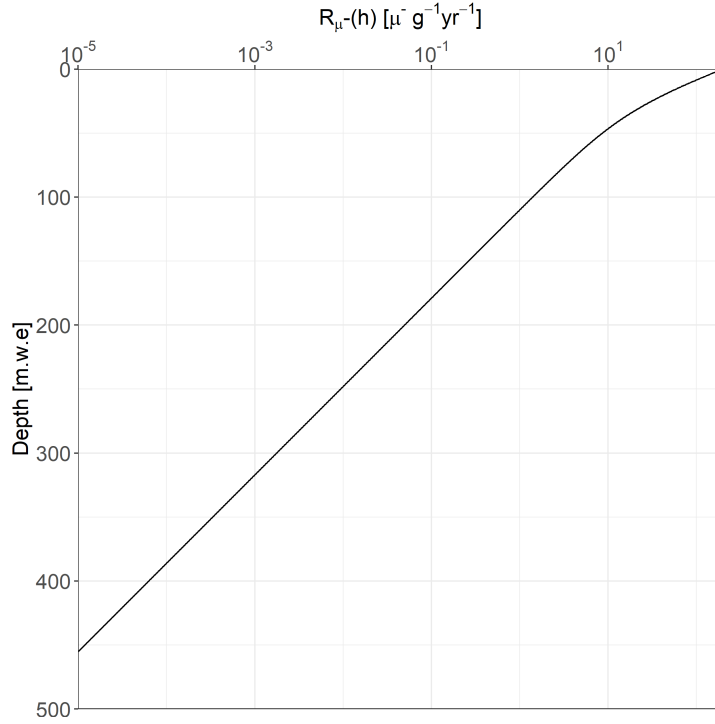


Figure 3.5: Negative muon stopping rate $R_{\mu^-}(h)$ approximated by Schaller et al. (2004)

the Coulomb Barrier of the target nucleus to form a compound nucleus. Since the electromagnetic repulsion value is proportional to the charge of the nucleus, the capture process only takes place on relatively low- Z target nuclides ($Z < 25$). A compound nucleus is only a short-lived intermediate state, which de-excites most of the time by dropping a neutron (for the energy range of the natural α particles), therefore constituting an (α, n) reaction (Figure 3.6). The nuclides with the highest neutron yield underground are: ^{27}Ar , ^{23}Na , ^{29}Si , ^{30}Si , ^{18}O , ^{26}Mg , ^{25}Mg .

To account for all energy dependencies along this chain, Šrámek et al. (2017) used the nuclear physics code TALYS (Koning and Rochman, 2012) to provide a Python script for the evaluation of the neutron (and ^{39}Ar) production rates underground. The mean energy for the (α, n) neutrons concluded by Šrámek et al. (2017) is between 1.6 and 1.8 MeV depending on the actinide chain. These particles can, however, reach 10 MeV for interactions with ^9Be , for example (Garrison, 2014).

In addition, spontaneous fission of ^{238}U produces 2.07 neutrons per fission (Shultis and Faw, 2002), with a mean energy of 1.7 MeV [approximated by Watt fission spectrum Watt (1952)]. ^{238}U is the only significant contributor to the natural rock radioactivity neutron production by fission.

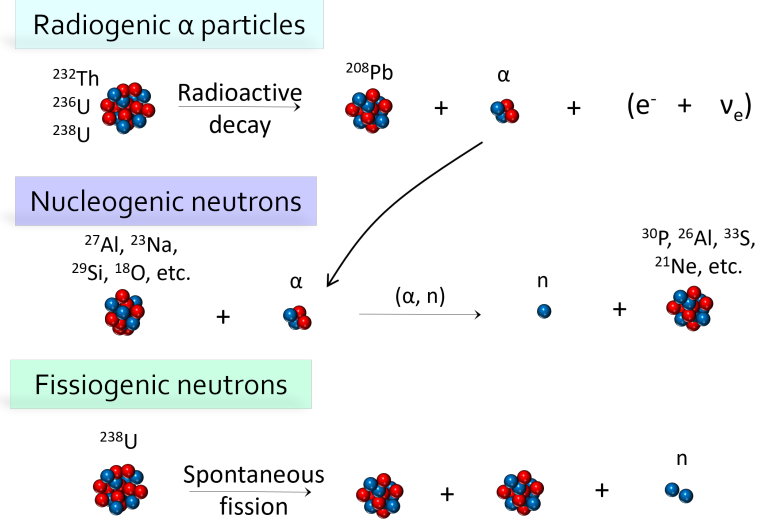


Figure 3.6: Neutron production rate from natural radioactivity in rocks: U and Th decay chains produce α particles, which in turn participate in (α, n) reactions on light elements (Modified from Šrámek et al. (2017))

Both reactions type [fission and (α, n)] give rise to a non-cosmogenic background neutron source in the subsurface (Stone et al., 1996). These neutrons can participate in reactions like scattering, or (n, p) reactions and produce radionuclides underground. Ultimately, they are also slowed down and thermalized. In this thesis, we use the code proposed by Šrámek et al. (2017) to account for the neutron production from natural radioactivity in rocks $P_{n,U/Th}$ [$\text{g}^{-1} \text{yr}^{-1}$]. The chemical composition measured in the rocks is entered as input values in the code.

3.1.2.2 Muon-induced neutrons

Muon-induced neutrons are produced underground from fast muon interactions (Wang et al., 2001; Mei and Hime, 2006; Malgin and Ryazhskaya, 2008) or de-excitation of the compound nucleus following slow negative muon-capture processes (Alfimov and Ivy-Ochs, 2009; Heisinger et al., 2002a). While the process following muon capture is quite well understood, the current situation regarding fast muon-induced neutrons is controversial. Its theoretical investigation is a many-sided problem involving determining the muon energy spectrum at a given depth, considering the processes which initiate the hadronic and electromagnetic showers in the matter, understanding the production of neutrons in these showers, and how these neutrons are transported in the matter (Malgin and Ryazhskaya, 2008; Palermo, 2016). In parallel, measurements highly depend on the geometry and the material composing the detector, as well as its environment. The comparisons between studies are, therefore, further complicated.

3.2 Radioargon (^{39}Ar and ^{37}Ar) production rates

3.2.1 Overview

Radioargon isotopes are produced underground by negative muon capture reactions and neutron activation on potassium (K) and calcium (Ca) atoms. The total production rate P_{Ar} [atoms $\text{g}^{-1} \text{yr}^{-1}$] (Eq. 3.19) as a function of lithospheric depth z [m] is the sum of the contributions from muon and neutron reactions. The most important reaction channels are summarized in Table 3.2 and illustrated in Figure 3.7.

$$P_{Ar}(z) = P_{Ar,n}(z) + P_{Ar,\mu}(z) \quad (3.19)$$

Table 3.2: Production channels for ^{39}Ar and ^{37}Ar in the underground by neutron activation and slow negative muon capture. The reactions underlined for neutron activation are considered in the underground production calculations in the following.

Argon-39	Argon-37
Neutron activation reactions	
$^{39}\text{K}(\text{n}, \text{p})^{39}\text{Ar}$	$^{39}\text{K}(\text{n}, \text{p}2\text{n})^{37}\text{Ar}$
$^{42}\text{Ca}(\text{n}, \alpha)^{39}\text{Ar}$	$^{40}\text{Ca}(\text{n}, \alpha)^{37}\text{Ar}$
Muon Capture reactions	
$^{40}\text{Ca}(\mu^-, \text{p})^{39}\text{Ar}$	$^{39}\text{K}(\mu^-, 2\text{n})^{37}\text{Ar}$
$^{39}\text{K}(\mu^-, \gamma)^{39}\text{Ar}$	$^{40}\text{Ca}(\mu^-, \text{p}2\text{n})^{37}\text{Ar}$
$^{44}\text{Ca}(\mu^-, \alpha\text{n})^{39}\text{Ar}$	

In this Section, the argon production rates P_{Ar} were calculated for three rock formations (sand, clayey till, and chalk). These formations constitute the shallow Danish hydrogeological system, which is described in Chapter 5. Table 3.3 summarizes the elemental weight fraction distribution of each rock type, measured by ICP-MS at the Geological Survey of Denmark and Greenland (GEUS). However, the radioargon and neutron production rates were also calculated for the typical rock compositions summarized by (Fabryka-Martin, 1988) and can be found in Appendix A.2.

As discussed in Section 3.1, the intensity of cosmogenic particle fluxes depends on the altitude, location in the geomagnetic field, and solar magnetic activity (Gordon et al., 2004). In the following, we use the reference scaling: the cosmogenic particle fluxes defined for a horizontal surface at high latitude ($> 60^\circ$) and sea level altitude (SLHL) with a mid-solar modulation. These conditions correspond to the situation in Denmark. The depth range particularly relevant for groundwater dating applications is $0 < z < 200$ m since the production rates decrease by several orders over this interval. In the following, we express the production profiles as function of standard rock ($A = 22$, $\rho_r = 2.65 \text{ g cm}^{-3}$) depth z [m] (Malgin, 2015).

Table 3.3: Elemental weight fraction distribution, and Ca/K ratio for the three rock types composing the Danish hydrogeological shallow system, and average neutron yield per captured muon y_i^n computed by Alfimov and Ivy-Ochs (2009) and Fabryka-Martin (1988)

Element i	Elemental weight fraction [-]			y_i^n [n]
	Sand	Clayey till	Chalk	
C	3.0×10^{-4}	1.0×10^{-2}	1.1×10^{-1}	0.8
O	4.4×10^{-1}	4.9×10^{-1}	4.8×10^{-1}	0.8
F	2.7×10^{-4}	5.0×10^{-4}	3.3×10^{-4}	
Na	3.3×10^{-3}	6.6×10^{-4}	4.0×10^{-4}	1.0
Mg	7.0×10^{-3}	1.3×10^{-2}	4.7×10^{-2}	0.6
Al	2.5×10^{-2}	1.0×10^{-1}	4.2×10^{-3}	1.3
Si	3.7×10^{-1}	2.4×10^{-1}	2.4×10^{-2}	0.9
K	1.1×10^{-2}	1.5×10^{-2}	1.1×10^{-3}	1.3
Ca	6.0×10^{-2}	1.1×10^{-1}	2.9×10^{-1}	0.8
Ti	1.5×10^{-3}	4.5×10^{-3}	4.0×10^{-4}	1.1
Fe	9.8×10^{-3}	3.3×10^{-2}	3.8×10^{-3}	1.1
Th	3.1×10^{-6}	7.2×10^{-6}	6.6×10^{-7}	1.9
U	1.1×10^{-6}	2.2×10^{-6}	3.5×10^{-7}	1.8
Ca/K	5.5	7.6	265.3	

The conversion of the equivalent depth of water with the same mass h [m.w.e] to z is given by:

$$z = h \cdot \rho_w / \rho_r \quad (3.20)$$

The loss of energy during muon travel underground ultimately slows them down to thermal energies. The negative fraction of the muon flux can then be captured by the nucleus Coulomb field. Captured muons quickly cascade to the innermost electron orbit, where they either decay or interact with the nucleus. This interaction is summarized by $p + \mu^- \rightarrow n + \nu_\mu$ and can yield nuclide products by nuclear de-excitation according to:

$$\mu^- + (Z, A) \rightarrow (Z - 1, A)^* + \nu_\mu \quad (3.21)$$

$$(Z - 1, A)^* \rightarrow (Z - 1, A - X) + X \cdot n \quad (3.22)$$

$X = 0, 1, 2 \dots$ is the number of neutrons released, which determines the product nucleus. This process is illustrated for radioargon products in Figure 3.7. These muon-induced neutrons further contribute to radioargon underground production.

Neutrons underground originate from lithogenic (Section 3.1.2) or cosmogenic (Section 3.1.1) sources. Lithogenic sources comprise neutrons from spontaneous fission and (α, n) reactions on light elements as part of U and Th decay chains (Šrámek et al., 2017). Cosmogenic sources include spallation and evaporation neutrons produced by cosmic ray nucleons (the so-called “hadronic component of cosmic rays”) and muon-induced reactions. Neutron

reactions with the component elements of the rock matrix are a very important source of radioisotope in the subsurface for many nuclides. These interactions, which are either high energy spallation or nuclear capture of lower-energy neutrons, are favored since no Coulomb barrier prevents the formation of intermediate excited states (Fabryka-Martin, 1988; Smith, 1989).

The production rates of neutrons from their different sources are the starting point for assessing neutron-induced radioargon production (Section 3.2.3.2). These neutrons can be emitted with energy in the MeV range, but as they travel through matter, they lose energy by elastic or inelastic scattering with nuclei, passing through the epithermal (0.1 MeV – 0.5 eV) up to the thermal energy (0.025 eV) ranges. Eventually, they are absorbed by the atoms in the medium (Gosse and Phillips, 2001). Because of the variation of the reaction cross sections with energy (Section 3.2.3.1), the production rate calculations require knowledge of the neutron energy distributions. Quantifying the subsurface neutron fluxes and the moderated energy profiles is likely the biggest challenge for assessing radioargon production rates. Estimating the neutron flux as a function of depth for each neutron source represents a sizeable task that is approached with Monte Carlo simulations (Section 3.2.3.3).

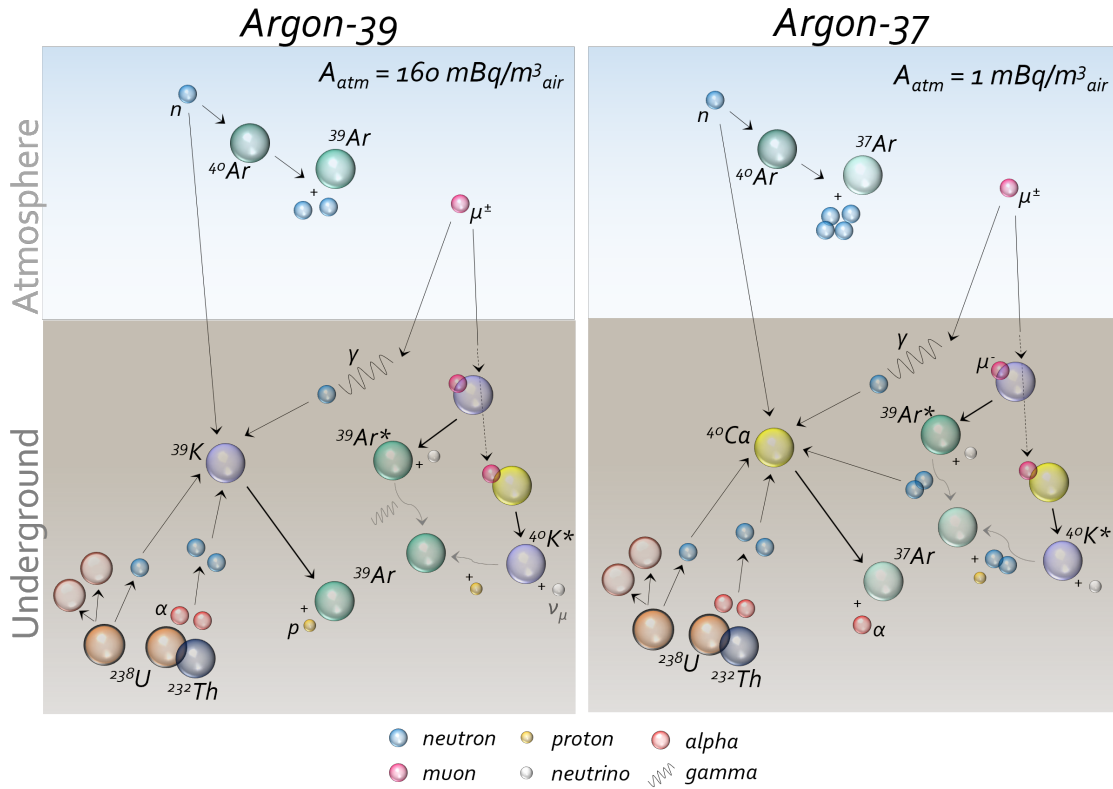


Figure 3.7: Overview of the most important production channels in the subsurface and the atmosphere, for ^{39}Ar and ^{37}Ar isotopes. A_{atm} are the natural atmospheric activities.

3.2.2 Muon capture reactions

The production of radioargon isotopes by muon capture $P_{Ar,\mu}$ is the product of the local muon stopping rate $R_{\mu^-}(z)$ [$\mu^- \text{g}^{-1} \text{yr}^{-1}$] and the yield of atoms produced per stopped negative muon $Y_{\mu^-}^{39}$ or $Y_{\mu^-}^{37}$ [atoms $(\mu^-)^{-1}$]:

$$P_{Ar,\mu}(z) = R_{\mu^-}(z) \cdot Y_{\mu^-}^{Ar} \quad (3.23)$$

The negative muon stopping rate $R(z)$ is approximated by the exponential depth-dependence proposed by Schaller et al. (2004) (Eq. 3.18). Once a muon stops, it can be captured by the atoms composing the matter in its vicinity (Figure 3.8). The yield of atom of argon produced per stopped negative muon $Y_{\mu^-}^{Ar}$ is estimated by:

$$Y_{\mu^-}^{Ar} = f_i \cdot f_d \cdot f_c \cdot f_r \quad (3.24)$$

Where f_i [-] is the target isotopic abundance, f_c [-] is the chemical compound factor, f_d [-] is the nuclear capture probability, and f_r [-] is the probability for the expected reaction to happen. The error on these parameters is assumed to be $\leq 10\%$ (Heisinger et al., 2002a).

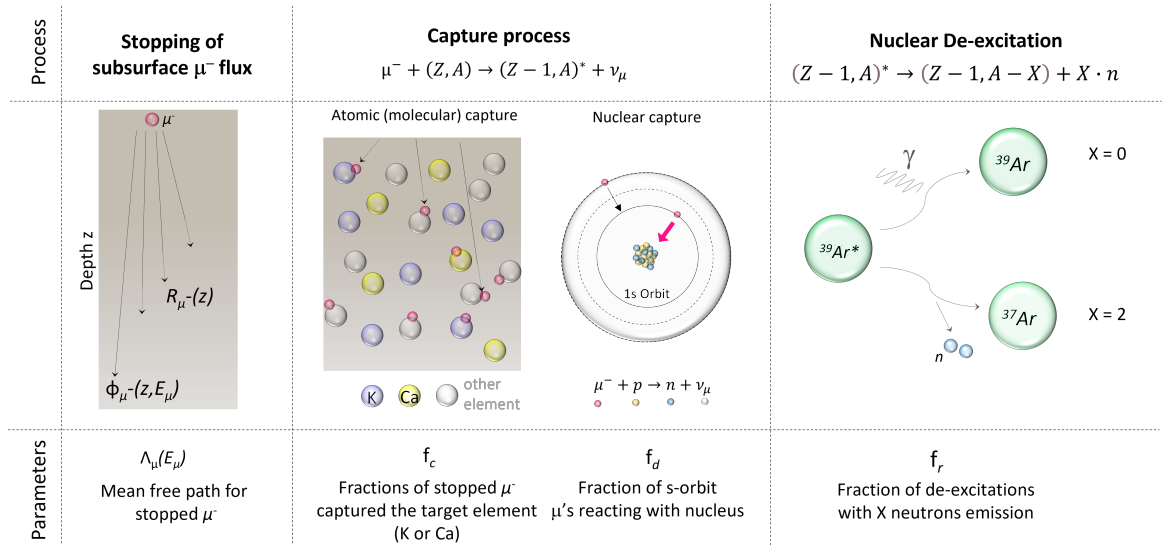


Figure 3.8: Slow negative muon capture reaction processes, and parameters for radioargon production

The chemical compound factor f_c is the fraction of stopping muons reaching the 1s muonic level of the target element when the element is one constituent of a compound. f_c (Eq. 3.26) is determined as the ratio of the probability to be captured on the target element j relative to oxygen (W_j , Eq. 3.25), in relation to the probability to be captured in the matrix material (von Egidy and Hartmann, 1982; Suzuki et al., 1987; Alfimov and Ivy-Ochs, 2009).

$$W_j = \frac{P(j)}{P(0)} \quad (3.25)$$

$$f_c = \frac{W_j \cdot N_j}{\sum_i W_i \cdot N_i} \quad (3.26)$$

N_i , resp. N_j [atoms g⁻¹] is the elemental concentration from the target element j , or any other element i , in the sample. W is the probability relative to oxygen to be captured by the Coulomb field on the element j or i . The values of W are taken from von Egidy and Hartmann (1982) and Suzuki et al. (1987).

The nuclear capture probability f_d is the probability for the muon "available" in the K-Shell to be captured in the nucleus before decaying. The probability that a muon stays in the 1s level (λ_0) is the sum of the probability that it decays λ_d and the probability that it is captured λ_c (Eq. 3.27). The probability for the muon to be captured from this K-Shell is then the product of the muon half-life in the atom τ_0 , which is inversely proportional to λ_0 , and the nucleus capture probability λ_c (Eq. 3.28) (Alfimov and Ivy-Ochs, 2009). These factors are calculated from the values compiled by Suzuki et al. (1987), and differ slightly from those computed by Alfimov and Ivy-Ochs (2009). However, this deviation is <5 % and therefore ignored.

$$\lambda_0 = \frac{1}{\tau_0} = \lambda_d + \lambda_c \quad (3.27)$$

$$f_d = \tau_0 \cdot \lambda_c = \frac{\lambda_c}{\lambda_0} \quad (3.28)$$

The high-energy neutron produced by the nuclear capture either leaves the nucleus, ejects a particle from the nucleus (through direct interactions), or transfers its energy to other nucleons, thereby putting the nucleus in an excited state (Fabryka-Martin, 1988). Since the release of charged particles is impeded by the Coulomb barrier, most of the time, the nucleus de-excites by the emission of one or more neutrons, together with γ -rays.

The probability of reaction or neutron multiplicity distribution f_r is then the probability for the excited $(Z-1, A)^*$ nucleus to yield the desired $(Z-1, A-X)$ nucleus. In other words, this is the probability of emission of the number X of neutrons and corresponds to the effective probability for production of the nuclide i after the negative muon capture in the target nucleus (Heisinger et al., 2002a). This neutron multiplicity depends on the target nucleus through the momentum of the proton capturing the muon. Charalambus (1970) proposed neutron emission probabilities for practical applications (Table 3.4). For other particles, we refer to the compilation of reactions from Fabryka-Martin (1988).

Table 3.4: Neutron emission probability for practical applications proposed by Charalambus (1970). X is the number of neutrons emitted after the μ^- capture (Eq.3.22)

X	0	1	2	3	4
f_r	0.1	0.6-0.7	0.15-0.2	0.05	0.02

The yield of radioargon atoms produced per stopped muons $Y_{\mu^-}^{Ar}$ (Eq. 3.24) was calculated for each reaction channel for ^{39}Ar and ^{37}Ar (Table 3.2). The total production yield for each isotope, $Y_{\mu^-}^{39}$ or $Y_{\mu^-}^{37}$, is then the sum of the contributions from all channels. While the factors f_i , f_r , and f_d are essentially independent of the rock composition, f_c and per extensions $Y_{\mu^-}^{Ar}$, are specific to a given rock (Table 3.5). Table 3.6 summarizes the total production yields $Y_{\mu^-}^{Ar}$ for both ^{39}Ar and ^{37}Ar as well as the contribution fraction of each reaction channel to $Y_{\mu^-}^{Ar}$. Depending on the composition of the rock, this contribution can vary greatly. Generally, for ^{39}Ar the $P_{Ar,\mu}$ is dominated by reactions on ^{39}K , except for ultramafic and carbonated rocks. For ^{37}Ar , both ^{39}K and ^{40}Ca reactions need to be accounted for in most of the rocks.

Table 3.5: Muon production channels for Argon isotopes. f_i is the isotopic abundance of the target nuclide, f_d is the nuclear capture probability in the target nuclide (Suzuki et al., 1987), f_r is the probability of the reaction (Fabryka-Martin, 1988), f_c is the chemical compound factor, and $Y_{\mu^-}^{Ar}$ is the yield of atom produced per stopped μ^- (Eq. 3.24) for each production channel. Here f_c and $Y_{\mu^-}^i$ are given as an example for the Denmark Sand rock formation.

	f_i	f_d	f_r	f_c	$Y_{\mu^-}^{Ar}$
Argon-39					
$^{40}\text{Ca}(\mu^-, p)^{39}\text{Ar}$	0.969	0.871	0.004	0.06	2.2×10^{-4}
$^{39}\text{K}(\mu^-, \gamma)^{39}\text{Ar}$	0.93	0.816	0.15	0.01	7.6×10^{-4}
$^{44}\text{Ca}(\mu^-, \alpha n)^{39}\text{Ar}$	0.021	0.81	0.06	0.06	6.8×10^{-4}
Argon-37					
$^{39}\text{K}(\mu^-, 2n)^{37}\text{Ar}$	0.93	0.816	0.19	0.01	7.6×10^{-4}
$^{40}\text{Ca}(\mu^-, p2n)^{37}\text{Ar}$	0.969	0.871	0.02	0.06	1.1×10^{-3}

Table 3.6: ^{39}Ar and ^{37}Ar isotopes (Eq. 3.24) for the three types of rock characterizing the Danish shallow hydrogeological system. The contribution of each production channel to the total yield is indicated. $Y_{\mu^-}^n$ is the average neutrons produced per muon captured in the rock (Eq. 3.34)

	$Y_{\mu^-}^{39}$				$Y_{\mu^-}^{37}$			$Y_{\mu^-}^n$
	$^{40}\text{Ca}(\mu^-, \text{p})^{39}\text{Ar}$	$^{39}\text{K}(\mu^-, \gamma)^{39}\text{Ar}$	$^{44}\text{Ca}(\mu^-, \alpha\text{n})^{39}\text{Ar}$	Total	$^{39}\text{K}(\mu^-, 2\text{n})^{37}\text{Ar}$	$^{40}\text{Ca}(\mu^-, \text{p}2\text{n})^{37}\text{Ar}$	Total	
Sand	21.4%	72.2%	6.5%	1.05×10^{-3}	40.3%	59.7%	1.88×10^{-3}	0.31
Clayey till	26.5%	65.5%	8.0%	1.42×10^{-3}	33.0%	67.0%	2.81×10^{-3}	0.33
Chalk	72.8%	5.1%	22.0%	1.27×10^{-3}	1.4%	98.6%	4.69×10^{-3}	0.29

3.2.3 Reactions with neutrons

The production rate for radioargon isotopes with neutrons $P_{Ar,n}$ [atoms $\text{g}^{-1} \text{yr}^{-1}$] is described by:

$$P_{Ar,n} = N_{tg} \cdot \int_0^{E_{n,max}} \sigma(E_n) \cdot \phi_n(E_n) dE \quad (3.29)$$

where N_{tg} [atoms g^{-1}] is the target concentration, $\sigma(E_n)$ [cm^2] is the reaction cross section, and $\phi_n(E_n)$ [$\text{cm}^{-2} \text{yr}^{-1}$] is the neutron flux.

3.2.3.1 Argon production cross sections

Figure 3.9 shows the energy distribution of the cross sections for radioargon production with neutrons. The ^{39}Ar production is dominated by reactions with high energy neutron on ^{39}K . In principle, the reaction on ^{42}Ca also exists but this channel is negligible due to the low cross section and ^{42}Ca concentration compared to ^{39}K . The significant cross sections for ^{37}Ar production are on ^{36}Ar at low energy, and on ^{40}Ca for neutrons ≥ 1 MeV. In aquifers, although ^{37}Ar may be produced on the ^{36}Ar dissolved in air equilibrated water, the reaction on ^{40}Ca is dominating in most cases due to the low ^{36}Ar abundance [$^{36}\text{Ar}/\text{Ar} = 0.33\%$; Musy et al. (2022)].

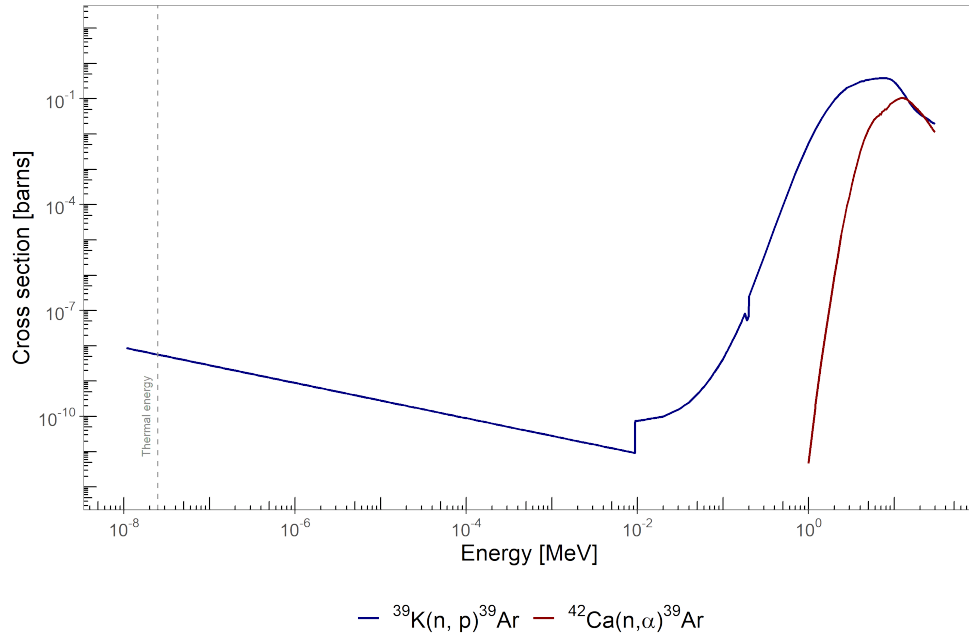
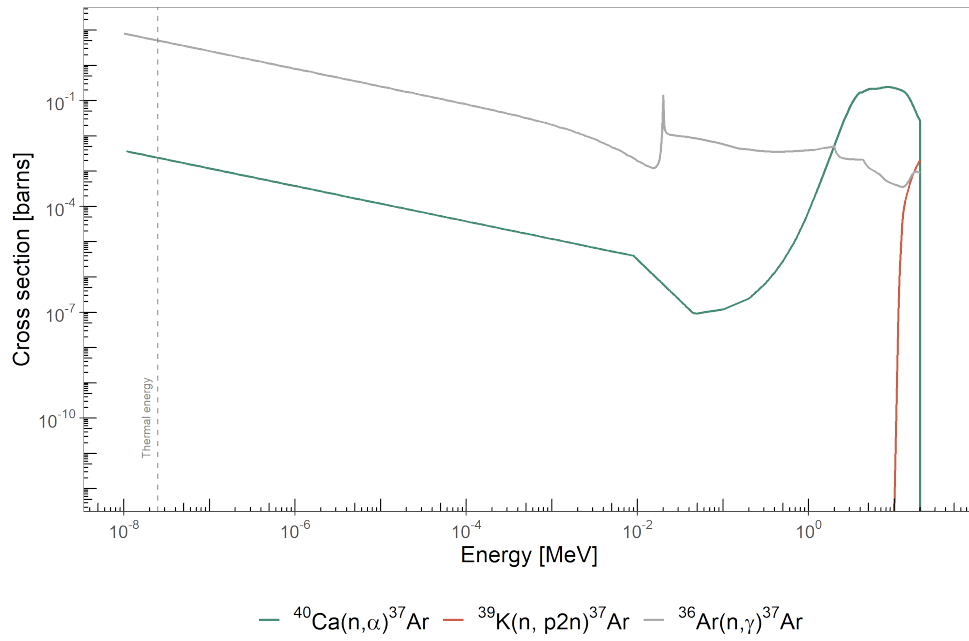
The total radioargon underground production rate with neutrons $P_{Ar,n}$ (Eq. 3.19 and Eq. 3.30) is the sum of the contributions from neutron interactions with neutrons from: (i) hadronic component of cosmic rays $P_{Ar(n,f)}$; (ii) slow negative muon-capture reactions $P_{Ar(n,\mu^-)}$; (iii) fast-muon induced reactions $P_{Ar(n,\mu_f)}$; (iv) from spontaneous fission and (α,n) reactions on light elements, with α from U/Th decay chains $P_{Ar(n,U/Th)}$. To compute the radioargon production rates with neutrons, we first need to quantify the neutron production rates.

$$P_{Ar,n} = P_{Ar(n,f)} + P_{Ar(n,\mu_f)} + P_{Ar(n,\mu^-)} + P_{Ar(n,U/Th)} \quad (3.30)$$

3.2.3.2 Neutron production rates

The overall neutron production rate at a given depth $P_n(z)$ [$\text{n g}^{-1} \text{yr}^{-1}$] is the sum of all neutron contributions:

$$P_n = P_{n,f} + P_{n,\mu_f} + P_{n,\mu^-} + P_{n,U/Th} \quad (3.31)$$

(a) ^{39}Ar cross section [JEFF 3.2.1 (Cabellos, 2012)](b) ^{37}Ar cross section [BROND 3.1 (Blokhin et al., 2016)]Figure 3.9: Nuclear cross sections for ^{39}Ar and ^{37}Ar production with neutrons

Hadronic component of cosmic rays Bombardment of nuclei by high-energy cosmic rays, chiefly protons, and secondary neutrons, produces neutrons by spallation and evaporation-fission processes. These neutrons are emitted with an average energy of 1 MeV but can range up to 10 MeV or more (Fabryka-Martin, 1988). The neutron production rate from cosmogenic spallation and evaporation origin, $P_{n,f}$ [$\text{n g}^{-1} \text{yr}^{-1}$], as function of lithospheric depth h [g cm^{-2}], is then described by :

$$P_{n,f} = P_{n,0} \cdot \exp\left(-\frac{h}{\Lambda_{n,f}}\right) \quad (3.32)$$

$P_{n,0} = 2525 \text{ n g}^{-1} \text{yr}^{-1}$ is the neutron production rate at the surface, normalized for sea level and high latitude (Heisinger et al., 2002b). For fast neutrons in standard rock, an attenuation length of $\Lambda_{n,f} = 160 \text{ g cm}^{-2}$ is now widely accepted (Gosse and Phillips, 2001), resulting in a mean free path of about 0.5 m (Fabryka-Martin, 1988). The neutron flux from the hadronic component of cosmic rays drops sharply with depth due to their high interaction characteristics. It becomes insignificant compared to neutrons from muon or natural radioactivity at depths greater than 2 - 3 m of standard rock ($\sim 5 \text{ m.w.e}$, Figure 3.10, (Bogdanova et al., 2006; Esch, 2001; Garrison, 2014)).

In the following of this thesis, we use the term "primary cosmogenic neutrons" as a synonym for the hadronic component of cosmic rays underground. Although the term "primary" is not strictly speaking correct, it is opposed to the neutrons induced by muons, which are also cosmogenic but result from secondary processes underground.

Neutrons from slow negative muon-capture reactions The muon capture reaction (μ^- , Xn) can yield up to 4 neutrons with substantial probabilities (Table 3.4), but generally, the capture reaction energy is dissipated by the evaporation of $X \leq 2$ neutrons (Malgin and Ryazhskaya, 2008). The neutron production rate induced by muon-capture reactions, $P_{n,\mu^-}(z)$ [$\text{n g}^{-1} \text{yr}^{-1}$] (Eq. 3.33) is described by the muon stopping rate R_{μ^-} and $Y_{\mu^-}^n$, which is the average number of neutrons produced per muon captured in the rock (Eq. 3.34, Table 3.6). After being captured in the target element i (f_c), interacting with the nucleus (f_d), each muon can yield neutrons. y_i^n [$\text{n} (\mu^-)^{-1}$] is the average neutron yield per capture muon in the element i (Table 3.3). In the capture reactions, most of the energy released is transferred to the neutrino, so on average only 4 - 8 MeV kinetic energy is transferred to the neutrons (Fabryka-Martin, 1988; Grieger, 2021; Malgin and Ryazhskaya, 2008).

$$P_{n,\mu^-}(z) = R_{\mu^-}(z) \cdot Y_{\mu^-}^n \quad (3.33)$$

$$Y_{\mu^-}^n = \sum_i f_{c,i} \cdot f_{d,i} \cdot y_i^n \quad (3.34)$$

Fast muon-induced neutrons Neutrons are produced from fast-muons via the following processes:

- (i) muon interaction with nuclei via a virtual photon producing nuclear disintegration
- (ii) muon elastic scattering with neutrons bound in nuclei
- (iii) photo-nuclear reactions associated with electromagnetic showers generated by muons
- (iv) (n,n) reactions with secondary neutron production following any of the above processes

(Malgin and Ryazhskaya, 2008; Niedermann, 2002; Palermo, 2016; Wang et al., 2001)

The fast muon-induced neutron production rate $P_{n,\mu_f}(z)$ [$\text{g}^{-1}\text{yr}^{-1}$] (Eq. 3.35) can be calculated from the total muon flux $\phi_\mu(z)$ [$\text{cm}^{-2}\text{s}^{-1}$] (Eq. 3.10) and the average muon energy $\bar{E}_\mu(z)$ [GeV] (Eq.3.15) in standard rock ($A = 22$, $Z = 11$, $\rho = 2.65 \text{ g cm}^{-3}$). In the following, we use the approach proposed by Heisinger et al. (2002a) based on the neutron yield fitted to the experimental data by Wang et al. (2001):

$$P_{n,\mu_f}(z) = 4.8 \times 10^{-6} \cdot \beta(z) \cdot \phi_\mu(z) \cdot \bar{E}_\mu^\alpha(z) \quad (3.35)$$

$\alpha \approx 0.75$ and $\beta(z)$ is an empirical factor that depends weakly on depth and can be approximated by :

$$\beta(h) = 0.846 - 0.015 \cdot \ln(h + 1) + 0.003139 \cdot (\ln(h + 1))^2 \quad (3.36)$$

$\beta(h)$ is parametrized as function of lithospheric depth h in g cm^{-2} but is expressed as function of the standard rock depth z in m for Eq. 3.35. Alternative parametrizations for the fast muon-induced neutron production rates are discussed in the Section 3.3.2.

Even though most fast-muon-induced neutrons are emitted with energies in the MeV range, their energy spectrum extends up to hundredths of GeV (Garrison, 2014; Malgin, 2017; Palermo, 2016; Wang et al., 2001). Generally, the energy distribution of these neutrons is very controversial since measuring energy spectra over a wide range is extremely complex and simulating the physics process involved in neutron production requires very sophisticated models. Grieger et al. (2020) proposes for the first time an assessment of the muon-induced neutron spectra in a shallow laboratory (140 m.w.e) based on a known muon flux (Ludwig et al., 2019). The outputs from these simulations are used for radioargon production calculations in the following.

Neutrons from U/Th decay chains The production process for neutrons from U and Th naturally present in rocks is described in Section 3.1.2. In the following, we use the code developed by Šrámek et al. (2017), with the measured rock compositions in Table 3.3 as input values to assess the $P_{n,U/Th}$ [$\text{n g}^{-1} \text{yr}^{-1}$] in the rock formations from the Danish shallow aquifer system (Table 3.7).

Table 3.7: Neutron production rate from natural rock radioactivity $P_{n,U/Th}$ [$\text{g}^{-1} \text{yr}^{-1}$] for the three formations from the Danish shallow hydrogeological system, calculated with the code proposed by Šrámek et al. (2017) and the rock composition in Table 3.3

Rock formation	$P_{n,U/Th}$
Sand	2.82 ± 0.37
Clayey till	6.59 ± 0.86
Chalk	0.61 ± 0.23

Figure 3.10 summarizes the neutron production rates in the three rock formations from the Danish shallow hydrogeological system. Except for $P_{n,U/Th}$, which are *in situ* produced neutrons, the production rates depend strongly on the depth of the rock overburden. Neutrons from the hadronic component of cosmic rays $P_{n,f}$, and fast-muon induced neutrons P_{n,μ_f} are essentially independent of the rock composition. Cosmogenic neutrons dominate $P_n(z)$ up to depths of about 20-30 m in the sand and clayey till formations, resp. 70 m in the chalk.

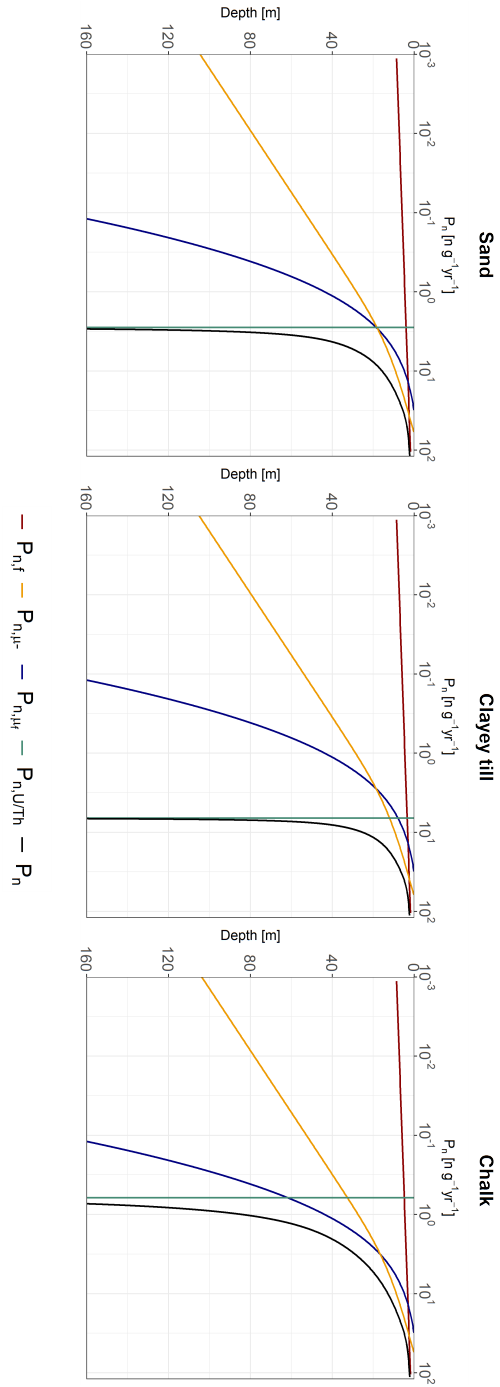


Figure 3.10: Neutron production rates P_n as a function of standard rock depth z in the rock formations from the Danish shallow aquifer system (Table 3.3).

3.2.3.3 Neutron fluxes and energy spectra

Since cross sections vary greatly with incident particle energy (Figure 3.9), the neutron energy distribution must be considered when calculating the radioargon production rate profile (Eq. 3.29). Depending on their production processes, these neutrons are emitted with primary energies up to several tens of MeV but lose their energy when they travel through matter (rock and water). The slowed-down (i.e., epithermal and thermal) neutrons are ultimately absorbed by the material through nuclear reactions (Gosse and Phillips, 2001). The assessment of the moderated secondary neutron energy spectrum is particularly difficult in the case of fast-muon-induced neutrons because of the complexity of their production channels (Section 3.2.3.2). Neutron energy spectra and fluxes underground can be estimated using Monte Carlo simulations (Zhang and Mei, 2014; Empl et al., 2014; Fassò et al., 2000; Grieger et al., 2020).

In the following, we use the neutron spectra simulated by Grieger et al. (2020) with the code FLUKA (Fassò et al., 2000) at the Felsenkeller (DE) Tunnel IV (140 m.w.e) for muon-induced neutrons (μ, n) and neutrons from natural rock radioactivity (i.e. (α, n) neutrons). In the following, a similar spectrum shape to (μ, n) is assumed for the primary cosmogenic neutrons. The simulations were performed for three locations in the tunnel: two measurement chambers (MK1 and MK2) and a workshop room (WS) (Figure 3.16a). An average of MK1 and WS spectra is used for the calculations in the following (see Section 3.3). (μ, n) neutrons comprehend neutrons from fast-muon and slow muon-capture reactions, for which similar energy characteristics are assumed. Both (α, n) and (μ, n) neutrons show a similar spectral shape from thermal energies up to 1 MeV, where (μ, n) flux peaks while (α, n) flux decreases. Above this energy, the (μ, n) spectrum extends to hundredths of MeV while the (α, n) flux drops (Figure 3.11).

The neutron flux ϕ_n [$\text{n cm}^{-2} \text{yr}^{-1}$] relates to the neutron production rates P_n [$\text{n g}^{-1} \text{yr}^{-1}$] following Eq. 3.37 (Gosse and Phillips, 2001; Malgin, 2015), where Λ_n is the attenuation length for isotropic neutron flux in rocks. Λ_n depends weakly on the chemical composition of the media but rather on the initial energy of the particle and the pore water content of the rock. For primary cosmogenic neutrons, $\Lambda_{n,f} = 160 \text{ g cm}^{-2}$ is used (Section 3.1.1). For muon-induced neutrons, we use the value $\Lambda_{n,\mu} = 35 \text{ g cm}^{-2}$ concluded by Malgin (2015).

$$\phi_n(z) = P_n \cdot \Lambda_n \quad (3.37)$$

The chemical composition of rocks controls the neutron production rates and, therefore, the total (energy-integrated) neutron flux. The neutron energy distribution (i.e. the shape of the neutron spectrum) is assumed to be relatively independent of the rock chemical composition (Lowrey, 2013). Implications of this assumption are discussed in Section 3.3.2.2.

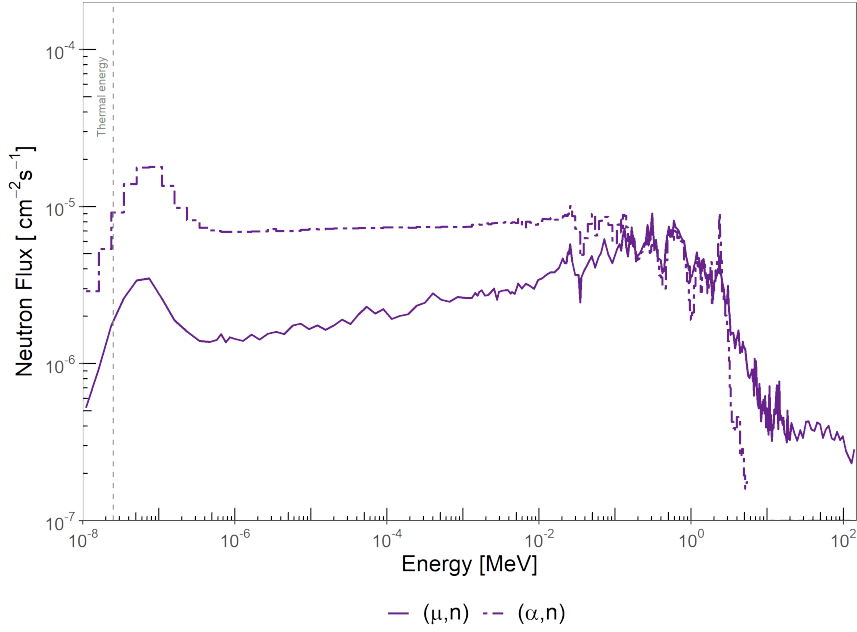


Figure 3.11: Muon-induced (μ,n) and (α,n) neutrons energy spectra simulated with FLUKA in the Felsenkeller Tunner Laboratory (140 m.w.e) by Grieger et al. (2020): average between the fluxes simulated at MK1 and WS locations.

The neutron spectra from the Felsenkeller Tunnel are normalized by their total energy-integrated neutron flux, resulting in a dimensionless neutron spectra (i.e. $[\text{cm}^{-2} \text{s}^{-1}][\text{cm}^{-2} \text{s}^{-1}]^{-1}$). In a subsequent step, these dimensionless spectra are multiplied with the neutron fluxes (Eq. 3.37) from all origins in the subsurface. The (μ,n) dimensionless spectrum is scaled with the neutron fluxes (ϕ_n) calculated from P_{n,μ_f} , P_{n,μ^-} and $P_{n,f}$. The (α,n) spectrum shape is used with the neutron flux calculated from $P_{n,U/Th}$.

The resulting $\phi_n(E)$ are then folded with the production cross sections (Figure 3.9), resulting in the ^{39}Ar and ^{37}Ar production rates (Eq. 3.29). Among the reaction channels with neutrons (Table 3.2), only the reactions $^{39}\text{K}(n,p)^{39}\text{Ar}$ and $^{40}\text{Ca}(n,\alpha)^{37}\text{Ar}$ are considered since the others contribute to less than 1 % of the total production.

3.2.4 Total radioargon production rate profiles

Figure 3.12 summarizes the total production rates for ^{39}Ar and ^{37}Ar (P_{Ar} , Eq. 3.19) with muon capture reactions ($P_{Ar,\mu}$, Eq. 3.23) and neutrons from all origins discussed previously ($P_{Ar,n}$, Eq. 3.30). The general trend is the following :

- The nucleonic component of cosmic rays is unquestionably the dominant production channel in the first few meters of the lithosphere, regardless of the rock chemical composition (Fabryka-Martin, 1988).
- At intermediate depth, the penetrating nature of muons results in dominating muon-induced reactions, including slow muon capture and reactions with muon-induced neutrons (Heisinger et al., 2002a,b).
- Ultimately, production with neutrons originating from the natural radioactivity (U/Th) in rocks is the prevailing process (Šrámek et al., 2017).

For both ^{39}Ar and ^{37}Ar , the production with cosmogenic particles (i.e. mainly muon-induced processes) is dominating up to 60 - 160 m in the sand and clayey till formations, and even deeper for the chalk formation due to the very low natural radioactivity in carbonates. This agrees with Smith (1989) who concluded that radioargon production is dominated by cosmogenic secondaries up to ~ 100 m depth. The reactions with muon-induced neutrons are important because of the high energy of these particles. For example, in the sand formation, the total production rate for neutrons is dominated by U/Th from ~ 20 m depth (Figure 3.10), but reactions with fast-muon-induced neutrons prevail up to depths of 75 - 120 m for the radioargon production rates. Since ^{39}Ar is produced by muon capture on both K and Ca targets, this reaction dominates up to 60 m in the chalk, where the $\text{Ca/K} = 265.3$ is two orders of magnitude larger compared to the other formations (Table 3.3). The relative importance of radioargon production with muon-capture reactions or with neutrons emitted following this process depends on the rock chemical composition.

These conclusions are in relative disagreement with Mei et al. (2010) who stated that (i) ^{39}Ar is produced predominantly by muon-capture reactions over reactions with muon-induced neutrons at all depths (in a rock with $\text{Ca/K} = 1.4$); and (ii) cosmogenic particles are dominating ^{39}Ar production up to 2 km.w.e (i.e. ~ 750 m of standard rock). This disagreement is likely due to the different empirical parametrization with depth for the total muon flux, as well as the other parameters that enter in the calculation (e.g. muon energy, stopping rate ratio etc.). The uncertainties on these parameters are discussed in Section 3.3 for our calculations. However, in the absence of a discussion about the uncertainties in Mei et al. (2010), no further conclusive comparison could be established.

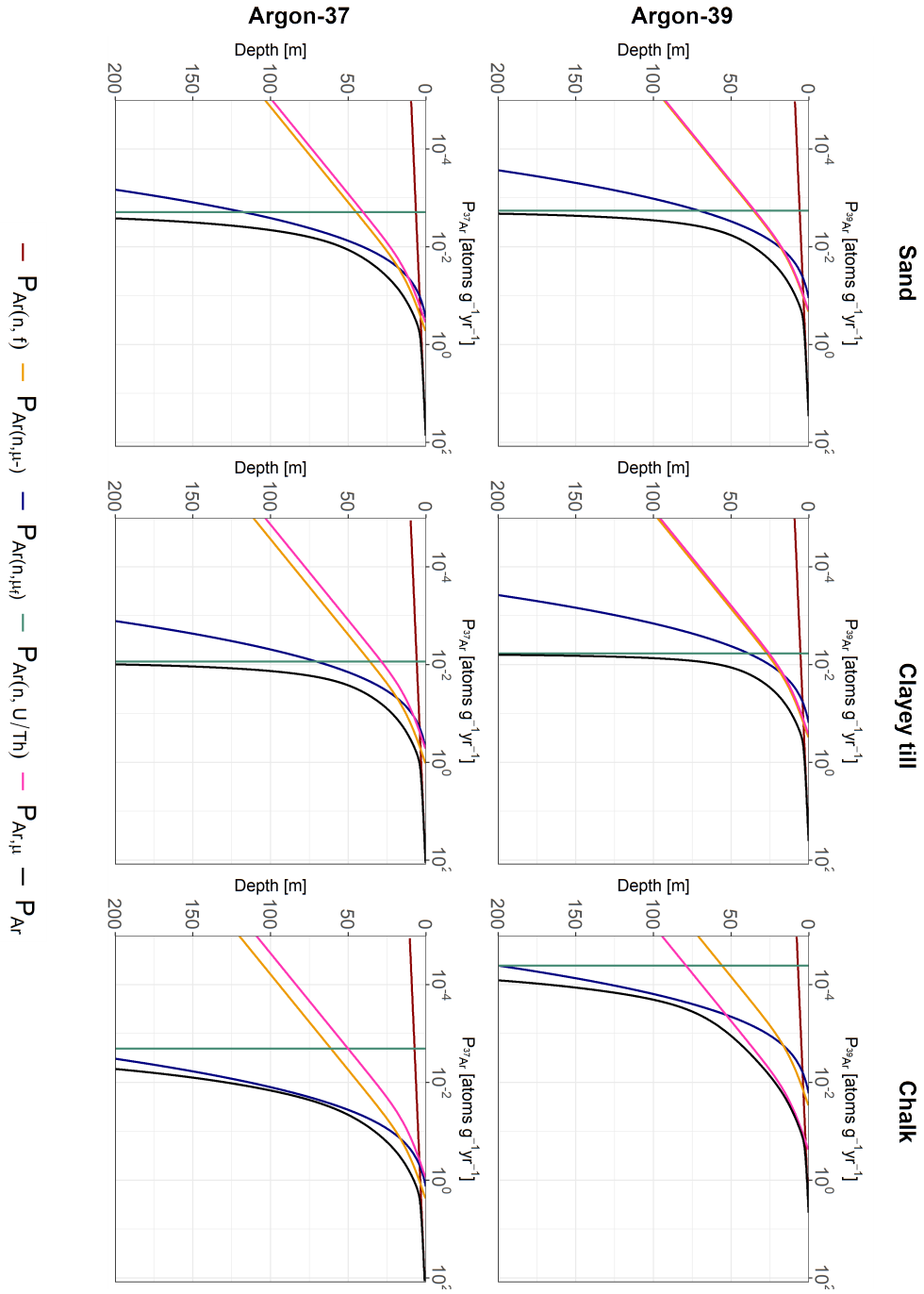
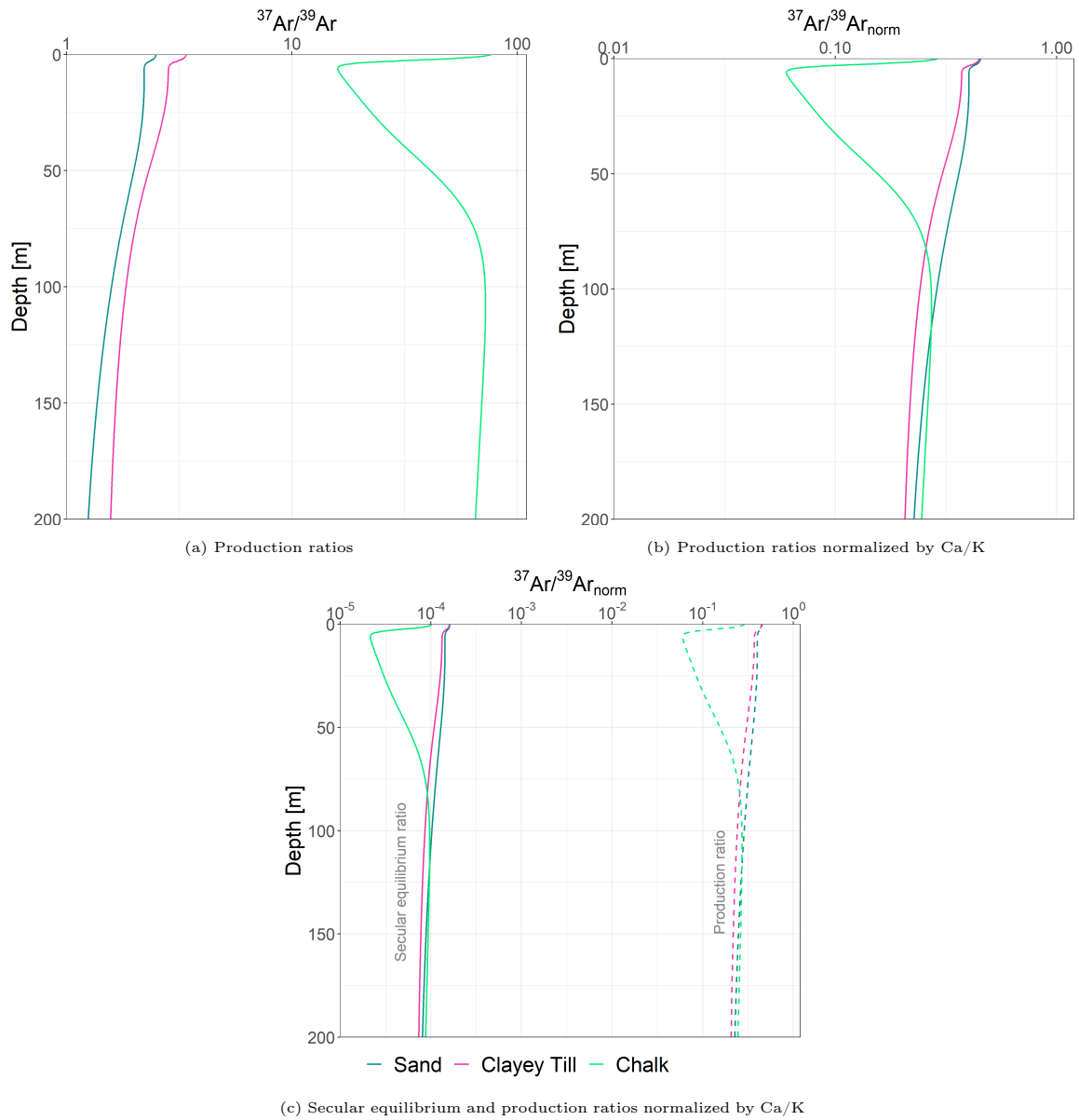


Figure 3.12: ^{39}Ar (upper row) and ^{37}Ar (lower row) production rate profiles as a function of standard rock depth z for all neutron and muon induced channels in the rock formations characterizing the Danish shallow aquifer system

3.2.4.1 $^{37}\text{Ar}/^{39}\text{Ar}$ ratios

The production rate of ^{39}Ar and ^{37}Ar following the reactions with neutrons is largely determined by the target concentration (^{39}K for ^{39}Ar , resp. ^{40}Ca for ^{37}Ar). This is clearly visible in the $^{37}\text{Ar}/^{39}\text{Ar}$ production rates in the Ca-rich chalk (Ca = 30 %wt, K = 0.01 %wt) formation, where the ^{37}Ar production rate is more than one order of magnitude higher than ^{39}Ar (Figure 3.13a). In contrast, in the sand (Ca = 6 % wt, K = 1 %wt) and clayey till (Ca = 11 %wt, K = 1.5 %wt) formations, the production rates for ^{37}Ar and ^{39}Ar are comparable for the whole depth range. By normalizing the production rates by the neutron target element concentrations (i.e. Ca for ^{37}Ar and K for ^{39}Ar), the neutron production rates converge for both rock types to a value of $^{37}\text{Ar}/^{39}\text{Ar} \sim 0.3$ (Figure 3.13b). In the chalk, the production rates at the surface and below 100 m depth are similar, whereas, at intermediate depths (between 4 - 100 m), the significant production of ^{39}Ar by muon-capture on Ca (Figure 3.12) reduces the normalized ratio.

The activity ratio of $^{37}\text{Ar}/^{39}\text{Ar}$ depends on the residence time of the fluid (gas or groundwater) in the underground or, in other words, on the time over which radioargon was produced and accumulated. In a rock in steady state, the ingrowth of ^{39}Ar compared to ^{37}Ar leads to a $^{37}\text{Ar}/^{39}\text{Ar}$ secular equilibrium activity ratio (i.e. $P_{37}/P_{39} \cdot \lambda_{39}/\lambda_{37}$) that is 2800 times lower than the ratio of production rates (full lines in Figure 3.13c). In the case of a pulse production event, the $^{37}\text{Ar}/^{39}\text{Ar}$ ratio will shift towards the production ratio (dashed lines in Figure 3.13c). One interesting application of $^{37}\text{Ar}/^{39}\text{Ar}$ ratios is therefore the detection of clandestine underground nuclear explosions (UNE) in the frame of the Comprehensive Nuclear-Test-Ban Treaty (CTBT). A UNE would correspond to a pulse production event, that could then be distinguished from the natural background situation ($^{37}\text{Ar}/^{39}\text{Ar} \sim 10^{-4}$) during an On-Site Inspection (OSI) by the order of magnitude of the $^{37}\text{Ar}/^{39}\text{Ar}$ ratio measured (McIntyre et al., 2017). Note that this assumes similar emanation rates for both isotopes (Chapter 4) and a fast diffusion from the activities from the site of explosion to the surface.

Figure 3.13: $^{37}\text{Ar}/^{39}\text{Ar}$ ratios

3.3 Uncertainties

The total uncertainty on the production rate profiles, which propagates from the uncertainties of the individual parameters, is estimated with Monte Carlo iterations. These uncertainties are independent and uncorrelated, and their propagation on the total $P_{Ar}(z)$ profile depends on the contributing fraction of the given production channel at the depth z . For each parameter, a value is randomly picked within a uniform distribution delimited by the uncertainty range. The assumption of uniform distribution is preferred to a normal distribution since the uncertainty on most of the parameters is defined from the spread of models. The whole production calculation is then performed with the randomly picked values. This process is repeated 10'000 times, resulting in the same number of production profiles, from which the average and standard deviation are computed as a function of depth.

3.3.1 Uncertainties on the muon-capture reaction

The uncertainty on the muon-capture reaction rate propagates from the muon stopping rate $R_{\mu-}(z)$ parametrization (Eq. 3.18) and the yield of atoms of radioargon produced for each stopped negative muon $Y_{\mu-}^{Ar}$ (Eq. 3.24). A 10 % overall uncertainty on $Y_{\mu-}^{Ar}$ was concluded in the context of ^{36}Cl underground production (Alfimov and Ivy-Ochs, 2009). Figure 3.14 shows the comparison between the $R_{\mu-}(z)$ parametrization from Schaller et al. (2004) used in the present study and previous literature values. An agreement within 30 % can be observed for up to 50 m with the exceptions of the simplified parametrization from Heisinger et al. (2002b) that results in a more attenuated $R_{\mu-}(z)$ from 30 m depths, and the study from Mei and Hime (2006) which results in an even lower $R_{\mu-}(z)$ at shallow depths (and a higher value at depths $z > 100$ m). This curve is calculated by using the total muon flux parametrized for depths $h < 2$ km.w.e (Barboudi and Rastin, 1983; Cassidy et al., 1973; Heisinger et al., 2002a; Miyake, 1963) in combination with the ratio of stopping to through-going muons [Eq. 7 in Mei and Hime (2006)]. However, this ratio was determined for depth-ranges relevant for deep laboratories ($h > 1$ km.w.e) and very high muon energies ($E_{\mu} \geq 1000$ GeV) and may, or may not be valid for our relatively shallow application. The depth range where reaction channels involving $R_{\mu-}$ are significant is below 40 m (Figure 3.12). For this reason, an uncertainty of 30 % is considered in the Monte Carlo simulations.

3.3.2 Uncertainties on the production with neutrons

The uncertainty associated with radioargon production with neutrons $P_{Ar,n}$ (Eq. 3.30) is computed from the uncertainties on the neutron production rates P_n , the neutron energy spectra simulated for the (μ,n) and (α,n) neutrons, and the nuclear cross sections. Uncertainty on the ICP-MS measurements is < 1 % and therefore the target concentrations are assumed to be exact values.

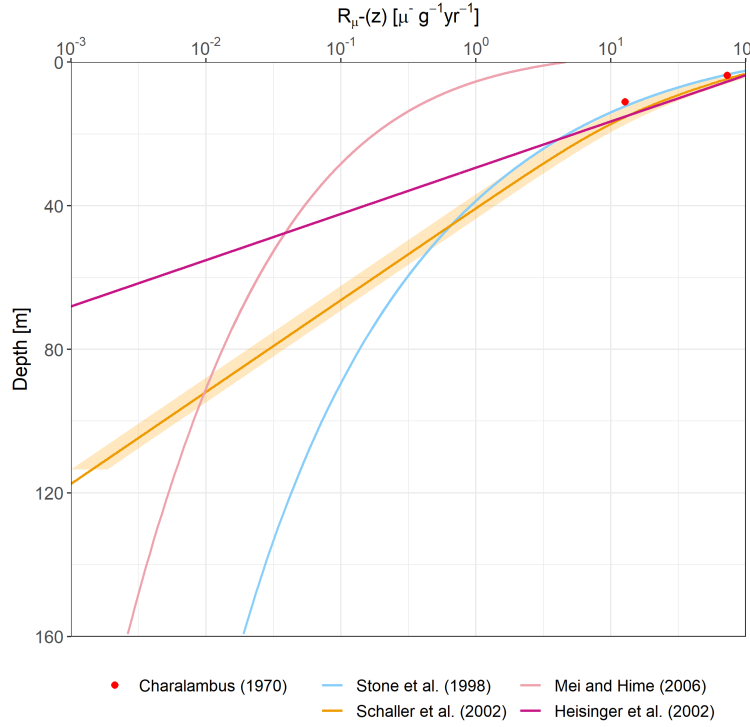


Figure 3.14: Muon stopping rate $R_{\mu^-}(z)$: comparison between the solution used in the present work (Schaller et al., 2004) and parametrizations from (Charalambus, 1970; Heisinger et al., 2002b; Mei and Hime, 2006; Stone et al., 1998). The yellow band represents a 30% uncertainty around the curve from Schaller et al. (2004).

The uncertainty on the cross sections is difficult to estimate since the nuclear data libraries do not provide estimations of the uncertainties. Šrámek et al. (2017) estimated an uncertainty of 30 % by comparing the experimental data available on EXFOR database (<https://www-nds.iaea.org/exfor>) with values from integrated cross sections. Therefore, an uncertainty of 30 % around the cross sections is used for the Monte Carlo iterations.

3.3.2.1 Uncertainties on the neutron production rates

The neutron production rate associated with the hadronic component of cosmic rays ($P_{n,f}$) is to this date well understood (Fabryka-Martin, 1988; Guillon et al., 2016; Riedmann and Purtschert, 2011). Since this process is negligible after the first few meters of the lithosphere, which corresponds to the unsaturated zone in the vast majority of cases, inaccuracies in calculations of $P_{n,f}$ would have a minimal impact on the activities measured in groundwater and are neglected in the following. The average neutron yield per muon capture $Y_{\mu^-}^n$ (Eq. 3.34), which controls P_{n,μ^-} has an uncertainty of about 10 %, similarly to $Y_{\mu^-}^{Ar}$ discussed previously.

The neutron production rate induced by fast-muon P_{n,μ_f} is an vividly debated topic in the literature. Alternative parametrizations to the solution proposed by Heisinger et al. (2002a) for $P_{n,\mu_f}(z)$ (Eq. 3.35) are shown in Figure 3.15. The approach proposed by Malgin (2015) consists in using the Universal formula [UF, Agafonova and Malgin (2013)] for the specific neutron yield and the average muon energy depth-profile from Groom et al. (2001). Early days approximations (Fabryka-Martin, 1988; Stone et al., 1996) consider only the neutron production by Bremsstrahlung induced γ -raysⁱ. An agreement within 50 % is observed between the empirical approach from Heisinger et al. (2002a) and the Monte Carlo simulations from Malgin (2015). Therefore, an uncertainty of 50 % is considered for $P_{n,\mu_f}(z)$ in our Monte Carlo iterations in the following.

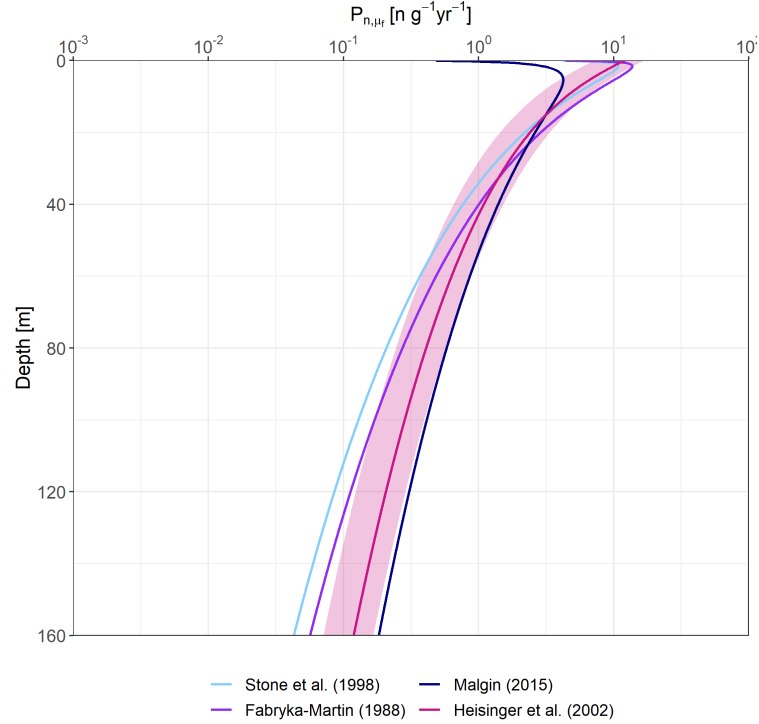


Figure 3.15: Fast muon-induced neutron production rate $P_{n,\mu_f}(z)$: comparison between the solution used in the present work (Heisinger et al., 2002a) and literature values from Fabryka-Martin (1988); Stone et al. (1998); Malgin (2015). The pink band represents a 50% uncertainty around the curve from Heisinger et al. (2002a).

The neutron production rates from U/Th decay chains and spontaneous fission $P_{n,U/Th}$ (Table 3.7) calculated with the code proposed by Šrámek et al. (2017) are compared with the production rate obtained with the early code SLOWN2 (Czubek, 1988) in Table 3.8. An agreement within 30 % is observed.

ⁱThey consider only the photo-nuclear reactions associated with em showers generated by muons, i.e. the channel (iii) in Section 3.2.3.2

Table 3.8: : $P_{n,U/Th}$ comparisons between the calculations with the code proposed by Šrámek et al. (2017) and SLOWN2 (Czubek, 1988).

Rock formation	$P_{n,U/Th}$	
	(Šrámek et al., 2017)	(Czubek, 1988)
Sand	2.82 ± 0.37	1.94 ± 0.58
Clayey till	6.59 ± 0.86	5.58 ± 1.67
Chalk	0.61 ± 0.23	0.46 ± 0.14

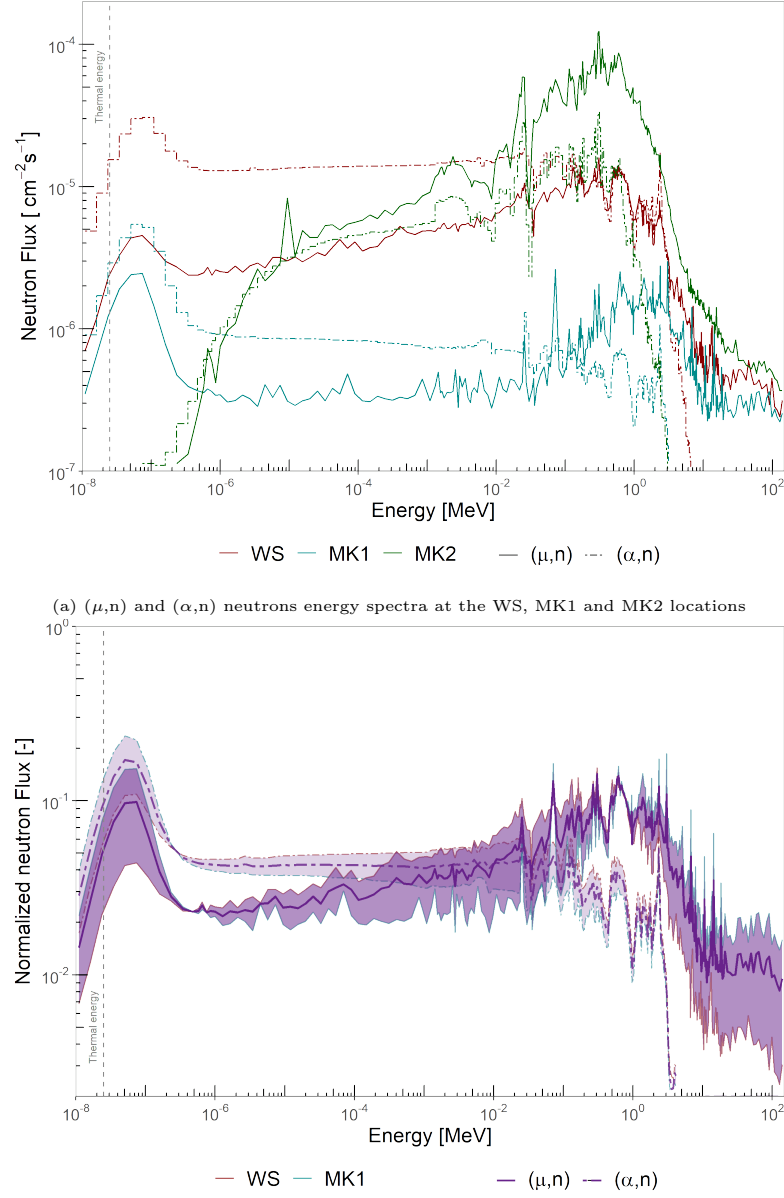
3.3.2.2 Uncertainties on the neutron energy spectra

The neutron energy distributions for the (μ,n) and (α,n) neutrons depend on the localization of the simulation in the Felsenkeller Tunnel, as well as the rock water content. Grieger et al. (2020) performed simulations for three different sites inside this γ -countings facility (Figure 3.16a): (i) MK1: a measurement chamber shielded with an estimated 160 g cm^{-2} total areal density (serpentine rock and pre-bomb steel); (ii) MK2: a measurement chamber shielded with an estimated 210 g cm^{-2} total areal density (steel, iron-pellets, lead); (iii) WS: a workshop shielded by 24 cm thick brick wall. At WS and MK1 locations, the total (energy-integrated) neutron fluxes from (α,n) reactions are dominating over (μ,n) (Table 3.9). This agrees with the neutron production rate calculated at 50 m depth of standard rock (= 140 m.w.e) in the frame of this thesis (Figure 3.10). The high-purity detector present in MK2 forms a significant target for (μ,n) neutrons. In this case, (α,n) neutrons dominate over (μ,n) neutrons.

Table 3.9: Energy-integrated neutron flux ϕ_{n} [$\text{cm}^{-2} \text{s}^{-1}$] simulated with FLUKA (μ,n) and (α,n) in the Felsenkeller Tunnel Laboratory at the WS, MK1 and MK2 locations (Grieger et al., 2020)

Measurement location	$\phi_{\mu,n}$ $\times 10^{-4}$	$\phi_{\alpha,n}$ $\times 10^{-4}$
WS	1.03 (6)	2.8 (6)
MK1	0.16 (6)	0.23 (5)
MK2	3.09 (21)	1.03 (21)

Since the neutron spectra are normalized by the total energy-integrated neutron fluxes, the absolute shielding differences between the measurements sites is not so important for our application. However, the materials and detectors present in the tunnel cavities, as well as the wall compositions affect the energy distributions by moderating the fluxes. For this reason, the simulations at the MK2 location were not used in the present study. Instead, we used an average of the normalized fluxes at the WS and MK1 locations (Figure 3.16b) and the area between the curves (shaded area in Figure 3.16b) was used as an uncertainty range in the Monte Carlo iterations.



(b) Neutron energy spectra normalized by their energy-integrated neutron fluxes for the WS and MK1 locations, as well as the average between these (Table 3.9)

Figure 3.16: Neutron energy spectra simulated with FLUKA in the Felsenkeller Tunnel Laboratory (Grieger, 2021)

These spectra assume a water content of 3 wt% while this value can go up to 12 wt% in aquifers [assuming fully saturated conditions, with $\phi = 30\%$; Grieger et al. (2020)]. A higher water content would have a minimal effect on the energy-integrated neutron flux. However, water being an efficient energy moderator, it is expected that the fraction of thermal neutrons would be increased in case of higher water content, compared to the spectra in Figure 3.16b. The cross sections for both ^{39}Ar and ^{37}Ar are peaking in the high-energy range (Figure 3.9), and therefore the $P_{Ar,n}$ fraction to the total P_{Ar} would likely be reduced. A more quantitative evaluation of this requires additional neutron fluxes simulations.

Finally, the whole method to calculate ^{39}Ar production rates with neutrons proposed in this thesis is evaluated by comparing the $P_{^{39}\text{Ar}(n,U/Th)}$:

- calculated with the normalized energy spectra simulated by Grieger et al. (2020), which are scaled with the neutron flux computed from Eq. 3.37 with $P_{n,U/Th}$ from Šrámek et al. (2017), and $\Lambda_n = 50 \text{ g cm}^{-2}$;
- directly simulated with the python script proposed by Šrámek et al. (2017). The latter uses the Monte Carlo N-Particle transport code MCNP6 to calculate the yield of ^{39}Ar production per neutron, by specifying the energy spectra for each (α, n) and SF neutron channel. The neutron energy spectra are calculated from the production rate of α particles, and their energy distribution;
- calculated with a modified version of SLOWN2 code (Yokochi et al., 2012), which considers the production with the moderated spectrum from a primary 2 MeV mono-energetic neutron spectrum;

The approach proposed in this thesis results in production rates lower by about a factor two, an agreement within the order of magnitude can be observed (Table 3.10). This agreement is considered as satisfactory considering all the assumptions involved in these calculations.

Table 3.10: $P_{^{39}\text{Ar}(n,U/Th)}$ [atoms $\text{kg}^{-1} \text{yr}^{-1}$] comparisons between the calculations with the energy integration of the (α, n) neutron spectra simulated with FLUKA (Grieger et al., 2020), the code proposed by Šrámek et al. (2017) and the SLOWN2 code (Czubek, 1988).

Rock formation	$P_{^{39}\text{Ar}(n,U/Th)}$		
	This study	(Šrámek et al., 2017)	(Czubek, 1988)
Sand	1.9 ± 0.5	3.1 ± 1.0	3.6 ± 1.2
Clayey till	5.9 ± 1.6	12.3 ± 3.7	10.6 ± 3.5
Chalk	0.04 ± 0.02	0.13 ± 0.04	0.22 ± 0.06

3.3.3 Total uncertainty on the production rate

The total uncertainty on radioargon production rates determined by the Monte Carlo simulations is shown in Figure 3.17. The full lines are the mean (μ) of the 10'000 iterations with the variable parameters, and the ranges are the 95 % ($\pm 2\sigma$) confidence interval. The uncertainties depend on the depth because the contribution of each production channel, and therefore the uncertainty associated with them, vary with depth. At intermediate depth ($25 < z < 150 \text{ m}$ of standard rock) the uncertainty range is larger because of the importance of muon-induced processes and the relatively high uncertainty associated with their parameters. The maximal relative uncertainty ($2\sigma/\mu$) is 66 % for ^{39}Ar , resp. 74 % for ^{37}Ar (right panel in Figure 3.17). Our calculations should therefore be considered a robust estimate of the order of magnitude of radioargon underground production.

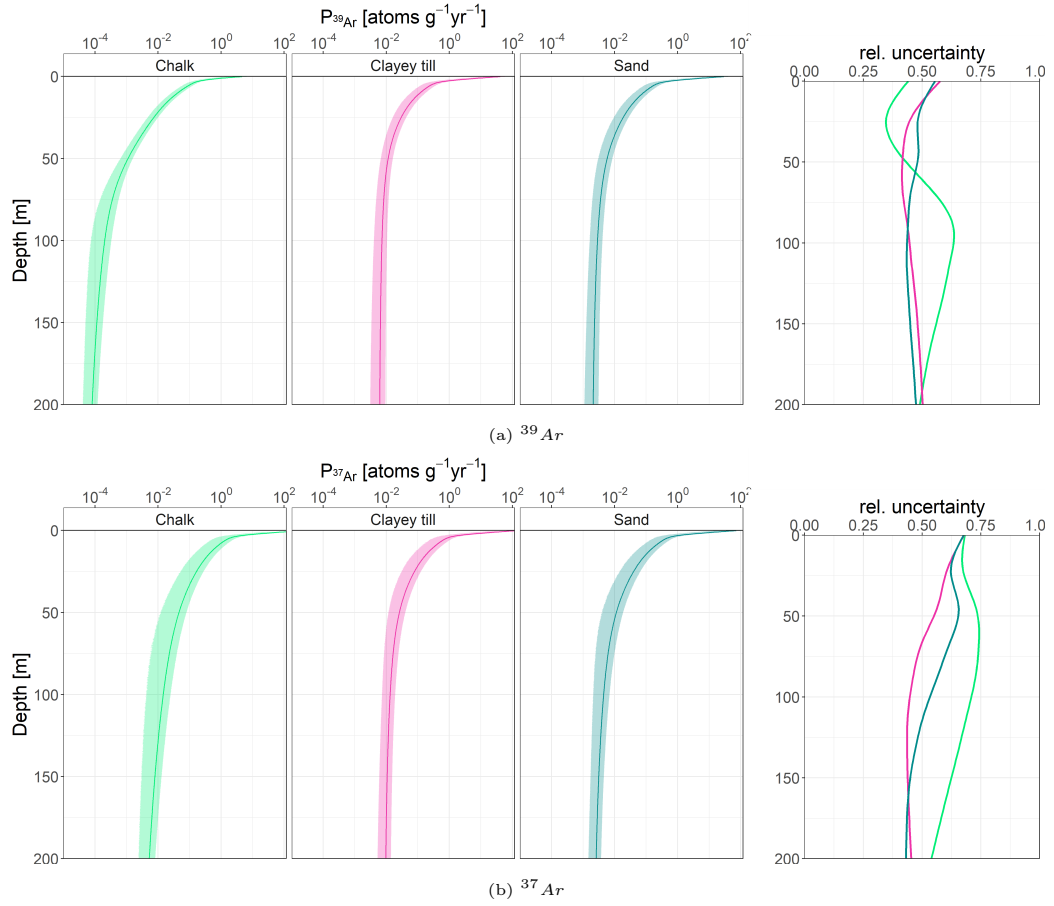


Figure 3.17: Radioargon production rates in the rock formations from the Danish shallow aquifer system. The range represents the 95% confidence interval calculated with Monte Carlo iterations. The relative uncertainty is defined as $2\sigma/\mu$

Figure 3.18 illustrates the $^{37}\text{Ar}/^{39}\text{Ar}$ production ratio normalized by the neutron target ratio (Ca/K) for the three rock formations from the Danish shallow aquifer system. The curves for the sand and the clayey till formations depict similar production rate ratios, and uncertainties with depth. In contrast, in the chalk aquifer, 95% confidence interval shows a wider range at depths between 60 and 120 m. This is associated with the importance of ^{39}Ar production by muon-capture reactions on Ca. In addition, this illustrates the importance of the rock chemical composition for assessing the uncertainty of the production rates.

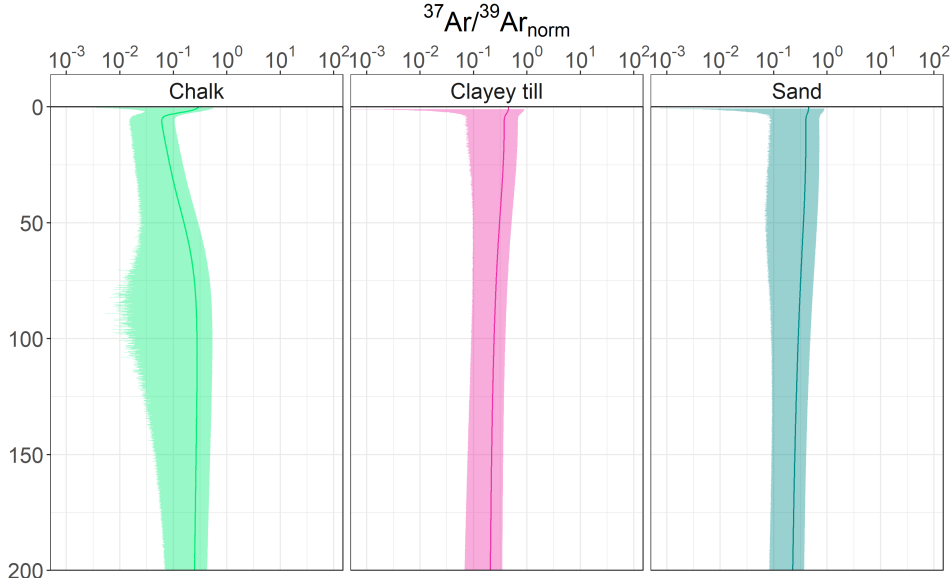


Figure 3.18: Normalized production rate $^{37}\text{Ar}/^{39}\text{Ar}_{\text{norm}}$ in the rock formations from the Danish shallow aquifer system. The range represents the 95% confidence interval calculated with Monte Carlo Simulations.

3.4 Conclusions and outlooks

A comprehensive review of the production channels for ^{39}Ar and ^{37}Ar underground production was done. The depth-dependent production rates for radioargon isotopes and neutrons were calculated for three different rock formations, whose chemical compositions were measured by ICP-MS. The radioargon production rate at a defined depth is the sum of the contributions from muon-capture and neutron reactions.

The neutrons in the underground originate either from lithogenic (i.e. natural U/Th decay chains in the rocks) or cosmogenic (i.e. hadronic component of cosmic rays, and muon-induced neutrons) sources. In all rocks investigated in this study, the neutron production rate profiles are dominated by cosmogenic particles up to depths of 50 - 200 m of standard rock. Below this, the neutrons produced by rock natural radioactivity are prevailing.

Nuclides production cross sections depend on the incident particle energy. Thus, the calculations of radioargon underground production rates require knowledge of the neutron moderated spectrum for each neutron origin. To this end, we used the (μ, n) and (α, n) spectra simulated with an integrated physics MonteCarlo code (FLUKA) in an underground facility at about 50 m (standard rock) depth. For the first time, the muon-induced neutrons contribution to ^{39}Ar and ^{37}Ar underground production could be considered for depth-ranges relevant for groundwater dating applications. Radioargon production profiles calculated for the sand, clayey till and chalk formations showed a significant contribution of muon induced

reactions at shallow - intermediate depth (3 - 150 m). Above this range, the energetic neutrons from the hadronic component of cosmic rays dominate, whereas at greater depths, the production is chiefly due to reactions with neutrons from U/Th in rocks.

The total uncertainties on the production rates were evaluated with Monte Carlo iterations. The maximal relative uncertainties are in the order of 66 % for ^{39}Ar and 74 % for ^{37}Ar . In particular, the neutron energy spectra are critical to the assessment of the muon-induced neutron contribution. The latter is the dominant process in the intermediate depth-range. More simulations, in different rock formations with various water contents would be beneficial for a better constrain of these processes. Even though the uncertainties ranges are relatively large, the present calculations can be considered as a robust estimation of the order of magnitude of the radioargon production rates with depth. In the following, these production rates will be used in combination with residence time distributions and emanation fraction estimations to evaluate the importance of ^{39}Ar and ^{37}Ar underground production for groundwater applications in Denmark.

References

- Agafonova, N. Y. and Malgin, A. S. (2013). Universal formula for the muon-induced neutron yield. *Physical Review D*, 87(11):113013.
- Aglietta, M., Alpat, B., Alyea, E. D., Antonioli, P., Badino, G., Ban, Y., Bari, G., Basile, M., Benelli, A., Berezhinsky, V. S., Bertoni, R., Bianco, S., Bizzeti, A., Bosco, A., Brugnola, G., Bruni, G., Cao, Y., Cara Romeo, G., Castagnoli, C., Castellina, A., Chen, K., Chen, R., Chiavassa, A., Chinellato, J. A., Cifarelli, L., Cindolo, F., Conforto, G., Cong, S., Contin, A., Dadykin, V. L., Desiati, P., De Pasquale, S., De Silva, A., Deutsch, M., Dominici, P., Dos Santos, L. G., Enikeev, R. I., Fabbri, F. L., Fulgione, W., Galeotti, P., Ghia, P., Giusti, P., Grianti, F., Gu, S., Guidi, G., Guo, Y., Hafen, E. S., Haridas, P., Iacobucci, G., Inoue, N., Khalchukov, F. F., Korolkova, E. V., Kortchaguin, P. V., Kortchaguin, V. B., Kudryavtsev, V. A., Landi, G., Lau, K., Lin, X., Lu, L., Luvisetto, M., Ma, J., Ma, Z., Maccarrone, G., Malguin, A. S., Mantovani, R., Mao, Z., Markov, M. A., Massam, T., Mayes, B., Melagrana, C., Mengotti Silva, N., Misaki, A., Mo, G. H., Monteleoni, B., Morello, C., Moromisato, J., Nania, R., Navarra, G., Panaro, L., Parks, D., Pelfer, P. G., Periale, L., Picchi, P., Pinna, P., Pinsky, L., Pless, I. A., Pu, M., Pyrlik, J., Qiu, J., Rysny, V. G., Ryazhskaya, O. G., Saavedra, O., Saitoh, K., Sanders, D., Santini, S., Sartorelli, G., Shen, D., Taborghna, N., Talochkin, V. P., Tang, H., Tang, J., Tian, W., Trincherro, G. C., Turtelli, A., Uman, I., Vallania, P., Vernetto, S., Vetrano, F., Vigorito, C., von Goeler, E., Votano, L., Wada, T., Wang, F., Wang, H., Wang, S., Weinstein, R., Widgoff, M., Xu, L., Xu, Z., Yakushev, V. F., Yamamoto, I., Zatsepin, G. T., Zhou, X., Zhu, Q., Zhu, X., Zhuang, B., and Zichichi, A. (1995). Neutrino-induced and atmospheric single-muon fluxes measured over five decades of intensity by LVD at Gran Sasso Laboratory. *Astroparticle Physics*, 3(4):311–320.
- Alfimov, V. and Ivy-Ochs, S. (2009). How well do we understand production of ^{36}Cl in limestone and dolomite? *Quaternary Geochronology*, 4(6):462–474.
- Allkofer, O. C. and Grieder, P. (1984). Cosmic rays on earth.
- Balco, G., Stone, J. O., Lifton, N. A., and Dunai, T. J. (2008). A complete and easily accessible means of calculating surface exposure ages or erosion rates from ^{10}Be and ^{26}Al measurements. *Quaternary Geochronology*, 3(3):174–195.
- Barbouti, A. I. and Rastin, B. C. (1983). A study of the absolute intensity of muons at sea level and under various thicknesses of absorber. *Journal of Physics G: Nuclear Physics*, 9(12):1577–1595.
- Berger, C., Fröhlich, M., Mönch, H., Nisius, R., Raupach, F., Schleper, P., Benadjal, Y., Blum, D., Bourdaries, C., Dudelzak, B., Eschstruth, P., Jullian, S., Lalanne, D., Laplanche, F., Longuemare, C., Paulot, C., Perdereau, O., Roy, P., Szklarz, G., Behr, L., Degrange, B., Minet, Y., Nguyen-Khac, U., Serri, P., Tisserant, S., Tripp, R. D., Arpesella, C., Bareyre, P., Barloutaud, R., Borg, A., Chardin, G., Ernwein, J., Glicenstein, J. F., Mosca, L., Moscoso, L., Becker, J., Becker, K. H., Daum, H. J., Demski, S., Jacobi, B., Kuznik, B., Mayer, R., Meyer, H., Möller, R., Schubnell, M., Seyffert, B., Wei, Y., and Wintgen, P. (1989). Experimental study of muon bundles observed in the Fréjus detector. *Physical Review D*, 40(7):2163–2171.
- Blokhin, A., Gai, E., Ignatyuk, A., Koba, I., Manokhin, V., and Pronyaev, V. (2016). New version of Neutron Evaluated Data Library BROND-3.1. *Problems of Atomic science and Technology*.
- Bogdanova, L. N., Gavrilov, M. G., Kornoukhov, V. N., and Starostin, A. S. (2006). Cosmic muon flux at shallow depths underground. *Physics of Atomic Nuclei*, 69(8):1293–1298.

- Borozdin, K., Greene, S., Lukić, Z., Milner, E., Miyadera, H., Morris, C., and Perry, J. (2012). Cosmic Ray Radiography of the Damaged Cores of the Fukushima Reactors. *Physical Review Letters*, 109(15):152501. Publisher: American Physical Society.
- Cabellos, O. (2012). *JEFF/DOC-1436: Processing of the JEFF-3.1.2 Cross Section Library into various formats (ACE, PENDF, GENDF, MATXS and BOXER) for testing purposes*.
- Cassiday, G. L., Keuffel, J. W., and Thompson, J. A. (1973). Calculation of the Stopping-Muon Rate Underground. *Physical Review D*, 7(7):2022–2031.
- Cecchini, S. and Spurio, M. (2012). Atmospheric muons: experimental aspects. *Geoscientific Instrumentation, Methods and Data Systems*, 1(2):185–196. Publisher: Copernicus GmbH.
- Charalambus, S. (1970). Nuclear transmutation by negative stopped muons and the activity induced by the cosmic-ray muons. *Nuclear Physics*, A166:145–161.
- Czubek, J. A. (1988). *SLOWN2.BAS Program for Calculation of the Rock Neutron Slowing Down Parameters*. PhD thesis, Institute of Nuclear Physics, Krakow.
- Dunai, T. J. (2000). Scaling factors for production rates of in situ produced cosmogenic nuclides: a critical reevaluation. In *Earth and Planetary Science Letters*, pages 157–169.
- Empl, A., Hungerford, E. V., Jasim, R., and Mosteiro, P. (2014). A Fluka study of underground cosmogenic neutron production. *Journal of Cosmology and Astroparticle Physics*, 2014(08):064–064. Publisher: IOP Publishing.
- Esch, E.-I. (2001). *Detectir development for dark matter research*. PhD, Hustus-Liebig Universität Giessen, Los Alamos.
- Fabryka-Martin, J. (1988). *Production of radionuclides in the earth and their hydrogeologic significance, with emphasis on chlorine-36 and iodine-129*. PhD Thesis, University of Arizona, Tucson.
- Fassò, A., Silari, M., and Ulrici, L. (2000). Predicting Induced Radioactivity at High-Energy Electron Accelerators. *Journal of Nuclear Science and Technology*, 37(sup1):827–834.
- Gaisser, T. K., Honda, M., Kasahara, K., Lee, H., Midorikawa, S., Naumov, V., and Stanev, T. (1996). Comparison of atmospheric neutrino flux calculations at low energies. *Physical Review D*, 54(9):5578–5584. Publisher: American Physical Society.
- Garrison, L. (2014). Measurement of Neutron and Muon Fluxes 100m Underground with the SciBath Detector. Technical Report FERMILAB-THESIS-2014-08, 1151758.
- Gordon, M., Goldhagen, P., Rodbell, K., Zabel, T., Tang, H., Clem, J., and Bailey, P. (2004). Measurement of the flux and energy spectrum of cosmic-ray induced neutrons on the ground. *IEEE Transactions on Nuclear Science*, 51(6):3427–3434.
- Gosse, J. C. and Phillips, F. M. (2001). Terrestrial in situ cosmogenic nuclides: theory and application. *Quaternary Science Reviews*, 20(14):1475–1560.
- Grieder, P. K. F. (2001). *Cosmic Rays at Earth : researcher’s reference manual and data book*. Elsevier Science. Bern.
- Grieger, M. (2021). *Neutronenfluss in Untertagelaboren*. PhD Thesis, Helmholtz-Zentrum Dresden-Rossendorf, TU, Dresden (main).

- Grieger, M., Hensel, T., Agramunt, J., Bemmerer, D., Degering, D., Dillmann, I., Fraile, L. M., Jordan, D., Köster, U., Marta, M., Müller, S. E., Szücs, T., Taín, J. L., and Zuber, K. (2020). Neutron flux and spectrum in the Dresden Felsenkeller underground facility studied by moderated ^3He counters. *Physical Review D*, 101(12):123027. arXiv: 2006.02696.
- Groom, D. E., Mokhov, N. V., and Striganov, S. I. (2001). Muon stopping power and range tables 10 MeV-100TeV. *Atomic Data and Nuclear Data Tables*, 78(2):183–356.
- Guillon, S., Sun, Y., Purtschert, R., Raghoo, L., Pili, E., and Carrigan, C. R. (2016). Alteration of natural ^{37}Ar activity concentration in the subsurface by gas transport and water infiltration. *Journal of Environmental Radioactivity*, 155-156:89–96.
- Heisinger, B., Lal, D., Jull, A., Kubik, P., Ivy-Ochs, S., Knie, K., and Nolte, E. (2002a). Production of selected cosmogenic radionuclides by muons: 2. Capture of negative muons. *Earth and Planetary Science Letters*, 200(3-4):357–369.
- Heisinger, B., Lal, D., Jull, A., Kubik, P., Ivy-Ochs, S., Neumaier, S., Knie, K., Lazarev, V., and Nolte, E. (2002b). Production of selected cosmogenic radionuclides by muons: 1. Fast muons. *Earth and Planetary Science Letters*, 200(3):345–355.
- Judge, R. and Nash, W. F. (1965). Measurements on the muon flux at various zenith angles.
- Kelley, K. (2004). Gadolinium-148 and Other Spallation Production Cross Section Measurements for Accelerator Target Facilities.
- Klinger, J., Clark, S. J., Coleman, M., Gluyas, J. G., Kudryavtsev, V. A., Lincoln, D. L., Pal, S., Paling, S. M., Spooner, N. J. C., Telfer, S., Thompson, L. F., and Woodward, D. (2015). Simulation of muon radiography for monitoring CO₂ stored in a geological reservoir. *International Journal of Greenhouse Gas Control*, 42:644–654.
- Koning, A. J. and Rochman, D. (2012). Modern Nuclear Data Evaluation with the TALYS Code System. *Nuclear Data Sheets*, 113(12):2841–2934.
- Kowatari, M., Ohta, Y., Satoh, S., Nagaoka, K., Abukawa, J., and Nakamura, T. (2007). Evaluation of Geomagnetic Latitude Dependence of the Cosmic-ray Induced Environmental Neutrons in Japan. *Journal of Nuclear Science and Technology*, 44(2):114–120.
- Lechmann, A., Mair, D., Ariga, A., Ariga, T., Ereditato, A., Nishiyama, R., Pistillo, C., Scampoli, P., Schlunegger, F., and Vladymyrov, M. (2018). The effect of rock composition on muon tomography measurements. preprint, Crustal structure and composition/Seismics, seismology, geoelectrics, and electromagnetics/Geophysics.
- Lowrey, J. D. (2013). Subsurface radioactive gas transport and release studies using the UTEX model. Accepted: 2013-10-15T20:18:40Z.
- Ludwig, F., Wagner, L., Al-Abdullah, T., Barnaföldi, G. G., Bemmerer, D., Degering, D., Schmidt, K., Surányi, G., Szücs, T., and Zuber, K. (2019). The muon intensity in the Felsenkeller shallow underground laboratory. *Astroparticle Physics*, 112:24–34. arXiv: 1904.11501.
- Malgin, A. (2017). On the Energy Spectrum of Cosmogenic Neutrons. *Journal of Experimental and Theoretical Physics*, 125:728–740.
- Malgin, A. S. (2015). Characteristics of neutrons produced by muons in a standard rock. *Physics of Atomic Nuclei*, 78(7):835–839.

- Malgin, A. S. and Ryazhskaya, O. G. (2008). Neutrons from muons underground. *Physics of Atomic Nuclei*, 71(10):1769–1781.
- McIntyre, J. I., Aalseth, C. E., Alexander, T. R., Back, H. O., Bellgraph, B. J., Bowyer, T. W., Chipman, V., Cooper, M. W., Day, A. R., Drellack, S., Foxe, M. P., Fritz, B. G., Hayes, J. C., Humble, P., Keillor, M. E., Kirkham, R. R., Krogstad, E. J., Lowrey, J. D., Mace, E. K., Mayer, M. F., Milbrath, B. D., Misner, A., Morley, S. M., Panisko, M. E., Olsen, K. B., Ripplinger, M. D., Seifert, A., and Suarez, R. (2017). Measurements of Argon-39 at the U20az underground nuclear explosion site. *Journal of Environmental Radioactivity*, 178-179:28–35.
- Mei, D.-M. and Hime, A. (2006). Muon-induced background study for underground laboratories. *Physical Review D*, 73(5).
- Mei, D.-M., Yin, Z.-B., Spaans, J., Koppang, M., Hime, A., Keller, C., and Gehman, V. M. (2010). Prediction of underground argon content for dark matter experiments. *Physical Review C*, 81(5).
- Miyake, S. (1963). Empirical Formula for Range Spectrum of Cosmic Ray μ Mesons at Sea Level.
- Morishima, K., Kuno, M., Nishio, A., Kitagawa, N., Manabe, Y., Moto, M., Takasaki, F., Fujii, H., Satoh, K., Kodama, H., Hayashi, K., Odaka, S., Procureur, S., Attié, D., Bouteille, S., Calvet, D., Filosa, C., Magnier, P., Mandjavidze, I., Riallot, M., Marini, B., Gable, P., Date, Y., Sugiura, M., Elshayeb, Y., Elnady, T., Ezzy, M., Guerriero, E., Steiger, V., Serikoff, N., Mouret, J.-B., Charlès, B., Helal, H., and Tayoubi, M. (2017). Discovery of a big void in Khufu’s Pyramid by observation of cosmic-ray muons. *Nature*, 552(7685):386–390. Number: 7685 Publisher: Nature Publishing Group.
- Musy, S., Casolaro, P., Dellepiane, G., Berger, A., Braccini, S., and Purtschert, R. (2022). Quantification of ^{37}Ar emanation fractions from irradiated natural rock samples and field applications. *Journal of Environmental Radioactivity*, 251-252:106966.
- Nakamura, K. and Group, P. D. (2010). Review of Particle Physics. *Journal of Physics G: Nuclear and Particle Physics*, 37(7A):075021. Publisher: IOP Publishing.
- Nakamura, T., Nunomiya, T., Abe, S., Terunuma, K., and Suzuki, H. (2005). Sequential Measurements of Cosmic-Ray Neutron Spectrum and Dose Rate at Sea Level in Sendai, Japan. *Journal of Nuclear Science and Technology*, 42(10):843–853.
- Niedermann, S. (2002). Cosmic-Ray-Produced Noble Gases in Terrestrial Rocks: Dating Tools for Surface Processes. *Reviews in Mineralogy and Geochemistry*, 47(1):731–784.
- Oláh, L., Tanaka, H. K. M., Ohminato, T., and Varga, D. (2018). High-definition and low-noise muography of the Sakurajima volcano with gaseous tracking detectors. *Scientific Reports*, 8(1):3207. Number: 1 Publisher: Nature Publishing Group.
- Palermo, M. (2016). *The muon-induced neutron indirect detection EXperiment, MINIDEX*. PhD thesis, Ludwig-Maximilians-Universität München.
- Riedmann, R. A. (2011). *Separation of Argon from atmospheric air and Measurement of ^{37}Ar for CTBT purposes*. PhD Thesis, Universität Bern, Bern.
- Riedmann, R. A. and Purtschert, R. (2011). Natural ^{37}Ar Concentrations in Soil Air: Implications for Monitoring Underground Nuclear Explosions. *Environmental Science & Technology*, 45(20):8656–8664.

- Schaller, M., Blanckenburg, F., Hovius, N., Veldkamp, A., van den Berg, M., and Kubik, P. W. (2004). Paleocorrosion Rates from Cosmogenic ^{10}Be in a 1.3 Ma Terrace Sequence: Response of the River Meuse to Changes in Climate and Rock Uplift. *The Journal of Geology*, 112(2):127–144. Publisher: The University of Chicago Press.
- Schaller, M., von Blanckenburg, F., Veldkamp, A., Tebbens, L. A., Hovius, N., and Kubik, P. W. (2002). A 30000 yr record of erosion rates from cosmogenic ^{10}Be in Middle European river terraces. *Earth and Planetary Science Letters*, 204(1):307–320.
- Shultis, J. K. and Faw, R. E. (2002). *Fundamentals of Nuclear Science and Engineering*. CRC Press, Boca Raton.
- Smith, B. (1989). *Naturally occurring nuclear reactions in rock formations and groundwaters*. PhD thesis, University of Bath.
- Stone, J., Allan, G., Fifield, L., and Cresswell, R. (1996). Cosmogenic chlorine-36 from calcium spallation. *Geochimica et Cosmochimica Acta*, 60(4):679–692.
- Stone, J., Evans, J., Fifield, L., Allan, G., and Cresswell, R. (1998). Cosmogenic chlorine-36 production in calcite by muons. *Geochimica et Cosmochimica Acta*, pages 433–454.
- Suzuki, T., Measday, D. F., and Roalsvig, J. P. (1987). Total nuclear capture rates for negative muons. *Physical Review C*, 35(6):2212–2224.
- von Egidy, T. and Hartmann, F. J. (1982). Average muonic Coulomb capture probabilities for 65 elements. *Physical Review A*, 26(5):2355–2360.
- Wang, Y.-F., Balic, V., Gratta, G., Fasso', A., Roesler, S., and Ferrari, A. (2001). Predicting Neutron Production from Cosmic-ray Muons. *Physical Review D*, 64(1):013012. arXiv: hep-ex/0101049.
- Watt, B. E. (1952). Energy Spectrum of Neutrons from Thermal Fission of ^{235}U . *Physical Review*, 87(6):1037–1041. Publisher: American Physical Society.
- Yokochi, R., Sturchio, N. C., and Purtschert, R. (2012). Determination of crustal fluid residence times using nucleogenic ^{39}Ar . *Geochimica et Cosmochimica Acta*, 88:19–26.
- Zhang, C. and Mei, D.-M. (2014). Measuring muon-induced neutrons with liquid scintillation detector at Soudan mine. *Physical Review D*, 90(12):122003. Publisher: American Physical Society.
- Šrámek, O., Stevens, L., McDonough, W. F., Mukhopadhyay, S., and Peterson, R. (2017). Subterranean production of neutrons, argon-39 and neon-21 : Rates and uncertainties. *Geochimica et Cosmochimica Acta*, 196:370–387.

Chapter 4

Determining emanation fractions for ^{39}Ar and ^{37}Ar through irradiation experiments

4.1 Introduction

A common issue for all methods based on (or strongly influenced by) isotopes produced in the subsurface is to quantify the proportion of the activity produced in the rock, that is transferred to the pore space. This relationship is commonly referred to as "emanation." Besides ^{39}Ar and ^{37}Ar , this is the case for instance for ^{222}Rn (Peel et al., 2022) and ^{81}Kr (Purtschert et al., 2021). Emanation can be quantified through field studies or irradiation experiments. The difficulty distinguishing between the production and transport mechanism is an inherent complication in constraining the emanation fractions in field studies. Therefore, a preferred method is the irradiation and storage of samples in closed chambers, in which activities build up over time. In this case, the activity produced in the rock can be calculated from the target concentration, and the folding of the reaction cross section and incident particle flux. Because of the important energy-dependency of the cross section, knowledge of the incident particles' energy spectrum is needed.

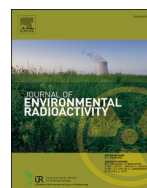
In the frame of this thesis, a methodology to determinate the emanation fractions for ^{37}Ar was developed in close collaboration with the High Energy Physics (group from Prof. Dr. Saverio Braccini) and Geology (Prof. Dr. Alfons Berger) departments of the University of Bern . This allowed for the assessment of emanation fractions from natural rock samples with grain sizes ranging from powder ($< 2 \mu\text{m}$) to macroscopic pebbles ($> 2 \text{ cm}$) in dry and wet conditions. The related publication is enclosed in Section 4.2. This method was then applied to quantify ^{39}Ar emanation fractions. The practical challenges associated with using higher energy neutrons and preliminary numbers are presented in Section 4.3. Finally, the extrapolation of the results obtained in laboratory conditions to real-aquifer situations is discussed in Section 4.4.

4.2 [Article]Quantification of ^{37}Ar emanation fractions from irradiated natural rock samples and field applications

Stéphanie Musy, Pierluigi Casolaro, Gaia Dellepiane, Alfons Berger, Saverio Braccini and Roland Purtschert

Published in *Journal of Environmental Radioactivity*, 106966, 251-252 (2022)
doi: 10.1016/j.jenvrad.2022.106966

Abstract Underground-produced ^{37}Ar can be used for underground nuclear explosions (UNE) detection and for groundwater dating. The quantification of the emanation, that is the fraction of activity produced in the rock that escapes to the pore space, is essential for predicting the background activity expected in natural environments. We propose an experiment in which artificial CaCO_3 powder and natural rock particles are irradiated with neutrons in a routinely operated medical cyclotron, whose energy spectrum is experimentally measured. The produced activity was quantified and compared with the emanated activity to determine the emanating fraction. The results showed consistent and reproducible patterns with a dominance of the recoil process at small scales ($< 2\text{ mm}$). We observed emanation values $\leq 1\%$ with a dependency on the grain size and the inner geometry of particles. Soil weathering and the presence of water increased the recoil emanation. The atoms produced that were instantaneously recoiled in the intra- or inter-granular pore space left macroscopic samples by diffusion on timescales of days to weeks ($D_{eff} = 10^{-12} - 10^{-16}\text{ m}^2\text{ s}^{-1}$). This diffusive transport determines the activity that prevails in the fluid-filled pore space accessible for groundwater or soil gas sampling.



Quantification of ^{37}Ar emanation fractions from irradiated natural rock samples and field applications

S. Musy^{a,*}, P. Casolaro^b, G. Dellepiane^b, A. Berger^c, S. Braccini^b, R. Purtschert^a

^a Climate and Environmental Physics and Oeschger Center for Climate Change Research, University of Bern, Sidlerstrasse 5, 3012, Bern, Switzerland

^b Albert Einstein Center for Fundamental Physics (AEC), Laboratory for High Energy Physics (LHEP), University of Bern, Sidlerstrasse 5, 3012, Bern, Switzerland

^c Institute of Geological Sciences, University of Bern, Baltzerstrasse 1+3, 3012, Bern, Switzerland

ARTICLE INFO

Keywords:

Emanation fraction
 ^{37}Ar
CTBT
Irradiated rocks
Neutron activation
Medical cyclotron

ABSTRACT

Underground-produced ^{37}Ar can be used for underground nuclear explosions (UNE) detection and for groundwater dating. The quantification of the emanation, that is the fraction of activity produced in the rock that escapes to the pore space, is essential for predicting the background activity expected in natural environments. We propose an experiment in which artificial CaCO_3 powder and natural rock particles are irradiated with neutrons in a routinely operated medical cyclotron, whose energy spectrum is experimentally measured. The produced activity was quantified and compared with the emanated activity to determine the emanating fraction. The results showed consistent and reproducible patterns with a dominance of the recoil process at small scales (<2 mm). We observed emanation values $\leq 1\%$ with a dependency on the grain size and the inner geometry of particles. Soil weathering and the presence of water increased the recoil emanation. The atoms produced that were instantaneously recoiled in the intra- or inter-granular pore space left macroscopic samples by diffusion on timescales of days to weeks ($D_{\text{eff}} = 10^{-12} - 10^{-16} \text{ m}^2 \text{ s}^{-1}$). This diffusive transport determines the activity that prevails in the fluid-filled pore space accessible for groundwater or soil gas sampling.

1. Introduction

In geoscience, isotopes produced underground are used for widespread applications like for example exposure dating [^{36}Cl , ^{10}Be (Alfimov and Ivy-Ochs, 2009; Schaller et al., 2002)], groundwater dating [^{39}Ar , ^{37}Ar , ^4He , ^{222}Rn (Lehmann and Purtschert, 1997; Peel et al., 2022; Schilling et al., 2017; Solomon et al., 1996)], or nuclear explosion monitoring [^{37}Ar , ^{131}Xe , ^{133}Xe (Aalseth et al., 2011; Guillon et al., 2016; Riedmann and Purtschert, 2011)]. The relationship between the number of atoms produced in the rock and the number of atoms released in the surrounding fluid phase is crucial for many of them. This so-called emanation fraction determines substantially the activities that are ultimately observed in the pore space. Emanation is commonly difficult to predict because it depends on many factors including the production mechanism, specific location of production in the grain, and rock characteristics. The release mechanisms involved include instantaneous recoil, time-dependent diffusion, and advective transport. Stable nuclides accumulate in the rock until a production-emanation equilibrium is achieved. Hence, the number of atoms produced equals the number of atoms reaching the fluid phase. In sedimentary aquifers this situation is

often realized for $^4\text{He}_{\text{RAD}}$, which is produced in the U/Th decay chains. In contrast, for radioactive nuclides emanation is limited because part of the produced atoms decays during the emanation process (Yokochi et al., 2012).

Among isotopes produced underground, ^{37}Ar is a radioactive noble gas [$t_{1/2} = 34.95 \pm 0.08$ days, Renne and Norman (2001)] with multiple applications. For instance, ^{37}Ar is used as an indicator of clandestine underground nuclear explosions (UNE) during on-site inspections (OSI) under the Comprehensive Nuclear Test-Ban Treaty (CTBT) (Aalseth et al., 2011; Carrigan et al., 1996). It is produced in large amounts by neutron activation of calcium (reaction channel: $^{40}\text{Ca}(n,\alpha)^{37}\text{Ar}$) in the cavity melt and in the rock surrounding an UNE cavity (Haas et al., 2010). Activity concentrations in subsurface gas exceeding natural background levels can thus be interpreted as a signal of a nuclear test (Guillon et al., 2016; Riedmann and Purtschert, 2011). ^{37}Ar is also used for young groundwater dating, where its activity in water is an indicator of the depth-integrated underground water residence time (Schilling et al., 2017). This is important for river water recharge in alluvial aquifers. ^{37}Ar has potential applications as an indicator of ^{39}Ar underground production (Edmunds et al., 2014; Forster et al., 1989).

* Corresponding author.

E-mail address: stephanie.musy@unibe.ch (S. Musy).

<https://doi.org/10.1016/j.jenvrad.2022.106966>

Received 28 March 2022; Received in revised form 27 June 2022; Accepted 11 July 2022

0265-931X/© 2022 The Authors. Published by Elsevier Ltd. This is an open access article under the CC BY license (<http://creativecommons.org/licenses/by/4.0/>).

^{37}Ar is naturally produced in the atmosphere by cosmic-ray neutron capture on ^{40}Ar (reaction channel: $^{40}\text{Ar}(n,4n)^{37}\text{Ar}$). The resulting tropospheric specific ^{37}Ar activity concentration is $\sim 1 \text{ mBq/m}^3_{\text{air}}$ (Johnson et al., 2015; Lal and Peters, 1962; Riedmann and Purtschert, 2011). These levels are negligible compared to ^{37}Ar activities produced and released in the underground. In shallow depths (up to a few meters), ^{37}Ar is predominantly produced by the activation of calcium (Ca) by cosmogenic neutrons via the reaction $^{40}\text{Ca}(n,\alpha)^{37}\text{Ar}$ (Fabryka-Martin, 1988). This leads to activity concentrations in soil air of up to $1000 \text{ mBq/m}^3_{\text{air}}$ (Riedmann and Purtschert, 2011). At greater depths, muon capture processes and reactions by muon-induced neutrons and neutrons from and U/Th decay chains become increasingly important (Heisinger et al., 2002; Spannagel and Fireman, 1972; Šrámek et al., 2017). However, the reaction $^{36}\text{Ar}(n,\gamma)^{37}\text{Ar}$ on argon dissolved in air equilibrated water is negligible in most cases: a rock with 1 wt% Ca, 20% porosity, and 1% emanation releases 300 times more ^{37}Ar than what is produced on ^{36}Ar dissolved in air saturated water.

Constraining emanation fractions in groundwater field studies or in soils is problematic because of the difficulty in distinguishing between production and transport mechanisms. Radioargon emanation fractions of 0.1–20% have been previously estimated in field scale studies (Andrews et al., 1991; Krishnaswami and Seidemann, 1988; Lehmann and Purtschert, 1997; Loosli et al., 1989; Pearson et al., 1991). $^{40}\text{Ar}/^{39}\text{Ar}$ rock dating studies reached similar conclusions (Jourdan et al., 2007; Onstott et al., 1995; Paine et al., 2006). Alternatively, emanation fractions can be determined under laboratory conditions, where soil samples are stored in closed chambers in which the activity builds up over time (Chau et al., 2005). An intrinsic complication is poor knowledge of the energy-dependent production cross-section, especially for thermal and epithermal neutrons. Few irradiation experiments have been performed to constrain the thermal production cross section (Forster et al., 1989; Wilson and Biegalski, 2015). Johnson et al. (2021, 2018) suggested an experimental setup to determine the ^{37}Ar emanation fractions. However, a systematic assessment of ^{37}Ar emanation in natural samples of various sizes and a broadening of the concepts to real aquifer cases are, to our knowledge, still lacking in the literature. Many experimental and numerical emanation studies have been conducted on radon (^{222}Rn). In particular, Sakoda and Ishimori (2017) presents a detailed review of the state-of-the-art in this domain, whose concepts can be applied to other isotopes, including ^{37}Ar .

Herein, we present an experiment in which natural samples are exposed to a low-intensity neutron field available at the medical cyclotron facility at the Bern University Hospital [Inselspital; (Braccini, 2016)]. Neutrons are produced using a (p,n) reaction and the neutron spectrum was measured using a novel neutron spectrometer, DIAMON (Pola et al., 2020). The emanated ^{37}Ar atoms were extracted, and their activity was measured in gas-proportional counters. The produced ^{37}Ar activity was calculated and the emanation fractions of (i) pure calcite powder, (ii) unconsolidated aquifer sediment powder, (iii) various size fractions of sieved aquifer material, (iv) aquifer pebbles, and (v) limestone fragments were determined as the ratio between the activity measured and the activity produced. A conceptual model of emanation in porous aquifers, describing a two-step process consisting of instantaneous recoil followed by time dependent diffusion, is proposed. The factors controlling recoil emanation, such as grain size, target element distribution, weathering, and the presence of water, are discussed based on our results. The importance of diffusion in the solid phase at various temperatures was assessed and further constrained using a heating experiment. Finally, the relevance of the diffusion processes in the pore space of macroscopic samples was examined using a simplified spherical grain model.

2. Methods

2.1. Experiment

2.1.1. Sample description and treatment

Five different groups of samples were investigated:

Group (i): As a simple model and reference material, ultrapure calcium carbonate powder [calcite ($=\text{CaCO}_3$); >99.95% purity, Sigma-Aldrich-398101] was used to determine the production of Ca^{2+} with limited structural effects or interfering reactions. This powder has a homogeneous mineralogy of pure calcite, which results in 40 wt% calcium, and an average particle size of $17 \pm 7 \mu\text{m}$ (determined by measurements on representative 30–50 grains in a light microscope). ^{37}Ar temperature-dependent emanation from this material was further investigated in a heating experiment (Section 4.4).

Group (ii): Natural soil and sediment samples were collected from a drill core (P-54, Table 1) in Emmental, an alluvial valley in west-central Switzerland. This aquifer is composed of Pleistocene glaciofluvial sediments: sandy gravels and cobbles, with a variable proportion of silts (Käser and Hunkeler, 2016; Schilling et al., 2017). The core was 8 m long and subdivided into 1 m sections. Each depth interval was mixed and sampled to assess its chemical composition. At “Activation Laboratories” (in Ontario, Canada), the samples were first dried at 105°C for several hours, pulverized, and fused with lithium metaborate/tetraborate before being digested in a weak nitric acid solution. The elemental composition was then analyzed by ICP-MS (Table A-1 in Appendix A; Actlabs, 2020). The proportion of calcium was stoichiometrically derived from the oxide form (CaO , Table 1). The average grain size of the powdered sediment samples was $1.9 \pm 0.8 \mu\text{m}$.

Group (iii): Sections ranging from 1 to 3 m of the above-described drill core were merged, mixed, and sieved into five different particle size categories (Fig. 1). The chemical composition of the merged sample P54-B is the average of the intervals P54-2 and P54-3.

Group (iv): Two solid-rock pebbles were collected from the drill core of borehole P54. After being cleaned with fresh water, the samples were dried for several hours at room temperature. After irradiation, petrographic thin sections were prepared for the structural analyses. The remainder of the samples were pulverized to determine their chemical composition. The first used pebble was a gneiss consisting mainly of quartz, albite, white mica, and chlorite with a micrometer-scale porosity of <1% which was visually estimated from the SEM images (Fig. B-1 in Appendix B). Calcium was less abundant (<1 wt%) than potassium (approximately 2 wt%). The second used pebble was siliceous limestone consisting of ~ 65 wt% calcite, ~ 35 wt% quartz, and accessory iron oxides (e.g., hematite and/or magnetite). Its porosity was also approximately <1%.

Group (v): The last type of sample was fragments of Cretaceous limestone (so-called “Pierre jaune de Neuchâtel” from the Hauterivian stage) collected from the Swiss Jura Massif (Strasser et al., 2016). This formation has a porosity of 8–19% (Rousset, 2006) and contains an average $33.7 (\pm 0.8) \text{ wt\% Ca}$ (Table 1). Two batches of 4–5 small samples were dried for 24 h at 110°C in a vacuum oven before being weighted. Half of the rock fragments were soaked in degassed water for more than 72 h. With the use of degassed water, interfering reactions on dissolved ^{36}Ar are minimized. The pore water saturation in the “dry” sample is assumed to be 0%, resp. > 50% in the “wet” sample. This was determined by the wet-dry mass difference and a total porosity of 12%.

2.1.2. Irradiation containers and conditions

An important criterion for the selection of suitable irradiation containers is a material featuring a low cross-section for neutron capture and neutron scattering. CaCO_3 powder samples were irradiated in tubes made of pure silica quartz (Heraeus HeraLux®) with a diameter of 8 mm and a volume of $\sim 10 \text{ cm}^3$ (Fig. 2A). Special attention was paid to avoid borosilicate materials because of the high absorption cross-section of boron for thermal neutrons. After loading the tubes with the sample

Table 1

Irradiated samples grouped in relation to sample origin and purpose of the irradiation experiment. The given depth ranges refer to merged drill-core intervals. The calcium content was calculated from the CaO content (Table A-1 in Appendix). The samples P54-1 to P54-8, as well as P54-B, refer to the Pleistocene glaciofluvial material from a drill-core in the Emmental Valley in Switzerland.

	Sample	Depth Range	Type	Irradiated mass [G]	Particle size ^a	CA [WT%]	Purpose
GROUP (I)	CaCO ₃		Powder	2.7 5 8 5.1 5 5.1	17 (±7) μm	40	Production mass dependency (20 °C)
GROUP (II)	P54-1 P54-2 P54-3 P54-4 P54-5 P54-8	0–1 m 1–2 m 2–3 m 3–4 m 4–5 m 7–8 m	Powder	50 7.59 7.66 50.8 7.39 51.1	1.9 (±0.8) μm	5.8 9.0 11.5 12.1 13.4 19	Heated for 8 h at 200 °C Heated for 8 h at 500 °C Heated for 8 h at 800 °C Recoil emanation assessment
GROUP (III)	P54-B	1–3 m	Sieved fraction	11.3 16.2 11.3 12.4 11.4	>2 mm 2 mm–600 μm 600 μm–212 μm 212 μm–63 μm <63 μm	10.3	Particle size emanation dependency
GROUP (IV)	Gneiss Siliceous limestone		Pebbles	31.5 31.32	3.5 × 4 × 1 cm 3 × 3 × 1.5 cm	0.4 26.4	Emanation from undisturbed macroscopic rock fragments
GROUP (V)	Yellow limestone		Limestone fragments	37–39	2 × 2 × 3 cm	33.7 (±0.8)	Water emanation dependency

^a For the pebbles, the “particle size” refers to the actual pebble size. For the limestone, the “particle size” refers to the average size of the irradiated fragments.

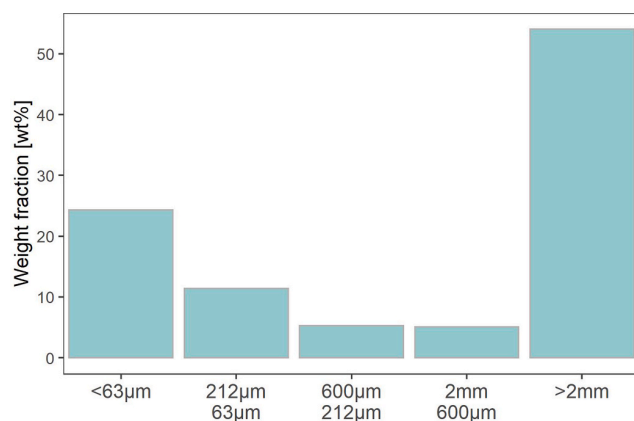


Fig. 1. Weight fraction in each particle size category for the sample P54-B. The material was first sieved through mesh apertures of 0.063, 0.212, 0.6 and 2.0 mm and weighted.

material, they were evacuated ($<10^{-2}$ mbar absolute pressure) to remove air from the pores before being fused under vacuum.

Natural samples from the drilling cores (groups ii–v) were irradiated in alloy vessels with a volume of 180 cm³. The volume section containing the sample material was isolated using filters with a mesh of 20 μm made of sintered bronze (Pfeiffer, ZRS122ZRS040) and a stainless-steel filter with a mesh of 60 μm (Swagelok, SS-4TF-60, Fig. 2B). Powder and sieved fraction samples were placed in small nylon bags (25 μm mesh). In contrast to the quartz tubes, each container was used multiple times and carefully cleaned with alcohol and compressed air between irradiation runs to prevent cross-contamination. After loading the containers and before irradiation, they were evacuated for at least 24 h ($<10^{-2}$ mbar). In contrast, dry and wet limestone samples were irradiated in a helium matrix at ~1 bar. The sample transfer from the degassed water to the irradiation container was also performed under a helium atmosphere to prevent air contamination.

Cross-control experiments were performed to compare the neutron

transparencies of the two types of containers (Appendix C). The results for identical samples but different irradiation runs and containers agreed within the uncertainties and confirmed the absence of systematic differences between the two types of containers.

2.1.3. Irradiation

The samples were irradiated at the cyclotron laboratory at the Bern University Hospital (Inselspital). This 18 MeV compact medical cyclotron is operated daily for the production of ¹⁸F, which is used in radiotracers for positron emission tomography (PET) (Auger et al., 2016; Braccini, 2016). ¹⁸F is produced by bombarding liquid targets via the ¹⁸O(p,n)¹⁸F reaction. A rich multidisciplinary scientific program is ongoing along with the industrial production of radiotracers (Braccini, 2013, 2016; Braccini et al., 2011). The samples were placed in the so-called background position in the cyclotron bunker (i.e. not in front of the targets for ¹⁸F production). The neutron energy spectrum was characterized by a spectrometer called DIAMON (direction-aware isotropic and active neutron MONitor with spectrometric capabilities; Pola et al., 2020) at this position. The signal processing and acquisition system included in DIAMON is conceived to continuously derive the 3D directional distribution of incoming neutrons in the energy range from thermal energy to 20 MeV. The neutron spectrum measured in the sample irradiation position is shown in Fig. 3 for an integrated beam current (IBC) of 0.15 μAh. The IBC is the total charge of the protons that hit the target during the irradiation run. As neutrons are generated by the proton-induced nuclear reaction ¹⁸O(p,n)¹⁸F, the neutron fluence scales linearly with the proton beam current. The neutron fluence for each irradiation run was calculated from the IBC and is listed in Table 3. The relative neutron energy distribution was similar for all runs: approximately 40% of the neutrons were in the thermal energy state (0.025 eV), and 20% had >1 MeV. For comparison, a moderated neutron flux from an average crust material rock (Czubek, 1988) is shown in Fig. 3. Note the seven orders of magnitude difference between the artificial and natural neutron fluxes. Besides the difference in absolute amplitude, the energy distribution of the cyclotron neutrons peaks in the high energies (≥ 1 MeV), whereas natural neutrons (i.e. from average crust) show a flatter spectrum in this range. For an identical total ³⁷Ar production, a larger fraction would arise from fast neutrons activation

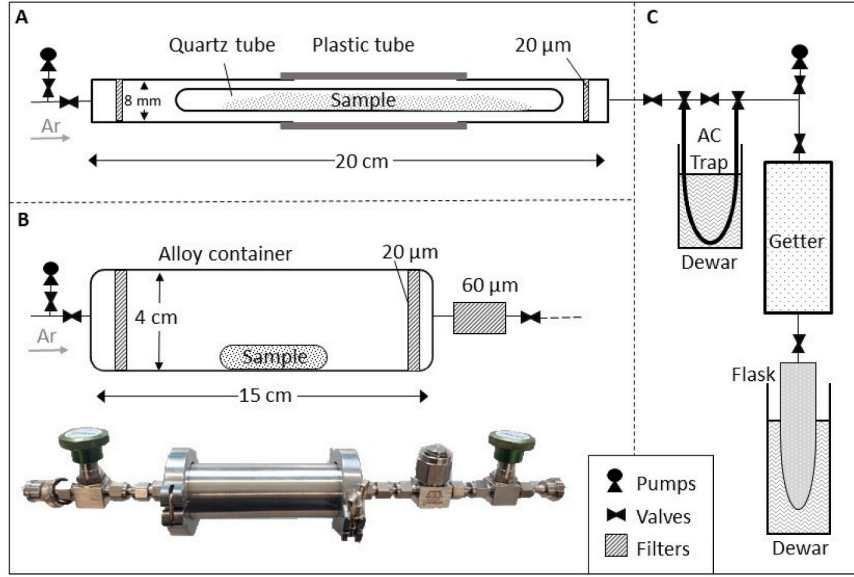


Fig. 2. Irradiation containers and transfer lines used to retrieve the emanated activity. A) Quartz tube in the cracker system; B) Alloy Vessel; C) Transfer line. Ultimately, the gas collected in the flask is used to fill low-level proportional counters.

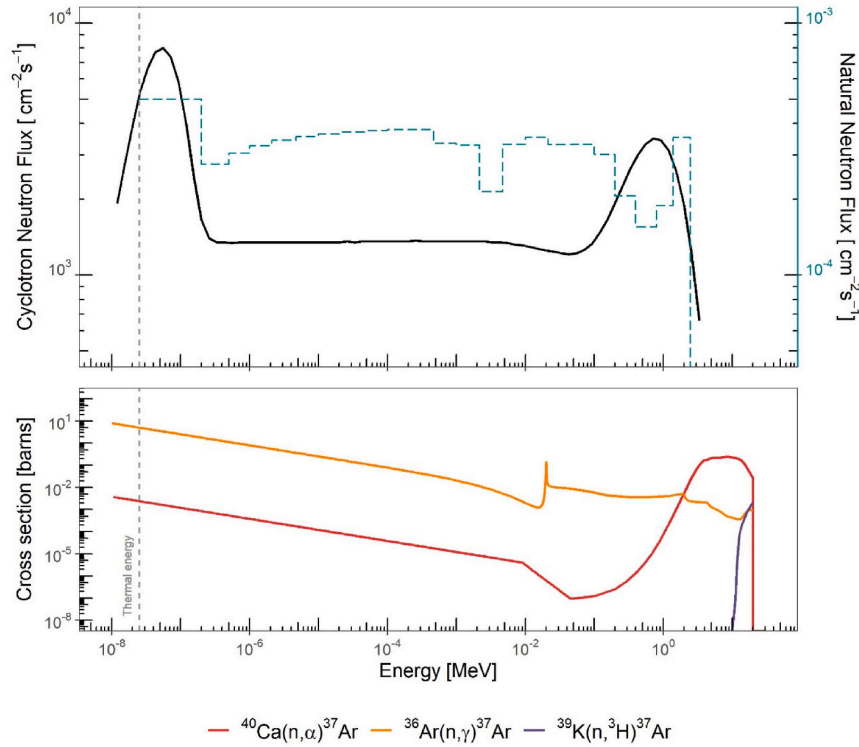


Fig. 3. (top) Measured neutron spectrum at the sample location in the cyclotron (black line) for an integrated beam current of 0.15 µAh, and moderated neutron spectrum from an average crust material rock (Czubek, 1988) (blue dashed line); (bottom) Reaction cross sections for the different ^{37}Ar production channels. (For interpretation of the references to color in this figure legend, the reader is referred to the Web version of this article.)

processes in the cyclotron; therefore, resulting in longer recoil ranges.

The ^{37}Ar production rate P_{37} is the product of the concentration of target atoms N_{tg} , energy-dependent reaction cross section $\sigma(E)$, and neutron flux $\Phi(E)$ (Eq.). The symbols used and units are listed in Table D-1 in Appendix D. The nuclear cross sections of the reaction channels for the ^{37}Ar production with incident neutrons from the

database BROND-3.1 are presented in Fig. 3 (Blokhin et al., 2016). Integrating the cross-section and neutron flux resulted in the production rate per target atom (Table 2).

$$P_{37} = N_{\text{tg}} \int_0^{E_{\text{max}}} \sigma(E) \cdot \Phi(E) dE \quad (1)$$

Table 2

^{37}Ar production channels. The production rate (per atom of target) resulting from the folding of the cyclotron neutron flux and the reaction cross section (Fig. 3) is normalized for IBC = 1 μAh . The contribution from each neutron energy range to the total production rate is also detailed.

Parent	Isotopic abundance	Reaction	Production rate [^{37}Ar s $^{-1}$ N $_{\text{g}}^{-1}$]	Contributing neutron energy ranges [%]		
				Thermal (≤ 0.025 eV)	Epithermal (0.025 eV–1 MeV)	Fast (≥ 1 MeV)
^{40}Ca	0.9694	$^{40}\text{Ca}(\text{n},\alpha)^{37}\text{Ar}$	1.65×10^{-22}	1.2	37.6	61.2
^{36}Ar	0.0033	$^{36}\text{Ar}(\text{n},\gamma)^{37}\text{Ar}$	1.06×10^{-19}	42.7	57.3	<0.1
^{39}K	0.9396	$^{39}\text{K}(\text{n},^3\text{H})^{37}\text{Ar}$	2.88×10^{-29}	0	0	100

Table 3

Neutron fluence (n_f), activity produced P_{37} , gross and net activities (A_{gross} , A_{net}), extrapolated background BG_{ext} , resulting emanation ε_T (Eq. (1)), and minimum detection activity (MDA) for all samples. The uncertainties on ε_T are absolute uncertainties. The activities are reported in mBq and corrected for decay between the end of the irradiation and the measurement. The P54-samples originate from Pleistocene glaciofluvial sediments.

Sample	n_f [cm ⁻²] × 10 ¹¹	P_{37} [Bq]			A_{gross} [mBq]			BG_{ext} [mBq]			A_{net} [mBq]			ε_T [%]			MDA [mBq]
Quartz tubes																	
CaCO ₃ 2.7 g	6.9	4.2 ± 0.3	1.0 ± 1.2	0.2 ± 0.9	0.8 ± 1.2	0.02 ± 0.03	0.3										
CaCO ₃ 5 g	6.9	7.7 ± 0.5	2.3 ± 0.8	0.2 ± 0.9	2.0 ± 0.8	0.03 ± 0.01	0.2										
CaCO ₃ 8 g	6.9	12.3 ± 0.9	4.3 ± 1.0	0.2 ± 0.9	4.0 ± 1.0	0.03 ± 0.01	0.1										
CaCO ₃ 5 g 200 °C	6.9	7.9 ± 0.6	5.2 ± 1.7	0.2 ± 0.9	4.9 ± 1.7	0.06 ± 0.03	0.3										
CaCO ₃ 5 g 500 °C	6.9	7.6 ± 0.5	106 ± 3	0.2 ± 0.9	105 ± 3	1.4 ± 0.1	0.2										
CaCO ₃ 5 g 800 °C	6.9	7.8 ± 0.6	776 ± 4	0.2 ± 0.9	776 ± 4	9.9 ± 0.7	0.2										
P54-2	6.9	1.5 ± 0.1	37 ± 2	0.2 ± 0.9	36 ± 2	2.4 ± 0.3	0.2										
Alloy vessels																	
P54-1	13.1	20 ± 1	1230 ± 18	36 ± 20	1195 ± 38	6.0 ± 0.6	1.3										
P54-2	3.9	1.5 ± 0.1	61 ± 10	11 ± 6	51 ± 16	3.3 ± 1.3	1.4										
P54-3	3.9	2.0 ± 0.2	44 ± 9	11 ± 6	33 ± 15	1.7 ± 0.9	1.3										
P54-4	13.1	42 ± 3	550 ± 17	36 ± 20	514 ± 37	1.2 ± 0.2	1.2										
P54-5	3.9	2.2 ± 0.2	50 ± 8	11 ± 6	40 ± 14	1.8 ± 0.8	1.3										
P54-8	13.1	66 ± 4	966 ± 24	36 ± 20	930 ± 44	1.4 ± 0.1	1.5										
P54-B > 2 mm	19.6	13.1 ± 0.8	104 ± 7	53 ± 29	51 ± 37	0.4 ± 0.3	2.0										
P54-B 2 mm–600 μm	3.9	3.8 ± 0.3	27 ± 5	11 ± 6	27 ± 11	0.7 ± 0.4	1.7										
P54-B 600 μm–212 μm	4.2	2.9 ± 0.3	22 ± 2	12 ± 6	11 ± 9	0.4 ± 0.3	0.3										
P54-B 212 μm–63 μm	19.6	12 ± 1	127 ± 9	53 ± 29	127 ± 38	1.0 ± 0.4	1.3										
P54-B < 63 μm	4.2	2.9 ± 0.3	27 ± 3	12 ± 6	16 ± 9	0.5 ± 0.4	0.9										
Gneiss	4.2	0.32 ± 0.04	33 ± 3	12 ± 6	22 ± 9	6.8 ± 3.8	0.3										
Siliceous limestone	4.2	20 ± 2	15 ± 2	12 ± 6	3 ± 8	0.02 ± 0.04	0.5										
Yellow limestone Dry	1.2	8.8 ± 1.5	31 ± 2	3 ± 2	28 ± 4	0.3 ± 0.1	0.4										
Yellow limestone Wet	1.2	9.1 ± 1.2	78 ± 3	3 ± 2	75 ± 4	0.8 ± 0.2	0.4										

2.1.4. Activity retrieving and measurement

After irradiation, the samples were stored for >1 day, allowing the high activity short-living radioisotopes to decay. The activity emanated from the calcite powder in the quartz tubes was extracted using a cracker system consisting of two stainless-steel tubes joined with a flexible plastic tube (Fig. 2A). After evacuating the cracker system, the glass was broken by bending the plastic tube. The cracker volume was then flooded with pure argon (~ 1 bar) and left for 30 min, allowing for the entire gas phase to equilibrate, thereby highly minimizing the risk that a volume of gas emanated stays trapped in the quartz tube (i.e. a “dead gas” pocket). In the final step, the carrier argon and the sample were passed over a getter (Omni1000, NuPure) to remove the remaining reactive gases and cryogenically transferred to an activated charcoal-filled sample flask (Fig. 2C). This gas flushing and capturing procedure was repeated five times, resulting in a total argon volume in the flask of 1.4–2 L.

The procedure to recover the emanated activity in the alloy vessels was similar: the evacuated vessel was flooded with pure argon (at ~ 1 bar) and left for gas equilibration for 10–15 min. The gas was then transferred over the getter and into the flask at liquid N_2 temperature. The entire flood-retrieval procedure was repeated four times for each sample, resulting in an argon volume transfer of 1.5 L.

This transfer procedure was slightly adapted for the dry and wet limestone samples that were irradiated in a helium matrix. For these samples, an additional activated charcoal (AC) trap was placed on the transfer line between the vessel and capture flask (Fig. 2C). In this

manner, argon, which was trapped at liquid N_2 temperatures, was separated from helium, which was not retained at this temperature and could be pumped out of the system.

Selected powder samples from the sediment powders and the two pebbles were stored in evacuated alloy vessels for 1–3 additional months before repeating the entire transfer procedure. The purpose of this procedure was to assess the efficiency of the initial transfer and investigate long-term emanation (Section 3.2).

For all samples, the gas was filled in proportional counters in the final step and measured by low-level counting (LLC) in the Deep Lab of the University of Bern (Riedmann and Purtschert, 2011). The decay corrected gross activities (A_{gross}) are reported in Table 3. Subtracting the background activity, which is described in the following section, results in the net activities (A_{net}). The total emanation ε_T is then calculated as following:

$$\varepsilon_T = \frac{A_{\text{net}}}{P_{37}} \quad (2)$$

2.2. Blanks and background activities

The pure carrier tank argon used to transfer the activity emanated to the counting system is subjected to ^{37}Ar production from cosmic ray neutron interactions. The resulting equilibrium activity concentration at sea level is $1.06 (\pm 0.15) \text{ mBq} \cdot \text{kg}_{\text{Ar}}^{-1}$ (Saldanha et al., 2019). At 20 °C [$\rho_{\text{Ar}} = 1.641 (\pm 0.003) \text{ kg} \cdot \text{m}^{-3}$], this corresponds to $1.3 (\pm 0.1) \times 10^{-6} \text{ mBq} \cdot \text{cm}_{\text{STP,Ar}}^{-3}$. This is three orders of magnitude lower than the average tropospheric ^{37}Ar activity concentration of $10^{-3} \text{ mBq} \cdot \text{cm}_{\text{STP,Ar}}^{-3}$.

(Purtschert, 2017), for which the production by high-energy neutrons in the high atmosphere and stratosphere layers represents the most significant source. The minimum detectable activity (MDA) is the activity allowing the detection of a peak with 95% confidence level. For each sample, the MDA is calculated as described in Riedmann and Purtschert (2011) (Table 3). In general, for typical measurement conditions (50 cm³ counter filled at 10 bars, 0.47 counting yield), it is about 8×10^{-4} mBq·cm³Ar⁻³. Thus, the specific activity concentration of the tank argon can be neglected.

Several background measurements were performed in both types of irradiation containers without samples. Background counts could originate from filters, seals, air contamination, and cross-sample contamination after cleaning and reusing the alloy containers. The activities measured in these blanks as a function of the neutron fluence from their irradiation runs are presented in Fig. 4. The quartz tube blank irradiation resulted in an activity of $0.2 (\pm 0.9)$ mBq (Table 3), which is in the order of the MDA for this sample. A first blank measurement of the empty alloy vessels resulted in an activity of $0.84 (\pm 0.07)$ mBq, for a neutron fluence of 3.9×10^{-11} n·cm⁻² (IBC = 1183 μAh), which is also in the MDA range. However, subsequent measurements in all vessels resulted in blank activities of up to $25 (\pm 2)$ mBq, with some correlation with neutron fluence (Fig. 4). Contamination of the vessel filters or the different elements along the transfer line (getter and tubes) was excluded by subsequent laboratory tests. The linear dependency of the background activity on the neutron fluence points to the production by interfering reactions. The most critical one is ³⁷Ar production on ³⁶Ar contained in the remaining traces of air in the sample, or from the outgassing of filters and rubber sealings. In the neutron energy range <2 MeV, the ³⁶Ar(n,γ)³⁷Ar reaction has a larger cross-section than that of ⁴⁰Ca (Fig. 3). To explain the observed scatter of background values, air volumes of 5–15 μL_{STP} (³⁶Ar/Ar = 0.33%) are sufficient (shaded area in Fig. 4). This corresponds to a residual pressure of ~0.05 mb in the 180 cm³TP containers, which is slightly higher than the vacuum applied prior to irradiation (<0.01 mb). The reason for the marginally elevated background values could not be conclusively identified. Based on the neutron fluence n_f for each measurement in the alloy vessels, background values were estimated as BG_{ext} [mBq] = $2.7 \times 10^{-11} \cdot n_f$ (solid line in Fig. 4 and values in Table 3).

In the cyclotron, as well as underground, ³⁷Ar is primarily produced by the ⁴⁰Ca(n,α)³⁷Ar reaction channel owing to the predominance of

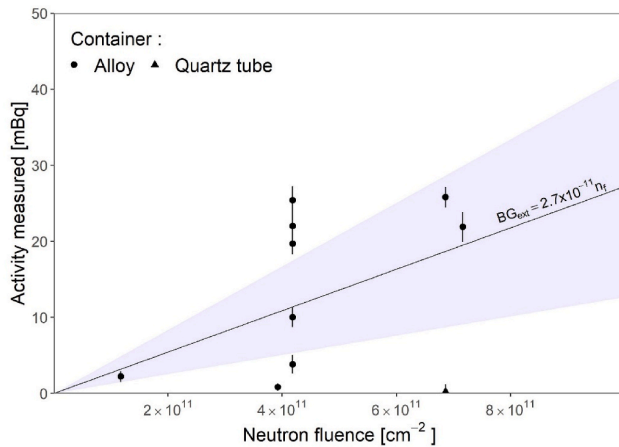


Fig. 4. Background measurements: ³⁷Ar activity produced as a function of the neutron fluence (calculated from the IBC) during the irradiation of the empty containers. The solid line is the linear least squares regression with the neutron fluence. Air volumes of 5–15 μL would result in background values indicated by the shaded area [from the reaction ³⁶Ar(n,γ)³⁷Ar]. This also corresponds to the 95% confidence interval of the linear fitting. The average MDA for the blank irradiation conditions is 0.44 mBq (not visible).

calcium atoms. Our emanations refer only to the calculated activity estimated for this production channel. Interfering reactions, defined as reactions occurring on targets other than ⁴⁰Ca, would thus lead to an emanation overestimation. The possible reaction on potassium, ³⁹K(n,γ)³⁷Ar, is insignificant owing to the very small reaction cross-section for neutron energies <9 MeV (Fabryka-Martin, 1988).

3. Results

3.1. Emanation fractions

The emanation fractions at room temperature for all the experiments are summarized in Fig. 5. The lowest emanation fractions in the powdered samples were observed for calcite, with a median value of 0.03 (±0.01)%. In addition, the CaCO₃ powder samples were used to confirm the constant production rate dependency on the mass of calcite at room temperature (Appendix E). For the sediment powder, an emanation of $1.8 (\pm 0.6)$ % was obtained, whereas particle sizes ranging from 63 μm to 2 mm resulted in $0.5 (\pm 0.3)$ % emanation (Table 3). The errors represent the standard deviations of the emanation values for each sample type and are absolute uncertainties. For the pebbles, the emanation was calculated from the activity measured directly after irradiation (A_{net}), as well as from the total activity after a storage time of approximately one month (described in Section 3.2, Table 4). These activities resulted in emanations of $7 (\pm 4)$ % and $10 (\pm 5)$ %, respectively, for the gneiss and $0.02 (\pm 0.04)$ % and $0.07 (\pm 0.06)$ %, respectively, for the siliceous limestone. Finally, the emanation fractions for the dry and wet limestone were $0.3 (\pm 0.1)$ % and $0.8 (\pm 0.2)$ %, respectively.

3.2. Sample storage

The results presented in the previous section correspond to the activity released shortly after irradiation. Selected samples were stored in an evacuated irradiation container for 1–3 months before repeating the transfer procedure. The residual activity A_s was then corrected for radioactive decay and compared to the net activity measured initially (A_{net} , Table 4). In the sediment powder samples, this residual fraction was between 0.3% and 12.6% of the previous net activities. In contrast, the residual fraction was 41% for the gneiss and 350% for the siliceous limestone. The sum of instantaneous and delayed released activities (last column in Table 4) is then compared with the calculated activity

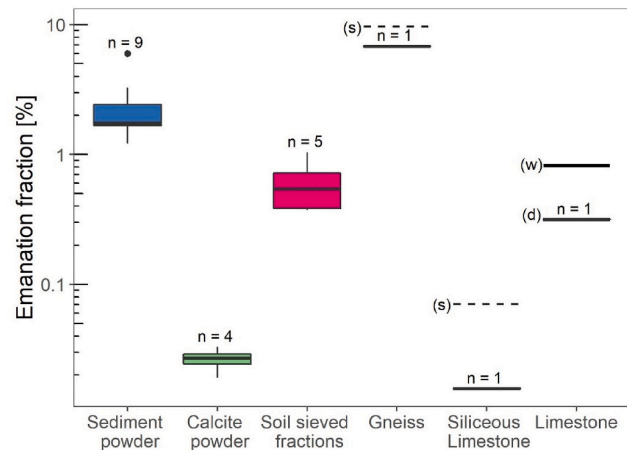


Fig. 5. Emanation fractions at room temperature. Lines (with ranges) refer to measurements shortly after irradiation. The dashed line for the gneiss and the siliceous limestone corresponds to the total emanation after one month of storage (s) (Table 4; Sections 3.2 and 4.5). Limestone values were measured for dry (d) and wet (w) samples. n refers to the number of measurements and the dot for the sediment powder is an outlier.

Table 4

Activity measured shortly after the irradiation (A_{net}) and activities A_S that emanated during an additional storage time of 1–3 months (decay corrected). The total activity is the sum of A_{net} and A_S .

	A_{net} [mBq]	Activities after storage A_S [mBq]			Residual fraction [%]			Total activity [mBq]
		1 month	2 months	3 months	1 month	2 months	3 months	
P54-1	1195	7.8 ± 2.0		3.3 ± 1.9	0.65 ± 0.17		0.27 ± 0.16	1206 ± 40
P54-2	51		3.1 ± 3.0			6.05 ± 6.27		53.7 ± 17.1
P54-3	33		4.2 ± 2.3			12.59 ± 8.94		37.5 ± 15.4
P54-4	514	4.6 ± 1.7			0.90 ± 0.34			519 ± 33
Gneiss	22	8.9 ± 2.4			41.4 ± 20.6			30.5 ± 8.2
Siliceous limestone	3.2	11.2 ± 2.7			350 ± 255			14.4 ± 9.4

produced P_{37} (Table 3), resulting in total emanation fractions of 9.5% for the gneiss resp. 0.07% for the siliceous limestone (dotted lines in Fig. 5). This delayed release is discussed in the context of diffusion emanation in Section 4.5.

4. Discussion

4.1. Conceptualization of the emanation process

The emanation process from the macroscopic samples can be described using a two-step process. First, the nuclide was transferred from the solid mineral phase into a pore space by instantaneous recoil. This process is described by recoil theories [(Onstott et al., 1995); Section 4.2] and is called the emanation power in the context of ^{222}Rn emanation (Semkow, 1990). The volume and geometry of the pore space in which the nuclide, in our case ^{37}Ar , is released, depend on the scale of the system considered. This can range from the internal structure of a grain (Fig. 6A) or a solid piece of rock (Fig. 6B) to a coarser porosity in the case of an aggregate of smaller sub-clasts (Fig. 6C). Herein, it is assumed that the production is homogeneous in all sub-compartments.

In the second step, the released nuclides migrate by time-dependent diffusion from the internal pore space to an outer macroscopic pore volume, where it is eventually sampled and measured (Section 4.5). The transport process from the site of production (i.e. the rock) to the volume available for advective transport is especially important during groundwater extraction in aquifers and gas extraction in soils. These methods are carried out in boreholes and drain the most conductive parts of the system, and therefore inherently resulting in flow averaged

concentrations (Musy et al., 2021). This is especially the case for ^{37}Ar , where large sample volumes are required for analysis (Loosli and Purtschert, 2005). Assessing the emanation at the aquifer scale (Fig. 6D) is then essential to constrain the importance of underground production in the activities measured.

In ^{222}Rn literature, diffusion through the pores of macroscopic samples is called exhalation (Sakoda and Ishimori, 2017). This is not to be confused with solid-phase diffusion in the crystal lattice that occurs simultaneously with recoil emanation (Flügge and Zimens, 1939; Maraziotis, 1996). This slow process can be neglected at ambient temperature for ^{37}Ar because of its relatively short half-life but becomes significant at higher temperatures (Section 4.4).

In nature, both the recoil and diffusion processes occur simultaneously in a production-decay-loss steady-state equilibrium. In contrast, in irradiation experiments, highly transient conditions prevail because production occurs over a much shorter timescale than the half-life of ^{37}Ar . We define the total emanation fraction ϵ_T , which is given by the product of the recoil emanation ϵ_R and macroscopic diffusion emanation (or exhalation) ϵ_D (Eq. (3)). Note that these two processes occur successively and are therefore described as a product in Eq. (3) in contrast to simultaneous processes, which would be parameterized by a sum. In the following section, we interpret our data using this simple concept. For a spherical grain with radius r_0 and recoil range R , the recoil emanation ϵ_R is described by Eq. (4) (Flügge and Zimens, 1939). When $2r_0 \gg R$, the second term can be neglected. Similarly, the steady-state diffusive emanation fraction ϵ_D can be defined from the particle size and effective diffusion coefficient D (Eq. (5)) for spherical conglomerates with radii larger than the diffusion length ($r_0 > L$). For short times t

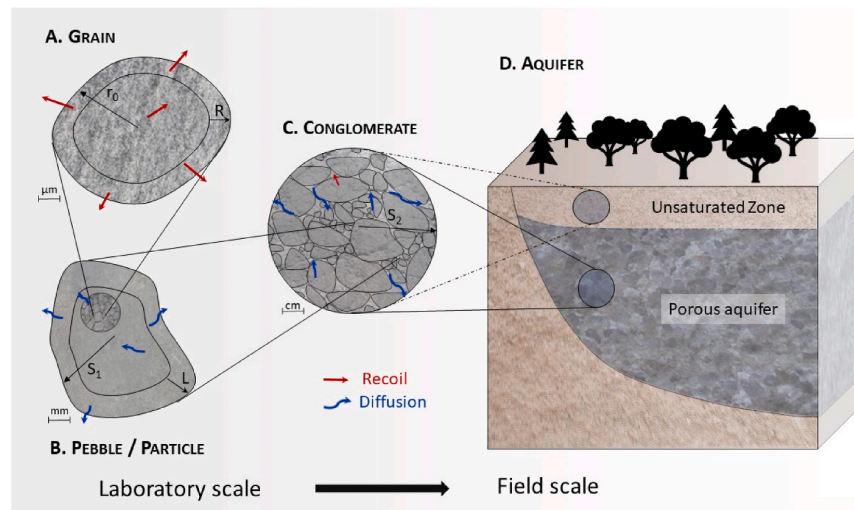


Fig. 6. Conceptualization of the emanation process on different spatial scales. A) Recoil emanation from a spherical grain with a radius r_0 and recoil range R followed by B) diffusive migration from macroscopic samples (particle) of size S_1 and diffusion length L or C) from conglomerates of dimension S_2 in D) natural systems. Our experiments provide information about the scales A) and B).

$\ll T = \lambda^{-1}$, the diffusion length L can be replaced by the depletion layer x_d [Eq. (6), Jourdan et al. (2007)].

$$\varepsilon_T = \varepsilon_R \cdot \varepsilon_D \text{ with } \varepsilon_T \leq \varepsilon_R \quad (3)$$

$$\varepsilon_R = \frac{3}{4} \frac{R}{r_0} - \frac{1}{16} \left(\frac{R}{r_0} \right)^3 \text{ for } 2r_0 \leq R \quad (4)$$

$$\varepsilon_D = 3 \frac{L}{r_0} \text{ with } L = \sqrt{\frac{D}{\lambda}} \quad (5)$$

$$x_d = \sqrt{D \cdot t} \quad (6)$$

The recoil range R of particle B , produced in a nuclear reaction of type $A(a,b)B$, depends on the momentum of the incident particle a , the masses of the reaction partners involved (A , b , and B), the reaction energy, and the density of the surrounding media. The recoil range of the reaction $^{40}\text{Ca}(n,\alpha)^{37}\text{Ar}$ in a medium with a density $\rho = 2.6 \text{ g cm}^{-3}$ has been estimated to be in the range of 0.1–0.3 μm (Onstott et al., 1995).

4.2. Recoil-dominated emanation

In irradiated pulverized samples, recoil emanation is likely the dominant process to consider, while diffusion is of minor importance. For a given recoil range, it is expected that the finer the powder, the larger the emanation fraction. The higher emanation observed in the sediment powder than in the calcite powder is attributed to the grain size difference. The average grain size ($= 2r_0$) of the calcite powder was 17 μm and only 1.9 μm in the sediment powder samples (Table 1). Using Eq. (4) with $R = 0.2 \mu\text{m}$, the theoretical recoil emanation was 18% for the sediment powder and 1.7% for the calcite powder. However, these values must be regarded as upper estimates because the process of implantation in the adjacent grain is not considered. If a recoiled atom has sufficient energy to cross the pore space, it can eventually end its course in the opposite grain, thereby reducing the fraction of recoil emanation (Fleischer, 1983). Therefore, assessing the effect of an average longer recoil range, associated for instance with a larger fraction of activity produced by high energy neutrons (as it is the case in the cyclotron, see Section 2.1.3) requires consideration of the pore geometry and saturation conditions.

The expected smaller emanations with increasing grain size seem to contradict the relatively uniform emanation values observed in the sieved material over a grain size range of 63 μm – 2 mm (Table 3, Fig. 7). The different sieved fractions can be seen as diversely sized aggregates of the same material (Fig. 6A and B). The recoil emanation is similar for all particle sizes of the same material because it depends on the grain

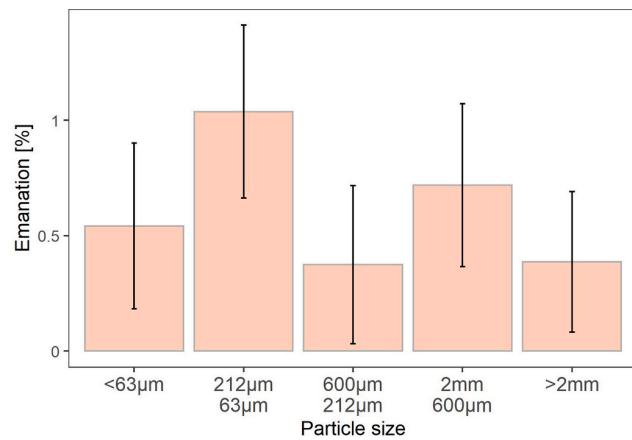


Fig. 7. Dependency of the emanation on the particle size in samples of differently sieved fractions.

packing, that is, the inner particle porosity (Peng et al., 2012). Assuming an effective pore diffusion coefficient of $D_{\text{eff}} = 10^{-11} \text{ m}^2 \text{ s}^{-1}$ (see below), the depletion layer over one week is $x_d \cong 2 \text{ mm}$ (Eq. (6)), which is sufficient for the total diffusion of the activity out of the particles, even for the largest ones.

After the first ^{37}Ar extraction procedure, the powdered sediment samples were stored for a second time for several weeks to investigate delayed release owing to diffusion out of the samples. Only a very minor fraction of total production resided in the samples after 1–3 months (0.2–12.5%, Table 4), which indicates that the yield of the extraction procedure (Section 2.1.4) was high, but also that emanation after irradiation occurred predominantly by recoil in the powdered samples. A different situation can be expected for the macroscopic samples (Section 4.5).

4.3. ^{37}Ar emanation in soil

The measured emanation fractions of the powdered sediment showed a clear trend with the depth from which the samples were collected (Fig. 8A, Table 3). Soil is defined as unconsolidated organic or mineral material on the immediate surface of the Earth. In our case, this likely represents the top few decimeters of the sediment core. The chemical and structural soil constitution is strongly influenced by weathering processes, which decrease with increasing soil depth (Burke et al., 2009; Suther et al., 2021). The degree of soil-weathering can be parameterized by chemical weathering indices (CWIs), which are commonly characterized by measuring the ratios between “immobile” and “mobile” oxides (Delvaux et al., 1989; Price and Velbel, 2003). Fig. 8B shows that the emanation fractions increase with Vogt’s residual index V (Liu et al., 2014), which characterizes the degree of weathering and hence the fraction of fine clay minerals in the shallow soil horizons. The positive correlation can be understood by the high cation exchange capacity (CEC) of clay minerals (CUCE, 2007; Radulov et al., 2011). Thereby, negatively charged sites on clay minerals and organic matter surfaces adsorb cations, including Ca^{2+} , and prevent their downwards leaching. This results in the agglomeration of Ca^{2+} ions at the external surface of the grains, thus enhancing ^{37}Ar production by the $^{40}\text{Ca}(n, \alpha)^{37}\text{Ar}$ reaction at sites from which ^{37}Ar easily escapes.

4.4. Diffusion in crystal lattices

In a mineral grain, the radionuclides that did not escape by recoil may still diffuse in the crystal lattice. This so-called “solid diffusion” contributes to the total activity emanated in the pore space and is thus available for pore diffusion (i.e. exhalation). To constrain the solid diffusion coefficients, a heating experiment was performed using CaCO_3 powder samples ($m = 5.0 \pm 0.1 \text{ g}$). After irradiation, the samples were placed in a furnace for 8 h at either 200 $^\circ\text{C}$, 500 $^\circ\text{C}$, or 800 $^\circ\text{C}$ before being transferred. The total emanation fraction ε_T was measured for each temperature (Fig. 9A). As solid diffusion and recoil emanation occur concurrently, ε_T is the sum of the constant recoil emanation ε_R and temperature-dependent diffusion emanation $\varepsilon_{D_s}(T)$ (Eq. (7)).

$$\varepsilon_T(T) = (\varepsilon_R + \varepsilon_{D_s}(T)) \quad (7)$$

For a heating time much shorter than the half-life ($t \ll T_{1/2}$), Eq. (8) applies to the relationship between diffusive emanation $\varepsilon_{D_s}(T)$ and the diffusion parameter D_s (Flügge and Zimens, 1939). $D_s(T)$ was then calculated for each temperature (Fig. 9B) using Eq. (9) and fitted using the Arrhenius equation (Eq. (10)). The activation energy E_a and frequency factor D_0 can be derived from the slope and y-intercept of the regression line, respectively, and ε_R is a free-fitting parameter for the regression. The resulting $\varepsilon_{D_s}(T)$ calculated from $D_s(T)$ in Eq. (8) are shown in Fig. 9A.

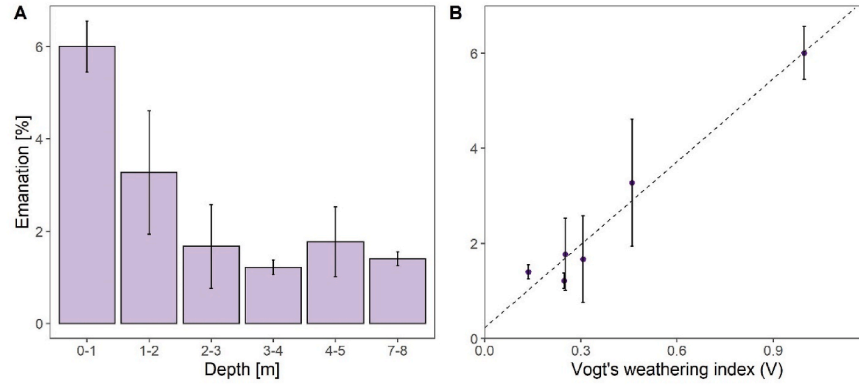


Fig. 8. Emanation dependency on A) depth below surface in the sediment powder samples; B) Vogt soil weathering index determined from the measured soil composition in Table A-1.

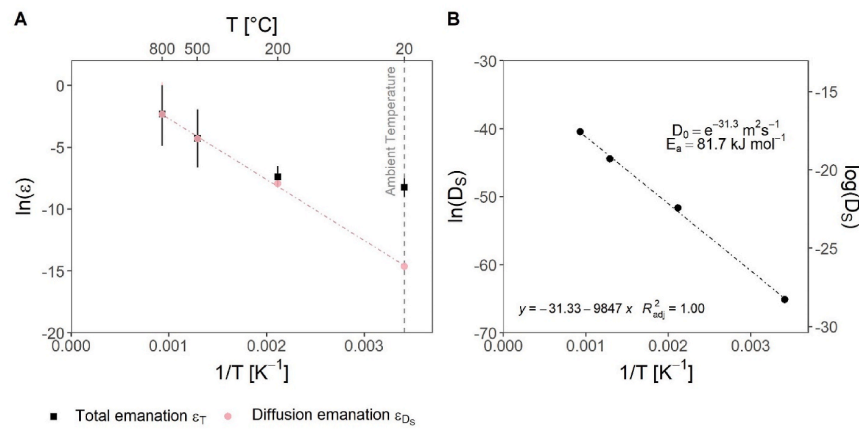


Fig. 9. A) Relationship between the emanations ε_T (black squares) and ε_{Ds} (pink dots) of the heated CaCO_3 measurements and the temperature (T); the pink line is the linear regression of ε_{Ds} with $\varepsilon_R = 0.026\%$. B) Arrhenius plot (Eq. (10)); the linear relationship between the solid diffusion coefficient D_s calculated with Eqs. (9) and $1/T$. (For interpretation of the references to color in this figure legend, the reader is referred to the Web version of this article.)

$$\varepsilon_{Ds}(T) = (\varepsilon_T(T) - \varepsilon_R) = \frac{3}{r_0} \sqrt{D_s(T) \cdot t} = C \cdot \sqrt{D_s(T)} \quad (8)$$

with $C = \frac{3 \cdot \sqrt{t}}{r_0}$

$$D_s(T) = (\varepsilon_T(T) - \varepsilon_R)^2 \cdot C^{-2} \quad (9)$$

$$D_s(T) = D_0 \cdot e^{-\frac{E_a}{R \cdot T}} \quad (10)$$

The linearity of the data ($R^2 = 1$) indicates a single-domain diffusion of Ar in calcite over the tested temperature range (Harrison and Lovera, 2014). The $\varepsilon_R = 0.026\%$ resulting from the linear fitting agreed with the median value for calcite powders at room temperature (Fig. 5). The activation energy $E_a = 81.7 \text{ kJ mol}^{-1}$ derived from the slope of the Arrhenius equation is comparable to the values concluded for plagioclase [85 kJ mol^{-1} (Schwarz, 2001);] or quartz [51 kJ mol^{-1} (Watson and Cherniak, 2003)]. The diffusion coefficient at room temperature was $D_s = 5.3 \times 10^{-29} \text{ m}^2 \text{ s}^{-1}$, which is consistent with previous estimates in the order of $10^{-26} - 10^{-28} \text{ m}^2 \text{ s}^{-1}$ (Riedmann and Purtschert, 2011; Watson and Cherniak, 2003). These values resulted in a diffusion length of $<1 \text{ nm}$, therefore not allowing any significant solid-diffusion emanation in a grain $>1 \mu\text{m}$ before ^{37}Ar decays.

4.5. Emanation from macroscopic samples

In contrast to the powder samples, the pebbles showed much larger

remaining activities after a one-month storage (Table 4), indicating diffusive transport at a larger scale. After the atoms are released by recoil, this macroscopic diffusion may take place along crystal imperfections, grain boundaries, or in an inner network of nanopores (Rama and Moore, 1984) like for instance, alpha-recoil tracks (so-called “radiation damages”) (Guenther et al., 2013; Morawska and Phillips, 1992). Consequently, the resulting effective diffusion coefficient D_{eff} in the pore space is scale-dependent (Lehmann and Purtschert, 1997). For a given scale and radioactive tracer, a slower diffusion (linked with a smaller D_{eff}) leads to a delayed emanation process, allowing more time for the radioactive decay and therefore an overall lower emanation fraction.

The delayed release observed during sample storage was interpreted in the framework of a transient diffusion transport model for spherical grains with radius r_0 . The concentration C_p of ^{37}Ar within the micropore space after recoil is given by Eq. (11), with the initial condition $C_p(r, 0) = C_0 = P_{37} \cdot \varepsilon_R$ being the activity concentration recoiled in the pore space instantaneously after the irradiation. The activity at the outer pebble boundary was assumed to be constant $C_p(r = r_0, t) = 0$. The differential equation was solved numerically using the R-Package ReacTran (Soetaert and Meysman, 2012). The flux $J(t)$ escaping the pebble with surface area S , as described by Fick's first law (Eq. (12)), decreased exponentially with time owing to mass conservation and radioactive decay.

$$\frac{\partial C_p(r, t)}{\partial t} = D_{eff} \frac{\partial^2 C_p(r, t)}{\partial r^2} - \lambda C_p(r, t) \quad (11)$$

$$J(t) = S \cdot D \cdot \left. \frac{\partial C_p}{\partial r} \right|_{r=r_0} \quad (12)$$

$$\frac{\partial C_v(t)}{\partial t} = J(t) - \lambda C_v(t) \quad (13)$$

The build-up of activity C_v in the storage container (Eq. (13)) was then fitted to the measured data with free parameters ε_R and D . The transfer procedure resets the activity in the container; therefore, the total emanated activity $C_{v,tot}$ is the sum of the activities measured before and after storage (at t_1 and t_2). The measured activities from Table 5 were not decay-corrected because radioactive decay is included in the model.

In the fitting procedure, ε_R controls the initial activity in the pore space C_0 ; thus, the magnitude of the signal is released, whereas D_{eff} controls the kinetics of the gas, that is, the time of maximal activity. Both ε_R and D_{eff} were optimized for the model to reproduce the activities measured within the uncertainties (95% confidence interval). The highest possible recoil emanation ($\varepsilon_R = 100\%$) is associated with the lower limit of the diffusion coefficient D_{min} . Equivalently, the upper limit D_{max} is projected with the minimum ε_R , which is restricted by the lowest possible C_0 that allows the simulation of the measured activities.

The resulting ranges of D_{eff} were $2.2 \times 10^{-12} - 2.5 \times 10^{-11} \text{ m}^2 \text{ s}^{-1}$ and $1 \times 10^{-16} - 9 \times 10^{-12} \text{ m}^2 \text{ s}^{-1}$ for the gneiss and siliceous limestone, respectively. The ε_R for the gneiss was 45–100% and for the limestone 0.4–100% (colored ribbons in Fig. 10). These values are in good agreement with the order of magnitude of radon diffusion coefficients in sandstones and granites reported by Liu et al. (2014) and Lehmann and Purtschert (1997), and many orders of magnitude larger than D_s concluded for CaCO_3 (Table 5).

In the simulation, a spatially and temporally constant diffusion coefficient D_{eff} was assumed. However, diffusion occurring in larger pores (with larger D_{eff}) in the first place, might be followed by diffusion in smaller pores in a second step. Such scale-dependent diffusion might be the reason for the increasing trend observed in the data, in contrast to the simulation.

4.6. Water influence on emanation

The influence of the presence of water on the emanation values was assessed by comparing the values of dry and wet limestones. Special attention was paid to the fast transfer of the wet sample in a helium atmosphere to avoid contact with air. In addition, the time between this transfer and the irradiation was minimized to avoid the drying of the sample. The emanation values were $0.3 (\pm 0.1)\%$ and $0.8 (\pm 0.2)\%$ for the dry and wet limestone samples, respectively (Fig. 5). This enhancement is explained by the higher stopping power of water compared with air, resulting in shorter recoil ranges. Therefore, recoiled atoms are more likely to be trapped in the pore space before implantation in the adjacent grain. Adler and Perrier (2009) and Sun and Furbish (1995) demonstrated that radon emanations reach maximal values from moisture contents of 20–40%. Radon emanation coefficients in saturated residues were reported to be 2–6 times higher than in dry residues

Table 5

Net activities $C_{v,m}$ measured before and after the storage of the pebble samples [group (iv)]. $t_1 = 17$ days is the time elapsed between the end of the irradiation and the first measurement; $t_2 = 48$ days is the time between the end of the irradiation and the second measurement. The total activity $C_{v,tot}(t_2) = C_{v,m}(t_1) + C_{v,m}(t_2)$.

	$C_{v,m}(t_1)$ [mBq]	$C_{v,m}(t_2)$ [mBq]	$C_{v,tot}(t_2)$ [mBq]
Gneiss	21.4 ± 2.7	3.6 ± 1.0	25.0 ± 7.4
Siliceous limestone	8.0 ± 2.1	3.9 ± 0.9	11.9 ± 4.2

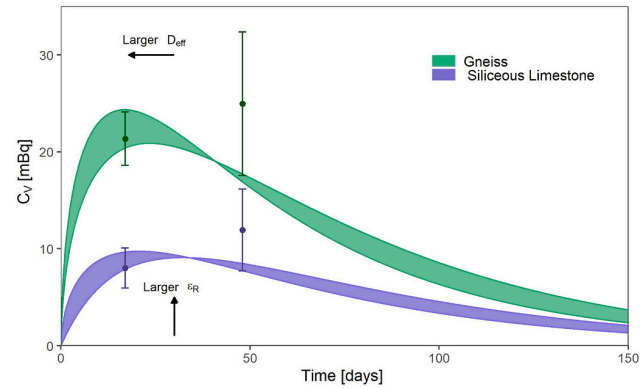


Fig. 10. Activity measured in the irradiation containers for the gneiss (green) and siliceous limestone pebbles (purple) (Table 5). The curves are calculated with the numerical solution of Eq. (13) for an inner porosity of $\phi = 1\%$, a radius $r_0 = 1$ cm and for produced activities $P_{37} = 20.4$ Bq in siliceous limestone and $P_{37} = 0.317$ Bq in gneiss. The areas represent the feasible range of D_{eff} and ε_R . (For interpretation of the references to color in this figure legend, the reader is referred to the Web version of this article.)

(Fleischer, 1983; IAEA, 2013; Sakoda and Ishimori, 2017; Semkow, 1990), which is in agreement with the value we observe.

Therefore, water has two counteracting effects, and the prevalence of one or the other depends on the saturation conditions and the scale considered. For example, in small particles in aquifers, where recoil dominates, water enhances the emanation. On a macroscopic scale, where diffusion in the pore space is important, water slows down the diffusion process. Diffusion coefficients in water are approximately four orders of magnitude smaller than those in air, leading to an overall reduced emanation in water filled pores. The observed apparent recoil emanation enhancement in the presence of water might therefore be partly masked by diffusive retardation.

5. Summary and conclusion

Using underground produced radioactive gas tracers for ground-water dating or nonproliferation purposes relies on knowledge of the production rate and the transfer process from the production site to the sampling point. The latter process is characterized by emanation, that can be described by a two-step mechanism, where the atoms produced are first recoiled into the pore space where diffusion occurs. As both processes are significant for the interpretation of field data, we addressed not only the recoil emanation fractions on the microscopic scale, but also the delay of ^{37}Ar escape owing to diffusive transport on macroscopic scales in our experiment.

Instantaneous ^{37}Ar recoil emanations $\leq 1\%$ were observed in powdered dry sediments and CaCO_3 samples. This is at the lower edge, but consistent with previous estimates (Johnson et al., 2021; Krishnaswami and Seidemann, 1988; Loosli et al., 1989). In soils, a clear depth-related systematic is observed with increased emanation fractions owing to weathering processes close to the surface. This effect induces differences of almost one order of magnitude over a few meters and has implications for the interpretation of the natural soil gas ^{37}Ar background (Carrigan et al., 1996; Haas et al., 2010; Riedmann and Purtschert, 2011). The first proof of principle assessment of the effect of water on recoil emanation indicates an enhancement of the recoil emanation fraction of at least a factor three in wet limestone compared to dry rock.

Surprisingly, the recoil emanation fraction in rock pebbles was not necessarily smaller than that in the powdered samples. This is likely the result of nanopores and structural imperfections within the macroscopic mineral rock samples. At this scale, the release of ^{37}Ar to the outer sample boundary was controlled by diffusive transport. We estimated

diffusion coefficients in the range $10^{-12} > D > 10^{-16} \text{ m}^2 \text{ s}^{-1}$ and diffusion lengths of $2 \text{ mm} \geq L \geq 20 \text{ }\mu\text{m}$ for gneiss and a siliceous limestone pebble. This implies that only a fraction of the rock volume contributes to its total emanation. This delayed diffusion emanation may explain why the significance of underground production (e.g., for ^{39}Ar) is relatively weakly correlated with the U and Th concentrations of the host rock but is linked to the aquifer type (Purtschert, 2012).

Diffusion emanation from the solid CaCO_3 mineral phase was investigated using a heating experiment. The resulting diffusion coefficient of the order of $10^{-29} \text{ m}^2 \text{ s}^{-1}$ at 20°C confirms that solid-phase diffusion emanation can be neglected for ^{37}Ar (and ^{39}Ar) applications. In addition, our diffusion parameters and activation energies for argon in CaCO_3 are consistent with literature values. This indicates that the proposed experimental procedure provides a coherent framework for the assessment of the emanation fractions in natural samples. In our experiments, we used a neutron field produced in a routinely operated medical cyclotron for the first time. The relatively easy access to such facilities offers promising and innovative possibilities for addressing transdisciplinary research questions. Similar experiments could be realized in the future by using higher-energy neutrons, for example, for ^{39}Ar emanation experiments.

A. Rock composition

Table A-1

Elemental composition for the natural sediment and rock samples (group ii-v).

Group	Sample	SiO ₂	Al ₂ O ₃	Fe ₂ O ₃	MnO	MgO	CaO	Na ₂ O	K ₂ O	TiO ₂	P ₂ O ₅	LOI	Si	Al	Fe	Mn	Mg	Ca	Na	K	O	Th	U
[wt.%]													[wt.%]								[ppm]		
(ii)	P54-1	62.0	8.7	3.2	0.1	1.2	8.1	1.0	1.6	0.4	0.1	13.0	29.0	4.6	2.3	0.1	0.7	5.8	0.7	1.3	41.7	6	1.8
	P54-2	65.2	5.4	2.2	0.1	0.9	12.6	0.8	1.1	0.2	0.1	11.5	30.5	2.9	1.5	0.1	0.5	9.0	0.6	0.9	42.4	5.3	1.6
	P54-3	61.9	4.4	1.5	0.1	0.6	16.1	0.8	1.0	0.2	0.1	13.4	28.9	2.3	1.0	0.1	0.4	11.5	0.6	0.8	40.8	5.8	1.8
	P54-4	61.8	3.7	1.5	0.1	0.6	17.0	0.6	0.8	0.1	0.1	14.1	28.9	2.0	1.0	0.0	0.4	12.1	0.5	0.7	40.6	4.1	1.1
	P54-5	54.4	4.4	1.8	0.1	1.1	18.8	0.7	0.8	0.2	0.1	16.5	25.4	2.3	1.2	0.0	0.7	13.4	0.5	0.6	37.8	3.1	1
	P54-8	44.3	3.2	2.2	0.2	1.0	26.5	0.5	0.6	0.1	0.1	22.2	20.7	1.7	1.5	0.1	0.6	18.9	0.4	0.5	34.1	3.4	1.1
(iii)	P54-B	63.5	4.9	1.8	0.1	0.7	14.4	0.8	1.1	0.2	0.1	12.5	29.7	2.6	1.3	0.1	0.4	10.3	0.6	0.9	41.6	3.8	1.2
(iv)	Gneiss	74.3	12.1	4.1	0.1	1.3	0.6	2.5	2.9	0.5	0.1	1.9	34.7	6.4	2.9	0.0	0.8	0.4	1.9	2.4	48.6	9.6	2.2
(v)	Siliceous limestone	30.5	0.2	0.3	0.0	0.5	37.0	0.1	0.0	0.0	0.0	29.1	14.2	0.1	0.2	0.0	0.3	26.4	0.0	0.0	27.2	0.3	0.3
	Yellow limestone	9.5	0.9	1.5	0.1	0.3	47.1	0.1	0.3	0.1	0.1	30.6	4.4	0.5	1.0	0.0	0.2	33.7	0.0	0.2	19.6	1.57	2.53

The oxide forms and the trace elements Th and U were measured using ICP-MS (Actlabs, 2020). The elements Si to O were calculated stoichiometrically from the oxide form.

B. Petrographic thin sections of sample group (iv)

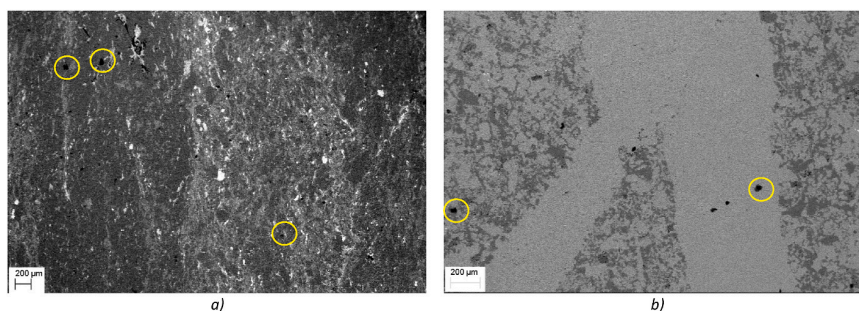


Fig. B-1. Backscattered electron (BSE) images of petrographic thin sections of a) the gneiss pebble and b) the siliceous limestone pebble. The thin section pictures are produced using ZEISS EVO50 scanning electron microscopy (SEM).

(a) The gneiss pebble consists of quartz and feldspars (dark grey), different micas (intermediate grey values) as well as oxides/hydroxides (rare bright spots). Some pores (black spots highlighted by the yellow circles) are visible at the micrometer scale. The elongated quartz and feldspars interlayered by micas form gneissic textures. (b) The siliceous limestone consists of a mixture of quartz and calcite. Veins are frequent (bright bands are pure calcite in the image). Calcite is estimated to represent ~65% of the rock composition, thereby explaining the relatively high ^{37}Ar activity produced ($P_{37} = 20.4 \text{ Bq}$). The remaining 35% mainly consists of quartz (SiO_2 = dark grey areas in the BSE image). The black areas (circled in yellow) represent isolated pores on scales of 10–30 μm . Diffusive transport, as observed in the pebbles, was reported to take place at the nanometer scale (Rama and Moore, 1984). Such small pores are not visible in these pictures.

E. Mass dependent production

A set of samples from group (i), ranging in mass between 2.7 g and 8 g, were simultaneously irradiated in pure quartz tubes with the same neutron fluence. The released atoms, without any heating, were collected and the activities were measured. These data revealed a linear relationship between the sample mass and activity (Fig. E-1). The regression line indicates an activity release of 0.5 mBq/g_{CaCO₃}. The intersection with the y-axis corresponds to the tank argon activity (6.5×10^{-7} mBq in a 50 cm³ counter filled at 10 bars). Compared to the activities produced during irradiation, this is regarded as zero.

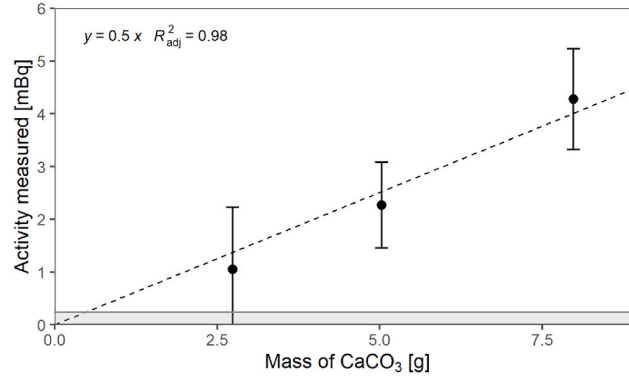


Fig. E-1. Relationship between the irradiated CaCO₃ mass [g] and the gross activity measured [mBq]. The shaded area indicates the average minimum detection activity (MDA) for the CaCO₃ samples (0.24 mBq). The dashed line is the linear least squares regression model fitted to the data..

C. Cross-control experiment between irradiation containers

For an evaluation of the reproducibility several aliquots of the sediment powder samples (core P54-2), were repeatedly irradiated in alloy vessels (Table C-1, Fig. C-1). In addition, results of different types of irradiation vessels were compared. The obtained emanation values all agreed within the range of uncertainties demonstrating the equivalence of different containers. The average emanation in the stainless steel vessels was 2.0 (±0.8)%. This is consistent with the emanation observed from the quartz tube irradiation of 2.4 (±0.3)%.

Table C-1

Results for multiple measurements of sample P54-2.

Container	Run	n_f [cm ⁻²] × 10 ¹¹	P_{37} [Bq]	A_{gross} [mBq]	BG_{ext} [mBq]	A_{net} [mBq]	ε_T [%]
Alloy	2	3.9	1.5 ± 0.1	61 ± 10	11 ± 4	51 ± 14	3.3 ± 1.3
Alloy	3	19.6	6.9 ± 0.4	173 ± 7	53 ± 19	119 ± 26	1.7 ± 0.6
Alloy	3	19.6	7.1 ± 0.4	177 ± 9	53 ± 19	124 ± 27	1.7 ± 0.6
Quartz Tube	7	6.9	1.5 ± 0.1	37 ± 2	0.2 ± 1.0	36 ± 2	2.4 ± 0.3

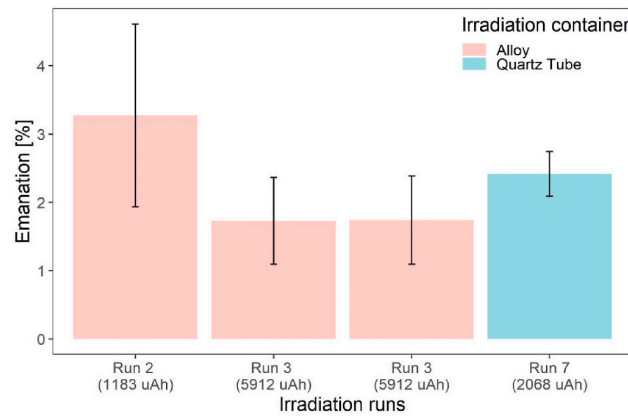


Fig. C-1. Emanation fractions for different irradiation runs and container types.

D. Symbols and units of the parameters used in the equations

Table D-1

Symbol	Unit	Parameter
P_{37}	$\text{atoms s}^{-1} = \text{Bq}$	^{37}Ar production rate or produced activity
N_{g}	atoms	Number of atoms of the target nuclide
$\sigma(E)$	$\text{barns} = 10^{-24} \text{ cm}^2$	Energy-dependent cross section
$\Phi(E)$	$\text{n cm}^{-2} \text{ s}^{-1} \text{ eV}^{-1}$	Neutron flux
ε_T	%	Total emanation fraction
ε_D	%	Diffusion emanation fraction (in pore space)
ε_R	%	Recoil emanation fraction
r_0	m	Spherical grain radius
R	m	Recoil range
L	m	Diffusion length
D_{eff}	$\text{m}^2 \text{ s}^{-1}$	Effective diffusion coefficient in the pore space
ε_{D_s}	%	Solid diffusion emanation fraction
D_s	$\text{m}^2 \text{ s}^{-1}$	Diffusion coefficient in crystal lattice
λ	s^{-1}	Radioactive constant for ^{37}Ar : $\lambda = 2.3 \times 10^{-7} \text{ s}^{-1}$
A_T, A_{D_s}, A_R	Bq	Activities emanated: total, by solid diffusive emanation, by recoil
E_a	kJ mol^{-1}	Activation energy

References

- Aalseth, C.E., Day, A.R., Haas, D.A., Hoppe, E.W., Hyronimus, B.J., Keillor, M.E., Mace, E.K., Orrell, J.L., Seifert, A., Woods, V.T., 2011. Measurement of ^{37}Ar to support technology for on-site inspection under the comprehensive nuclear-test-BanTreaty. Nucl. Instrum. Methods Phys. Res. Sect. A Accel. Spectrom. Detect. Assoc. Equip. 652, 58–61. <https://doi.org/10.1016/j.nima.2010.09.135>.
- Actlabs, 2020. Sample Preparation (RX1) and Lithogeochemistry (4Litho).
- Adler, P.M., Perrier, F., 2009. Radon emanation in partially saturated porous media. Transport Porous Media 78, 149–159. <https://doi.org/10.1007/s11242-008-9291-z>.
- Alfimov, V., Ivy-Ochs, S., 2009. How well do we understand production of ^{36}Cl in limestone and dolomite? Quat. Geochronol. 4, 462–474. <https://doi.org/10.1016/j.quageo.2009.08.005>.
- Andrews, J.N., Florkowski, T., Lehmann, B.E., Loosli, H.H., 1991. Underground production of radionuclides in the milk river aquifer, Alberta, Canada. Appl. Geochem. 6, 425–434. [https://doi.org/10.1016/0883-2927\(91\)90042-N](https://doi.org/10.1016/0883-2927(91)90042-N).
- Auger, M., Braccini, S., Ereditato, A., Häberli, M., Kirillova, E., Nesteruk, K.P., Scamporrì, P., 2016. Accelerator and detector physics at the Bern medical cyclotron and its beam transport line. Nukleonika 61, 11–14. <https://doi.org/10.1515/nuka-2016-0009>.
- Blokhin, A.I., Gai, E.V., Ignatyuk, A.V., Koba, I.I., Manokhin, V.N., Pronyaev, V.G., 2016. New Version of Neutron Evaluated Data Library BROND-3.1. Problems of Atomic Science and Technology, Series: Nuclear and Reactor Constants.
- Braccini, S., 2016. Compact Medical Cyclotrons and Their Use for Radioisotope Production and Multi-Disciplinary Research 6.
- Braccini, S., 2013. Particle Accelerators and Detectors for Medical Diagnostics and Therapy. <https://doi.org/10.7892/BORIS.75806>.
- Braccini, S., Ereditato, A., Scamporrì, P., Von Bremen, K., 2011. The New Bern Cyclotron Laboratory for Radioisotope Production and Research. Presented at the Proceedings of IPAC2011, Spain.
- Burke, B.C., Heimsath, A.M., Dixon, J.L., Chappell, J., Yoo, K., 2009. Weathering the escarpment: chemical and physical rates and processes, south-eastern Australia. Earth Surf. Process. Landforms 34, 768–785. <https://doi.org/10.1002/esp.1764>.
- Carrigan, C.R., Heinle, R.A., Hudson, G.B., Nitao, J.J., Zucca, J.J., 1996. Trace gas emissions on geological faults as indicators of underground nuclear testing. Nature 382, 528–531. <https://doi.org/10.1038/382528a0>.
- Chau, N.D., Chrusciel, E., Prokolski, L., 2005. Factors controlling measurements of radon mass exhalation rate. J. Environ. Radioact. 82, 363–369. <https://doi.org/10.1016/j.jenvrad.2005.02.006>.
- CUCE, 2007. Cation Exchange Capacity (CEC). (No. #22), Agronomy Fact Sheet Series. Cornell University. Cornell University Cooperative Extension. Department of Crop and Soil Sciences, College of Agriculture and Life Sciences.
- Czubek, J.A., 1988. SLOWN2.BAS Program for Calculation of the Rock Neutron Slowing Down Parameters. Institute of Nuclear Physics, Krakow.
- Delvaux, B., Herbillon, A.J., Vielvoe, L., 1989. Characterization of a weathering sequence of soils derived from volcanic ash in Cameroon. Taxonomic, mineralogical and agronomic implications. Geoderma 45, 375–388. [https://doi.org/10.1016/0016-7061\(89\)90017-7](https://doi.org/10.1016/0016-7061(89)90017-7).
- Edmunds, W.M., Darling, W.G., Purtschert, R., Corcho Alvarado, J.A., 2014. Noble gas, CFC and other geochemical evidence for the age and origin of the Bath thermal waters, UK. Appl. Geochem. 40, 155–163. <https://doi.org/10.1016/j.apgeochem.2013.10.007>.
- Fabryka-Martin, J.T., 1988. Production of Radionuclides in the Earth and Their Hydrogeologic Significance, with Emphasis on Chlorine-36 and Iodine-129. University of Arizona.
- Fleischer, R.L., 1983. Theory of alpha recoil effects on radon release and isotopic disequilibrium. Geochem. Cosmochim. Acta 47, 779–784. [https://doi.org/10.1016/0016-7037\(83\)90111-4](https://doi.org/10.1016/0016-7037(83)90111-4).
- Flügge, S., Zimens, K.E., 1939. Die Bestimmung von Korngrößen und von Diffusionskonstanten aus dem Emanationsvermögen. Z. Phys. Chem. B. 42, 179–220.
- Forster, M., MOSER, H., RAMML, K., Hietel, B., 1989. Investigating the Neutron-Induced Subsurface Production of Environmental Isotopes ^{37}Ar , ^{39}Ar , ^3H and ^{36}Cl with Neutron Irradiation of Aquifer Material 8.
- Guenther, W.R., Reiners, P.W., Ketcham, R.A., Nasdala, L., Giester, G., 2013. Helium diffusion in natural zircon: radiation damage, anisotropy, and the interpretation of zircon (U-Th)/He thermochronology. Am. J. Sci. 313, 145–198. <https://doi.org/10.2475/03.2013.01>.
- Guillon, S., Sun, Y., Purtschert, R., Raghoo, L., Pili, E., Carrigan, C.R., 2016. Alteration of natural ^{37}Ar activity concentration in the subsurface by gas transport and water infiltration. J. Environ. Radioact. 155 (156), 89–96. <https://doi.org/10.1016/j.jenvrad.2016.02.021>.
- Haas, D.A., Orrell, J.L., Bowyer, T.W., McIntyre, J.L., Miley, H.S., Aalseth, C.E., Hayes, J. C., 2010. The Science Case for ^{37}Ar as a Monitor for Underground Nuclear Explosions (No. PNNL-19458, 992009). <https://doi.org/10.2172/992009>.
- Harrison, T.M., Lovera, O.M., 2014. The multi-diffusion domain model: past, present and future. Geol. Soc. Lond. Special Publ. 378, 91–106. <https://doi.org/10.1144/SP378.9>.
- Heisinger, B., Lal, D., Jull, A.J.T., Kubik, P., Ivy-Ochs, S., Neumaier, S., Knie, K., Lazarev, V., Nolte, E., 2002. Production of selected cosmogenic radionuclides by muons 1. Fast muons. Earth Planet Sci. Lett. 11.
- IAEA, 2013. Measurement and Calculation of Radon Releases from NORM Residues, Technical Reports Series/International Atomic Energy Agency. Internat. Atomic Energy Agency, Vienna.
- Johnson, C., Armstrong, H., Wilson, W.H., Biegalski, S.R., 2015. Examination of radon production by cosmic neutron interactions. J. Environ. Radioact. 140, 123–129. <https://doi.org/10.1016/j.jenvrad.2014.10.016>.
- Johnson, C., Lowrey, J.D., Alexander, T., Mace, E., Prinke, A., 2021. Measurements of the emanation of ^{37}Ar and ^{39}Ar from irradiated rocks and powders. J. Radioanal. Nucl. Chem. 329, 969–974. <https://doi.org/10.1007/s10967-021-07827-4>.
- Johnson, C., Prinke, A., Lowrey, J.D., Humble, P., Mace, E., Alexander, T., Riley, B.J., Williams, R., 2018. A method to quantify the ^{37}Ar emanation fraction in powders and rocks. J. Radioanal. Nucl. Chem. 318, 297–303. <https://doi.org/10.1007/s10967-018-6024-9>.
- Jourdan, F., Matzel, J.P., Renne, P.R., 2007. ^{39}Ar and ^{37}Ar recoil loss during neutron irradiation of sanidine and plagioclase. Geochem. Cosmochim. Acta 18.
- Käser, D., Hunkeler, D., 2016. Contribution of alluvial groundwater to the outflow of mountainous catchments. Water Resour. Res. 52, 680–697. <https://doi.org/10.1002/2014WR016730>.
- Krishnaswami, S., Seidemann, D.E., 1988. Comparative study of ^{222}Rn , ^{40}Ar , ^{39}Ar , and ^{37}Ar leakage from rocks and minerals: implications for the role of nanopores in gas transport through natural silicates. Geochem. Cosmochim. Acta.
- Lal, D., Peters, B., 1962. Cosmic ray produced isotopes and their application to problems in geophysics. Prog. Elem. Part. Cosmic Ray Phys. 6, 1–74.
- Lehmann, B.E., Purtschert, R., 1997. Radioisotope dynamics — the origin and fate of nuclides in groundwater. Appl. Geochem. 12, 727–738. [https://doi.org/10.1016/S0883-2927\(97\)00039-5](https://doi.org/10.1016/S0883-2927(97)00039-5).
- Liu, Chengshuai, Wang, Y., Li, F., Chen, M., Zhai, G., Tao, L., Liu, Chuanping, 2014. Influence of geochemical properties and land-use types on the microbial reduction of Fe(III) in subtropical soils. Environ. Sci.: Process. Impacts 16, 1938–1947. <https://doi.org/10.1039/C4EM00217B>.

- Loosli, H.H., Lehmann, B.E., Balderer, W., 1989. Argon-39, argon-37 and krypton-85 isotopes in Stripa groundwaters. *Geochim. Cosmochim. Acta* 53, 1825–1829. [https://doi.org/10.1016/0016-7037\(89\)90303-7](https://doi.org/10.1016/0016-7037(89)90303-7).
- Loosli, H.H., Purtschert, R., 2005. Rare gases. In: *Isotopes in the Water Cycle: Past, Present and Future of a Developing Science*. I.A.E.A., pp. 91–95.
- Maraziotis, E.A., 1996. Effects of intraparticle porosity on the radon emanation coefficient. *Environ. Sci. Technol.* 30, 2441–2448. <https://doi.org/10.1021/es950386r>.
- Morawska, L., Phillips, C.R., 1992. Dependence of the radon emanation coefficient on radium distribution and internal structure of the material. *Geochim. Cosmochim. Acta*.
- Musy, S., Meyzonnat, G., Barbecot, F., Hunkeler, D., Sültenfuss, J., Solomon, D.K., Purtschert, R., 2021. In-situ sampling for krypton-85 groundwater dating. *J. Hydrol. X* 11, 100075. <https://doi.org/10.1016/j.jhydroa.2021.100075>.
- Onstott, T.C., Miller, M.L., Ewing, R.C., Arnold, G.W., Walsh, D.S., 1995. Recoil refinements: implications for the $^{40}\text{Ar}/^{39}\text{Ar}$ dating technique. *Geochim. Cosmochim. Acta* 59, 1821–1834. [https://doi.org/10.1016/0016-7037\(95\)00085-E](https://doi.org/10.1016/0016-7037(95)00085-E).
- Paine, J.H., Nomade, S., Renne, P.R., 2006. Quantification of ^{39}Ar recoil ejection from GA1550 biotite during neutron irradiation as a function of grain dimensions. *Geochim. Cosmochim. Acta* 70, 1507–1517. <https://doi.org/10.1016/j.gca.2005.11.012>.
- Pearson, F.J., Balderer, W., Loosli, H.H., Lehmann, B.E., Matter, A., Peters, T.J., Schmassmann, H., Gautschi, A., 1991. Applied Isotope Hydrogeology: A Case Study in Northern Switzerland (Nagra Technical Report No. NTB 88-01). Nagra.
- Peel, M., Kipfer, R., Hunkeler, D., Brunner, P., 2022. Variable ^{222}Rn emanation rates in an alluvial aquifer: limits on using ^{222}Rn as a tracer of surface water – groundwater interactions. *Chem. Geol.*, 120829 <https://doi.org/10.1016/j.chemgeo.2022.120829>.
- Peng, S., Hu, Q., Hamamoto, S., 2012. Diffusivity of rocks: gas diffusion measurements and correlation to porosity and pore size distribution: GAS diffusion and rock porosity and pore size. *Water Resour. Res.* 48 <https://doi.org/10.1029/2011WR011098>.
- Pola, A., Rastelli, D., Treccani, M., Pasquato, S., Bortot, D., 2020. DIAMON: a portable, real-time and direction-aware neutron spectrometer for field characterization and dosimetry. *Nucl. Instrum. Methods Phys. Res. Sect. A Accel. Spectrom. Detect. Assoc. Equip.* 969, 164078 <https://doi.org/10.1016/j.nima.2020.164078>.
- Price, J.R., Velbel, M.A., 2003. Chemical weathering indices applied to weathering profiles developed on heterogeneous felsic metamorphic parent rocks. *Chem. Geol.* 202, 397–416. <https://doi.org/10.1016/j.chemgeo.2002.11.001>.
- Purtschert, R., 2017. Ar-37, Be-7, and Xe-133 in the Atmosphere.
- Purtschert, R., 2012. Ar-39 dating of groundwater: how limiting is underground production? Goldschmidt 2012 Conference Abstracts. *Mineral. Mag.* 76, 1401–2639. <https://doi.org/10.1180/S0026461X00008434>.
- Radulov, I., Berbeca, A., Sala, F., Crista, F., Lato, A., 2011. Mineral Fertilization Influence on Soil pH, Cationic Exchange Capacity, and Nutrient Content 6.
- Rama, Moore, W.S., 1984. Mechanism of transport of U-Th series radioisotopes from solids into ground water. *Geochim. Cosmochim. Acta* 48, 395–399. [https://doi.org/10.1016/0016-7037\(84\)90261-8](https://doi.org/10.1016/0016-7037(84)90261-8).
- Renne, P.R., Norman, E.B., 2001. Determination of the half-life of ^{37}Ar by mass spectrometry. *Phys. Rev. C* 63, 047302. <https://doi.org/10.1103/PhysRevC.63.047302>.
- Riedmann, R.A., Purtschert, R., 2011. Natural argon-37 concentrations in soil air: implications for monitoring underground nuclear explosions. *Environ. Sci. Technol.* 45, 8656–8664. <https://doi.org/10.1021/es201192u>.
- Rousset, B., 2006. Pierre Jaune de Neuchâtel; Rapport final (No. EC/BR/02601-03). Service de la Protection des Monuments et des Sites, Lausanne.
- Sakoda, A., Ishimori, Y., 2017. Mechanisms and modeling approaches of radon emanation for natural materials. *Jpn. J. Health Phys.* 52, 296–306. <https://doi.org/10.5453/jhps.52.296>.
- Saldanha, R., Back, H.O., Tsang, R.H.M., Alexander, T., Elliott, S.R., Ferrara, S., Mace, E., Overman, C., Zalavadia, M., 2019. Cosmogenic production of Ar 39 and Ar 37 in argon. *Phys. Rev. C* 100, 024608. <https://doi.org/10.1103/PhysRevC.100.024608>.
- Schaller, M., von Blanckenburg, F., Veldkamp, A., Tebbens, L.A., Hovius, N., Kubik, P.W., 2002. A 30 000 yr record of erosion rates from cosmogenic ^{10}Be in Middle European river terraces. *Earth Planet. Sci. Lett.* 204, 307–320. [https://doi.org/10.1016/S0012-821X\(02\)00951-2](https://doi.org/10.1016/S0012-821X(02)00951-2).
- Schilling, O.S., Gerber, C., Partington, D.J., Purtschert, R., Brennwald, M.S., Kipfer, R., Hunkeler, D., Brunner, P., 2017. Advancing physically-based flow simulations of alluvial systems through atmospheric noble gases and the novel argon-37 tracer method: integrating tracers with models. *Water Resour. Res.* 53 <https://doi.org/10.1002/2017WR020754>.
- Schwarz, W., 2001. Argon-Geochemie von Mineralen hydrothermaler Bildung (Zeolithes; Serizite in Plagioklas) (PhD). Ruprecht-Karls-Universität, Heidelberg.
- Semkow, T.M., 1990. Recoil-emanation theory applied to radon release from mineral grains. *Geochim. Cosmochim. Acta* 54, 425–440. [https://doi.org/10.1016/0016-7037\(90\)90331-E](https://doi.org/10.1016/0016-7037(90)90331-E).
- Soetaert, K., Meysman, F., 2012. Reactive transport in aquatic ecosystems: rapid model prototyping in the open source software R. *Environ. Model. Software* 32, 49–60. <https://doi.org/10.1016/j.envsoft.2011.08.011>.
- Solomon, D.K., Hunt, A., Poreda, R.J., 1996. Source of radiogenic helium 4 in shallow aquifers: implications for dating young groundwater. *Water Resour. Res.* 32, 1805–1813. <https://doi.org/10.1029/96WR00600>.
- Spannagel, G., Fireman, E.L., 1972. Stopping rate of negative cosmic-ray muons near sea level. *J. Geophys. Res.* 77, 5351–5359. <https://doi.org/10.1029/JA077i028p05351>.
- Šrámek, O., Stevens, L., McDonough, W.F., Mukhopadhyay, S., Peterson, R.J., 2017. Subterranean production of neutrons, ^{39}Ar and ^{21}Ne : rates and uncertainties. *Geochim. Cosmochim. Acta* 196, 370–387. <https://doi.org/10.1016/j.gca.2016.09.040>.
- Strasser, A., Charollais, J., Conrad, M.A., Clavel, B., Pictet, A., Mastrangelo, B., 2016. The Cretaceous of the Swiss Jura Mountains: an improved lithostratigraphic scheme. *Swiss J. Geosci.* 109, 201–220. <https://doi.org/10.1007/s00015-016-0215-6>.
- Sun, H., Furbish, D.J., 1995. Moisture content effect on radon emanation in porous media. *J. Contam. Hydrol.* 18, 239–255. [https://doi.org/10.1016/0169-7722\(95\)00002-D](https://doi.org/10.1016/0169-7722(95)00002-D).
- Suther, B.E., Leigh, D.S., West, L.T., 2021. Soil chemistry and clay mineralogy of an alluvial chronosequence from the North Carolina sandhills of the upper coastal plain, USA. *Soil Systems* 6, 1. <https://doi.org/10.3390/soilsystems6010001>.
- Watson, E.B., Cherniak, D.J., 2003. Lattice diffusion of Ar in quartz, with constraints on Ar solubility and evidence of nanopores. *Geochim. Cosmochim. Acta* 67, 2043–2062. [https://doi.org/10.1016/S0016-7037\(02\)01340-6](https://doi.org/10.1016/S0016-7037(02)01340-6).
- Wilson, W.H., Biegalski, S.R., 2015. Evaluating the feasibility of a simple experiment to validate the existence of a low-energy component to the $^{40}\text{Ca}(n,\alpha)^{37}\text{Ar}$ reaction cross-section. Isotopes and radiation: general. In: *American Nuclear Society Annual Meeting. Presented at the Nuclear Technology: an Essential Part of the Solution, San Antonio, Texas*.
- Yokochi, R., Sturchio, N.C., Purtschert, R., 2012. Determination of crustal fluid residence times using nucleogenic ^{39}Ar . *Geochim. Cosmochim. Acta* 88, 19–26. <https://doi.org/10.1016/j.gca.2012.04.034>.

4.3 Quantification of ^{39}Ar emanation fractions: preliminary results

The methodology developed for the assessment of ^{37}Ar emanation fractions can be used to quantify ^{39}Ar emanation fractions. This is associated with two main technical challenges: firstly, higher energy neutrons are needed for producing significant ^{39}Ar activities; and secondly, the important ^{37}Ar activity produced in the presence of calcium atoms in the sample with the high energy neutrons hinders the measurement of ^{39}Ar activities with LLC methods. The cross section for ^{39}Ar production with neutrons is seven orders of magnitude larger in the high energy range compared to the thermal range (Figure 3.9a). In contrast, contributions to ^{37}Ar production are more equally distributed over the whole energy range (Figure 3.9b). As a consequence, the neutron flux at the background location (BG) in the cyclotron (Figure 4.1; where the samples for ^{37}Ar were placed), is not sufficiently energetic to produce measurable ^{39}Ar . To address this issue, samples were placed directly behind the liquid target for ^{18}F production, at the so-called "High Energy" (HE) position. Similarly, than for the BG position, the neutron flux and energy spectrum were measured with the neutron detector DIAMON (Pola et al. (2020), Figure 4.2). The distribution between thermal - epithermal - fast energy domains is respectively 40% - 40% - 10% for the BG location, whereas at the HE location, it is 10% - 36% - 54%. For a similar total energy-integrated neutron flux, a larger fraction is in the high energy range for the HE position.

In natural rocks, Ca is a ubiquitous mineral, which is typically more abundant than K by one or two orders of magnitude (Fabryka-Martin, 1988). The higher neutron energy induces significant production of ^{39}Ar (on K), but also a high ^{37}Ar production (on Ca). Despite their lower (and discrete) energy, the electrons emitted by this important ^{37}Ar activity result in a broad peak that overlaps a significant portion of ^{39}Ar activity spectrum, and therefore prevents its measurement with LLC methods (Chapter 2). A simple solution would be to take advantage of the relatively short half-life of ^{37}Ar and wait until it decays to measure ^{39}Ar . McIntyre et al. (2017) estimated that after an UNEⁱ in an average crust rock, ^{39}Ar is dominating the spectra after approximately 10 half-lives of ^{37}Ar (~ 1 year). An alternative solution is to measure ^{37}Ar by LLC and ^{39}Ar with ATTA methods (Ritterbusch et al., 2014).

ⁱan UNE is basically an irradiation with high energy neutrons

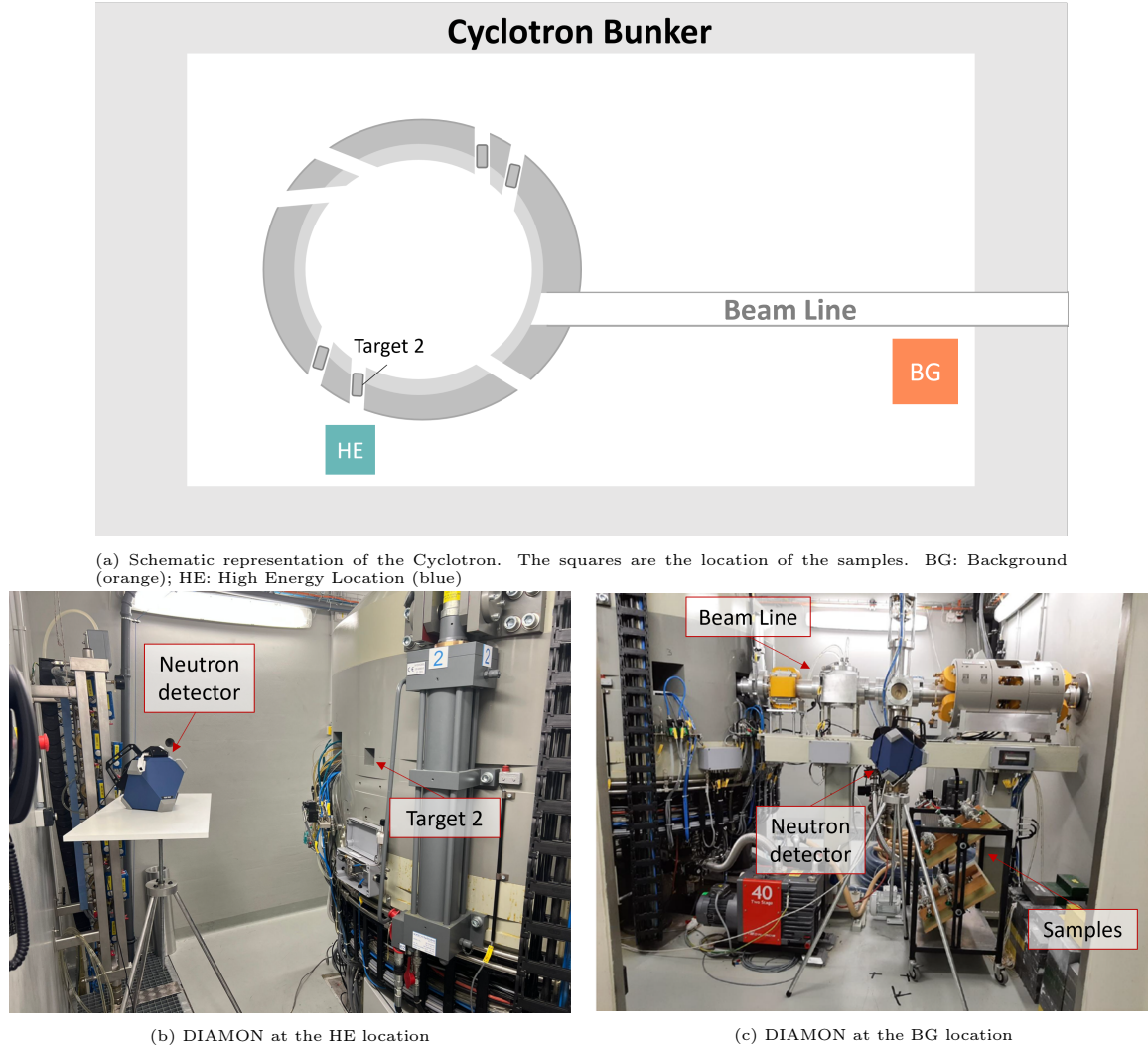


Figure 4.1: Samples position and neutron detector at the HE and BG locations in the Cyclotron from the University Hospital of Bern

As a proof of principle, ^{39}Ar emanation was quantified in an artificial pure KCl powder (Grogg Chemie AG, art. G286). The results from the irradiation of $m_{\text{KCl}} = 18.3 \text{ g}$ at the HE position in the cyclotron are compiled in Table 4.1. The cross section for ^{37}Ar production on K only exists for neutrons $> 10 \text{ MeV}$ (Figure 3.9b), which are relatively rare at the EH location (Figure 4.2). Consequently, the calculated ^{37}Ar activity produced on K in the sample is $P_R = 0.04 \text{ Bq}$. This is substantially lower than the activity effectively measured in the sample $A_{\text{net}} = 5.3 \text{ Bq}$ and no ^{37}Ar emanation fraction could be inferred in this sample. This high activity may be produced on ^{36}Ar atoms contained in the remaining traces of air in the sample. However, a volume of 13 cm^3 of air ($^{36}\text{Ar}/\text{Ar} = 0.33 \%$) would need to be irradiated with the sample to produce such activity. This volume corresponds to a residual pressure of $\sim 71 \text{ mb}$ in the 183 cm^3 container, which is unlikely to occur. A

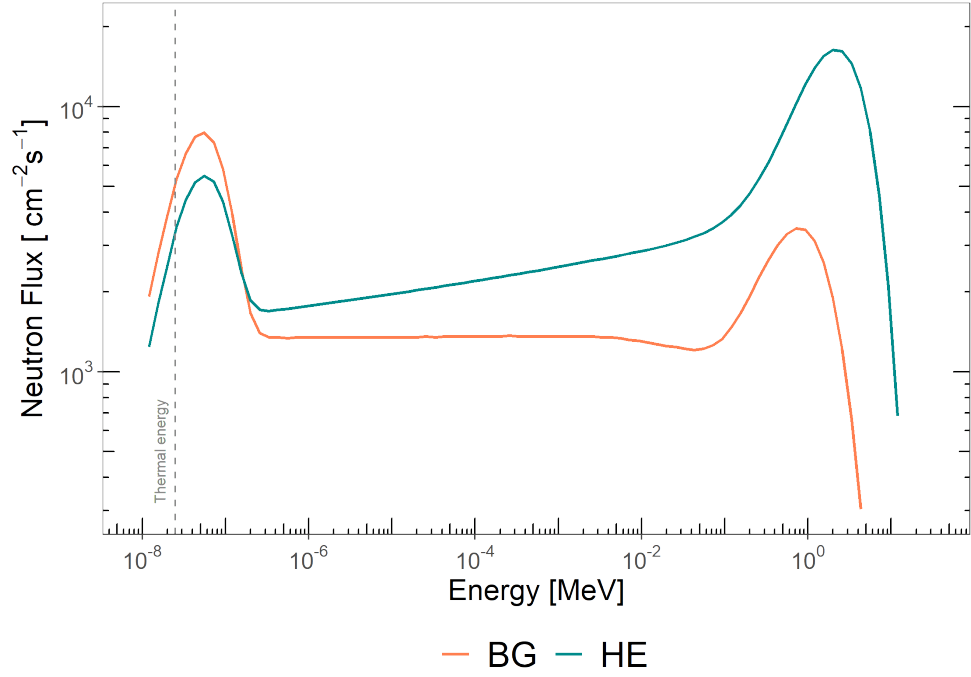


Figure 4.2: Measured neutron spectrum at the BG (pink) and HE (blue) sample locations in the cyclotron for integrated beam currents of $0.15 \mu\text{Ah}$, resp. $0.02 \mu\text{Ah}$

more realistic explanation is the presence of calcium atoms in the residual dust from previous samples in the filters of the irradiation container. Assuming a Ca weight factor of 10 wt% (i.e. the average from the previous samples in this container), a mass $<0.05 \text{ g}$ of soil would be sufficient to reach the activity of 5.3 Bq .

Because of the broad peak produced by this high activity, the sample was stored for > 1 year between ^{37}Ar and ^{39}Ar activity measurements. The total ^{39}Ar emanation of 1.5 % (Table 4.1) is one order of magnitude lower than the value concluded by Johnson et al. (2021) for potassium carbonate (K_2CO_3) powder and one to two orders of magnitude larger than early literature estimations (Krishnaswami and Seidemann, 1988; Loosli et al., 1989). The main reason for these discrepancies is probably the uncertainties on the neutron fluxes and energy spectra, as well as on the cross sections. In addition, the time and spatial scales of the experiments need to be accounted for quantifying the total emanation because of the importance of the diffusion emanation fraction. This is highlighted in the discussion of the extrapolation of laboratory values to field-scale experiments in the following (Section 4.4).

Table 4.1: Results from the irradiation of KCl ($m = 18.3$ g) powder with fast neutrons. ΔT is the time between the end of the irradiation and the measurement; P_R is the activity produced in the rock, calculated from the folding of $\sigma(E)$ and $\phi_n(E)$ and the target concentration; A_{net} is the net total activity measured in the sample, corrected for decay during ΔT and background; ε_T is the total emanation fraction

Isotope	Measurement date	ΔT [d]	P_R [Bq]	A_{net} [Bq]	ε_T [%]
^{37}Ar	02.11.2020	130	0.04 ± 0.02	5.33 ± 0.05	-
^{39}Ar	05.03.2022	618	2.3 ± 1.1	$(4.41 \pm 0.03) \times 10^{-2}$	1.5 ± 0.5

4.4 Discussion: from the laboratory experiments to the field scale applications

Extrapolating results from controlled experiments in laboratories to real aquifer applications requires information about the pore space water saturation and the diffusion scale. In this thesis, we define the diffusion scale as the distance between the place where the recoil process occurs and the place where the movement of the atoms is dominated by advection (so-called "drainable" pore space).

The recoil energy imparted to ^{39}Ar nuclei by the reaction $^{39}\text{K}(n, p)^{39}\text{Ar}$ is lower than the one to ^{37}Ar in the reaction $^{40}\text{Ca}(n, \alpha)^{37}\text{Ar}$, resulting in shorter recoil ranges. The influence of this effect on recoil emanation fractions is delicate to quantify due to partial compensations by implantation processes in the adjacent grains, as well as pore geometry and saturation dependencies. In the subsequent diffusion process, the longer half-life of ^{39}Ar results in longer diffusion lengths. Therefore for hypothetically similar recoil fractions, there is a higher probability for ^{39}Ar atoms to reach the drainable pore volume before they decay. In other words, the short half-life of ^{37}Ar is more likely to reduce its total emanation, whereas ^{39}Ar may not be affected by this process.

This can be illustrated by a spherical pebble model. The total emanation fraction ε_T is, per definition, the ratio between the flux that escapes the pebble $J(t)$ and the production rate in the rock P_R :

$$\varepsilon_T = \frac{J(t)}{P_R} \quad (4.1)$$

The flux escaping the pebble is described by Fick's first law [Eq. 12 in Musy et al. (2022)]. The radioargon concentration in the pore space C_p is calculated by solving the partial differential equation (PDE) 4.2 for dispersion, production and decay. Note that this equation is similar to Eq. 11 in Musy et al. (2022) except that here, a constant production rate is assumed, whereas in the irradiation experiment, a pulse production occurs. The emanation rate in the inner-pebble pore space P_W [atoms $\text{cm}^{-3} \text{yr}^{-1}$] relates to the production in the rock P_R [atoms $\text{g}^{-1} \text{yr}^{-1}$]

with the recoil emanation ε_R , the inner-pebble porosity ϕ , and the rock density ρ_R (Eq: 4.3). Note that depending on the scale investigated, P_W may represent the emanation rate in the pore space or directly in the drainable porosity. In the latter case, the relevant emanation fraction to consider is the total emanation ε_T (Chapter 5, Eq. 5.1). The PDE 4.2 is numerically solved using the R-Package *ReacTran* (Soetaert and Meysman, 2012).

$$\frac{\partial C_p(r, t)}{\partial t} = D_{eff} \frac{\partial^2 C_p(r, t)}{\partial r^2} + P_W - \lambda C_p(r, t) \quad (4.2)$$

$$P_W = P_R \cdot \frac{\varepsilon_R}{\phi} \cdot \rho \quad (4.3)$$

Figure 4.3 presents the total emanation fraction ε_T out of a pebble with a radius between 1 and 500 cm, an inner porosity of $\phi = 1\%$ and a pore space diffusion coefficient of $D_{eff} = 1 \times 10^{-14} \text{ m}^2 \text{ s}^{-1}$. The initial condition is $C_p(t = 0) = 0$. The recoil emanations fractions are $\varepsilon_{R,39} = 1.5\%$, and $\varepsilon_{R,37} = 10\%$. These numbers are assumed according to the shorter recoil range for ^{39}Ar than for ^{37}Ar . Note that ε_T does not depend on the P_R .

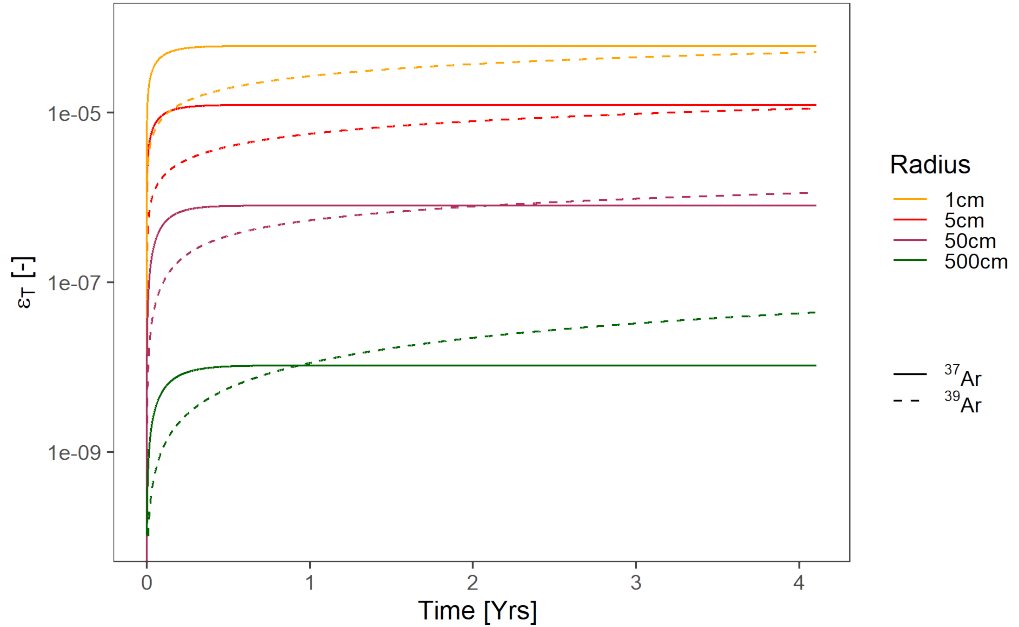


Figure 4.3: Total emanation out of a spherical pebble with a radius between 1 and 500 cm, assuming $\phi = 1\%$, $D_{eff} = 1 \times 10^{-14} \text{ m}^2 \text{ s}^{-1}$, $\varepsilon_{R,39} = 1.5\%$, and $\varepsilon_{R,37} = 10\%$

^{37}Ar total emanation fraction reaches a steady-state value after a few months, whereas ^{39}Ar emanation keeps increasing according to its longer half-life and, therefore, diffusion length. The bigger the pebble, the smaller the total emanation, and the more pronounced the difference between both isotopes. Therefore, on short time-, and small spatial- scales, the total ^{37}Ar emanation is larger than ^{39}Ar emanation. However, for long times and/or large particles, ^{39}Ar emanation fraction is overall larger despite $\varepsilon_{R,39} < \varepsilon_{R,37}$. The difference between both isotopes is also exacerbated if the diffusion is slowed down (i.e. for smaller diffusion coefficients) as it would be the case in fully saturated pore space conditions.

Finally, all the above discussions about emanation fractions assume that this process is similar independently of the incident particle energy and the production channel. This is very likely an oversimplification. High-energy neutrons produce radioargon by spallation reactions, whereas low-energy neutrons are thermally captured. The different nature of these reactions possibly results in distinct recoil energies, whose influence on recoil emanation fractions is still unclear. The nature of the muon-capture reaction is also singular, and the emanation following this production process might therefore differ from the neutron reactions.

4.5 Conclusions and outlooks

The irradiation experiments conducted in the frame of this thesis allowed to significantly better understand the processes for radioargon emanation. The quantification of ^{37}Ar emanation fractions in multiple-scale samples allowed for (i) a better constrain of the controlling factors (water, pore geometry, etc.); and (ii) the understanding of the two-steps nature of the emanation process. These experiments opened the way for reflections about the importance of spatial and time scales when extrapolating laboratory results to aquifer scale studies for radioactive nuclides.

The development of the methodology for quantifying emanation fractions allowed for a first estimate of ^{39}Ar emanation fraction in a KCl powder. Some of the technical issues associated with the higher energy neutrons could be addressed. The main challenge is the important ^{37}Ar production on calcium, which can not be avoided in natural samples and which prevents ^{39}Ar activity measurement by LLC. This issue could be avoided by measuring ^{39}Ar with ATTA methods.

Looking ahead, a better understanding of the importance of the production channels, and the recoil energies associated with them on the emanation fractions is needed. Moreover, the effect of the pore space saturation conditions on the production and diffusion processes is also of interest for CTBT and groundwater dating applications. These open questions would greatly benefit from more irradiation experiments with variable neutron energy distributions and saturation conditions. Finally, a complete understanding of the importance of muon-capture processes for radioargon production will require irradiation experiments with muon beams in the future.

References

- Fabryka-Martin, J. (1988). *Production of radionuclides in the earth and their hydrogeologic significance, with emphasis on chlorine-36 and iodine-129*. PhD Thesis, University of Arizona, Tucson.
- Johnson, C., Lowrey, J. D., Alexander, T., Mace, E., and Prinke, A. (2021). Measurements of the emanation of ^{37}Ar and ^{39}Ar from irradiated rocks and powders. *Journal of Radioanalytical and Nuclear Chemistry*, 329(2):969–974.
- Krishnaswami, S. and Seidemann, D. E. (1988). Comparative study of ^{222}Rn , ^{40}Ar , ^{39}Ar and ^{37}Ar leakage from rocks and minerals: Implications for the role of nanopores in gas transport through natural silicates. *Geochimica et Cosmochimica Acta*, 52(3):655–658.
- Loosli, H., Lehmann, B., and Balderer, W. (1989). Argon-39, argon-37 and krypton-85 isotopes in Stripa groundwaters. *Geochimica et Cosmochimica Acta*, 53(8):1825–1829.
- McIntyre, J. I., Aalseth, C. E., Alexander, T. R., Back, H. O., Bellgraph, B. J., Bowyer, T. W., Chipman, V., Cooper, M. W., Day, A. R., Drellack, S., Foxe, M. P., Fritz, B. G., Hayes, J. C., Humble, P., Keillor, M. E., Kirkham, R. R., Krogstad, E. J., Lowrey, J. D., Mace, E. K., Mayer, M. F., Milbrath, B. D., Misner, A., Morley, S. M., Panisko, M. E., Olsen, K. B., Ripplinger, M. D., Seifert, A., and Suarez, R. (2017). Measurements of Argon-39 at the U20az underground nuclear explosion site. *Journal of Environmental Radioactivity*, 178-179:28–35.
- Musy, S., Casolaro, P., Dellepiane, G., Berger, A., Braccini, S., and Purtschert, R. (2022). Quantification of ^{37}Ar emanation fractions from irradiated natural rock samples and field applications. *Journal of Environmental Radioactivity*, 251-252:106966.
- Peel, M., Kipfer, R., Hunkeler, D., and Brunner, P. (2022). Variable ^{222}Rn emanation rates in an alluvial aquifer: Limits on using ^{222}Rn as a tracer of surface water – Groundwater interactions. *Chemical Geology*, 599:120829.
- Pola, A., Rastelli, D., Treccani, M., Pasquato, S., and Bortot, D. (2020). DIAMON: A portable, real-time and direction-aware neutron spectrometer for field characterization and dosimetry. *Nuclear Instruments and Methods in Physics Research Section A: Accelerators, Spectrometers, Detectors and Associated Equipment*, 969:164078.
- Purtschert, R., Yokochi, R., Jiang, W., Lu, Z.-T., Mueller, P., Zappala, J., Van Heerden, E., Cason, E., Lau, M., Kieft, T., Gerber, C., Brennwald, M., and Onstott, T. (2021). Underground production of ^{81}Kr detected in subsurface fluids. *Geochimica et Cosmochimica Acta*, 295:65–79.
- Ritterbusch, F., Ebser, S., Welte, J., Reichel, T., Kersting, A., Purtschert, R., Aeschbach-Hertig, W., and Oberthaler, M. K. (2014). Groundwater dating with Atom Trap Trace Analysis of Argon-39. *Geophysical Research Letters*, 41(19):6758–6764.
- Soetaert, K. and Meysman, F. (2012). Reactive transport in aquatic ecosystems: Rapid model prototyping in the open source software R. *Environmental Modelling & Software*, 32:49–60.

Chapter 5

Field application: Dating groundwater with ^{39}Ar - Underground production in the Danish shallow aquifer system

5.1 Introduction

The Danish aquifer system has been used for water supply for over 100 years (Hinsby et al., 2006). Due to increasing problems in water quality, a lot of effort has been invested in the past years to understand better the groundwater flow fields and the distribution of residence times in the aquifer systems. In this context and in a collaborative effort between the Danish Geological Survey (GEUS), the local water works, and the University of Bern, multiple sampling campaigns were carried out between 2005 and 2021. As a result, a comprehensive data set including ^{85}Kr , ^{37}Ar and ^{39}Ar is available for this area. The main objective was the determination of the age stratigraphy in the sedimentary basin, focusing on the water fraction recharged in preindustrial times. This fraction is especially interesting since it is likely not affected by elevated nitrate and pesticide concentrations. From the timescale of its applications, ^{39}Ar is the most suitable tracer to describe it.

Most of ^{39}Ar data showed decreasing ^{39}Ar activities with depth below the water table. The apparent aging rate is about 6 yr m^{-1} , suggesting a regionally averaged recharge velocity of $\sim 160 \text{ mm yr}^{-1}$. These sub-modern (i.e. $< 100 \%$ modern) ^{39}Ar activities, combined with low ^{85}Kr and ^3H concentrations therefore demonstrated the validity of the radio-noble gas dating methods. However, at specific locations, some samples revealed ^{39}Ar activities up to 250% modern, which can only be explained by underground production. Surprisingly, none of the aquifer rocks presented elevated U and Th contents. Most of the affected samples showed low but measurable ^{85}Kr concentrations, providing indications that waters with intermediate residence times (and percolation depths) are mainly prone to underground production.

One of the key research questions that have driven this thesis is whether such elevated activities in these specific rock formations and depths can solely result from the production with neutrons produced in-situ in the U/Th decay chains and to what extent the primary cosmogenic neutrons contribute to the observed ^{39}Ar excess. These two channels were previously believed to be the only significant contributors to ^{39}Ar underground production. In this chapter, we demonstrate that considering only them is not adequately reproducing the activities observed in Denmark. Reaction channels related to cosmogenic muons cannot be ignored for a successful simulation of the activities observed. The deconvolution of the controlling factors affecting ^{39}Ar production requires additional information from other tracers. ^{37}Ar is produced by very similar mechanisms (Chapter 3) but is characterized by a much shorter half-life (35 days). Therefore, this tracer allows for a focus on local underground production processes on timescales of weeks to months.

The depth-dependent distribution of vertical recharge velocities, and thus the time span a water parcel resides at a certain depth, is crucial information for calculating the activities emanated in the porous space. In the study area in Denmark, the local infiltration rates could be determined by particle tracking simulations with the Danish National Resources Model [DK-Model; Henriksen et al. (2003)] thanks to the support of Dr. Lars Trolldord and Dr. Klaus Hinsby from GEUS. In the following, the production rate profiles calculated in Chapter 3 and the emanation fractions concluded in Chapter 4 are combined with vertical flow velocity distributions simulated with the DK-model in two selected wells. The calculated ^{39}Ar and ^{37}Ar activity concentrations in groundwater as a function of depth were compared with the activities measured in these wells. Finally, the ages inferred by considering ^{39}Ar underground production were further constrained with ^{85}Kr and $^3\text{H}/^3\text{He}$ age information.

5.2 Climatic, geological, and hydrogeological settings of the study area

Denmark is a lowland characterized by a glaciomorphological topography formed by glacial activity during the main Weichselian (northeast) and the Young Baltic (southeast). Advances and recessions of the glaciers resulted in meltwater streams that deposited large amounts of sand, gravel, and clay, forming floodplain valleys. The topology is defined by an undulating surface between 0 and 170 m above sea level (a.s.l) cut by numerous rivers. The estimated net recharge is 240 mm yr^{-1} , and most of the precipitation ($> 90 \%$) occurs in the cold season (October-March) (Hinsby et al., 2006; Trolldborg et al., 2008).

The near-surface geology is characterized by glacial Quaternary deposits with a thickness ranging from a few meters up to 150 m, forming a complex sequence of clayey tills and glaciofluvial sands (Figure 5.1b). Pre-quaternary deposits are Paleocene marls and clays, which form the lower impermeable boundary of the quaternary shallow aquifer system. The Danien Limestone formation constitutes the bedrock. This bryozoan reef carbonate interbedded with chert is comprised in the upper part of the so-called “Chalk group,” which includes the stratigraphic boundary between Mesozoic and Cenozoic rocks. Locally, the Danian Limestone layers outcrop directly below the quaternary deposits due to glacial valleys burial through the tertiary layers (Henriksen et al., 2003; Hinsby et al., 2006; Schack and Gravesen, 2010; Trolborg et al., 2008).

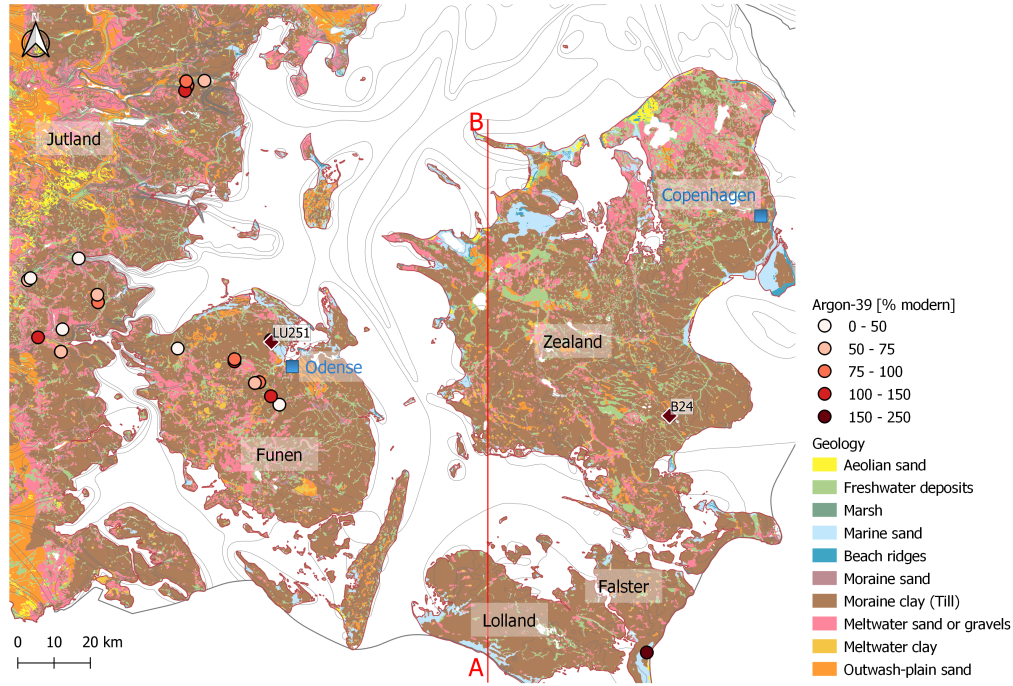
The glaciofluvial sands constitute the main aquifers for Denmark water supply. In some places, drinking water is also abstracted from the Danian limestone. However, in this formation, increased chloride concentrations linked with the locally up-coning of saline waters are an increasing issue (Knudsen et al., 2021). The clayey tills, which confine the aquifers in most areas, have varying fracture density, sand and clay contents, and therefore a very heterogeneous conductivity (Chalikakis et al., 2009; Hinsby et al., 2006). Although the thickness distribution of the layers may vary from one island to another, the layered conceptual model (Figure 5.1b) extends over the whole area of interest for this study.

5.3 Material and methods

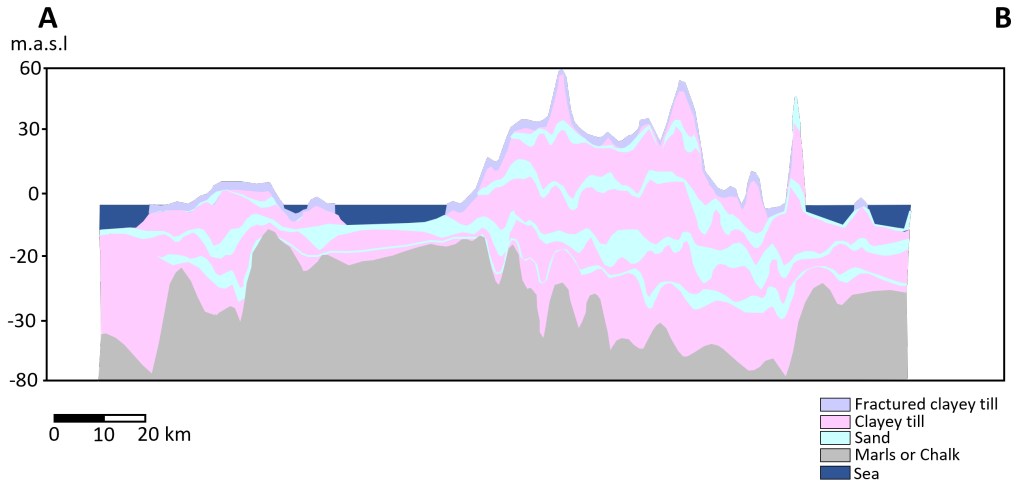
5.3.1 Tracer Data

Several field campaigns took place between 2005 and 2021 across a large part of Denmark: stretching from the east of Jutland Island until the south of Zealand Island (area of Faxe), Falster Island, including the central part of Funen Island, and more specifically the area around the city of Odense (Figure 5.1). This resulted in a database compiling > 100 wells sampled and measured for ^{39}Ar , ^{37}Ar , ^{85}Kr , ^3H , $^3\text{He}/^4\text{He}$, stable noble gases, ^{36}Cl , ^{222}Rn , ^{14}C , $\delta^{13}\text{C}$, $\delta^{18}\text{O}$, $\delta^2\text{H}$, and water chemistry. The radioactive noble gases from this database, which are foreseen for a hydrogeological study at the Denmark national scale, can be found in Appendix A.4. The spatial distribution of ^{39}Ar activities is illustrated in Figure 5.1.

As a case study for assessing the importance of underground production, two wells located in the two aquifer types were selected for particle tracking simulations with the DK-model because of their over-modern ^{39}Ar activities at relatively shallow depths (~ 30 m). Figure 5.2 illustrates cross sections of the geology in the areas around these wells. LU251 is located in the Quaternary glacial deposits (Figure 5.2a). The filter depth is between 23 - 35 m, which corresponds to the high-permeability sand layer.



(a) Outcropping geology in Denmark and ^{39}Ar activities sampled between 2005 and 2021 (rounds). The two wells of interest for the present study are represented by the diamond shapes. The cross section cut Lolland and Zealand islands.



(b) S-N Cross section through Lolland and Zealand islands [modified from (Henriksen et al., 2003)]

Figure 5.1: Outcropping geology of Denmark in the area of the wells sampled for this study, as well as S-N cross section through Zealand Island

The latter is entirely confined by ~ 18 m of clayey till. B24 borehole is drilled through the Quaternary deposits up to the chalk layers (Danian limestone), where the filter is located (i.e. 23 - 44 m, Figure 5.2b). This formation is also entirely confined by multiple clayey till layers up to a depth of ~ 20 m.

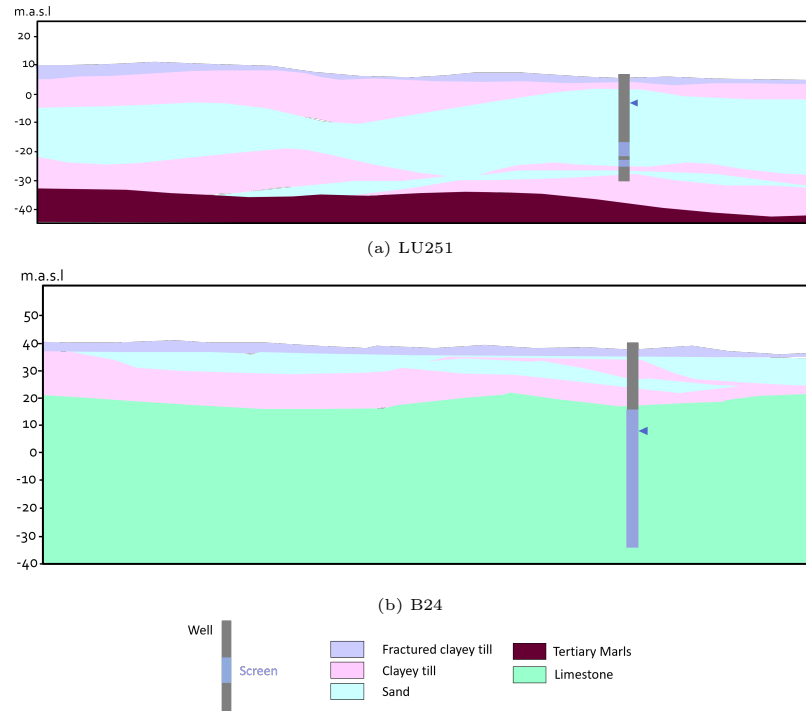


Figure 5.2: Geological profiles of the areas around the wells of interest, extracted from the Danish geological 3D model with GeoScene-3D

The ^{39}Ar , ^{37}Ar , ^{85}Kr , ^3H , $^3\text{He}/^4\text{He}$, ΔNe , and $^4\text{He}_{\text{RAD}}$ activities or concentrations for the two wells of interest are compiled in Table 5.1. ^{39}Ar , ^{37}Ar and ^{85}Kr were measured by LLC at the University of Bern (Loosli and Purtschert, 2005; Riedmann and Purtschert, 2011). ^3H , $^3\text{He}/^4\text{He}$ and stable noble gases were measured at the University of Bremen (Sültenfuß et al., 2009). $^4\text{He}_{\text{RAD}}$ was calculated assuming a recharge temperature of 9 °C (i.e. the mean annual temperature in Denmark) and a seal-level recharge elevation. Both wells present over-modern ^{39}Ar combined with ^{85}Kr activities $\leq 4.5 \text{ dpm cc}_{\text{Kr}}^{-1}$ and ^3H values $\leq 2 \text{ TU}$. B24, located in the chalk aquifer, has a substantially higher ^{37}Ar activity than LU251.

Apparent tracer ages are calculated from the tracer concentrations (Table 5.1) assuming a piston flow (Table 5.2). ^{39}Ar , ^{85}Kr and $^3\text{H}/^3\text{He}$ ages are calculated from their respective radioactive decay rate (Gilmore et al., 2021; Loosli, 1983; Purtschert et al., 2013). $^4\text{He}_{\text{RAD}}$ is constantly produced in U/Th decay chains and accumulates in the underground (see Section 7.1.1). Due to the large uncertainty on the accumulation rate of this isotope at such a large scale, $^4\text{He}_{\text{RAD}}$ ages were not computed in the following. The “negative ^{39}Ar ages” are calculated from the over-modern ^{39}Ar activity concentrations. An estimate based on the ingrowth of activities due to underground production processes is discussed in Section 5.5.

Table 5.1: Radioactive and stable noble gases data; the formation refers to the main rock type at screen depth; z is the average groundwater extraction depth from the DK-Model; ^{39}Ar [%modern] is calculated with $[^{39}\text{Ar}/\text{Ar}]_{\text{mod}} = 1 \text{ Bq g}^{-1} = 8.03 \text{ atoms cc}_W^{-1}$; The DGU is a unique reference number to the well in the system from GEUS

Well	DGU	Location	Aquifer	z [m]	^{39}Ar [% mod]	^{37}Ar [At cc_W^{-1}] $\times 10^{-3}$	^{85}Kr [dpm $\text{cc}_{\text{Kr}}^{-1}$]	$^3\text{He}/^4\text{He}$ $\times 10^{-7}$	ΔNe [%]	$^4\text{He}_{\text{RAD}}$ [cc g^{-1}] $\times 10^{-7}$	$^3\text{He}_{\text{trit}}$ [TV]	^3H [TV]
LU251	136.891	Lunde	Sand	29.0 ± 6.1	174 ± 14	1.0 ± 0.4	1.4 ± 0.4	5.9	26.0	1.3	10.6	0.6
B24	217.863	Fakse	Chalk	33.9 ± 10.8	198 ± 16	9.5 ± 0.5	4.4 ± 0.7	9.6	44.2	0.6	11.6	1.6

Table 5.2: Piston flow ages calculated from ^{39}Ar , ^{85}Kr , and $^3\text{H}/^3\text{He}$ tracers (Table 5.1)

Well	z [m]	^{39}Ar age [yr]	^{85}Kr age [yr]	$^3\text{H}/^3\text{He}$ age [yr]
LU251	29.0 ± 6.1	-215 ± 31	48 ± 2	51 ± 10
B24	33.9 ± 10.8	-265 ± 31	36 ± 2	37 ± 7

5.3.2 Groundwater Model

Starting in 1996, the Geological Survey of Denmark and Greenland developed a National Ressources Model (commonly referred to as “DK-Model”) aiming for a more accurate assessment of exploitable groundwater resources. This integrated surface water - groundwater hydrological model has a 1 km^2 grid and is constructed from MIKE SHE code and comprehensive national databases for geology, soil, topography, rivers, climate, and hydrology data (Henriksen et al., 2003; Trolborg et al., 2008).

Despite the complexity and heterogeneity of the aquifer system, homogeneous and continuous glaciofluvial and sedimentary units could be identified throughout the study areas. The rock chemical compositions are assumed to be homogeneous in these formations and are summarized in Table 3.3 (Section 3.2.1). They were used for the calculation of the ^{39}Ar and ^{37}Ar production rate profiles in Chapter 3. The hydraulic conductivity of the clayey till is controlled by its heterogeneity, such as the presence of smaller sand pockets and fractures. To represent this geological complexity in the model, sand lenses were included in the clay layers. The hydraulic conductivity in the uppermost 1 - 5 m of the clayey till is significantly higher than the deeper layers due to a higher fracture concentration. To represent this in the model, a distinct 3.5 m thick layer with a high density of fractures is included (Henriksen et al., 2003; Harrar et al., 2007; Sidle et al., 1998). In the case of the two wells of interest, the recharge is assumed to take place by percolation through these low-permeability layers (Mortensen et al., 2004).

The DK-Model was used to simulate the depth-dependant residence time distributions for the two wells of interest (Table 5.1). For this purpose, 10'000-30'000 particles were released continuously from the bottom of the fractured clayey till layer and tracked down to the well (Figure 5.3). The model was run over 2000 years with a recycling of the current climatic parameters every 30 years. The total residence time of each particle, as well as the precise depth where it is sampled (within the filter range) are recorded in the simulations. In addition, each time a particle crosses a so-called "registration layer," a position (x,y,z) and time (t) data point is created. Placing a registration layer at the bottom of the confining clayey till layer therefore allowed to subdivide the residence time of the particles between the clay and the aquifer layers ($t_{tot} = t_{clay} + t_{aqu}$). Note that for B24, the registration layer is located at the bottom of the very last clayey till layer. Therefore, the alternation of glacial

sands and clays (Figure 5.2b) is seen as one single unit (Figure 5.3). The average vertical velocity in the clayey till, resp. in the aquifer is calculated from the average travel time and depth from the simulations.

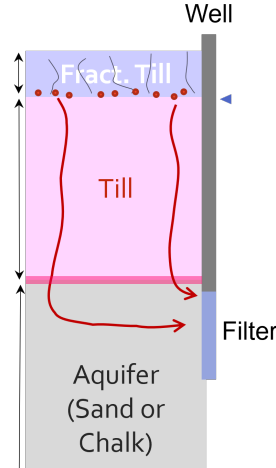


Figure 5.3: Residence time distribution simulation with the DK-Model. The red dots represent particles released at the top of the confining till layer and tracked through the registration layer (pink line) up to the well.

5.3.3 Emanation fractions

The escape process for the atoms from their site of production (i.e. the rock) into the pore space is extensively discussed in Chapter 4. The emanation rate in the water $P_W(z)$ [atoms $\text{cm}^{-3}\text{yr}^{-1}$] relates to the production rate in rock $P_R(z)$ [atoms $\text{g}^{-1}\text{yr}^{-1}$] using Eq. 5.1. At a macroscopic scale, $P_W(z)$ is representing the emanation rate in the drainable pore space, which we defined by the scale where advection becomes the dominant transport process, and therefore where sampling and subsequent activity measurement take place. In this case, the relevant emanation fraction to consider is ε_T , which comprises recoil and diffusion processes that occur at smaller scales (see also the discussion about the extrapolation from the laboratory to the field scale in Section 4.4).

$$P_W(z) = P_R(z) \cdot \varepsilon_T \cdot \frac{1 - \phi}{\phi} \cdot \rho \quad (5.1)$$

The rock porosities ϕ assumed for the three rock formations from the Danish shallow aquifer system are listed in Table 5.3. The chalk and the clayey till formations are typically described by double-porosity systems, where the bulk of groundwater is stored in a low transmissivity porous matrix, and the flow occurs in a high-transmissivity fracture network (Harrar et al., 2007; Mortensen et al., 2004). In the following, this differentiation is not considered, and the porosities are described by the values in the lower edge of their ranges (i.e. the porosity of the matrix) (Henriksen et al., 2003).

Table 5.3: Porosities assumed for the three formations from the Danish shallow hydrogeological system (Henriksen et al., 2003)

Rock formation	ϕ [-]
Sand	0.2
Clayey till	0.03
Chalk	0.05

For ^{37}Ar , total emanation fractions in natural samples range from $0.2\% \leq \varepsilon_{37} \leq 6\%$ depending on the geometry of pore space inside the particle (Johnson et al., 2021; Musy et al., 2022). For ^{39}Ar , average emanation fractions values of $0.35 \pm 0.2\%$ were concluded for natural samples by Johnson et al. (2021). The irradiation of the KCl powder, performed in the frame of this thesis, resulted in an ^{39}Ar emanation fraction of 1.5% . In the following, the range $0.1\% \leq \varepsilon_{39} \leq 1\%$ will be used. Note that these values are towards the higher end but generally agree with estimations of early literature (Krishnaswami and Seidemmann, 1988; Loosli et al., 1989).

5.4 Results

5.4.1 Residence time and vertical velocities distributions

The distributions of residence times simulated for the two wells of interest (i.e. the total residence time) are illustrated by the boxplot in Figure 5.4. t_{well} varies from a few decades up to thousands of years, highlighting the importance of dispersion processes. This was also observed in tracing experiments, where transport through complex fracture networks and matrix diffusion were linked with long tailing of solute breakthrough curves (Harrar et al., 2007). The mean (\pm standard deviation) of the depth z and travel time t to the well (t_{well}), the clay layer (t_{clay}), as well as the aquifer (t_{aqu}) are compiled in Table 5.4. The residence time at the bottom of the 3.5 m of fractured till is expected to be $\ll 1$ year (Harrar et al., 2007). The average vertical velocities are $0.3 - 1 \text{ m yr}^{-1}$ in the clayey till layer, resp. $0.2 - 0.8 \text{ m yr}^{-1}$ in the aquifers. This relatively uniform vertical velocity contrasts with the horizontal velocity distributions. The water moves dominantly vertically in the clayey till layer and therefore, the v_x and v_y are negligible. In the aquifers, the horizontal velocities are expected to be one to two orders of magnitude faster than v_z because the flow is predominantly horizontal. Averaging the vertical velocities is equivalent to assuming a linear increase of the cumulated residence time for each formation, which is more realistic for the clayey till layer than for the aquifers. For depth-dependent production processes, this assumption is however acceptable since most of the production occurs in the tills.

Table 5.4: Statistics for the particle tracking simulations with the DK-Model: mean values \pm std deviation for the sampling depth z , residence time t to the well t_{well} , in the clayey till t_{clay} and in the sand/chalk aquifer t_{aqu} layers. The average vertical velocities v_z are calculated for each layer from their respective depth z , and travel time t .

Well	z [m]	t_{well} [yr]	z_{clay} [m]	t_{clay} [yr]	$v_{z,clay}$ [m yr $^{-1}$]	z_{aqu} [m]	t_{aqu} [yr]	$v_{z,aqu}$ [m yr $^{-1}$]
LJ251	29.0 ± 6.1	32.7 ± 36.8	17.8 ± 3.6	18.4 ± 5.2	1.0 ± 0.2	12.2 ± 4.9	14.4 ± 20.2	0.8 ± 1.5
B24	33.9 ± 10.8	167.3 ± 128.7	21.1 ± 3.8	88.4 ± 41.0	0.3 ± 0.1	13.9 ± 6.5	78.9 ± 97.2	0.2 ± 0.3

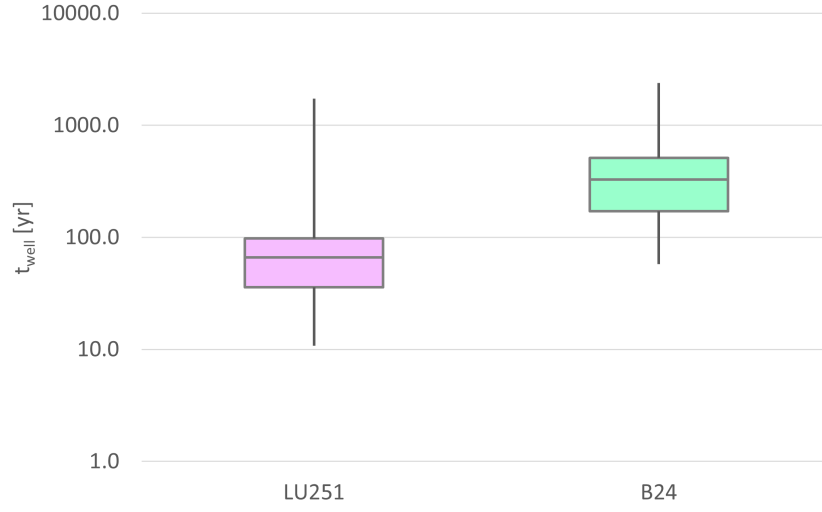


Figure 5.4: Total residence time (t_{well}) distribution from the output of the particle tracking with the DK-Model, for the two wells of interest.

5.4.2 Activity concentration profiles

In a 1D profile, the activity concentrations of a radionuclide in groundwater as a function of time and depth are described by the general advection-dispersion-reaction differential equation:

$$\frac{\partial C}{\partial t} = D \frac{\partial^2 C}{\partial z^2} - v_z \frac{\partial C}{\partial z} + P_W - \lambda C \quad (5.2)$$

The activity concentration C_i [atoms cm^{-3}] in the i th depth interval (Eq. 5.3) is obtained by solving the PDE for steady-state and neglecting the dispersive term, with the boundary condition $C_i(0) = C_{i-1}$ (Eq. 5.3). The residence time of the water Δt in a depth interval i , is controlled by the vertical velocity v_z such as $\Delta t_i = \Delta z_i / v_{z,i}$ (Figure 5.5). Intuitively, the solution (Eq. 5.3) means that the concentration C_i is the sum of the activity concentration emanated in the depth interval i ($P_{W,i}/\lambda$), and the activity concentration inherited from the previous interval (C_{i-1}), i.e. the activity dissolved in the groundwater that enters the interval. Of course, these activity concentrations also decay during the Δt_i in the interval. $P_{W,i}$ is the emanation rate in the water as function of depth z (i.e. $P_{W,i} = P_W(z_i)$, defined in Eq. 5.1). λ is the isotope decay constant for Argon: $\lambda_{39} = 2.6 \times 10^{-3} \text{ yr}^{-1}$ resp. $\lambda_{37} = 7.2 \text{ yr}^{-1}$. The more time a water parcel spends at a given depth, the more time its dissolved activity has to build up towards the secular equilibrium $P_W(z)/\lambda$. Likewise, the longer the half-life of an isotope, the further away its activity is transported (for instance, from the shallow, high-productivity layers, to the deeper levels).

$$C_i = \frac{P_{W,i}}{\lambda} \cdot (1 - \exp(-\lambda \Delta t_i)) + C_{i-1} \cdot \exp(-\lambda \Delta t_i) \quad (5.3)$$

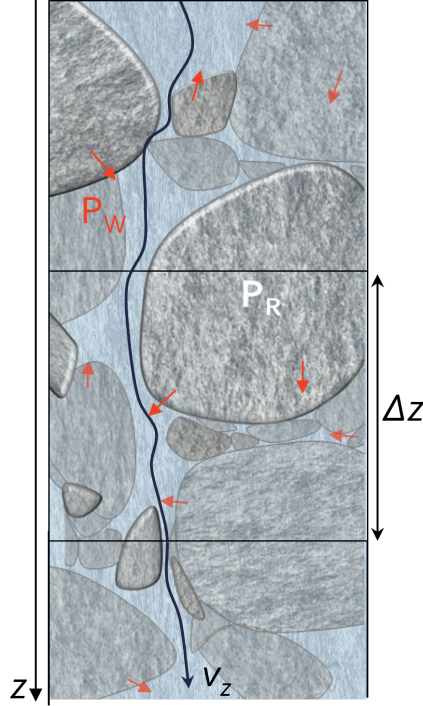
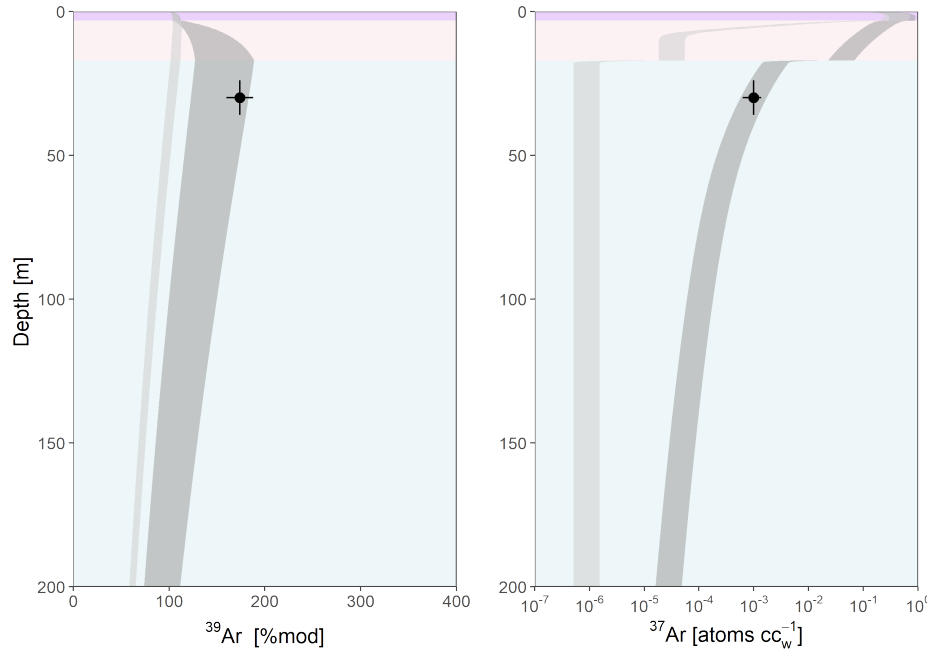


Figure 5.5: Ingrowth process for the dissolved activity concentration of a radionuclide C in a 1D vertical profile. The red arrows illustrate the emanation process (Eq. 5.1); P_R is the production rate in the rock; the blue arrow is the groundwater flow path, which has an average velocity v_z .

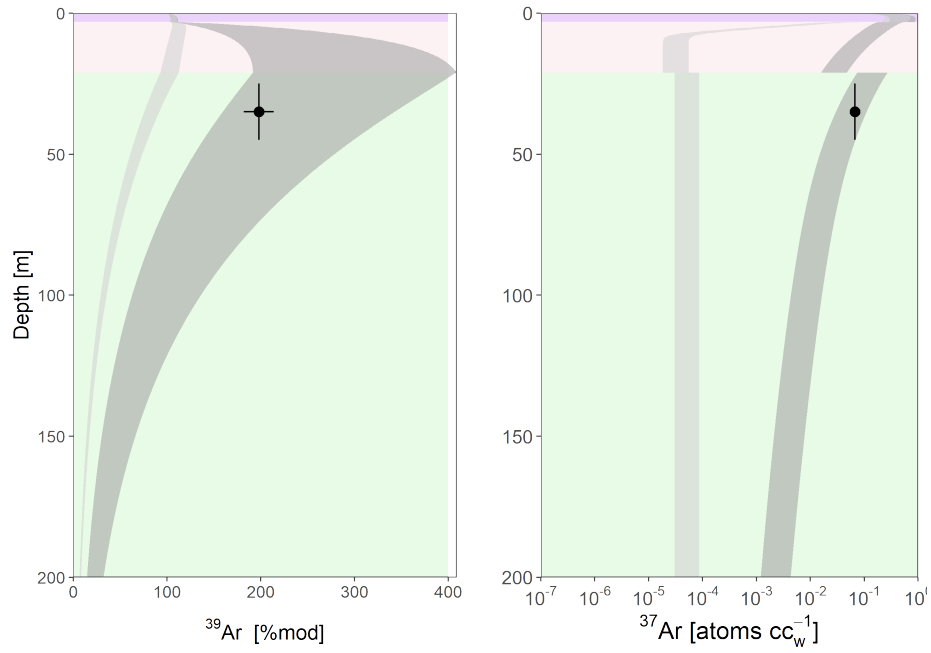
To compute the ingrowth of the dissolved ^{39}Ar and ^{37}Ar activity concentrations in the hydrogeological contexts of the wells LU251 and B24 in Denmark:

1. The emanation rates in water $P_W(z)$ were assessed with Eq. 5.1, the porosities from Table 5.3 and the production rates $P_R(z)$ calculated in Chapter 3 for each rock formation assuming :
 - (a) contributions solely from the production channels with the primary cosmogenic neutrons and neutrons from U/Th decay chains
 - (b) contributions from all production channels, including the muon-induced processes (i.e. capture processes and reactions with muon-induced neutrons)
2. The vertical velocities averaged for each rock formation, inferred from the simulations of particle tracking with the DK-Model (Table 5.4) were used to calculate the dissolved activity concentrations as a function of depth $C(z)$ according to Eq. 5.3.

Figure 5.6 shows the ^{39}Ar and ^{37}Ar calculated activity concentrations profiles in groundwater in combination with the measured data in the wells LU251 (Figure 5.6a) and B24 (Figure 5.6b). The ranges correspond to emanation fractions between $0.1 \% \leq \varepsilon_{39} \leq 1 \%$ and $0.2 \% \leq \varepsilon_{37} \leq 6 \%$. The sharp limits between the layers are due to the fact that only advection is considered here. In reality, dispersive effects would smooth these limits.



(a) LU251



(b) B24

■ With muon-induced processes
 ■ Cosmogenic and U/Th neutrons only

Figure 5.6: Activity concentration profiles for ^{39}Ar (left) and ^{37}Ar (right) in the hydrogeological context of wells LU251 (upper panel) and B24 (lower panel). The black dots are the activities sampled in these wells. The ranges correspond to $0.1\% \leq \varepsilon_{39} \leq 1\%$ and $0.2\% \leq \varepsilon_{37} \leq 6\%$. The light grey curves consider only the production with neutrons from the hadronic component of cosmic rays and natural rock radioactivity; the dark grey curve includes all muon-induced processes (Chapter 3).

5.5 Discussion

Figure 5.6 demonstrates that the activities observed in the wells LU251 and B24 can not be reproduced if only the production channels with the primary cosmogenic neutrons and U/Th decay chains are considered. In particular, the ^{37}Ar activities measured are orders of magnitude higher than the activities produced by these channels alone. This is unequivocally demonstrating the significance of muon-induced processes for radioargon underground production. Owing to its short half-life, the fraction of the ^{37}Ar activity concentration inherited from upper layers is negligible. This highlights its importance as an indicator of local underground production. In contrast, ^{39}Ar activity concentrations in the aquifers below the confining layers are mostly controlled by the production and emanation fractions in the clayey till, where most of the activity is produced and then transported towards lower layers.

The calculated ^{39}Ar activity concentrations can be plotted as function of the cumulative flow-time in order to compare the ^{39}Ar – "ages" with the ^{85}Kr and $^3\text{H}/^3\text{He}$ piston flow ages (Table 5.2). In this case, the age is not calculated based on the radioactive decay of the tracer but rather on its ingrowth rate, which is specific to a given situation. Figure 5.7 shows the ^{39}Ar ingrowth (calculated in Section 5.4.2 and considering all the production channels) as a function of the flow-time underground for LU251 and B24. The measured ^{39}Ar activities (and their uncertainties) are represented by the horizontal pink lines. The range of possible ^{39}Ar – "ages" are bounded by the intersection of the calculated and observed activities: 15 - 50 years for LU251, resp. 2 - 400 years for B24. This is a rather poor constrain of groundwater ages, which is linked with the relatively large uncertainties on the emanation fractions. Further constraining the mean residence time is possible by considering the ^{85}Kr and $^3\text{H}/^3\text{He}$ piston flow ages, which are also shown in Figure 5.7. The latter are in very good agreement with each other. A mean residence time of 50 ± 10 years in LU251, resp. 37 ± 7 years in B24 can be concluded. Using the piston flow assumption is justified in this context because the ingrowth curves are calculated based on average vertical velocities, meaning that the effects of dispersion and mixing are neglected. Strictly speaking, this assumption is not realistic but is, however, acceptable in the context of this study, whose purpose is to constrain the order of magnitude of ^{39}Ar underground production.

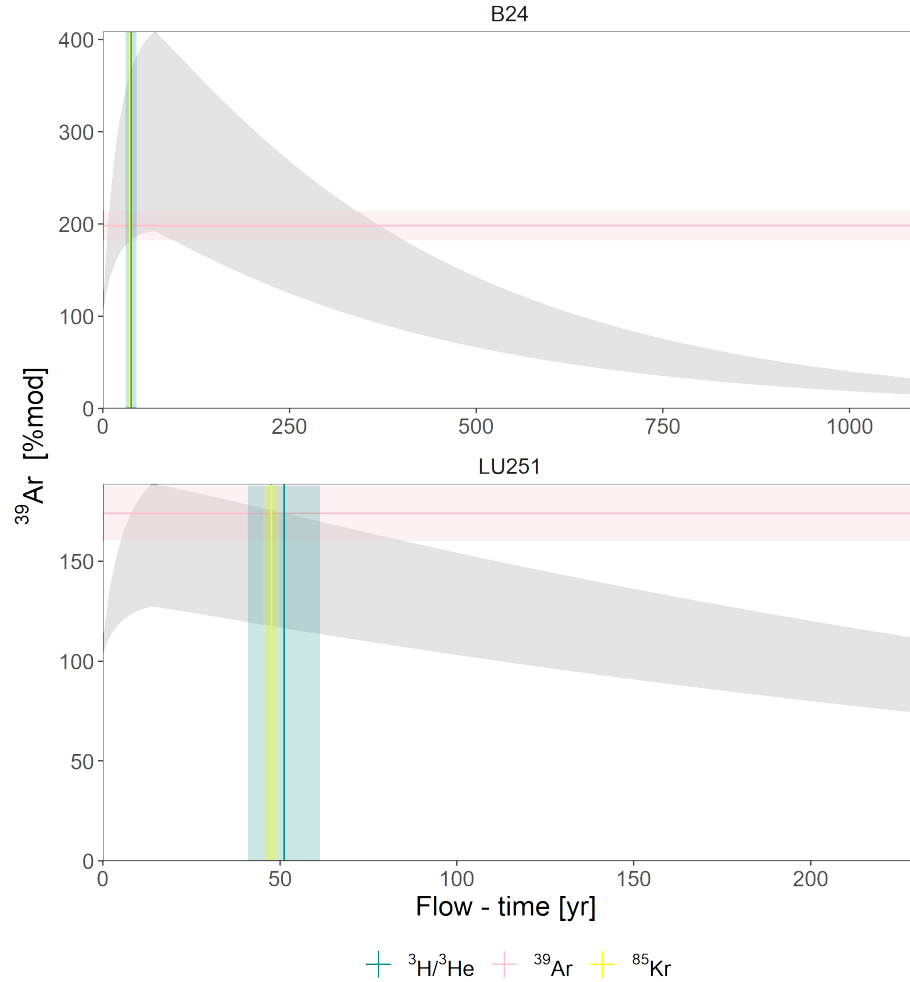


Figure 5.7: ^{39}Ar activities as a function of the flow time in the underground calculated: the grey zone is the calculated ingrowth described in Section 5.4.2, including muon-induced production channels; the pink line is the activity observed in the well. The vertical lines are the piston-flow ages for ^{85}Kr (yellow), and $^3\text{H}/^3\text{He}$ (blue)

5.6 Conclusions and outlooks

In the case of the Danish shallow aquifer system, the importance of muon-induced channels for ^{39}Ar and ^{37}Ar underground production was demonstrated by calculating the ingrowth of radioargon activities in a 1D vertical profile and comparing them with measurements. A sound constraint of the distribution of vertical velocities was possible thanks to particle tracking simulations with a numerical model (DK-Model). The residence time distribution with depth is key information to predict the activities produced in the rocks, and by extension, the activities emanated in the pore space. Despite relatively large uncertainties on the emanation fractions, it appears clearly that the activities measured can not be reproduced if the production rate calculations consider only the channels with neutrons from the hadronic component of cosmic rays and natural rock radioactivity.

Groundwater dating applications with ^{39}Ar , and more recently with ^{37}Ar [see Chapter 7, Schilling et al. (2017)] have never considered muon-induced processes as significant. This study demonstrates unequivocally and for the first time that (i) the muon-induced processes are responsible for significant underground production in the case where a low-permeability layer impedes the groundwater infiltration at shallow - intermediate depths, and (ii) ^{37}Ar is an interesting indicator of ^{39}Ar underground production rate at a local scale. Measuring ^{37}Ar in samples foreseen for ^{39}Ar groundwater dating is a minimal effort with LLC methods and could provide insightful information on the production rate in the aquifer.

These two wells in Denmark were selected because of their obvious $> 100\%$ modern ^{39}Ar activities. However, the extent of the importance of underground production on the other samples from the Danish shallow aquifer system is still unclear. The regionally averaged apparent recharge velocity concluded from the sub-modern ^{39}Ar data (160 mm yr^{-1}) is lower than the local precipitation data (240 mm yr^{-1}), suggesting that all the data could be affected by underground production. In the future, additional particle tracking simulations should allow for better capturing the extent of underground production in Denmark.

In a broader context, the infiltration in this shallow low-permeability layer should be regarded as an "extreme" case of recharge pattern. In many natural settings, the water tends to traverse the shallower levels quickly due to the relatively porous nature of Quaternary deposits (e.g. alluvial aquifers), and/or to weathering processes. Other recharge scenarios, for instance the infiltration in a fully unconfined porous aquifer, are discussed in Chapter 6.

References

- Chalikakis, K., Nielsen, M., Legchenko, A., and Hagensen, T. (2009). Investigation of sedimentary aquifers in Denmark using the magnetic resonance sounding method (MRS). *Comptes Rendus Geoscience - C R GEOSCI*, 341:918–927.
- Gilmore, T., Cherry, M., Gastmans, D., Humphrey, E., and Solomon, D. (2021). The 3H/3He Groundwater Age-Dating Method And Applications. *Derbyana*, 42.
- Harrar, W. G., Murdoch, L. C., Nilsson, B., and Klint, K. E. S. (2007). Field characterization of vertical bromide transport in a fractured glacial till. *Hydrogeology Journal*, 15:1473–1488. ADS Bibcode: 2007HydJ...15.1473H.
- Henriksen, H. J., Trolborg, L., Nyegaard, P., Sonnenborg, T. O., Refsgaard, J. C., and Madsen, B. (2003). Methodology for construction, calibration and validation of a national hydrological model for Denmark. *Journal of Hydrology*, 280(1):52–71.
- Hinsby, K., Trolborg, L., Purtschert, R., and Corcho Alvarado, J. (2006). Integrated dynamic modelling of tracer transport and long term groundwater/surface water interaction using four 30 year 3 h time series and multiple tracers for groundwater dating. Conference IAEA-TECDOC-CD-1507, IAEA, Vienna.
- Johnson, C., Lowrey, J. D., Alexander, T., Mace, E., and Prinke, A. (2021). Measurements of the emanation of ^{37}Ar and ^{39}Ar from irradiated rocks and powders. *Journal of Radioanalytical and Nuclear Chemistry*, 329(2):969–974.
- Knudsen, C., Hinsby, K., Jakobsen, R., Kjærgård, L. J., and Rasmussen, P. (2021). Fingerprinting sources of salinity in a coastal chalk aquifer in Denmark using trace elements. *GEUS Bulletin*, 47.
- Krishnaswami, S. and Seidemann, D. E. (1988). Comparative study of ^{222}Rn , ^{40}Ar , ^{39}Ar and ^{37}Ar leakage from rocks and minerals: Implications for the role of nanopores in gas transport through natural silicates. *Geochimica et Cosmochimica Acta*, 52(3):655–658.
- Loosli, H. (1983). A dating method with ^{39}Ar . *Earth and Planetary Science Letters*, 63(1):51–62.
- Loosli, H., Lehmann, B., and Balderer, W. (1989). Argon-39, argon-37 and krypton-85 isotopes in Stripa groundwaters. *Geochimica et Cosmochimica Acta*, 53(8):1825–1829.
- Loosli, H. and Purtschert, R. (2005). Rare Gases. In Aggarwal, P. K., Gat, J. R., and Froehlich, K. F., editors, *Isotopes in the Water Cycle: Past, Present and Future of a Developing Science*, pages 91–96. Springer Netherlands, Dordrecht.
- Mortensen, A. P., Jensen, K. H., Nilsson, B., and Juhler, R. K. (2004). Multiple Tracing Experiments in Unsaturated Fractured Clayey Till. *Vadose Zone Journal*, 3(2):634–644. _eprint: <https://onlinelibrary.wiley.com/doi/pdf/10.2136/vzj2004.0634>.
- Musy, S., Casolaro, P., Dellepiane, G., Berger, A., Braccini, S., and Purtschert, R. (2022). Quantification of ^{37}Ar emanation fractions from irradiated natural rock samples and field applications. *Journal of Environmental Radioactivity*, 251-252:106966.
- Purtschert, R., Yokochi, R., and Sturchio, N. C. (2013). Krypton-81 dating of old groundwater. In *Isotope methods for dating old groundwater*, pages 91–124. Vienna, i.a.e.a library edition. OCLC: 844871473.
- Riedmann, R. A. and Purtschert, R. (2011). Natural ^{37}Ar Concentrations in Soil Air: Implications for Monitoring Underground Nuclear Explosions. *Environmental Science & Technology*, 45(20):8656–8664.

- Schack, S. and Gravesen, P. (2010). Low- and intermediate level radioactive waste from Risø, Denmark. Location studies for potential disposal areas. Geological Survey of Denmark and Greenland reports 3, GEUS, Copenhagen.
- Schilling, O. S., Gerber, C., Partington, D. J., Purtschert, R., Brennwald, M. S., Kipfer, R., Hunkeler, D., and Brunner, P. (2017). Advancing Physically-Based Flow Simulations of Alluvial Systems Through Atmospheric Noble Gases and the Novel Argon-37 Tracer Method: Integrating tracers with models. *Water Resources Research*, 53(12).
- Sidle, R. C., Nilsson, B., Hansen, M., and Fredericia, J. (1998). Spatially varying hydraulic and solute transport characteristics of a fractured till determined by field tracer tests, Funen, Denmark. *Water Resources Research*, 34(10):2515–2527. _eprint: <https://onlinelibrary.wiley.com/doi/pdf/10.1029/98WR01735>.
- Sültenfuß, J., Roether, W., and Rhein, M. (2009). The Bremen mass spectrometric facility for the measurement of helium isotopes, neon, and tritium in water†. *Isotopes in Environmental and Health Studies*, 45(2):83–95.
- Troldborg, L., Jensen, K. H., Engesgaard, P., Refsgaard, J. C., and Hinsby, K. (2008). Using Environmental Tracers in Modeling Flow in a Complex Shallow Aquifer System. *Journal of Hydrologic Engineering*, 13(11):1037–1048.

Chapter 6

Simulations: Using numerical modeling to constrain the importance of radioargon underground production

6.1 Introduction

Witnessing the importance of ^{39}Ar underground production in the Danish shallow aquifer system (Chapter 5) naturally leads one to question its contribution in other recharge conditions. More specifically, the importance of the newly assessed muon-induced production reactions in typical recharges scenarios is of interest for dating applications. The occurrence of underground production is unquestionable in the presence of over-modern ^{39}Ar activities. However, the situation is not so obvious when the activities are depleted. In this case, assessing the importance of underground production is particularly important to avoid biases in the ages concluded from the activities.

In the present chapter, these issues are approached with numerical modeling methods. The production rates profiles calculated in Chapter 3 are implemented in an integrated surface and subsurface hydrological model [ISSHM, Paniconi and Putti (2015)] called Hydrogeosphere [HGS, Aquanty Inc. (2022)]. Six recharge scenarios with various degrees of confinement and U/Th rock contents were set up. The modeling effort was successful thanks to a collaboration with the group from Prof. Dr. Philip Brunner at the Center for Hydrogeology and Geothermics (CHYN) from the University of Neuchatel. The radioargon groundwater activities were explicitly simulated through the solution of the advection-dispersion equation (Turnadge and Smerdon, 2014; Goode, 1996; Delottier et al., 2022) in the different hydrogeological situations. Specific recharge patterns are inherent to each scenario, allowing to constrain the situations where underground production has a significant impact on dissolved activities. In collaboration with Dr. Sophie Guillon, from MINES ParisTech (France), the modeling procedure was verified by repeating simulations with another Reactive transport code called HYTEC (Van der Lee et al., 2003).

In the unsaturated zone (USZ), emanated gases partition between the aqueous and the gaseous phase as a function of their solubility and water saturation. Rigorous modeling of accumulating tracers requires the consideration of equilibrium between these two phases, especially when the production rate is depth-dependent. This was made possible in HGS thanks to the new implementation of a “zero order source partitioning coefficient” in HGS, which scales the production according to water saturation (Delottier et al., 2022).

6.2 Material and methods

6.2.1 Groundwater models

6.2.1.1 Hydrogeosphere

Hydrogeosphere (HGS) is a 3D fully integrated surface and subsurface flow and transport simulator (Aquanty Inc., 2022). Using the control volume finite element approach, it supports simulations of variably-saturated fractured or granular aquifers, including pumping/injection wells, streams or drains with external flow stresses (rainfall, evapotranspiration, snowmelt, aquifer pumping, etc.) and transport fluxes (concentrations, masses, temperatures, etc.).

To generate hydrogeological scenarios, a synthetic model was set up with a spatial extend of $1000 \times 1 \times 200$ m in the x-, y-, and z-directions respectively. Note that the y-direction exists for mass balance purposes, but the model flows and transports in 2D (x - z). The discretization is carried out by rectangular elements of dimensions $1 \times 1 \times 0.1$ m. The left and bottom boundaries ($x = 0, z = 0$) are set to no-flow boundaries. A fixed hydraulic head of $H < 200$ m was applied as an outflow boundary condition (BC) to create an unsaturated zone (USZ). A meteoric groundwater recharge BC of 240 mm yr^{-1} was applied at the top nodes of the subsurface flow domain (Figure 6.1). In the different scenarios described in the following, three rock formations were used: (i) a high-permeability formation, (ii) a low-permeability formation, and (iii) a U/Th-rich rock formation with high permeability. Each element was assigned an isotropic hydraulic conductivity K [m d^{-1}], porosity ϕ [-] and radioargon rock production rate P_R [$\text{atoms d}^{-1} \text{g}^{-1}$] (Table 6.1) depending on which rock formation it belongs to. The unsaturated zone was assumed homogeneous, and the variably saturated flow was solved using the Van Genuchten model (Van Genuchten, 1980) with $\alpha = 1.9 \text{ m}^{-1}$ and $\beta = 6.0$ (default parameters in HGS).

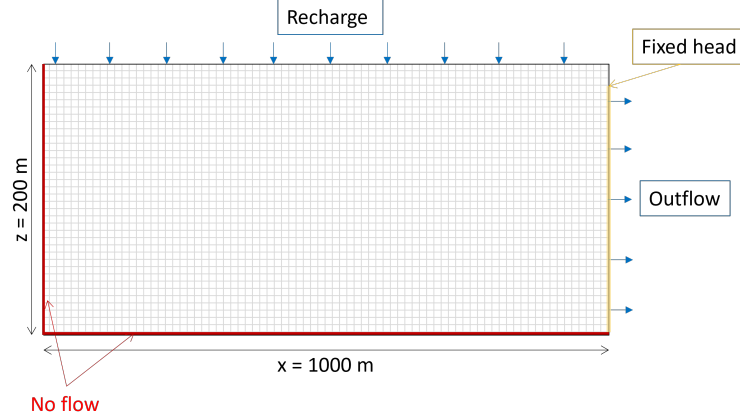


Figure 6.1: The synthetic conceptual model for the radioargon underground production simulations in HGS with boundary conditions

Table 6.1: Production and hydraulic parameters assigned to the elements in the synthetic model for the low-, resp. high-permeability (K) and U/Th-rich rock formations. The rock production rates P_R correspond to those calculated for the Danish hydrogeological system in Chapter 3, resp. to the typical rock composition for a shale (Table A.1 in Appendix A.2)

Formation	P_R	ϕ	$K [m s^{-1}]$
High-K	Sand	20%	1×10^{-4}
Low-K	Clayey till	3%	1×10^{-8}
High-U/Th	Shale	20%	1×10^{-4}

The transport equations were solved for three tracers: ^{39}Ar , ^{37}Ar , and mean groundwater age. The age-mass concept, which sets a solute mass-production rate equal to ϕ with a decay constant of 0 (and $H^{cc} = 1$), is used to simulate the mean age as a tracer (Goode, 1996). The emanation of ^{39}Ar and ^{37}Ar in groundwater $P_W(z)$ (Eq. 5.1) was set according to a zero-order source with partitioning (Delottier et al., 2022). This feature was recently implemented in HGS in parallel to this thesis, and the corresponding article can be found in Appendix A.5. In summary, the zero-order source with partitioning assumes that every produced atom in the USZ will partition immediately into the gas and aqueous phases according to a fixed partitioning coefficient: $H^{cc} = 0.0413$ for Argon [10°C water, Cook and Herczeg (2000)]. Emanation fractions were set to constant values $\varepsilon_{39} = 0.1 \%$, resp. $\varepsilon_{37} = 1 \%$. The disintegration was simulated with a first-order decay according to the decay rate $\lambda_{39} = 7.1 \times 10^{-6} [d^{-1}]$, resp. $\lambda_{37} = 2.0 \times 10^{-2} [d^{-1}]$. The dispersivities were fixed to $\alpha_l = 0.3 \text{ m}$ for the longitudinal component, resp. $\alpha_t = 0.03 \text{ m}$ for the transverse component (Schulze-Makuch, 2005). Lateral transport BC at $x = 0$, $z = 0$ were set to zero-mass gradient. At the top nodes, a third-type BC was set with fixed radioargon concentration at the atmospheric dissolved activities: $C_w(0) = 7.76 \times 10^6 \text{ atoms m}^{-3}$ ($\approx 160 \text{ mBq m}_{\text{air}}^{-3}$) for ^{39}Ar , resp. $C_w(0) = 170.1 \text{ atoms m}^{-3}$ ($\approx 1 \text{ mBq m}_{\text{air}}^{-3}$) for ^{37}Ar . The initial tracer concentrations were set to zero. For each simulation, the model was run for 2000 years, allowing both ^{39}Ar and ^{37}Ar to reach secular equilibrium.

6.2.1.2 Hytec

HYTEC is a coupled reactive transport code chiefly used for groundwater pollution transport, safety assessment of nuclear waste disposals, geochemical studies, and interpretation of laboratory column experiments. The model can account for the alteration of hydrodynamic parameters (porosity, permeability) due to precipitation and dissolution of mineral phases (Van der Lee et al., 2003). This model is computationally more expensive than HGS.

Verification of the modeling procedure was performed by simulating ^{39}Ar activities in a homogeneous, fully unconfined flow and transport model in the high-permeability formation (i.e. a sandbox). For simplification reasons, the hydraulic conditions were slightly different than those used for the recharged scenarios (described in Section 6.2.1.1). Namely, the fixed head for the outflow BC was fixed to 200 m (i.e. fully saturated flow), and the values for the dispersivities were fixed to $\alpha_l = 1$ m and $\alpha_t = 0.1$ m.

6.2.2 Recharge scenarios

To represent a range of infiltration patterns, six scenarios were set up in HGS (Figure 6.2):

- (A) A highly-permeable homogeneous unconfined aquifer with a 3m USZ
- (B) A highly-permeable homogeneous unconfined aquifer with a 30m USZ
- (C) A highly-permeable homogeneous aquifer (with 3m USZ) fully confined by a low-permeability layer located at $3 < z < 30$ m
- (D) A highly-permeable homogeneous aquifer (with 3m USZ) partially confined by a low-permeability layer located at $3 < z < 30$ m. The recharge window is a high-permeability section in the confining layer located at $0 < x < 300$ m
- (A2) A homogeneous unconfined aquifer (with 3m USZ) composed of a rock formation with a high U/Th content
- (C2) A homogeneous, fully confined aquifer (with 3m USZ) composed of a rock formation with a high U/Th content

The $P_R(z)$ for the sand and the clayey till calculated in Chapter 3 were used for the high permeability, resp. the low permeability formations (Table 6.1). The purpose of scenarios A2 and C2 is to simulate a porous aquifer with higher natural rock radioactivity. In this case, the $P_R(z)$ calculated for a typical shale rock (according to the chemical compositions compiled by Fabryka-Martin (1988) were used ($\text{Th} = 22$ ppm, $\text{U} = 3.2$ ppm; Appendix A.2).

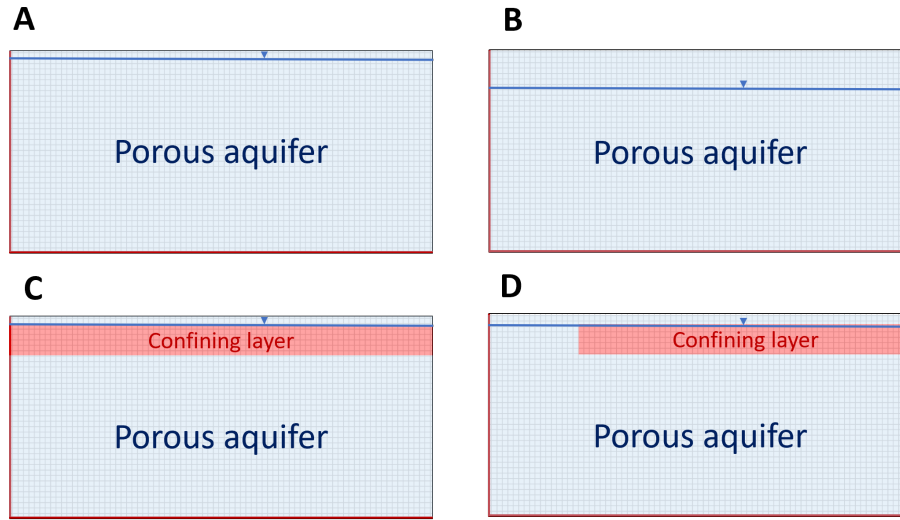


Figure 6.2: Scenarios simulated in HGS. The porous aquifer corresponds to the high permeability layer; the confining layer is the low permeability layer. The blue line represents the groundwater level.

Although some of these simulations resemble the situation in Denmark (Chapter 5), it should be clearly stated that a comparison of the dissolved activities between the simulations and the ingrowths curves calculated with the output velocities from the particle tracking in the DK-Model (Figure 5.5) is not relevant. The DK-Model integrates an incredibly more complex situation, with soil and geological heterogeneity, transient climatic recharge input data, and 3-D flow in the catchment area. The simulations performed with HGS depict a synthetic situation to compare the impact of underground production in various recharge contexts. However, the validation of the method may open the way for implementing depth-dependent underground produced isotopes in large-scale models.

6.3 Results and discussion

6.3.1 Verification with Hytec

The verification with Hytec was performed by extracting a vertical profile at $X = 205$ m in both HGS and Hytec models and comparing the ^{39}Ar activities simulated. Figure 6.3 shows the dissolved activities as a function of the depth below the surface. Both models agree within a 10 % range. The slightly different shape close to the surface is possibly due to the model's treatment of dispersivity values. The agreement observed is considered satisfactory, and the modeling procedure used in the following is therefore validated.

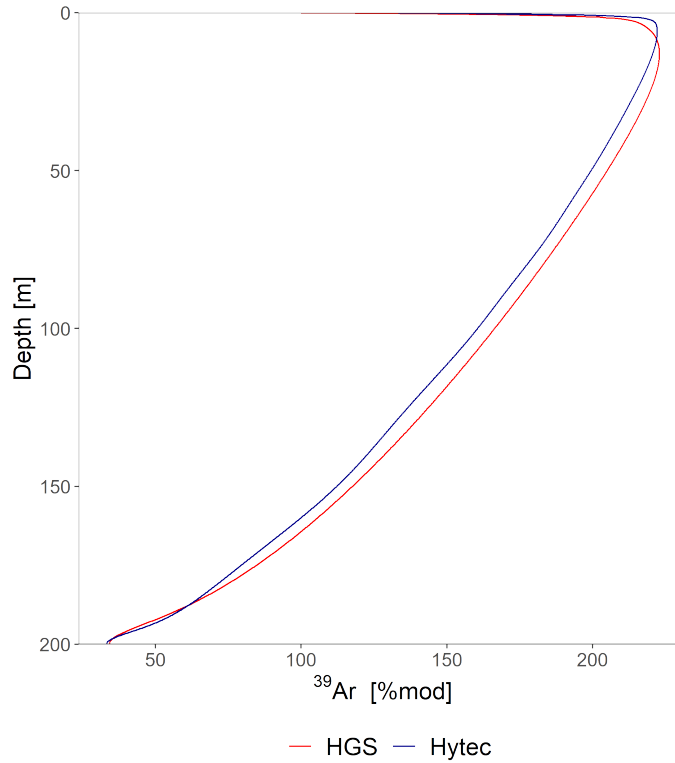


Figure 6.3: Vertical profile ($X = 205$ m) of ^{39}Ar activities as a function of depth z extracted from the 2D Hytec and HGS simulations for validation purposes.

6.3.2 ^{39}Ar , ^{37}Ar and mean age simulations

Figure 6.4 shows the flow velocity in combination with the permeability values, the dissolved groundwater activities for ^{39}Ar , ^{37}Ar , and the mean age for scenarios A-D. In the USZ, the activity concentrations are those dissolved in the residual saturation, defined as the fraction of the pore space volume occupied by water. In our simulations, the residual saturation is 20 %. Comparing the two unconfined models with the USZ thickness of 3 and 30 m indicates no difference in the activities in the USZ. Therefore, the zero-order source with partitioning method is validated.

For the unconfined scenarios (A and B), the overall relatively short residence time in the shallow layers (saturated or not) does not allow for ingrowth to over-modern ^{39}Ar activities. In contrast, ^{37}Ar activities close to the surface are higher than the concentration of the infiltrating water (1.7×10^{-5} atoms cc_W^{-1}). Thus, a significant underground production occurs for this isotope. Owing to its short half-life, ^{37}Ar reaches its secular equilibrium faster than ^{39}Ar . The counterpart of this is that activities can not be transported to deeper levels. In contrast, for ^{39}Ar , the 100 % modern activities in the infiltrating water are carried on for tens of meters underground. The mean age is exponentially increasing from zero at the

infiltration to ~ 1000 years at the bottom of the model. This agrees with the age profile that would theoretically be expected in an unconfined aquifer with constant thickness (Cook and Böhlke, 2000), the so-called "Vogel Model" (Vogel, 1967).

The low-permeability confining layer (C) induces slow velocities, resulting in long residence times close to the surface. This long residence time, combined with the lower porosity, results in high radioargon dissolved activities in this layer. For ^{39}Ar , high activities are transported below the confining layer. However, due to the very slow velocities and, therefore, rapid aging of the water, a sharp activity decrease is observed below the depth of 60 m. In contrast, ^{37}Ar production is increased in the confining layer and has a sharp boundary at the limit with the porous aquifer (note the logarithmic scale). Below this impeding layer, the ^{37}Ar activities are similar to the same depth in the unconfined situation (A). This is another demonstration of the potential of ^{37}Ar to indicate the degree of underground production at a local scale, while for ^{39}Ar , the fraction inherited from higher layers is important.

In the presence of a recharge window (D), the water preferentially infiltrates from this section. Below the confined section, aging with the distance x can be observed. This contrasts with the free aquifer situation, where the aging only occurs with depth z , and agrees with theoretical models Cook and Böhlke (2000). The ^{39}Ar activities below the confined section are then entirely controlled by the infiltration pattern in the high permeability section, resulting in similar profiles to the unconfined situation (A).

Alternately, the effect of a confining layer can be visually illustrated by plotting the $\Delta^{39}\text{Ar}$, which we define as the relative ^{39}Ar activities produced in the confined (C), or partially confined (D) scenarios, compared to the free aquifer (A) situation (Eq. 6.1, Figure 6.5). For the entirely confined scenario, the dissolved activities are higher by a factor of 5 - 7 in large part of the confining layer (except for edge effects on the outflow boundary). In the partially confined situation, the water that recharges on top of the low-permeability section can run off (i.e. "escape") on both sides of the layer. Therefore, the water tends to accumulate less on the impermeable layer, resulting in a lower hydraulic head and an even slower flow within this layer. As a result, ^{39}Ar dissolved activities are a factor of 10 - 15 higher in the low-permeability layer, compared to the free aquifer situation.

$$\Delta^{39}\text{Ar} = \frac{{}^{39}\text{Ar}_{C,D} - {}^{39}\text{Ar}_A}{{}^{39}\text{Ar}_A} \quad (6.1)$$

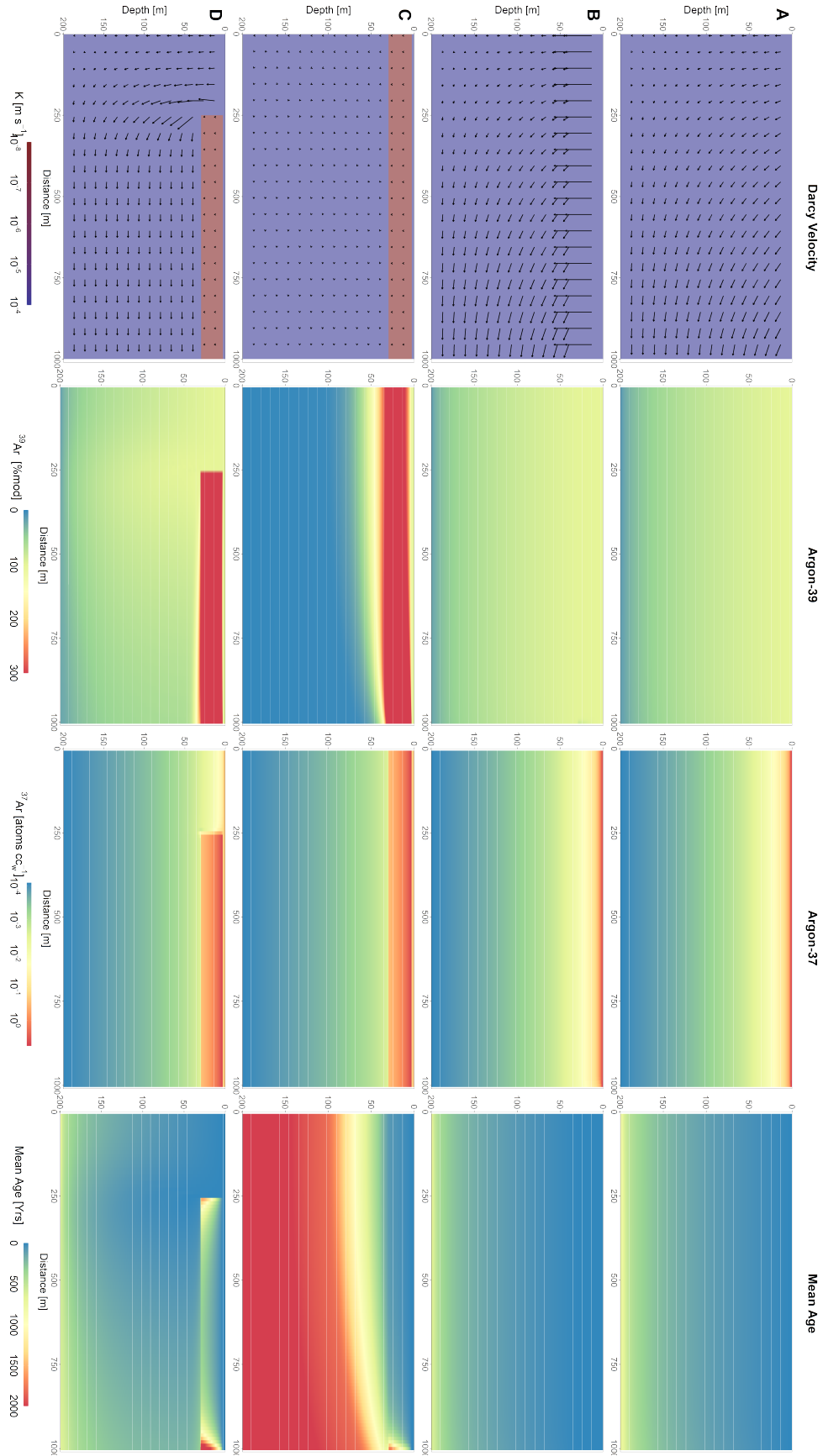


Figure 6.4: Permeability and Darcy velocities (arrows), ^{39}Ar , ^{37}Ar and mean age simulated with Hydrogeosphere for the scenarios A-D. The arrows are a qualitative illustration of the velocities.

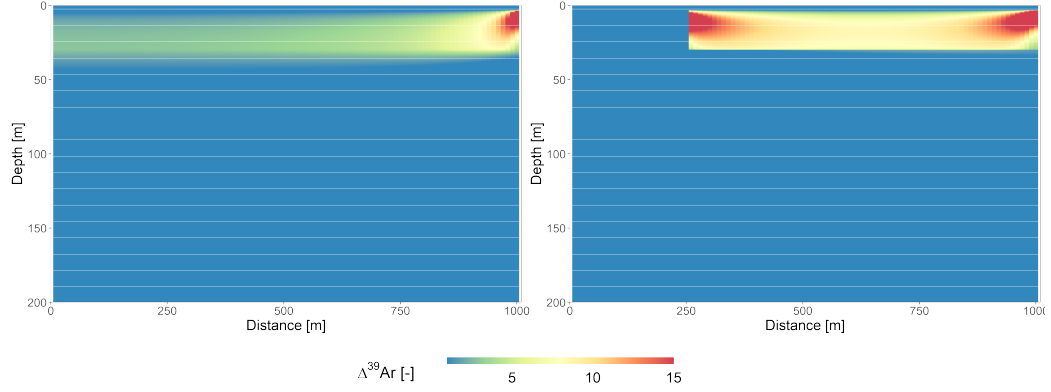


Figure 6.5: $\Delta^{39}\text{Ar}$ for the scenarios C-A (left) and D-A (right)

6.3.3 Importance of radioargon underground production

To assess the importance of the muons production channels for ^{39}Ar dissolved activities for each scenario, the simulations were repeated with the production profiles P_R considering only the primary cosmogenic neutrons ($P_{Ar(n,f)}$), and those from U/Th decay chains ($P_{Ar(n,U/Th)}$). A vertical profile was then extracted at $X = 750$ m. Figure 6.6 shows the ^{39}Ar activities as a function of the mean residence time along this profile. The aim is the comparison of three situations:

- Real case, including all production channels:

$$P_{Ar} = P_{Ar(n,f)} + P_{Ar(n,\mu^-)} + P_{Ar(n,\mu_f)} + P_{Ar(n,U/Th)} + P_{Ar,\mu}$$
- Case neglecting muon-induced processes: $P_{Ar} = P_{Ar(n,f)} + P_{Ar(n,U/Th)}$
- Case neglecting all subsurface production processes: $P_{Ar} = 0$

In the case where $P_{Ar} = 0$, the activities dissolved are simply calculated from the mean residence time t following the radioactive decay of the 100 % modern infiltrating activity $^{39}\text{Ar}_0$:

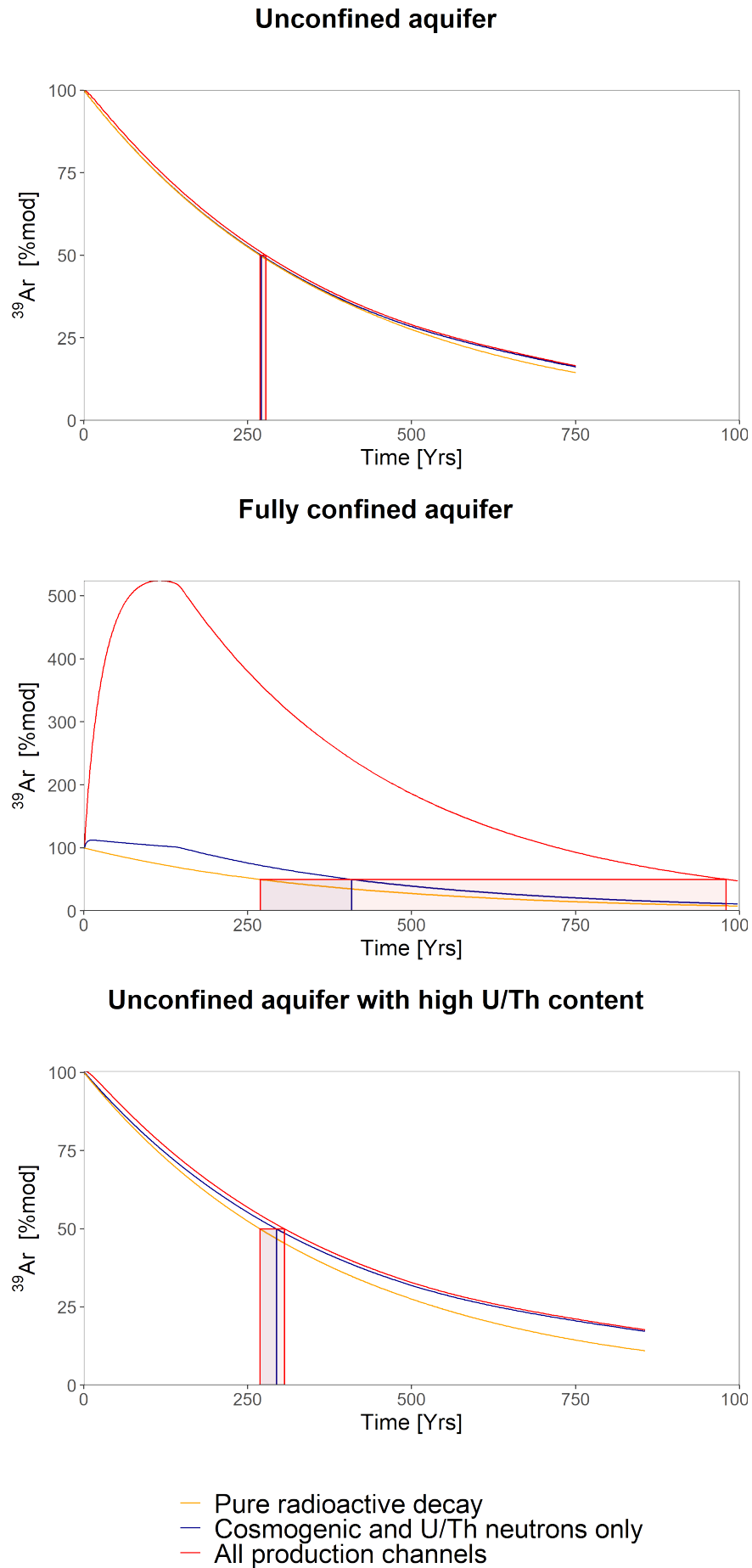
$$^{39}\text{Ar}(t) = ^{39}\text{Ar}_0 \cdot \exp(-\lambda_{39} \cdot t) \quad (6.2)$$

In a real-life field, over-modern ^{39}Ar activities can not be converted to an age (in the absence of information about the infiltrating velocities), but sub-modern activities can be interpreted as an age. These sub-modern activities are then also susceptible to be biased towards "too young" values if subsurface production occurs and is not correctly accounted for. For hypothetically measured activities, the age biases are illustrated by the difference between the real residence time and the apparent pure radioactive decay time (Figure 6.6).

In the unconfined situation (A), the underground production induces a negligible deviation from the simple radioactive decay situation. Thus the age biases are negligible (< 10 yrs). The reason for this is that the fast infiltration of the water in the shallow domain (Figure 6.4) does not allow sufficient residence time for underground production with neither muon-induced processes nor neutrons from primary cosmogenic origin. The $P_{Ar(n,U/Th)}$ is also negligible in this low-U/Th rock.

In the confined scenario (C), the long residence time of the water in the depth range where muon-induced production processes are important creates an over-shoot of the ^{39}Ar activities. The confining layer is located at a depth where the primary neutron flux is already attenuated by ~ 3 orders of magnitude. The contribution of this production channel is thereby negligible. However, the effect of the long residence time in the confining layer, combined with its low porosity, is sufficient for the production with the neutrons from U/Th chains to maintain the activities at 100% modern for about 180 years. In a hypothetical 50 % modern sample, neglecting $P_{Ar(n,U/Th)}$ results in an age bias of 140 years (blue line), whereas not accounting for all the production channels (i.e. muon-induced processes) results in an age bias of 710 years (red line).

In the case of an unconfined aquifer composed of U/Th-rich rock (A2), an age bias due to the production with the neutrons from U/Th decay chains occurs. The depth-dependent processes only make a negligible difference since the water infiltrates fast. In a 40 - 50 % modern sample, the age biases are 25 - 35 years.

Figure 6.6: ^{39}Ar activities as a function of the mean residence time along a vertical profile extracted from the 2D

The areas with over-modern dissolved ^{39}Ar , where age can not be computed, can be visualized in 2D thanks to the ratio R_t (Eq. 6.3) between the age t_R , calculated from the activities simulated (including underground production, i.e. the "real" age) and the "decay" age t_D (Eq.6.2).

$$R_t = \frac{t_R}{t_D} = \frac{\lambda_{39}^{-1} \cdot \ln \frac{A_0}{A_R}}{\lambda_{39}^{-1} \cdot \ln \frac{A_0}{A_D}} = \frac{\ln(A_0) - \ln(A_R)}{\ln(A_0) - \ln(A_D)} \quad (6.3)$$

$R_t < 0$ where the "real" dissolved activities are higher than the 100 % modern activity ($A_R > A_0$), i.e. where over-modern dissolved activities occur. This is illustrated in Figure 6.7 for the unconfined (A) and the fully confined (C) scenarios. Since underground production is negligible for unconfined conditions, $R_t > 0$ everywhere. In contrast, in the fully confined scenario, ^{39}Ar activities sampled up to depths of ~ 40 m are expected to be over-modern and, therefore, in practical useless for groundwater dating.

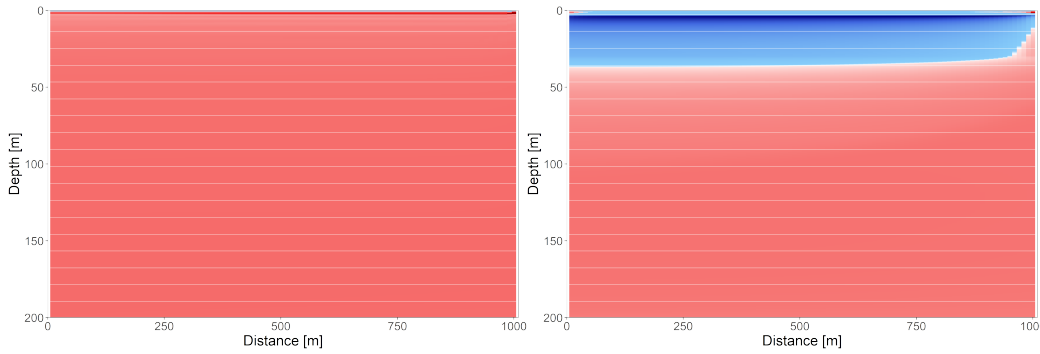


Figure 6.7: Ratio between the ages calculated from the activities simulated (t_R) and "decay" ages (t_D), R_t for the scenario A (left) and C (right). The areas where $R_t < 0$ are where over-modern ^{39}Ar dissolved activities are occurring.

6.3.4 ^{39}Ar groundwater dating clock

Intuitively, the principle of ^{39}Ar groundwater dating can be pictured as a clock (or a stopwatch), which starts at the moment a water molecule infiltrates the subsurface. In the absence of underground production, this is a perfectly valid illustration. However, in a U/Th-rich rock, the dissolved activities keep being alimented by new ^{39}Ar atoms, resulting in an apparent slower decay rate (Figure 6.8A). This translates as a slower "ticking rate" of the groundwater dating clock. Alternately, in the situation where the water stalls at shallow - intermediate depths (Figure 6.8B), over-modern dissolved ^{39}Ar activities delay the starting time of the dating clock. The higher the overshoot, the longer the retardation. Finally, in the situation where the water is slowed down at shallow depth, in an U/Th-rich rock aquifer, the activities overshoot is conserved for a longer time underground (Figure 6.8C)

In this context, the starting time of the groundwater dating clock is defined as the time for which pure radioactive decay from 100 % modern activity results in the activity observed. This concept is illustrated in Figure 6.8C-F for a hypothetical measured activity at 20% modern ^{39}Ar . Depending on the importance of underground production, the starting time is between ~ 160 years to ~ 840 years. Although this parameter has a limited practical application, it illustrates how the underground production processes and recharge pattern affect the ^{39}Ar dating method.

6.4 Conclusions and outlooks

A synthetic 2D model was developed to understand better the influence of the recharge patterns on the ^{39}Ar activities dissolved in porous aquifers. The depth-production rates, including the newly assessed muon-induced processes, were implemented in Hydrogeosphere as a zero-order source, with partitioning in the unsaturated zone. The model was run for 2000 years with different confining conditions, ranging from a free, unconfined aquifer to a fully confined situation with a low permeability layer located at shallow depths (3 - 30 m).

The ^{39}Ar and ^{37}Ar activities were simulated in combination with the mean age of the water. In the presence of an impeding layer, the slowing down of the water and, to some extent, the low porosity of the layer results in increased activity concentrations in the water. While ^{39}Ar activities can be transported towards deeper levels, ^{37}Ar can be used to attest to underground production rates on a local scale. If a preferential infiltration option exists for the water, like a recharge window, the ^{39}Ar activities in the aquifer are chiefly controlled by the fraction infiltrated through this section. In addition, picturing ^{39}Ar groundwater dating as a clock that starts as soon as the water infiltrates the underground is a convenient but incomplete picture. Underground production affects not only the moment the clock starts but also how fast it is ticking.

In summary, numerical modeling demonstrated to be an appropriate tool to constrain the situations where underground production of ^{39}Ar may result in age biases for groundwater dating. In this thesis, only a few "extreme" scenarios were simulated. Nevertheless, a large room for intermediate situations exists and may be explored in the future. In general, in the absence of information about the infiltration processes, particular attention should be paid to the hydrogeological context when interpreting the ^{39}Ar activities for groundwater dating.

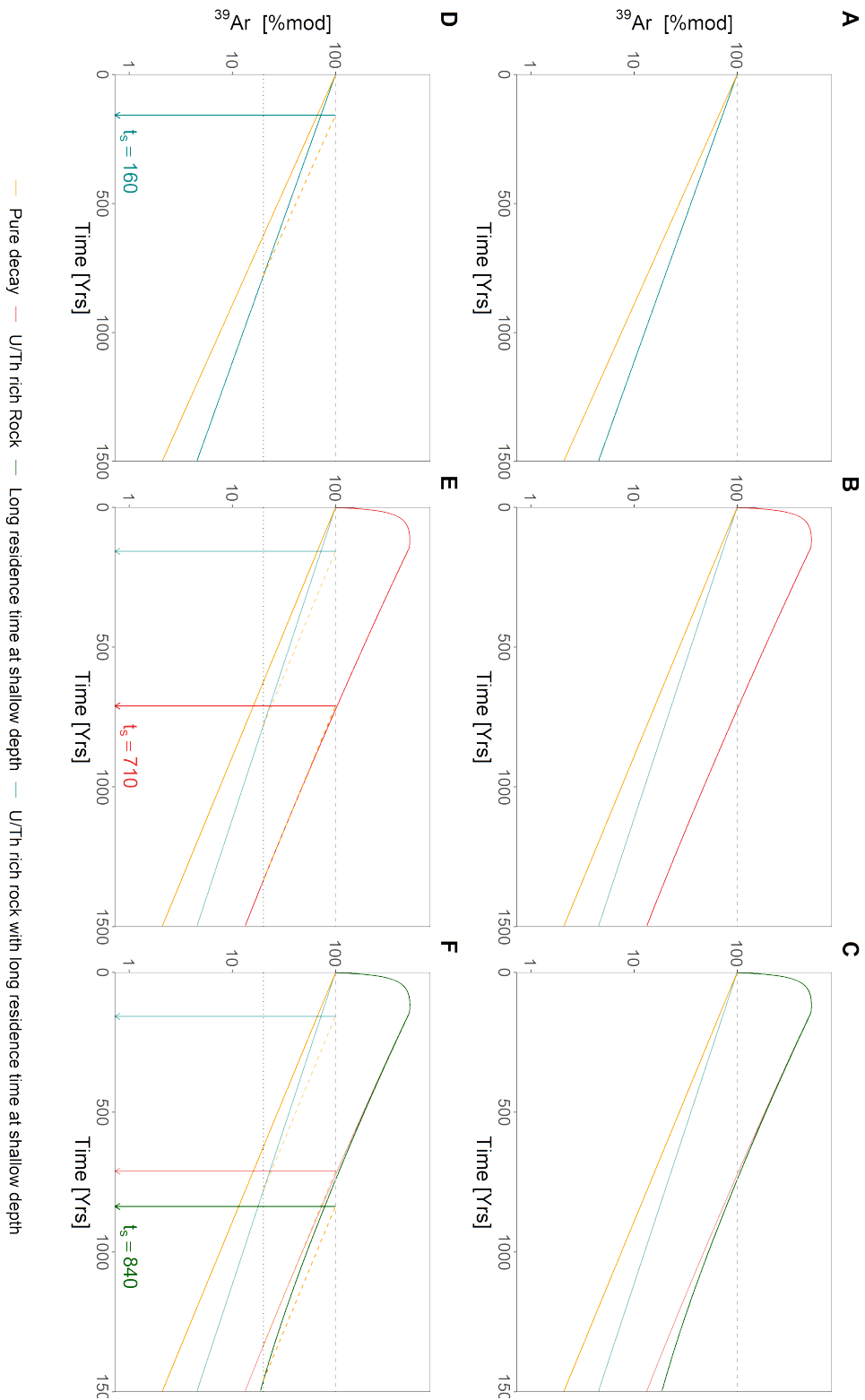


Figure 6.8: ^{39}Ar activities as a function of the mean residence time in situations depending on the recharge pattern and the U/Th content of the host rock (upper line). The lower line illustrated the starting time t_s of the groundwater dating clock in each situation

References

- Aquanty Inc., H. (2022). Theory Manual. Technical report, Waterloo (CA).
- Cook, P. G. and Böhlke, J.-K. (2000). Determining timescales for groundwater flow and solutes transport. In *Environmental Tracers in Subsurface Hydrology*, pages 1–30. Cook Peter G., Herczeg Andrew L., CSIRO Land and Water, Glen Osmond, Australia, springer science+business media, llc edition.
- Cook, P. G. and Herczeg, A. L., editors (2000). *Environmental Tracers in Subsurface Hydrology*. Springer US, Boston, MA.
- Delottier, H., Peel, M., Musy, S., Schilling, O., Purtschert, R., and Brunner, P. (2022). Explicit simulation of environmental gas tracers with integrated surface and subsurface hydrological models. *Frontiers in Water*, 4.
- Fabryka-Martin, J. (1988). *Production of radionuclides in the earth and their hydrogeologic significance, with emphasis on chlorine-36 and iodine-129*. PhD Thesis, University of Arizona, Tucson.
- Goode, D. J. (1996). Direct Simulation of Groundwater Age. *Water Resources Research*, 32(2):289–296. _eprint: <https://onlinelibrary.wiley.com/doi/pdf/10.1029/95WR03401>.
- Paniconi, C. and Putti, M. (2015). Physically based modeling in catchment hydrology at 50: Survey and outlook. *Water Resources Research*, 51(9):7090–7129. _eprint: <https://onlinelibrary.wiley.com/doi/pdf/10.1002/2015WR017780>.
- Schulze-Makuch, D. (2005). Longitudinal dispersivity data and implications for scaling behavior. *Groundwater*, 43(3):443–456. _eprint: <https://onlinelibrary.wiley.com/doi/pdf/10.1111/j.1745-6584.2005.0051.x>.
- Turnadge, C. and Smerdon, B. D. (2014). A review of methods for modelling environmental tracers in groundwater: Advantages of tracer concentration simulation. *Journal of Hydrology*, 519:3674–3689.
- Van der Lee, J., Windt, L., Lagneau, V., and Goblet, P. (2003). Module-oriented Modeling of Reactive Transport with HYTEC. *Computers & Geosciences*, 29:265–275.
- Van Genuchten, M. (1980). A Closed-form Equation for Predicting the Hydraulic Conductivity of Unsaturated Soils¹. *Soil Science Society of America Journal*, 44.
- Vogel, J. (1967). Investigation of groundwater flow with radiocarbon. *Isotopes in Hydrology*.

Chapter 7

Field application: Using ^{37}Ar to trace Surface water - Groundwater interactions in an alluvial aquifer

7.1 Introduction

Alluvial systems typically host dynamic and complex interactions between surface water and groundwater (SW-GW) on timescales from weeks to months. These systems are usually associated with high productivity because of their high permeability and the large exchange fluxes, making them a preferred choice for drinking water supply (Boano et al., 2014; Gerber, 2017). In such systems, groundwater quality and quantity (Krause et al., 2014), as well as ecosystems and organisms (Boano et al., 2014; Harvey and Gooseff, 2015; Krause et al., 2014), directly depend on the short-, and long-term variability in river water discharged (Holman, 2006). The alpine and pre-alpine areas are projected to undergo substantial changes in storage patterns with the retreat of glaciers and earlier snowmelt induced by climate change (IPCC, 2001; Viviroli and Weingartner, 2004). Therefore, they are considered especially vulnerable in the upcoming decades (Käser and Hunkeler, 2016).

One example of such a system is the Upper Emme catchment, located in central Switzerland, where the aquifer serves as an important drinking water resource, providing 50 % of the water consumption for the city of Bern (Biaggi et al., 2004; Schilling et al., 2017; Käser and Hunkeler, 2016). In the past, large combined multitracer and modeling experiments allowed a better insight into the origin, pathways, and residence times of groundwater in this area (Schilling et al., 2017; Käser and Hunkeler, 2016). In January 2019, an important pumping experiment was carried out by the local authorities to evaluate the effect of increased groundwater abstraction on the hydrological system. The gradual increase of the pumping rates induced transient conditions in the drainage basin, which were monitored by multiple tracers.

In this context, the high-resolution analyses of dissolved noble gases, and more specifically ^4He concentrations, were combined with continuous ^{222}Rn activity measurements to (i) assess the mixing ratio of GW-SW and (ii) estimate the travel time of the freshly infiltrated river water. Conclusions drawn from the experimental tracer measurements were supported by an important numerical effort with the fully-integrated model HydroGeoSphere (HGS) to simulate system response to the change in forcing parameters. The study was carried out as a large collaboration between the ETH (group from Prof. Dr. Rolf Kipfer, Eawag), the Universities of Bern (Environmental radionuclide group) and Neuchâtel (group from Prof. Dr. Philip Brunner, CHYN), and resulted in the published paper found in Section 7.2.

In addition to ^4He and ^{222}Rn , punctual sampling of ^{37}Ar activities was performed during the pumping experiment. These data were not included in the above-mentioned publication and are therefore discussed in the frame of this thesis in Section 7.3. The next Section shortly recapitulates the information that can be retrieved from these isotopes in the frame of SW-GW interaction studies.

7.1.1 Principles of using ^4He , ^{222}Rn and ^{37}Ar for the assessment of SW-GW interactions

The accumulation of underground produced isotopes is typically used to trace the residence time of the infiltrating water (Harvey and Gooseff, 2015; Peel et al., 2022; Vogt et al., 2010). The radioactive tracers ^{222}Rn ($t_{1/2} = 3.8$ d) and ^{37}Ar ($t_{1/2} = 35$ d) are particularly interesting because they are sensitive to the age, and the proportion of water with residence times of weeks to months. In addition, ^{37}Ar also depends on the recharge process and the percolation depth because of the depth-dependency of its production rate. In contrast, ^4He , ^{222}Rn production is part of ^{238}U decay chain, and its rate does not especially depend on the vertical direction (Hoehn et al., 1992; Cecil and Green, 2000; Solomon et al., 1996). For all these isotopes, surface water has a negligible concentration or activity. Therefore, the dissolved concentration or activity builds up on their path underground.

Radioactive tracers reach a production-decay equilibrium, which represents the upper range for their dating application. Predicting the secular equilibrium inherently requires knowledge of the production rate, as well as the emanation fraction. For ^{37}Ar , these parameters are extensively discussed in Chapters 3 and 4. For ^{222}Rn , Peel et al. (2022) recently highlighted the constant emanation rate at depths greater than a few meters. At shallow depth, emanation is significantly increased due to weathering processes [similarly to ^{37}Ar , Musy et al. (2022)]. The relatively simple constant emanation contrasts with the difficulty of accounting for the important spatial variability of ^{222}Rn production (Peel et al., 2022). The production rate of radiogenic ^4He can be calculated from the U and Th chemical concentra-

tion in the rock. However, observed rates frequently exceed predicted values. According to the literature, this discrepancy can be explained by (i) an external flux from deeper formations (Torgersen and Stute, 2013) or (ii) outgassing of He from the aquifer solids (Solomon et al., 1996). An alternative to the calculation of the background concentrations or activities is the defining end-members, which are assumed to be representative of the water at radioactive or dissolution equilibrium with the host aquifer matrix at the study scale (Popp et al., 2021; Peel et al., 2022; Cecil and Green, 2000).

Deviations from these background concentrations or activities are associated with the infiltration of fresh water from a losing stream for example (Figure 7.1). Depending on the tracer production rate, and half-life for radioactive nuclides, the proportion of the freshly infiltrated water, and/or its residence time in the aquifer, can be estimated. In presence of an operating pumping plant, both the distance from where the water is drained and the flow velocities are increased.

^4He does not significantly accumulate over the timescales of the infiltrating river water (days - months) and is therefore used to quantify the mixing ratio between river water and the regional aquifer water, which is sufficiently old to have accumulated significant ^4He (Figure 7.1a). Continuous ^4He measurements allow for the calculation of the transient fraction of river water (F_{rw}). Once F_{rw} is known, ^{222}Rn and ^{37}Ar activities can be used to estimate the travel times of the freshly infiltrated water. ^{222}Rn reaches its secular equilibrium in ~ 20 days (Delottier et al., 2022), which limits its application to very permeable aquifers and/or short distances (Figure 7.1b). ^{37}Ar applies over longer timescales owing to its longer half-life and has the advantage that additional information can be extracted from the depth-dependency of its secular equilibrium (Figure 7.1c).

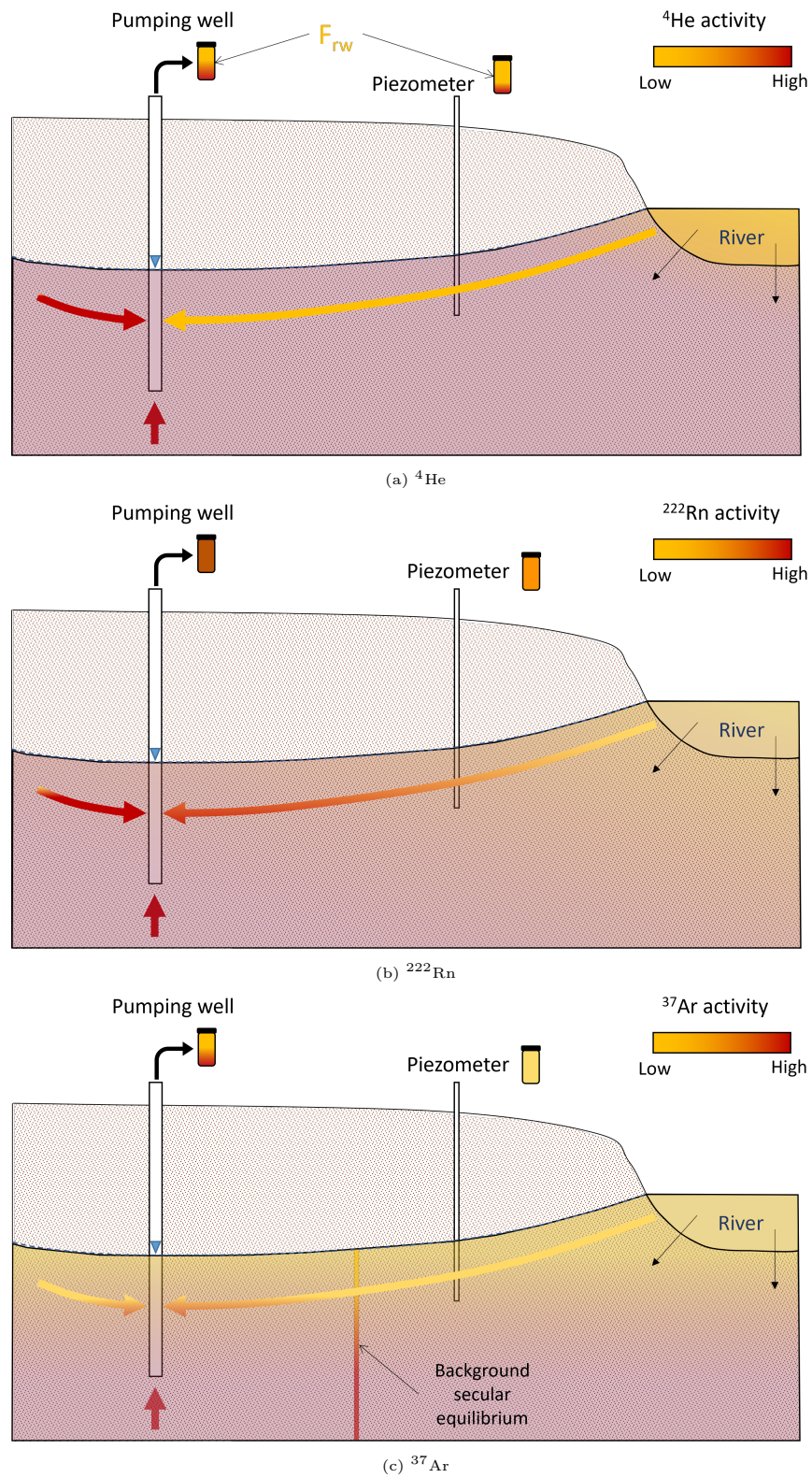


Figure 7.1: Effect of increased pumping rates on a losing river on ^{222}Rn and ^{37}Ar measured concentrations in a conceptual alluvial system

7.2 [Article]A Framework for Untangling Transient Groundwater Mixing and Travel Times

Andrea Popp, Álvaro Pardo-Álvarez, Oliver Schilling, Andreas Scheidegger, **Stephanie Musy**, Morgan Peel, Philip Brunner, Roland Purtschert, Daniel Hunkeler, and Rolf Kipfer

Published in *Water Resources Research*, 57, e2020WR028362, 2021
doi: 10.1029/2020WR028362

Abstract Understanding the mixing between surface water and groundwater as well as groundwater travel times in vulnerable aquifers is crucial to sustaining a safe water supply. Age dating tracers used to infer apparent travel times typically refer to the entire groundwater sample. A groundwater sample, however, consists of a mixture of waters with a distribution of travel times. Age dating tracers only reflect the proportion of the water that is under the dating range of the used tracer, thus their interpretation is typically biased. Additionally, end-member mixing models are subject to various sources of uncertainties, which are typically neglected. In this study, we introduce a new framework that untangles groundwater mixing ratios and travel times using a novel combination of in-situ noble gas analyses. We applied this approach during a groundwater pumping test carried out in a pre-alpine Swiss valley. First, we calculated transient mixing ratios between recently infiltrated river water and regional groundwater present in a wellfield, using helium-4 concentrations combined with a Bayesian end-member mixing model. Having identified the groundwater fraction of recently infiltrated river water (F_{rw}) consequently allowed us to infer the travel times from the river to the wellfield, estimated based on radon-222 activities of F_{rw} . Furthermore, we compared tracer-based estimates of F_{rw} with results from a calibrated numerical model. We demonstrate (i) that partitioning of major water sources enables a meaningful interpretation of an age dating tracer of the water

Water Resources Research



RESEARCH ARTICLE

10.1029/2020WR028362

Key Points:

- We introduce a framework to estimate mean travel times of a groundwater fraction consisting of recently infiltrated river water (F_{rw})
- We test the influence of temporally variable end-member tracer concentrations on estimated mixing ratios
- We demonstrate that the streambed has a major control on the travel times of F_{rw}

Supporting Information:

- Supporting Information S1

Correspondence to:









A. L. Popp,
andrea.popp@geo.uio.no

Citation:

Popp, A. L., Pardo-Álvarez, Á., Schilling, O. S., Scheidegger, A., Musy, S., Peel, M., et al. (2021). A framework for untangling transient groundwater mixing and travel times. *Water Resources Research*, 57, e2020WR028362. <https://doi.org/10.1029/2020WR028362>

Received 11 JUL 2020
Accepted 22 FEB 2021

A Framework for Untangling Transient Groundwater Mixing and Travel Times

Andrea L. Popp^{1,2,3,4} , Álvaro Pardo-Álvarez³ , Oliver S. Schilling^{3,5} ,
Andreas Scheidegger¹ , Stéphanie Musy⁶ , Morgan Peel³ , Philip Brunner³ ,
Roland Purtschert⁶ , Daniel Hunkeler³ , and Rolf Kipfer^{1,2,7}

¹Eawag, Swiss Federal Institute of Aquatic Science and Technology, Dübendorf, Switzerland, ²Department of Environmental Systems Science, ETH Zurich, Zurich, Switzerland, ³Centre d'Hydrogéologie et de Géothermie, University of Neuchâtel, Neuchâtel, Switzerland, ⁴Now at Department of Geosciences, University of Oslo, Oslo, Norway, ⁵Département de géologie et de génie géologique, Université Laval, Quebec City, Canada, ⁶Climate and Environmental Physics, University of Bern, Bern, Switzerland, ⁷Department of Earth Sciences, ETH Zurich, Zurich, Switzerland

Abstract Understanding the mixing between surface water and groundwater as well as groundwater travel times in vulnerable aquifers is crucial to sustaining a safe water supply. Age dating tracers used to infer apparent travel times typically refer to the entire groundwater sample. A groundwater sample, however, consists of a mixture of waters with a distribution of travel times. Age dating tracers only reflect the proportion of the water that is under the dating range of the used tracer, thus their interpretation is typically biased. Additionally, end-member mixing models are subject to various sources of uncertainties, which are typically neglected. In this study, we introduce a new framework that untangles groundwater mixing ratios and travel times using a novel combination of in-situ noble gas analyses. We applied this approach during a groundwater pumping test carried out in a pre-alpine Swiss valley. First, we calculated transient mixing ratios between recently infiltrated river water and regional groundwater present in a wellfield, using helium-4 concentrations combined with a Bayesian end-member mixing model. Having identified the groundwater fraction of recently infiltrated river water (F_{rw}) consequently allowed us to infer the travel times from the river to the wellfield, estimated based on radon-222 activities of F_{rw} . Furthermore, we compared tracer-based estimates of F_{rw} with results from a calibrated numerical model. We demonstrate (i) that partitioning of major water sources enables a meaningful interpretation of an age dating tracer of the water fraction of interest and (ii) that the streambed has a major control on the estimated travel times.

1. Introduction

Climate change is anticipated to alter the seasonality and quantity of water resources in mountainous regions (e.g., Hock et al., 2019) by affecting snow cover dynamics (e.g., Fiddes et al., 2019), glacier melt (e.g., Huss & Hock, 2015), groundwater storage (Cochand et al., 2019), and river discharge (e.g., Addor et al., 2014; Blöschl et al., 2019; Michel et al., 2020). Although these changes will profoundly influence groundwater recharge and discharge in mountainous environments (Hayashi, 2019), they have largely been ignored so far (Somers et al., 2019). Since surface water and groundwater resources are closely coupled, an improved understanding of surface water-groundwater interactions is highly relevant for a sustainable water governance as well as for water-dependent ecosystems in mountainous regions (e.g., Holman, 2006; Krause et al., 2014; Schilling et al., 2020).

Within the last two decades, studies on river-aquifer exchange dynamics have substantially improved the understanding of the drivers (e.g., river discharge) and controls (e.g., riverbed hydraulic conductivity) of water exchange patterns and their impact on biogeochemical cycling of solutes (e.g., reviews by Boano et al., 2014; Brunner et al., 2017; Lewandowski et al., 2019 and references therein). Particularly, the continued recognition and investigation of riverbed dynamics as key controls on river-aquifer exchange have brought substantial scientific progress in the field of surface water-groundwater interactions (e.g., Mutiti & Levy, 2010; Tang et al., 2018). However, the spatiotemporal dynamics of surface water-groundwater interactions still remain elusive, mainly due to a lack of high-resolution field data (Barthel & Banzhaf, 2016; Boano

© 2021 The Authors.

This is an open access article under the terms of the [Creative Commons Attribution-NonCommercial License](https://creativecommons.org/licenses/by-nc/4.0/), which permits use, distribution and reproduction in any medium, provided the original work is properly cited and is not used for commercial purposes.

et al., 2014; Brunner et al., 2017; Krause et al., 2014; Partington et al., 2017). Consequently, further progress for an improved conceptual understanding as well as model development (which depends on high-resolution field data for model calibration and validation) is limited by the quantity and quality of data available (e.g., Barthel & Banzhaf, 2016; Paniconi & Putti, 2015; Schilling, Cook, & Brunner, 2019).

Environmental tracers such as stable water isotopes or dissolved noble gases have been proven to be highly beneficial to study groundwater flow paths, travel times, and water source partitioning. These tracers deliver an integrated signal over the entire catchment and thus carry important information on water flow paths on large scales (Cook & Herczeg, 2000; Jasechko, 2019; Sprenger et al., 2019 and references therein). Therefore, recent review papers (Brunner et al., 2017; Jasechko, 2019; Schilling, Cook, & Brunner, 2019; Sprenger et al., 2019) emphasize the need for novel, more efficient (isotope) tracer measurement techniques to enhance the understanding of complex feedback mechanisms occurring in river-aquifer systems. Fortunately, recent advances in tracer-based hydrological modeling (e.g., Schilling et al., 2017) have proceeded synchronously with rapid methodological developments in tracer hydrology (Brunner et al., 2017; Paniconi & Putti, 2015)—the latter allowing for high-resolution (e.g., multiple measurements per hour), on-site sampling of stable water isotopes (e.g., Herbstritt et al., 2019; Von Freyberg et al., 2017) or dissolved noble gases (e.g., Mächler et al., 2012). One such technique enabling high-resolution (noble) gas analysis is a recently developed Gas Equilibrium-Membrane Inlet Mass Spectrometer (GE-MIMS; Brennwald et al., 2016) system, which can analyze a multitude of reactive and noble gas species including helium-4 (^4He). Noble gases analyzed with portable mass spectrometry have shed light on various hydrological processes within recent years (e.g., Chatton et al., 2017; Hoffmann et al., 2020; Popp et al., 2020; Schilling et al., 2021; Vautier et al., 2020). Likewise, the noble gas radon-222 (^{222}Rn) is another often used tracer to study surface water-groundwater interactions (e.g., Gleeson et al., 2018). With a half-life of 3.8 days, ^{222}Rn can be used to assess apparent travel times (from here on referred to as travel times or TTs) of up to ~15 days of infiltrating river water to groundwater (e.g., Hoehn & Von Gunten, 1989).

However, an accurate interpretation of age dating tracers such as ^{222}Rn activities is inherently challenging because every water sample consists of a mixture of waters with various ages (e.g., Cook & Herczeg, 2000; Jasechko, 2019; Sprenger et al., 2019). Thus, disentangling major flow paths and identifying groundwater mixing processes is key to allow for an accurate interpretation of travel times using age dating tracers (e.g., Sprenger et al., 2019).

The ongoing evolution of mixing models for source partitioning within the hydrological sciences (e.g., Beria et al., 2020; Popp et al., 2019) and beyond (e.g., Stock et al., 2018) provides an often neglected set of toolboxes to account for the various sources of uncertainties related to mixing models. One major limitation of groundwater mixing modeling is to identify end-members correctly and the inability to observe end-members over time (e.g., Carrera et al., 2004; Delsman et al., 2013; McCallum et al., 2010). The assumption of constant end-members cannot be verified or falsified if tracer time-series are unavailable. In fast changing systems though, end-members might in fact be transient. Moreover, a delay between the time a source enters the system and the time it is observed in the mixture is rarely considered (Beria et al., 2020).

In this study, we present a framework with the key objective to determine travel times of a groundwater fraction consisting of recently infiltrated river water (F_{rw}) by first, assessing groundwater mixing between infiltrated river water and regional groundwater using ^4He concentrations combined with a Bayesian end-member mixing model (Popp et al., 2019) and second, inferring transient travel times of F_{rw} employing the mixing adjusted ^{222}Rn activities of F_{rw} . To this end, we continuously analyzed dissolved noble gases (^4He , ^{222}Rn) on-site during a pumping test lasting seven weeks conducted at a wellfield used for the drinking water supply of Bern, Switzerland. The obtained data set is unique in that it provides high-resolution time-series of noble gas concentrations for an end-member and the water mixture. Finally, to test our assumptions as well as to validate the tracer-based results, we compared groundwater mixing ratios obtained from the noble gas analysis with those derived from a fully coupled and calibrated numerical surface water-groundwater model of the wellfield built in *HydroGeoSphere* (HGS; Aquanty Inc., 2015).

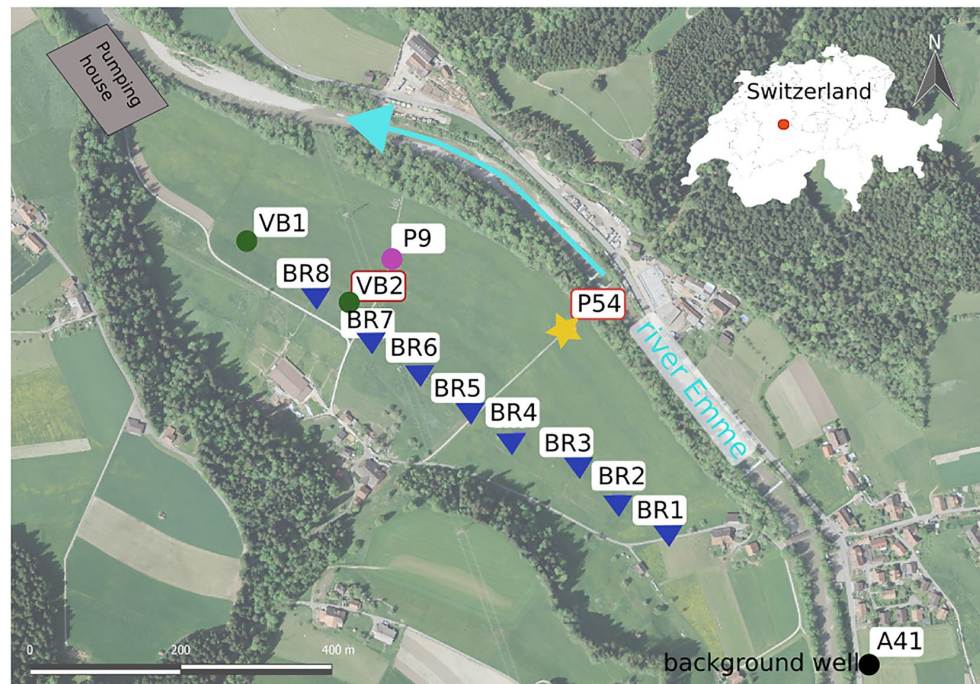


Figure 1. Study area showing the pumping well gallery (BR1–BR8 in blue), two newly installed pumping wells (VB1 and VB2 in green), the location of the pumping house as well as the piezometers P54 (orange), P9 (magenta), and A41 (black). The red dot on the Swiss map indicates the location of the study site.

2. Materials and Methods

2.1. Site Description

This study was conducted in the alluvial catchment of the river Emme, located at the northern margin of the Swiss Alps (Figure 1). We focus on the lower part of the catchment, which consists of the river Emme and the underlying alluvial aquifer. The river exhibits a coarse gravel and sand riverbed with a very dynamic discharge, which is usually highest during snowmelt from April to May (Käser & Hunkeler, 2015).

The alluvial aquifer has an average thickness of about 25 m and can extend up to 46 m. At our study location, the valley is between 200 and 400 m wide (Würsten, 1991). The upper part of the aquifer is predominantly unconfined, and is filled with coarse sandy gravel and cobbles with variable fractions of silt. The saturated hydraulic conductivity of the alluvial aquifer is relatively high (~ 500 m/d), compared to the estimated mean hydraulic conductivity of the river bed (~ 2.5 m/d) (Schilling et al., 2017). The lower part of the alluvium overlying the bedrock consists of up to 3 m thick silty material, which hydraulically disconnects the bedrock from the alluvial aquifer (Blau & Muchenberger, 1997).

A wellfield consisting of eight wells (BR1–BR8), aligned in parallel to the river Emme abstracts on average a total of 24,000 L/min of groundwater (Figure 1). Wells BR1 to BR3 pump water from 10 m depth, whereas wells BR4 to BR8 withdraw water from 15 m depth (Käser & Hunkeler, 2015).

Water source partitioning as well as groundwater travel times at this study site are particularly important in the context of current and projected environmental changes. Michel et al. (2020), for example, found that between 1999 and 2018 the annual discharge of the Emme already decreased each decade by $12\% \pm 4\%$. Additionally, Addor et al. (2014) showed that river discharge in the Emmental catchment is projected to further decrease by 25%–45% in summer (for the years 2070–2099) in response to increasing air temperatures. Changes in river discharge naturally also alter groundwater recharge patterns and are likely to impact water

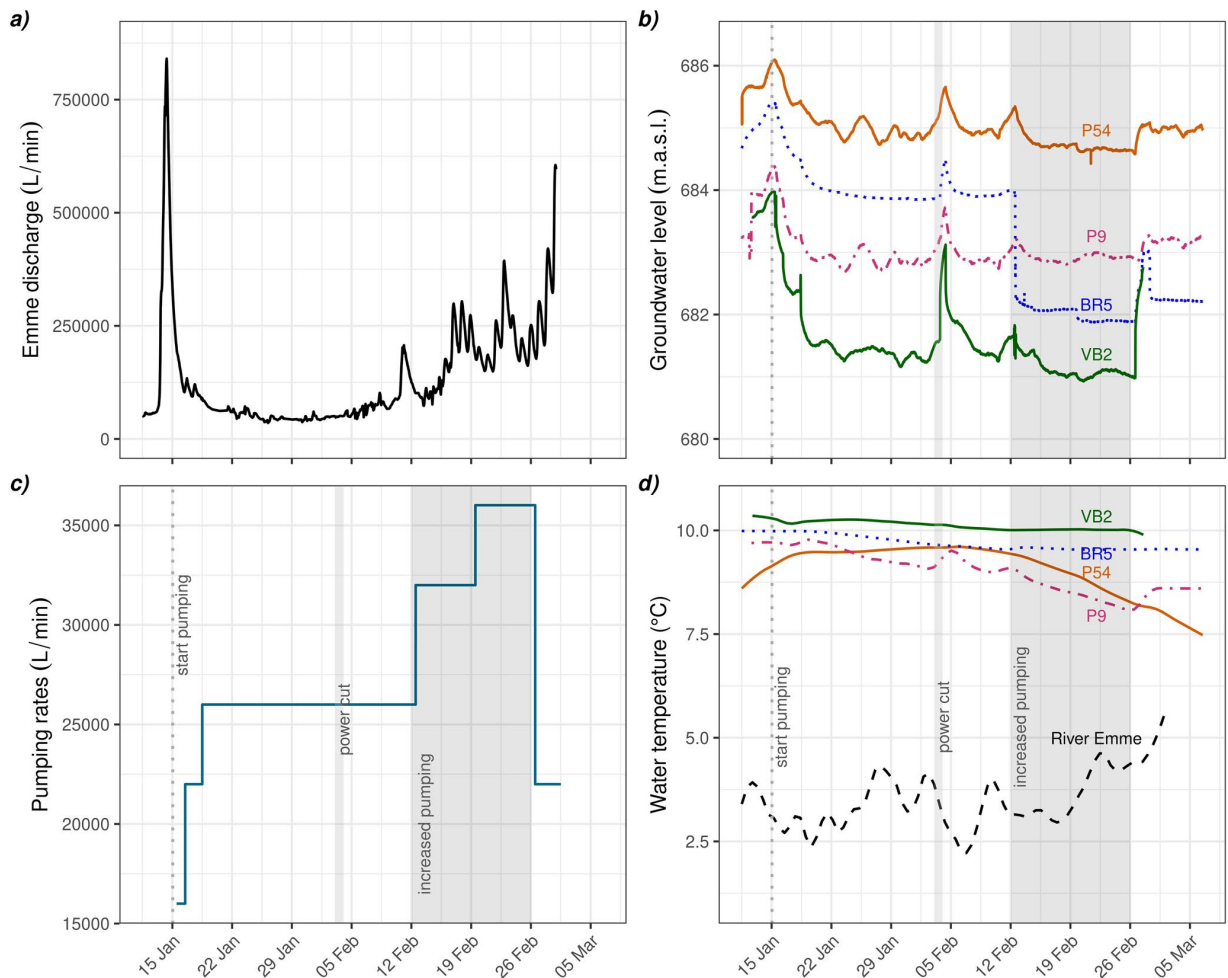


Figure 2. Prevailing conditions during the experiment: (a) the discharge of the Emme (recorded at Heidbühl-Eggwil ~8 km upstream of the study site), (b) groundwater levels of P54 (orange), VB2 (green), BR5 (dotted, blue) and P9 (dashed, magenta), (c) the total sum of groundwater pumped and (d) water temperatures of P54, VB2, BR5, P9 and the river Emme (dashed, black). The dark gray segment indicates the period of increased pumping (February 12–26). Light gray bands indicate an electric power cut occurring at the study site, which caused a shutdown of all wells from February 3, 6:30 p.m., to the following morning at 10 a.m.

quality (Hock et al., 2019). Consequently, anticipated environmental changes are expected to negatively affect the drinking water production of the study area.

2.2. Controlled Forcing of the System Through a Pumping Test

From January 15 to February 26, 2019, a pumping test was conducted, primarily using two newly installed wells (VB1 = 41 m deep and VB2 = 26 m deep, screened from 6 m depth to the bottom of the borehole) as well as already existing wells (BR4–BR8; Figure 1).

Figure 2a and 2b show the dynamics of the prevailing hydraulic conditions during the pumping test, and Figure 2d shows the water temperatures. Figure 2c depicts the three main phases of the pumping test: (1) January 15 marks the beginning of the pumping test when pumping started with 16,000 L/min equally withdrawn from VB1 and VB2, and was gradually increased to 26,000 L/min (14,000 L/min from VB1 and 12,000 L/min from VB2) until January 18; (2) from February 12 to 26, pumping was further increased to reach an overall maximum pumping rate of 36,000 L/min by employing BR4 to BR8 (11,000 L/min) in

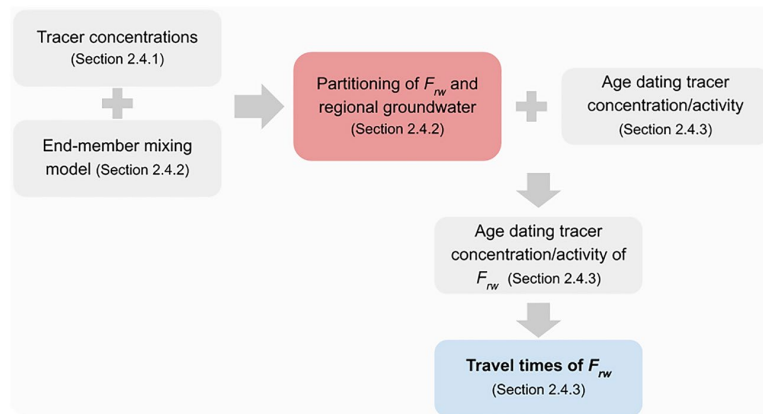


Figure 3. Framework illustrating the approach of determining travel times of a water fraction based on the previous estimation of mixing ratios using a combination of tracer data and end-member mixing modeling.

addition to VB1 (14,000 L/min) and VB2 (11,000 L/min); (3) on February 26, the pumping test was completed and the pumping regime at the drinking water production site went back to normal operating conditions (i.e., using BR1–BR8 only). Please note that there was a complete shutdown of all pumps from January 10 to 15. All pumping rate data can be found in Table S1 (Supporting Information).

2.3. Methodological Framework

Figure 3 illustrates the framework introduced by this study. The aim is to first partition the major groundwater sources (red box) to ultimately infer the travel times of the recently infiltrated water fraction (F_{rw} ; blue box). The following sections explain the used tracer data and modeling approaches.

2.4. Tracer-Based Approach

2.4.1. Theory and Dissolved (Noble) Gas Analyses

The activities of the radioactive noble gas ^{222}Rn increase non-linearly in groundwater and eventually reach a secular equilibrium after ~ 20 days (~ 5 half-lives; Krishnaswami et al., 1982). The Earth's atmosphere has virtually no source of ^{222}Rn , therefore, water in equilibrium with the atmosphere is practically devoid of radon (e.g., Cook & Herczeg, 2000; Figure 4). The absence of ^{222}Rn in air-equilibrated water and its

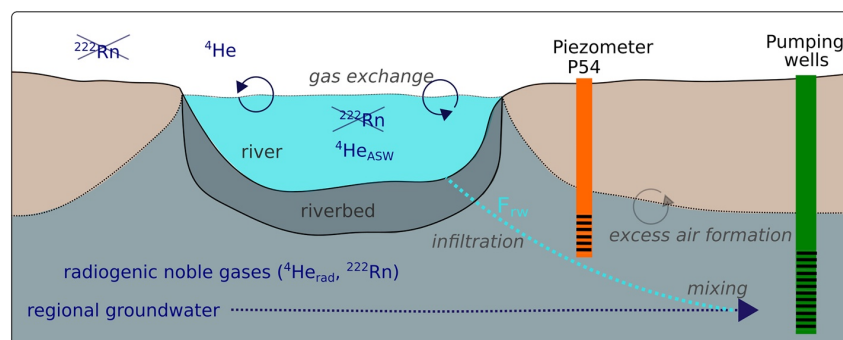


Figure 4. Conceptual model of processes (in *italics*) affecting the noble gas composition of groundwater at a losing stream reach: the ^4He concentration of the river is solely affected by gas exchange with the atmosphere; once the river infiltrates, ^4He is added due to excess air formation. The admixture of $^4\text{He}_{\text{rad}}$ -enriched older groundwater causes a further increase in ^4He concentrations. ^{222}Rn starts to accumulate once river water infiltrates. Please note that the groundwater flow paths are mostly parallel to the river (see Figure S4, SI).

short half-life render ^{222}Rn an excellent tracer to study surface water-groundwater interactions (e.g., Bourke et al., 2014; Gleeson et al., 2018; Hoehn et al., 1992).

Different to ^{222}Rn , ^4He is a stable noble gas (isotope), which is either of atmospheric or radiogenic origin (Figure 4). The concentration of ^4He dissolved in groundwater ($^4\text{He}_{\text{gw}}$) is given by

$$^4\text{He}_{\text{gw}} = ^4\text{He}_{\text{asw}} + ^4\text{He}_{\text{ea}} + ^4\text{He}_{\text{rad}} \quad (1)$$

where $^4\text{He}_{\text{asw}}$ corresponds to the helium in air-saturated water (ASW) at a given water temperature, pressure and salinity, $^4\text{He}_{\text{ea}}$ is helium originating from excess air formation (i.e., the partial dissolution of air entrapment at recharge and water table fluctuations; Heaton & Vogel, 1981) and $^4\text{He}_{\text{rad}}$ represents radiogenic helium accumulated underground (e.g., Cook & Herczeg, 2000).

Recently infiltrated river water presumably does not contain any $^4\text{He}_{\text{rad}}$ (Gardner et al., 2011). Thus, any excess in $^4\text{He}_{\text{gw}}$ (relative to atmospheric-derived ^4He , i.e., $^4\text{He}_{\text{asw}}$ and $^4\text{He}_{\text{ea}}$) indicates an admixture of older groundwater containing $^4\text{He}_{\text{rad}}$ due to longer travel times (Figure 4). In this study, we assume (i) that the observed dynamics of helium concentrations are governed by changes in excess air formation in end-member 1 (i.e., recently recharged water from the river), (ii) that the helium in end-member 2 (i.e., the regional groundwater) remains constant within the studied wellfield, and (iii) that no additional excess air is formed after the point in time when the end-members were analyzed in the piezometers P54 and A41, respectively. We consequently use the total helium concentration differences between the two end-members for the end-member mixing model, as it is done with any other conservative tracer.

The dissolved (noble) gases were analyzed at two locations: in Piezometer P54 and in the pumping house (Figure 1). P54 serves as a proxy for infiltrated river water due to its close proximity to the Emme (~50 m). There, a submersible pump (Comet ECO-PLUS_20000) abstracted ~3 L/min from a depth of 6 m (well depth is 8 m with 2 m screen at the bottom). In the pumping house, we first only analyzed water originating from the newly installed pumping well VB2. VB2 is located in about 220 m distance to the river. Water from VB2 was abstracted by two submersible pumps (8 and 10 m below ground) and parts of it were diverted to the pumping house. The remaining part of the water abstracted at VB2 and all water pumped at VB1 were discharged to the river, thus, the water pumped from VB1 (by two submersible pumps, 8 and 10 m below ground) was at no point of this experiment contributing to the water mixture analyzed in the pumping house. To increase the pumping rate, the existing Wells BR4-8 were turned on progressively on February 12 (Table S1) and all the pumped water mixture went to the pumping house. At the same time, all water from VB2 was discharged into the river. This means that from February 12 on, the water being analyzed in the pumping house was a water mixture originating from the wellfield (i.e., BR4-8; Table S1). At both locations (i.e., inside the pumping house and inside a wooden hut at P54; Figure S1), we continuously analyzed dissolved ^{222}Rn using a Rad7 instrument (DURRIDGE, 2019) as well as ^4He employing the GE-MIMS system. The two instruments were operated in parallel by allocating ~1.5 L/min of pumped water to each instrument. Sampling resolution of the Rad7 was 30 min per sample and ~10 min per sample for the GE-MIMS. For air-water equilibration, we used commercially available membrane modules (3M Liqui-Cel, 2017) for all instruments. Gas sampling and analysis were conducted in exactly the same way at both locations. More details on continuous noble gas analyses are available in Text S1.

2.4.2. Tracer-Based Mixing Ratios

As previously shown (e.g., Carrera et al., 2004; Delsman et al., 2013; Hooper, 2003; Popp et al., 2019), estimated water mixing ratios based on tracer-aided end-member mixing models can exhibit large uncertainties. Uncertainties can originate, for instance, from using tracers that are not truly conservative (e.g., Valder et al., 2012), by not identifying all end-members correctly (Carrera et al., 2004; Delsman et al., 2013) and because end-members (and their associated tracer signals) are not constant in time (e.g., Hooper et al., 1990). These uncertainties are still often neglected, preventing a meaningful analysis of model errors, which can in turn lead to an erroneous interpretation of the results.

To quantify and account for these uncertainties, we applied a Bayesian groundwater mixing approach (see Popp et al., 2019) using hourly aggregated ^4He concentrations as tracers. This approach allows to explicitly account for sampling and measurement uncertainties (Popp et al., 2019). The model in this study was

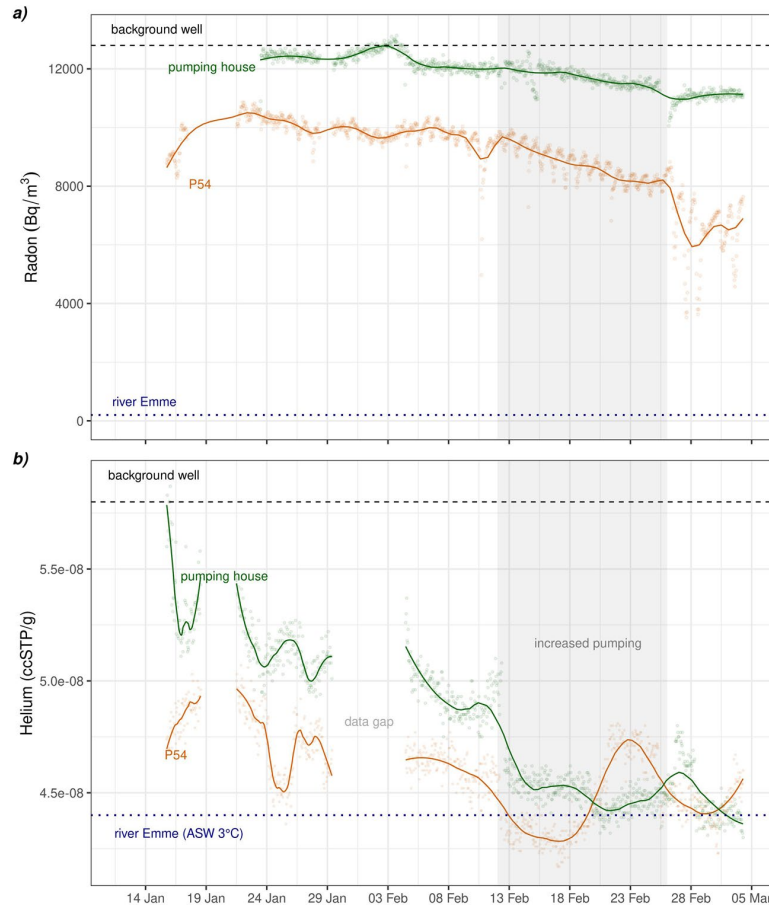


Figure 5. (a) ^{222}Rn activities and (b) ^4He concentrations continuously analyzed at P54 (orange) and in the pumping house (green); the background well (A41, black dashed line) represents regional groundwater; ASW (blue dotted line) represents the average ^4He concentration of the river water. Gray segments indicate the period of increased pumping. Note that no error bars are shown because the analytical uncertainty of both tracer methods is lower than the temporal variability seen in the data points.

simplified by excluding the possibility of unknown end-members based on a sound conceptual understanding of the area from previous studies (Käser & Hunkeler, 2015; Schilling et al., 2017; Tang et al., 2018). Accordingly, we defined two end-members. For the end-member mixing modeling approach, end-member 1 (E_1) is represented by P54, given its proximity to the river. We thereby assume that E_1 consists entirely of recently infiltrated river water, containing excess air but no $^4\text{He}_{\text{rad}}$ —an assumption that was supported by the numerical model (see Section 3.2). End-member 2 (E_2) is represented by piezometer A41 (~20 m deep; Figure 1), that previously served as background piezometer for regional groundwater by Schilling et al. (2017). There are no high-resolution tracer data available for the background well. However, following Schilling et al. (2017), time-series data seem dispensable since this piezometer was identified to hardly be affected by seasonal changes or groundwater pumping. The ^4He concentration of end-member E_2 is thus assumed to be constant over time, which is why there is no time dependency given for E_2 in Equation 2. The measured ^4He concentrations at E_1 , however, are dynamic (Figure 5). Consequently, we assume, similar to Brewer et al. (2002), that for every point in time t the following relationship holds for the water mixture $C_{\text{mix}}(t)$ observed in the pumping house:

$$C_{\text{mix}}(t) = F_{\text{rw}}(t)\tilde{C}_{E1}(t) + F_{\text{ogw}}(t)C_{E2} \quad (2)$$

where F_{rw} is the fraction of recently infiltrated river water, F_{ogw} the fraction of older, regional groundwater, C_{E_2} is the concentration of a tracer observed at end-member E_2 and $\tilde{C}_{E_1}(t)$ is a *time averaged* concentration observed at the dynamic end-member E_1 . Equation 2 is solved for F_{rw} , while F_{ogw} is per definition $1 - F_{rw}$.

Since the transit time between end-member 1 and the wellfield is unknown, we tested the sensitivity of estimated mixing ratios to potential delays, that is, the time the water/tracer needs to travel from P54 to the wellfield. To this end, we imposed different time lags (1–10 days) with one day increments on the tracer used for the mixing model, where the tracer time series was shifted for a particular time lag and the mixing ratios were calculated for the according tracer concentrations shifted in time. The 10 days represent the upper end of the possible time lag—an assumption based on artificial tracer tests (using uranine and naphthionat), which were conducted as part of the pumping experiment. The artificial tracer tests suggest groundwater flow rates between 45 and 100 m/d within the study domain. To represent the delay in flow time and dispersion, the mixing ratios are calculated with the averaged concentration

$$\tilde{C}_{E_1}(t) = \int_0^\infty \omega(\tau) C_{E_1}(t - \tau) d\tau \quad (3)$$

where $w(\tau)$ is the density function of a gamma distribution with a mean μ_{delay} and a relative standard deviation σ_{delay} , defined as 15% of μ_{delay} . We choose a gamma distribution, however, a different parametric family, for instance an inverse Gaussian distribution, would lead to the same results as long as the mode is far from zero (which is the case for how we defined the distribution). Therefore, the choice of the parametric family is negligible if the shape parameter is larger than one. As prior we used a uniform Dirichlet distribution with $\alpha = 1$.

The only constraints of our mixing modeling approach are that the mixing ratios are positive and sum up to one. Mixing ratios are estimated for every point in time independently. Deviations from Equation 2 are assumed to stem only from observational errors due to tracer-related uncertainties. These errors were modeled as normal distributions with relative standard deviations.

Employing the Bayesian mixing model, we assumed an overall uncertainty of 5% for E_1 and for each individual measurement of the analyzed water mixtures. These uncertainties are based on analytical errors ($\sim 2\%$) plus $\sim 3\%$ due to inconsistencies in sampling and analytical procedures. For E_2 , we allocated an overall uncertainty of 10% due to the strong assumptions of having steady-state conditions at this location and that A41 truly represents regional groundwater (similar to Popp et al., 2019). The aforementioned uncertainties also acknowledge the possibility of other water sources (such as snowmelt) contributing to the water mixture, which we assume to have a negligible impact on the tracer concentrations.

This approach consequently allowed us to estimate the recently infiltrated river water fraction of the groundwater mixtures analyzed in the pumping house.

2.4.3. Estimating Travel Times of F_{rw}

Having estimated F_{rw} , we were able to determine the radon activities originating from this water fraction ($Rn_{F_{rw}}$) assuming that ^{222}Rn activities of E_2 (Rn_{E_2}) equal those of the background well. We assume that the water in the background well exhibits steady-state ^{222}Rn activities due to its long residence time (Schilling et al., 2017):

$$Rn_{F_{rw}(t)} = \frac{(Rn_{\text{mix}}(t) - (1 - F_{rw}(t))Rn_{E_2})}{F_{rw}(t)} \quad (4)$$

where $Rn_{(\text{mix})}$ is the ^{222}Rn activity of the water mixture analyzed in the pumping house.

Consequently, we estimated travel times in days (d) using hourly aggregated ^{222}Rn activities (number of observations, $n = 911$) analyzed in the pumping house by means of the ^{222}Rn in-growth approach (Hoehn & Von Gunten, 1989; see Figure S2 for the in-growth curve):

$$TT(t) = \lambda^{-1} * \ln \frac{(Rn_{E_2} - Rn_{river})}{(Rn_{E_2} - Rn_{Fw}(t))} \quad (5)$$

where λ is the radioactive decay constant (0.183 day^{-1} ; Hoehn & Von Gunten, 1989) and Rn_{river} corresponds to the mean radon activity analyzed in the river Emme. Please note that the ^{222}Rn activities of P54 are not included in the calculation of the travel times. While the water of P54 represents an end-member for the ^4He concentrations, it is not an end-member for ^{222}Rn due to its short half-life.

2.5. Simulation-Based Approach

To compare and validate tracer-based mixing ratios with those from a calibrated numerical model (from here on referred to as simulation-based mixing ratios), we used a model built in HGS combined with the *Hydraulic Mixing-Cell* flow tracking tool (HMC; Partington et al., 2011) to determine water mixing throughout the model domain.

HGS is able to simulate both surface water and groundwater flow in a fully integrated way, that means, precipitation partitions into all parts of the water cycle (e.g., groundwater recharge, snow, streamflow, evapotranspiration) in a physically based manner, making it unnecessary to artificially impose these components as boundary conditions. HGS solves a modified version of the Richard's equation using the van Genuchten parametrization. This allows for the simulation of variably saturated subsurface flow, which is particularly important when simulating river-aquifer interactions (Brunner & Simmons, 2012; Schilling et al., 2017). Different to particle tracking, HMC is based on an efficient mixing cell approach (Harrington et al., 1999; Rao & Hathaway, 1989), automatically tracking all water that enters the model domain via specified boundary conditions. HMC thus provides transient mixing ratios of all water sources in every model cell at every time step, and this for marginal extra computational costs (Partington et al., 2011).

We adopted the existing model built and calibrated by Schilling et al. (2017), thus our model setup equals the description therein. Before the transient simulation of the pumping experiment, a quasi-steady-state simulation with constant forcing for 2,586 days (corresponding to the forcing observed at the beginning of the transient simulation period) was carried out, to obtain an equilibrated initial distribution of water sources for subsequent transient HMC analyses. For the transient simulations, all boundary conditions (i.e., river discharge, groundwater heads and precipitation) were updated according to corresponding values at the time of our experiment. In contrast to Schilling et al. (2017), we explicitly simulated snow accumulation and snowmelt (Jonas et al., 2009; Magnusson et al., 2014; Schilling, Park, et al., 2019), because winter conditions were prevalent during a significant part of our experiment.

3. Results

3.1. Continuously Analyzed Dissolved (Noble) Gases

Figure 5 shows the ^{222}Rn activities (a) and ^4He concentrations (b) synoptically analyzed at P54 and in the pumping house. The illustrated data were hourly aggregated (single data points) and smoothed to facilitate visualization (data line). For data smoothing, we applied local polynomial regression fitting (i.e., LOESS; Jacoby, 2000) to all data sets shown in Figures 5 and 7 to reduce noise and increase readability.

As expected, ^{222}Rn activities and ^4He concentrations are lower at P54 than the observations made in the pumping house, except for a short period in February. The ^{222}Rn activities observed in the pumping house temporarily reached the secular equilibrium (i.e., $12,500 \pm 1,300 \text{ Bq/m}^3$ observed at A41, $n = 14$). ^{222}Rn activities recorded at P54, however, have not reached the secular equilibrium. The activities obtained at P54 indicate the relative long time the river water needs to pass through the streambed, which has a low hydraulic conductivity compared to the aquifer (Schilling et al., 2017; Tang et al., 2018). ^4He concentrations observed at P54 are closer aligned to the ^4He concentrations of air-saturated water (ASW) at 3°C (reflecting the ^4He concentration of the prevalent mean Emme water temperature) than the background well.

Although both tracers (^4He and ^{222}Rn) exhibit temporal fluctuations, the overall trend shows a decrease in both tracers for the duration of our experiment. Please note that we assumed the tracer activity/concentration

for end-member 2 (i.e., the background well) to be constant over time. Also note that we did not detect any considerable ^{222}Rn activities in the river Emme during sporadic sampling (mean activity $199 \pm 139 \text{ Bq/m}^3$, $n = 13$), which indicates that the river was not gaining any relevant amounts of groundwater during the period of our experiment.

3.2. Tracer-Based and Simulation-Based Estimates of F_{rw}

Figure 6 shows the estimated fraction of recently infiltrated river water for the wellfield (i.e., water mixture analyzed in the pumping house) inferred from the tracer-based (various colors) and the simulation-based approach (dashed, black). Since F_{rw} observed in the pumping house results from a mixture of waters coming from different pumping wells, we calculated the simulated F_{rw} values (derived from the numerical model) as a weighted mean according to the relative water contribution from each well to the water mixture. The dashed black line in Figure 6 thus illustrates a weighted mean of F_{rw} equivalent to the groundwater mixture analyzed in the pumping house.

Figure 5 highlights that the assumption of time-invariant end-members does not hold for our data because the tracer concentrations observed at P54 vary within the observation period. However, Figure 6 shows no distinct differences in mixing ratios when imposing different time delays (i.e., 1–10 days), suggesting that the influence of a potential time lag on the estimated mixing ratios is negligible. Consequently, all data regarding F_{rw} correspond from here on to the estimated mixing ratios with no imposed time lag (pink data shown in Figure 6).

Generally, the tracer-based and simulation-based mixing ratios agree reasonably well within the calculated uncertainties, except for the beginning of the experiment. For the entire duration of the experiment, the tracer-based and simulation-based estimates predict an average of $67\% \pm 23\%$ and $70\% \pm 4\%$ of water originating from recently infiltrated river water, respectively. The experiment can be divided in three major phases: before, during and after the pumping was increased (Table 1 and Figure 2c). The tracer-based calculations show an increase from about $57\% \pm 25\%$ (period before the pumping increased) to a mean value of $75\% \pm 21\%$ for the time of increased pumping. After the pumping regime went back to normal operation conditions, F_{rw} first slightly dropped but then increased again. The simulated estimates of F_{rw} show a different trend: after pumping increased, estimates slightly decreased from $74\% \pm 7\%$ to $67\% \pm 3\%$. In the last phase, simulated estimates of F_{rw} slightly increased again to $73\% \pm 3\%$. Although these differences fall in the range of the estimated uncertainties, the trends of the tracer-based and simulation-based mixing ratios do not necessarily correlate (see Discussion for model limitations).

Mixing ratios simulated at P54 confirm that its water consists almost exclusively ($\sim 90\%$) of infiltrated river water. Thus, the assumption to use ^4He concentrations of P54 to characterize the ^4He concentrations of F_{rw} for the groundwater mixing model seems justified.

3.3. Travel Times of F_{rw}

Knowing the fraction of river water within the pumped groundwater, we can use the ^{222}Rn activities of F_{rw} to infer the travel times of F_{rw} to the wellfield. In accordance with the decreasing ^{222}Rn activities observed at P54 and the pumping house (Figures 5 and 7), the estimated TTs show the same decreasing trend over time. On average, the travel time from the river to the wellfield is in the range of 12 ± 3 days. With 14 ± 4 days, the period before the pumping was increased showed the highest mean travel time (Table 1). After pumping was increased, TTs generally decrease until the end of the experiment. Toward the end of February, we obtained travel times as low as 7 ± 2 days.

From the ^{222}Rn activities shown in Figure 5a, it becomes apparent that the recently recharged river water (observed in P54) has already accumulated a substantial amount of the total ^{222}Rn measured in the pumping house, which indicates that a large portion of the total travel time occurs between the stream and P54. Consequently, the travel time between P54 and the wellfield is comparatively fast. This phenomenon can be explained by the lower hydraulic conductivity of the riverbed that the infiltrating river water needs to pass first. For the remaining distance between P54 and the wellfield ($\sim 200\text{--}300 \text{ m}$), the recently recharged

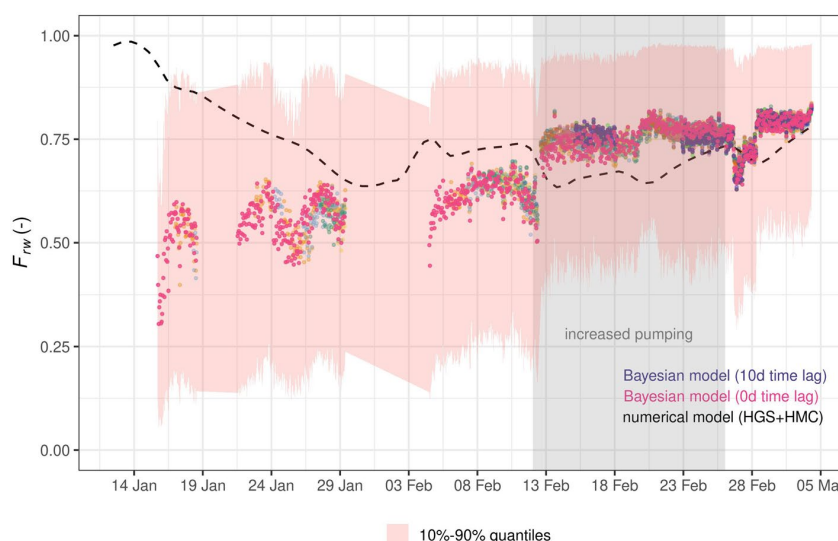


Figure 6. Estimates of F_{rw} (for the water mixture analyzed in the pumping house) from the numerical model (dashed, black line) and from the tracer-based Bayesian model with no time lag (pink), a 10 days time lag (dark-blue) and 1–9 days time lag scenarios (various colors). Error bars indicate the 10% and 90% quantiles derived from the Bayesian model (no time lag).

river water only takes a few days, which aligns well with the results of the artificial tracer test suggesting groundwater flow rates of up to 100 m/d within the aquifer.

Finally, the average travel time (12 ± 3 days; Table 1) using the mixing-corrected ^{222}Rn activities aligns well with the travel time obtained through the artificial tracer test, which revealed a travel time from the injection well (i.e., A41) to VB2 of ~seven days (Figure S3). Since the tracer was directly injected into the groundwater, the travel time between the point of injection and VB2 is expected to be lower than the TT of F_{rw} because the river water has to pass the low hydraulic conductivity zone of the riverbed before entering the aquifer.

4. Discussion

4.1. Validation of Tracer-Based and Simulation-Based Mixing Ratios

The estimated mixing ratios of the tracer-based and simulation-based approaches agree acceptably well, considering the underlying assumptions and associated uncertainties of both approaches (Figure 6). At the beginning of the pumping test, however, the simulated and tracer-based mixing ratios show considerable dissimilarities. There are also contrasting effects between the two approaches during the three different phases of the pumping test (Table 1): the simulations generally show lower estimates of F_{rw} during the increased pumping period, whereas the tracer-based estimates of F_{rw} increase steadily from the first to the third phase. These differences most likely reflect the heterogeneity (e.g., causing preferential flow paths) of the aquifer, which the numerical model does not adequately reproduce because the aquifer and the streambed are both represented by homogeneous hydraulic conductivities.

Besides comparing tracer-based and simulation-based mixing ratios, we can also compare our tracer-based results with results of Schilling et al. (2017). Using a combination of different tracers including ^{222}Rn , ^{37}Ar , $^3\text{H}/^3\text{He}$, and noble gas recharge temperatures, Schilling et al. (2017)

Table 1
Estimates of F_{rw} as Well as Travel Times During the Three Major Phases of the Pumping Test

	Increased pumping		
	Before	During	After
Tracer-based F_{rw} (%)	57 ± 25	75 ± 21	76 ± 20
Simulated F_{rw} (%)	74 ± 7	67 ± 3	73 ± 3
TT (d)	14 ± 4	12 ± 3	9 ± 2

Note. Uncertainty of the simulated F_{rw} refers to the standard deviation of the simulated mean over the respective period.

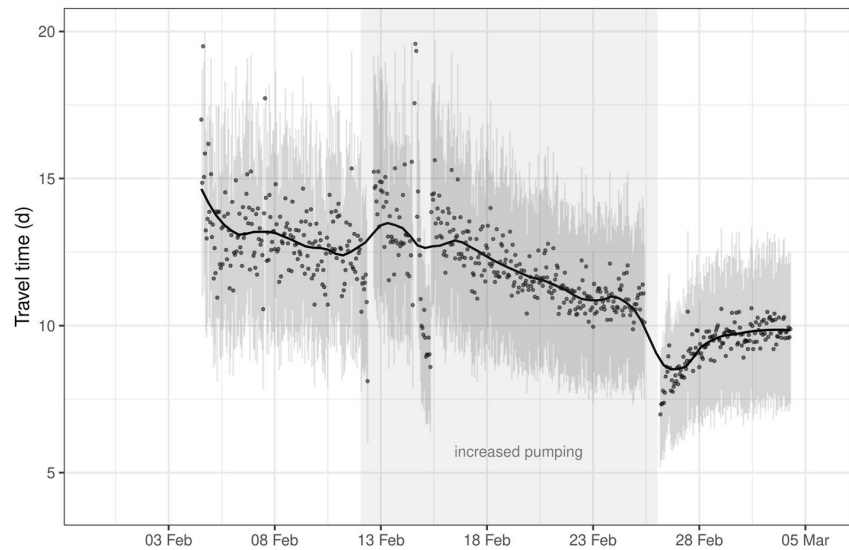


Figure 7. Estimated TTs of F_{rw} for the water mixture analyzed in the pumping house. Error bars indicate propagated uncertainty derived from the Bayesian mixing model (no time lag) and analytical uncertainties.

observed fractions of recently infiltrated river water within a similar range (between 70%–80%) at BR7. Consequently, our estimates of F_{rw} agree reasonably well with previous results.

The cause for the rise in ^4He concentrations observed in P54 from February 19 to February 23 remains unclear and is not possible to explain without another conservative tracer available. The lack of such is a major shortcoming of this study. We intended to use electrical conductivity as additional conservative tracer, however, the probe we installed in piezometer P54 was not working properly and thus yielded no usable data. Also, the water temperature measurements (Figure 2d) do not provide any additional insight on this matter.

4.2. Impact of Controlled Forcing on Groundwater Levels, Mixing Ratios, and Travel Times

Figure 2b and 2c show that groundwater pumping clearly has an effect on groundwater levels and a minor effect on water temperatures. During the increased pumping phase the tracer-based estimates show an increase in F_{rw} of about 18%, while the estimated travel times decrease about 14% in comparison to the previous phase (Table 1). These changes are most likely related to the change in the pumping regime once pumping was increased because the analyzed water originated no longer from VB2 but from a mixture of waters from different wells that are about 10 m less deep than VB2. We hypothesize that the elevated well depths, in turn, most likely influence F_{rw} .

From previous (e.g., Schilling et al., 2017; Tang et al., 2018) and our own results, we conclude that groundwater flow paths and travel times exhibit a temporal variability, which are only to some extent governed by the applied groundwater pumping rates. We explain this relatively low sensitivity against hydraulic forcing by the high hydraulic conductivity of an aquifer with a large transmissivity and thus high storage capacity: the high hydraulic conductivity enables large amounts of river water to infiltrate at various locations upstream of the catchment. An infiltration spread over a large area results in an overall large F_{rw} in the groundwater mixture, regardless of the intensity of the applied groundwater pumping. Another factor is the high hydraulic gradient (Figure 2b), which induces a high groundwater flux relative to pumping. Moreover, temporal trends of F_{rw} (e.g., increase in F_{rw} and decrease in travel times) also seem partially controlled by the rise in river discharge (thereby enhancing infiltration rates) over the duration of this experiment (Figure 2a). This assumption is also supported by the increase in mixing ratios (Figure 6) within the last days of the experiment (after pumping was shut-down), which can only be explained by an increased river discharge (Figure 2a) and not by any pumping-related activities. Consequently, river discharge appears to have a large control of mixing between river water and groundwater in the studied aquifer. We would like to

highlight though that the mixing ratios and travel times are governed by several processes (i.e., the changes in pumping rates and pumping wells and their depths as well as the river discharge). The methods we used here do not allow us to disentangle the different effects, which is, however, also beyond the purpose of this study.

4.3. Limitations of Estimated F_{rw} and Travel Times

Despite the acceptable agreement of estimated mixing ratios by two independently executed methods, this study has several limitations. Since any water sample is a mixture of waters with a distribution of travel times, any interpretation of tracer data is challenging and potentially erroneous (e.g., Jasechko, 2019; Sprenger et al., 2019). Ideally, we would have analyzed multiple age-dating tracers (e.g., ^{37}Ar , ^{35}S , and $^3\text{H}/^3\text{He}$) to capture a wider range of potential water ages. However, such tracer studies cannot be carried out at a high spatial and temporal resolution since they are typically costly and unfeasible to sample with a high temporal resolution. Also, only specialized laboratories are able to conduct such analyses. Additionally, it would have been very helpful to better constrain the mixing ratios by using a combination of conservative tracers because the tracer set size and composition can influence the estimated mixing ratios (Barthold et al., 2011; Popp et al., 2019).

We are also aware that not everyone has two portable GE-MIMS systems and two Rad7 instruments available. Another potential way of using the introduced framework would be a combination of high-resolution sampling of other, cheaper conservative tracers (e.g., electrical conductivity) and grab sampling of specialized tracers (e.g., noble gases such as ^4He or ^{37}Ar).

Moreover, we acknowledge that the possible dating range of ^{222}Rn might not capture the actual distribution of travel times of F_{rw} . As indicated by the results of this study (Figure 7) and Schilling et al. (2017), travel times temporarily exceed the reliable dating range of ^{222}Rn (i.e., 0–15 days). However, we argue that in the context of drinking water production from bank filtrate, the identification of water fractions younger than two weeks is most relevant. This is particularly true for Switzerland where, according to the water protection law (GSchV, SR 814.201), groundwater used for drinking water production must have a travel time of at least 10 days within the relevant protection zone. Thus, in terms of drinking water supply, a conservative estimate of the lower limit of travel times of recently infiltrated surface water is of the highest interest.

Lastly, we would like to acknowledge the assumption that the infiltration signal at P54 is representative of the entire reach, although the infiltrated river water observed at P54 only integrates a small fraction of the aquifer. By using the tracer signal of P54 we assume that no natural variability of the river bed and bank exists (e.g., variable riverbed thickness or hydraulic conductivity), which could potentially influence stream water infiltration pattern.

5. Conclusions and Implications

The primary goal of this study was to develop a framework (Figure 3) that enables a meaningful interpretation of a water age dating tracer by first partitioning major water sources and second interpreting the age dating tracer concentration/activity of the water fraction of interest. We applied this approach using a combination of in-situ analyzed tracer data and modeling under partially controlled forcing conditions (i.e., a groundwater pumping test). In summary, the study provides the following methodological advancements for tracer hydrology:

- Partitioning major water sources enables the interpretation of an age dating tracer (here ^{222}Rn activities) of the recently infiltrated water fraction (Figure 7)
- We explicitly account for all uncertainties related to model assumptions and tracer measurements by employing a Bayesian mixing model. This approach enables us to quantify model uncertainties, propagate these uncertainties to the estimated travel times and generally allows us to test assumptions posteriori (Figure 6)
- We demonstrate the continuous, on-site use of state-of-the-art tracer techniques to elucidate the transience of water sources and mixtures (Figure 5). Without high-resolution time-series data, the system

response to forcing (either in the form of groundwater pumping or increased river discharge) cannot be assessed properly

- Furthermore, the continuous observation of an end-member demonstrates that the common assumption of constant end-members can be inaccurate. At the same time, testing the sensitivity of the estimated mixing ratios to different imposed time lags (i.e., the delay between the time a source/end-member enters the system and the time it is observed in the mixture) showed that a time lag seems to have negligible influence on the estimated mixing ratios, at least for the studied wellfield and the available data set
- Although applied here with two specific tracers, the framework can be used with other suitable tracers (dependent on the system of interest)

Additionally, our results imply the following insights for an improved system understanding of an alluvial, pre-alpine aquifer and water resources management:

- On average, a substantial fraction ($\sim 70\%$) of abstracted groundwater originates from recently infiltrated river water (Table 1 and Figure 6)
- F_{rw} exhibits travel times in the order of two weeks but can be as low as 7 ± 2 days (Figure 7)
- Our findings (i.e., observed ^{222}Rn activities) indicate that the streambed has a major control on the travel times of infiltrating stream water (Figure 5a) causing relatively long travel times between the stream and the streambank, relative to the total estimated travel times from the stream to the wellfield
- All three previous points are highly relevant for drinking water supply systems at similar sites using bank filtrate

Overall, these findings (particularly the high fraction of F_{rw} in the abstracted groundwater and its short travel times) suggest that the system studied is vulnerable to current and anticipated environmental changes such as increasing contamination and summer droughts.

Data Availability Statement

All data and code used in this study can be found in the Supplementary Information.

Acknowledgments

The authors thank three anonymous reviewers and the associate editor for their constructive comments, which helped to improve this manuscript. The authors thank Laurent Marguet, Roberto Costa, Reto Britt, and Kay Fries for their support in the field. The authors thank the Tracerlabor Dr. Wernli and the Bau- und Verkehrsdirektion des Kantons Bern for providing the artificial tracer test data. Moreover, the authors are grateful for the fieldwork planning support from the Bau- und Verkehrsdirektion des Kantons Bern as well as for the model input data provided by the Federal Office for the Environment (BAFU), MeteoSwiss and the Canton of Bern. Andrea L. Popp and Álvaro Pardo-Álvarez gratefully acknowledge financial support for this work from the EU Framework Programme for Research and Innovation Horizon 2020 ITNs “Hypotrain” (grant no. 641939) and “Enigma” (grant no. 722028), respectively. Andrea L. Popp also acknowledges financial support from Eawag. Oliver S. Schilling and Morgan Peel gratefully acknowledge the funding provided by the Swiss National Science Foundation (grant no. P2NEP2_171985 and 200021_179017, respectively).

References

- Addor, N., Rössler, O., Köplin, N., Huss, M., Weingartner, R., & Seibert, J. (2014). Robust changes and sources of uncertainty in the projected hydrological regimes of Swiss catchments. *Water Resources Research*, 50(10), 7541–7562. <https://doi.org/10.1002/2014WR015549>
- Aquanty Inc. (2015). *HGS reference manual*. Waterloo. Retrieved from <https://static1.squarespace.com/static/54611cc8e4b0f88a2c1abc57/t/59cea33846c3c4384b8e5de1/1506714438873/hydrosphere%5Ctext%5B%5C%5F%5Duser.pdf>
- Barthel, R., & Banzhaf, S. (2016). Groundwater and surface water interaction at the regional-scale—A review with focus on regional integrated models. *Water Resources Management*, 30(1), 1–32. <https://doi.org/10.1007/s11269-015-1163-z>
- Barthold, F. K., Tyralla, C., Schneider, K., Vaché, K. B., Frede, H.-G., & Breuer, L. (2011). How many tracers do we need for end member mixing analysis (EMMA)? A sensitivity analysis. *Water Resources Research*, 47(8), 1–14. <https://doi.org/10.1029/2011WR010604>
- Beria, H., Larsen, J. R., Michelson, A., Ceperley, N. C., & Schaeffli, B. (2020). HydroMix v1.0: A new Bayesian mixing framework for attributing uncertain hydrological sources. *Geoscientific Model Development*, 13(5), 2433–2450. <https://doi.org/10.5194/gmd-13-2433-2020>
- Blau, R. V., & Muchenberger, F. (1997). *Grundlagen für Schutz und Bewirtschaftung der Grundwasser des Kantons Bern (Technical Report)*. Bern: Wasser- und Energiewirtschaftsamt des Kantons Bern, Geotechnisches Institut AG.
- Blöschl, G., Hall, J., Viglione, A., Perdigão, R. A. P., Parajka, J., Merz, B., et al. (2019). Changing climate both increases and decreases European river floods. *Nature*, 573(7772), 108–111. <https://doi.org/10.1038/s41586-019-1495-6>
- Boano, F., Harvey, J. W., Marion, A., Packman, A. I., Revelli, R., Ridolfi, L., & Wörman, A. (2014). Hyporheic flow and transport processes: Mechanisms, models, and biogeochemical implications. *Reviews of Geophysics*, 52(4), 603–679. <https://doi.org/10.1002/2012RG000417>
- Bourke, S. A., Cook, P. G., Shanafield, M., Dogramaci, S., & Clark, J. F. (2014). Characterisation of hyporheic exchange in a losing stream using radon-222. *Journal of Hydrology*, 519, 94–105. <https://doi.org/10.1016/j.jhydrol.2014.06.057>
- Brennwald, M. S., Schmidt, M., Oser, J., & Kipfer, R. (2016). A portable and autonomous mass spectrometric system for on-site environmental gas analysis. *Environmental Science & Technology*, 50, 13455. <https://doi.org/10.1021/acs.est.6b03669>
- Brewer, M. J., Soulsby, C., & Dunn, S. M. (2002). A Bayesian model for compositional data analysis. In W. Härdle, & B. Rönz (Eds.), *Comstat* (pp. 105–110). Physica-Verlag HD.
- Brunner, P., & Simmons, C. T. (2012). HydroGeoSphere: A fully integrated, physically based hydrological model. *Ground Water*, 50(2), 170–176. <https://doi.org/10.1111/j.1745-6584.2011.00882.x>
- Brunner, P., Therrien, R., Renard, P., Simmons, C. T., & Franssen, H.-J. H. (2017). Advances in understanding river-groundwater interactions. *Reviews of Geophysics*, 55(3), 818–854. <https://doi.org/10.1002/2017RG000556>
- Carrera, J., Vázquez-Suñé, E., Castillo, O., & Sánchez-Vila, X. (2004). A methodology to compute mixing ratios with uncertain end-members. *Water Resources Research*, 40(12), 1–11. <https://doi.org/10.1029/2003WR002263>
- Chatton, E., Labasque, T., de La Bernardie, J., Guühéneuf, N., Bour, O., & Aquilina, L. (2017). Field continuous measurement of dissolved gases with a cf-mims: Applications to the physics and biogeochemistry of groundwater flow. *Environmental Science & Technology*, 51(2), 846–854. <https://doi.org/10.1021/acs.est.6b03706>

- Cochand, M., Christe, P., Ornstein, P., & Hunkeler, D. (2019). Groundwater storage in high alpine catchments and its contribution to streamflow. *Water Resources Research*, 55(4), 2613–2630. <https://doi.org/10.1029/2018WR022989>
- Cook, P., & Herczeg, A. L. (2000). Environmental tracers in subsurface hydrology (53, No. 9). New York, NY: Springer Science+Business Media. <https://doi.org/10.1017/CBO9781107415324.004>
- Delsman, J. R., Essink, G. H. P. O., Beven, K. J., & Stuyfzand, P. J. (2013). Uncertainty estimation of end-member mixing using generalized likelihood uncertainty estimation (GLUE), applied in a lowland catchment. *Water Resources Research*, 49(8), 4792–4806. <https://doi.org/10.1002/wrcr.20341>
- DURRIDGE. (2019). *Rad7 electronic radon detector—user manual*. Billerica, MA: DURRIDGE Company Inc. Retrieved from <https://www.durridge.com/documentation/RAD7Manual.pdf>
- Fiddes, J., Aalstad, K., & Westermann, S. (2019). Hyper-resolution ensemble-based snow reanalysis in mountain regions using clustering. *Hydrology and Earth System Sciences*, 23(11), 4717–4736. <https://doi.org/10.5194/hess-23-4717-2019>
- Gardner, W. P., Harrington, G. A., Solomon, D. K., & Cook, P. G. (2011). Using terrigenic ⁴He to identify and quantify regional groundwater discharge to streams. *Water Resources Research*, 47(6), 1–13. <https://doi.org/10.1029/2010WR010276>
- Gleeson, T., Manning, A. H., Popp, A., Zane, M., & Clark, J. F. (2018). The suitability of using dissolved gases to determine groundwater discharge to high gradient streams. *Journal of Hydrology*, 557, 561–572. <https://doi.org/10.1016/j.jhydrol.2017.12.022>
- Harrington, G. A., Walker, G. R., Love, A. J., & Narayan, K. A. (1999). A compartmental mixing-cell approach for the quantitative assessment of groundwater dynamics in the Otway Basin, South Australia. *Journal of Hydrology*, 214(1–4), 49–63. [https://doi.org/10.1016/S0022-1694\(98\)00243-1](https://doi.org/10.1016/S0022-1694(98)00243-1)
- Hayashi, M. (2019). Alpine hydrogeology: The critical role of groundwater in sourcing the headwaters of the world. *Groundwater*. <https://doi.org/10.1111/gwat.12965>
- Heaton, T. H. E., & Vogel, J. C. (1981). “Excess air” in groundwater. *Journal of Hydrology*, 50, 201–216. [https://doi.org/10.1016/0022-1694\(81\)90070-6](https://doi.org/10.1016/0022-1694(81)90070-6)
- Herbstritt, B., Gralher, B., & Weiler, M. (2019). Continuous, near-real-time observations of water stable isotope ratios during rainfall and throughfall events. *Hydrology and Earth System Sciences*, 23(7), 3007–3019. <https://doi.org/10.5194/hess-23-3007-2019>
- Hock, R., Rasul, G., Adler, C., Cáceres, B., Gruber, S., Hirabayashi, Y., et al. (2019). Chapter 2: High mountain areas (Tech. Rep.). In H.-O. Pörtner, D. C. Roberts, V. Masson-Delmotte, P. Zhai, M. Tignor, E. Poloczanska, et al. (Eds.), *IPCC special report on the ocean and cryosphere in a changing climate*. NM.
- Hoehn, E., & Von Gunten, H. R. (1989). Radon in groundwater: A tool to assess infiltration from surface waters to aquifers. *Water Resources Research*, 25(8), 1795–1803. <https://doi.org/10.1029/WR025i008p01795>
- Hoehn, E., Von Gunten, H. R., Stauffer, F., & Dracos, T. (1992). Radon-222 as a groundwater tracer. A laboratory study. *Environmental Science & Technology*, 26(4), 734–738. <https://doi.org/10.1021/es00028a010>
- Hoffmann, R., Goderniaux, P., Jamin, P., Chatton, E., de La Bernardie, J., Labasque, T., et al. (2020). Continuous dissolved gas tracing of fracture-matrix exchanges. *Geophysical Research Letters*, 47(17), e2020GL088944. <https://doi.org/10.1029/2020GL088944>
- Holman, I. P. (2006). Climate change impacts on groundwater recharge- uncertainty, shortcomings, and the way forward? *Hydrogeology Journal*, 14(5), 637–647. <https://doi.org/10.1007/s10040-005-0467-0>
- Hooper, R. P. (2003). Diagnostic tools for mixing models of stream water chemistry. *Water Resources Research*, 39(3), 55–61. <https://doi.org/10.1029/2002WR001528>
- Hooper, R. P., Christophersen, N., & Peters, N. E. (1990). Modelling streamwater chemistry as a mixture of soilwater end-members—An application to the Panola Mountain catchment, Georgia, U.S.A. *Journal of Hydrology*, 116(1–4), 321–343. [https://doi.org/10.1016/0022-1694\(90\)90131-G](https://doi.org/10.1016/0022-1694(90)90131-G)
- Huss, M., & Hock, R. (2015). A new model for global glacier change and sea-level rise. *Frontiers of Earth Science*, 3, 1–22. <https://doi.org/10.3389/feart.2015.00054>
- Jacoby, W. G. (2000). Loess: A nonparametric, graphical tool for depicting relationships between variables. *Electoral Studies*, 19(4), 577–613. [https://doi.org/10.1016/S0261-3794\(99\)00028-1](https://doi.org/10.1016/S0261-3794(99)00028-1)
- Jasechko, S. (2019). Global isotope hydrogeology—Review. *Reviews of Geophysics*, 57(3), 835–965. <https://doi.org/10.1029/2018RG000627>
- Jonas, T., Marty, C., & Magnusson, J. (2009). Estimating the snow water equivalent from snow depth measurements in the Swiss Alps. *Journal of Hydrology*, 378(1–2), 161–167. <https://doi.org/10.1016/j.jhydrol.2009.09.021>
- Käser, D., & Hunkeler, D. (2015). Contribution of alluvial groundwater to the outflow of mountainous catchments. *Water Resources Research*, 51, 9127–9140. <https://doi.org/10.1002/2014WR016259>
- Krause, S., Boano, F., Cuthbert, M. O., Fleckenstein, J. H., & Lewandowski, J. (2014). Understanding process dynamics at aquifer-surface water interfaces: An introduction to the special section on new modeling approaches and novel experimental technologies. *Water Resources Research*, 50(2), 1847–1855. <https://doi.org/10.1002/2013WR014755>
- Krishnaswami, S., Graustein, W. C., Turekian, K. K., & Dowd, J. F. (1982). Radium, thorium and radioactive lead isotopes in groundwaters: Application to the in situ determination of adsorption-desorption rate constants and retardation factors. *Water Resources Research*, 18(6), 1663–1675. <https://doi.org/10.1029/WR018i006p01663>
- Lewandowski, J., Arnon, S., Banks, E., Batelaan, O., Betterle, A., Broecker, T., et al. (2019). Is the hyporheic zone relevant beyond the scientific community? *Water*, 11(11), 2230. <https://doi.org/10.1002/2016WR019516>
- Mächler, L., Brennwald, M. S., & Kipfer, R. (2012). Membrane inlet mass spectrometer for the quasi-continuous on-site analysis of dissolved gases in groundwater. *Environmental Science & Technology*, 46(15), 8288–8296. <https://doi.org/10.1021/es3004409>
- Magnusson, J., Gustafsson, D., Hüsler, F., & Jonas, T. (2014). Assimilation of point SWE data into a distributed snow cover model comparing two contrasting methods. *Water Resources Research*, 50(10), 7816–7835. <https://doi.org/10.1002/2014WR015302>
- McCallum, J. L., Cook, P. G., Brunner, P., & Berhane, D. (2010). Solute dynamics during bank storage flows and implications for chemical base flow separation. *Water Resources Research*, 46(7), 1–11. <https://doi.org/10.1029/2009WR008539>
- Michel, A., Brauchli, T., Lehning, M., Schaeffli, B., & Huwald, H. (2020). Stream temperature and discharge evolution in Switzerland over the last 50 years: Annual and seasonal behaviour. *Hydrology and Earth System Sciences*, 24(1), 115–142. <https://doi.org/10.5194/hess-24-115-2020>
- Mutiti, S., & Levy, J. (2010). Using temperature modeling to investigate the temporal variability of riverbed hydraulic conductivity during storm events. *Journal of Hydrology*, 388(3–4), 321–334. <https://doi.org/10.1016/j.jhydrol.2010.05.011>
- Paniconi, C., & Putti, M. (2015). Physically based modeling in catchment hydrology at 50: Survey and outlook. *Water Resources Research*, 51(9), 7090–7129. <https://doi.org/10.1002/2015WR017780>

- Partington, D., Brunner, P., Simmons, C. T., Therrien, R., Werner, A. D., Dandy, G. C., & Maier, H. R. (2011). A hydraulic mixing-cell method to quantify the groundwater component of streamflow within spatially distributed fully integrated surface water-groundwater flow models. *Environmental Modelling & Software*, 26(7), 886–898. <https://doi.org/10.1016/j.envsoft.2011.02.007>
- Partington, D., Therrien, R., Simmons, C. T., & Brunner, P. (2017). Blueprint for a coupled model of sedimentology, hydrology, and hydrogeology in streambeds. *Reviews of Geophysics*, 55(2), 287–309. <https://doi.org/10.1002/2016RG000530>
- Popp, A. L., Manning, C. C., Brennwald, M. S., & Kipfer, R. (2020). A new in situ method for tracing denitrification in riparian groundwater. *Environmental Science & Technology*, 54(3), 1562–1572. <https://doi.org/10.1021/acs.est.9b05393>
- Popp, A. L., Scheidegger, A., Moeck, C., Brennwald, M. S., & Kipfer, R. (2019). Integrating Bayesian groundwater mixing modeling with on-site helium analysis to identify unknown water sources. *Water Resources Research*, 55(12), 10602–10615. <https://doi.org/10.1029/2019WR025677>
- Rao, B. K., & Hathaway, D. L. (1989). A three-dimensional mixing cell solute transport model and its application. *Ground Water*, 27(4), 509–516. <https://doi.org/10.1111/j.1745-6584.1989.tb01971.x>
- Schilling, O. S., Cook, P. G., & Brunner, P. (2019). Beyond classical observations in hydrogeology: The advantages of including exchange flux, temperature, tracer concentration, residence time, and soil moisture observations in groundwater model calibration. *Reviews of Geophysics*, 57(1), 146–182. <https://doi.org/10.1029/2018RG000619>
- Schilling, O. S., Cook, P. G., Grierson, P. F., Dogramaci, S., & Simmons, C. T. (2020). Controls on interactions between surface water, groundwater and riverine vegetation along intermittent rivers and ephemeral streams in arid regions. *Water Resources Research*, e2020WR028429.
- Schilling, O. S., Gerber, C., Partington, D. J., Purtschert, R., Brennwald, M. S., Kipfer, R., et al. (2017). Advancing physically-based flow simulations of alluvial systems through atmospheric noble gases and the novel ^{37}Ar tracer method. *Water Resources Research*, 53(12), 10465–10490. <https://doi.org/10.1002/2017WR020754>
- Schilling, O. S., Parajuli, A., Tremblay Otis, C., Müller, T. U., Antolinez Quijano, W., Tremblay, Y., et al. (2021). Quantifying groundwater recharge dynamics and unsaturated zone processes in snow-dominated catchments via on-site dissolved gas analysis. *Water Research*, 57, e2020WR028479. <https://doi.org/10.1029/2020WR028479>
- Schilling, O. S., Park, Y.-J., Therrien, R., & Nagare, R. M. (2019). Integrated surface and subsurface hydrological modeling with snowmelt and pore water freeze thaw. *Groundwater*, 57(1), 63–74. <https://doi.org/10.1111/gwat.12841>
- Somers, L. D., McKenzie, J. M., Mark, B. G., Lagos, P., Ng, G. H. C., Wickert, A. D., et al. (2019). Groundwater buffers decreasing glacier melt in an Andean watershed but not forever. *Geophysical Research Letters*, 46(22), 13016–13026. <https://doi.org/10.1029/2019GL084730>
- Sprenger, M., Stumpp, C., Weiler, M., Aeschbach, W., Allen, S. T., Benettin, P., et al. (2019). The demographics of water: A review of water ages in the critical zone. *Reviews of Geophysics*, 57(3), 800–834. <https://doi.org/10.1029/2018RG000633>
- Stock, B. C., Jackson, A. L., Ward, E. J., Parnell, A. C., Phillips, D. L., & Semmens, B. X. (2018). Analyzing mixing systems using a new generation of Bayesian tracer mixing models. *PeerJ*, 6, 1–27. <https://doi.org/10.7717/peerj.5096>
- Tang, Q., Schilling, O. S., Kurtz, W., Brunner, P., Vereecken, H., & Hendricks Franssen, H. J. (2018). Simulating flood induced riverbed transience using unmanned aerial vehicles, physically based hydrological modeling, and the ensemble Kalman filter. *Water Resources Research*, 54(11), 9342–9363. <https://doi.org/10.1029/2018WR023067>
- Valder, J. F., Long, A. J., Davis, A. D., & Kenner, S. J. (2012). Multivariate statistical approach to estimate mixing proportions for unknown end members. *Journal of Hydrology*, 460–461, 65–76. <https://doi.org/10.1016/j.jhydrol.2012.06.037>
- Vautier, C., Abhervé, R., Labasque, T., Laverman, A. M., Guillou, A., Chatton, E., et al. (2020). Mapping gas exchanges in headwater streams with membrane inlet mass spectrometry. *Journal of Hydrology*, 581, 124398. <https://doi.org/10.1016/j.jhydrol.2019.124398>. Retrieved from <https://linkinghub.elsevier.com/retrieve/pii/S0022169419311333>
- Von Freyberg, J., Studer, B., & Kirchner, J. W. (2017). A lab in the field: High-frequency analysis of water quality and stable isotopes in stream water and precipitation. *Hydrology and Earth System Sciences*, 21(3), 1721–1739. <https://doi.org/10.5194/hess-21-1721-2017>
- Würsten, M. (1991). *GWB-Hydrogeologische untersuchungen aeschau: Schlussbericht (Technical Report)*. Zurich: Geotechnisches Institut.
- 3M Liqui-Cel. (2017). *A high level of consistency and control*. Germany: Wuppertal. Retrieved from <http://multimedia.3m.com/mws/media/14124850/3m-liqui-cel-membrane-contactors-liquid-degasgasc-1096-pdf>

7.3 ^{37}Ar as an indicator of SW-GW interactions

^{37}Ar was punctually sampled at the pumping well VB2, in the background well A41, as well as in four other piezometers: P51, P52, RB1, and P48 (orange dots in Figure 7.2). The sampling campaign took place between the 31st of January 2019 and the 19th of March 2019. The ^{37}Ar data and their sampling depth are compiled in Table 7.1.

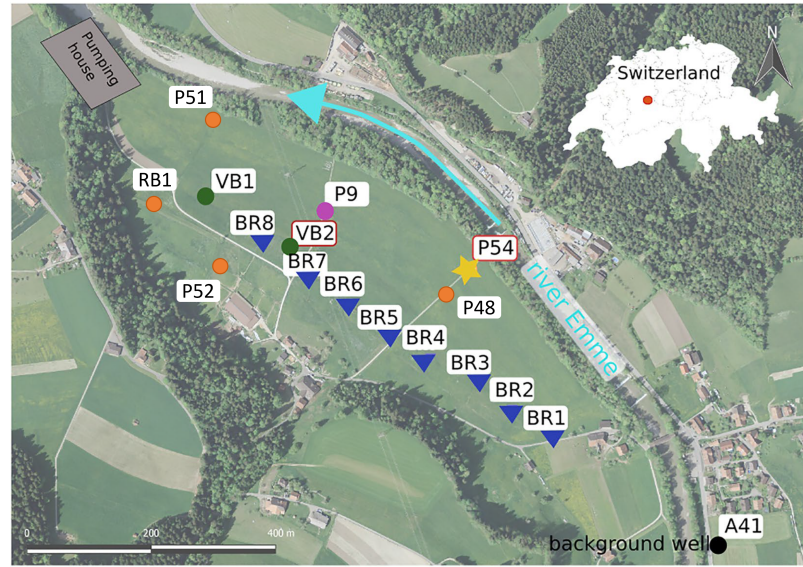


Figure 7.2: Study area: the pumping well gallery (BR1-BR8 in blue), two newly installed pumping wells (VB1 and VB2 in green), the location of the pumping house, as well as the piezometers P54 (yellow), P9 (purple), the 4 additional piezometers sampled for ^{37}Ar (P51, P52, RB1, and P48; orange dots) and the background well A41 (black) [Figure modifier from Popp et al. (2021)]

7.3.1 Background secular equilibrium profile

The background well (A41) is composed of four piezometers at depths between 7 and 22.5 m which are nested together. A depth profile was fitted to the activities sampled at each depth (dashed line in Figure 7.3). In the frame of the Schilling et al. (2017) study, A41 was already sampled in 2015. The almost perfect agreement between these data points sampled four years apart, indicates that the ^{37}Ar activities are in equilibrium (Figure 7.3).

When the piezometers P54 and P52 were drilled, rock samples were conserved to measure their elemental chemical composition, which is compiled in Table 7.2. Assuming a homogeneous vertical chemical composition, the ^{37}Ar production rate profile was calculated considering all production channels discussed in Chapter 3 (Figure 7.4). These two production profiles were then averaged, and implemented in

Table 7.1: ^{37}Ar sampling date and activities measured in the frame of the Emmental project. z is the average sampling depth; the error on z is the vertical extent of the filter. *The values sampled in 2015 in the background well (A41) are taken from Schilling et al. (2017)

Well	Sampling date	Depth z [m]			$^{37}\text{Ar} \times 10^{-3}$ [mBq L $^{-1}$]		
P51	08.01.2019	5	\pm	3	2.30	\pm	0.19
P48	08.01.2019	7	\pm	3	2.78	\pm	0.35
RB1	09.01.2019	20	\pm	18	2.08	\pm	0.16
P52	09.01.2019	7	\pm	3	1.78	\pm	0.27
VB2	17.01.2019	16	\pm	10	1.69	\pm	0.24
P48	23.01.2019	7	\pm	3	2.47	\pm	0.26
RB1	23.01.2019	20	\pm	18	2.45	\pm	0.28
P52	23.01.2019	7	\pm	3	1.87	\pm	0.42
VB2	31.01.2019	16	\pm	10	0.88	\pm	0.12
VB2	12.02.2019	16	\pm	10	1.83	\pm	0.25
P48	14.02.2019	7	\pm	3	2.91	\pm	0.29
RB1	14.02.2019	20	\pm	18	2.35	\pm	0.25
P52	14.02.2019	7	\pm	3	1.86	\pm	0.33
VB2	21.02.2019	16	\pm	10	2.16	\pm	0.28
RB1	04.03.2019	20	\pm	18	2.08	\pm	0.29
P52	04.03.2019	7	\pm	3	0.98	\pm	0.18
P48	05.03.2019	7	\pm	3	3.10	\pm	0.33
A41	19.03.2019	23	\pm	1	1.35	\pm	0.20
A41	19.03.2019	17	\pm	1	1.39	\pm	0.24
A41	19.03.2019	13	\pm	1	1.73	\pm	0.24
A41*	2015	23	\pm	1	1.28	\pm	0.14
A41*	2015	17	\pm	1	1.45	\pm	0.15
A41*	2015	13	\pm	1	2.23	\pm	0.24
A41*	2015	7	\pm	1	2.95	\pm	0.31

the HydroGeoSphere numerical model in order to simulate the ^{37}Ar secular equilibrium in a fully saturated unconfined aquifer (i.e. similar to Scenario A in Chapter 6). The flow parameters were chosen to resemble the local conditions in Emmental: permeability $K = 1 \times 10^{-4} \text{m s}^{-1}$, porosity $\phi = 20 \%$, and recharge rate $R = 240 \text{mm yr}^{-1}$. The production-advection-dispersion equation was solved for ^{37}Ar assuming a longitudinal, resp. transversal dispersivity of $D_l = 1.5 \text{m}$ and $D_t = 0.5 \text{m}$, and an emanation of $\varepsilon_{37} = 1 \%$. The model was run for 100 years, allowing for sufficient time for ^{37}Ar to reach secular equilibrium (solid line in Figure 7.3). Note that this model does not consider any infiltration of river water.

The fitted and simulated background profiles agree reasonably well at depths below 30 m (Figure 7.3), demonstrating that the activities observed can be reproduced with the calculated production rates and realistic emanation, transport, and flow parameters. In addition, activities measured at the piezometer RB1, which is located

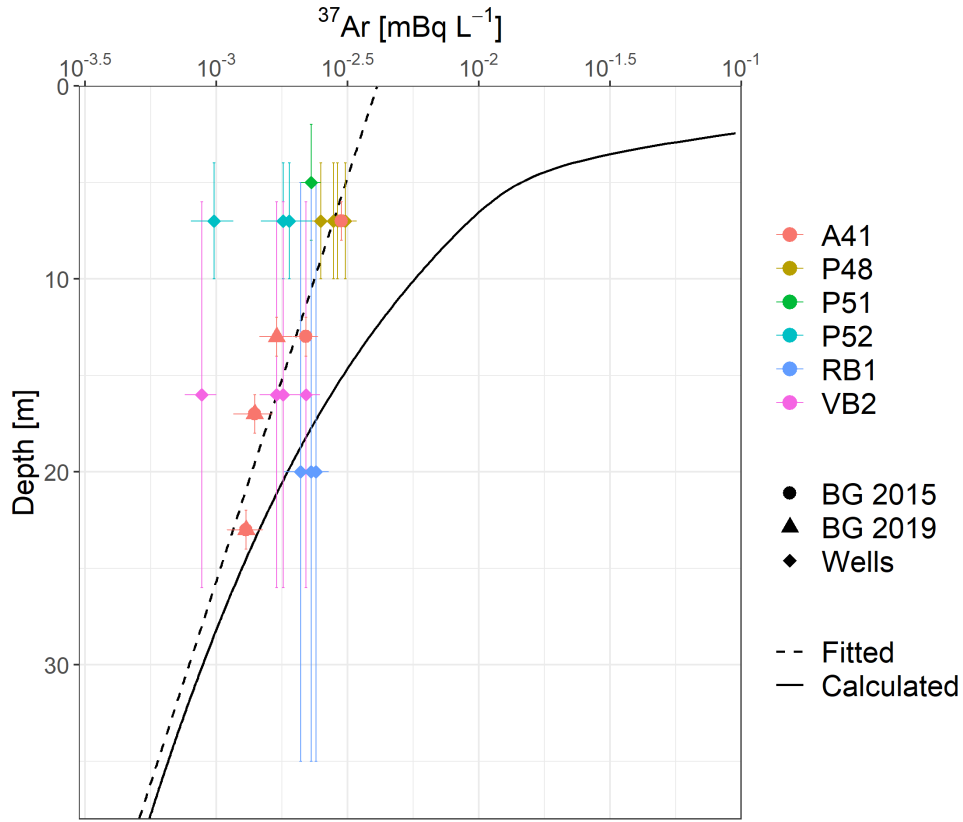


Figure 7.3: ^{37}Ar activities in the lower Emme catchment. The screened filter intervals are indicated by the vertical error bars. The Background piezometer (BG, A41) was sampled in 2015 [orange rounds, from Schilling et al. (2017)] and in 2019 [orange triangles, current study]. The dashed line is the exponential least squares regression model fitted to the BG data point. The solid line is the secular equilibrium simulated with HGS for a fully saturated unconfined aquifer using the elemental rock composition compiled in Table 7.2 and assuming $\varepsilon_{37} = 1\%$, $D_l = 1.5\text{ m}$, $D_t = 0.5\text{ m}$, $\phi = 20\%$, $K = 1 \times 10^{-4}\text{ m s}^{-1}$

the farthest away from the river, are in good agreement with the secular equilibrium simulated (assuming an equal contribution of all depths within the filter extend). For these reasons, in the following, we assume that the simulated secular equilibrium profile is accurately representing the activities in the situation where the Emmmental aquifer would solely be recharged by precipitation.

7.3.2 Infiltrating river water fraction and activity concentration

Measured activity concentrations (C_{meas}) that are lower than the local secular equilibrium (C_{eq}) are caused by the admixture of river water with a residence time shorter than the lifetime of ^{37}Ar . The degree of depletion depends on the fraction (F_{rw}), and the activity concentration (C_{rw}) in the river water (Eq. 7.1). The latter is function of the infiltration and percolation times (t_i , resp. t_p) and depths (z_i , resp. z_p).

$$C_{meas}(z) = (1 - F_{rw}) \cdot C_{eq} + F_{rw} \cdot C_{rw}(z_i, z_p, t_i, t_p) \quad (7.1)$$

Table 7.2: Elemental weight fraction distribution for the rocks from the P54, and P52 core samples, from the Emmental field area.

Element i	P52	P54
C	2.97×10^{-2}	3.76×10^{-2}
O	4.21×10^{-1}	3.97×10^{-1}
F	3.30×10^{-4}	3.30×10^{-4}
Na	6.07×10^{-3}	5.55×10^{-3}
Mg	4.17×10^{-3}	5.16×10^{-3}
Al	2.60×10^{-2}	2.53×10^{-2}
Si	3.04×10^{-1}	2.75×10^{-1}
K	8.37×10^{-3}	8.36×10^{-3}
Ca	9.66×10^{-2}	1.19×10^{-1}
Ti	1.22×10^{-3}	1.18×10^{-3}
Fe	1.32×10^{-2}	1.30×10^{-2}
Th	3.93×10^{-6}	3.79×10^{-8}
U	1.24×10^{-6}	1.26×10^{-8}

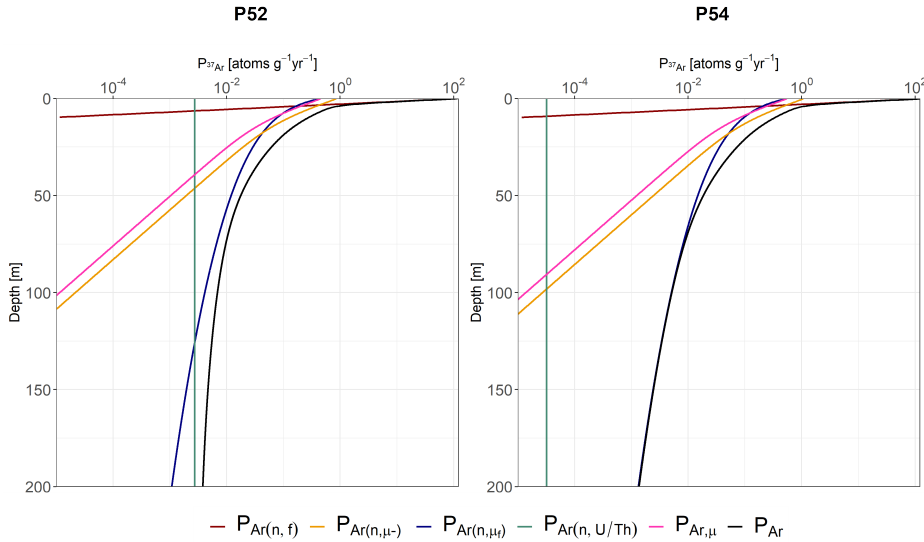


Figure 7.4: ^{37}Ar production rate in the rock composing the piezometers P54 and P52 from the Emmental field area.

A large proportion of the travel time for the river water occurs when the water passes the low-conductivity zone of the riverbed as indicated by the ^{222}Rn activities close to equilibrium at P54 [see Section 3.3 in Popp et al. (2021)]. Since ^{37}Ar production is highly dependent on the depth z , we need to distinguish between two components for the C_{rw} : (i) the activity C_i that builds up during the infiltration time t_i in the riverbed at the shallow depth z_i and (ii) the activity C_p that accumulates during the percolation time t_p at the depth z_p (Eq. 7.2, Figure 7.5). C_i is subject to radioactive decay during the percolation. We only consider the horizontal water flow time (i.e. fast vertical flow from the infiltration depth z_i to the percolation depth $z = z_p$).

The percolation time is defined by the horizontal distance to the river, and the aquifer groundwater velocity $t_p = d_{rw}/v_{aq}$.

$$\begin{aligned} C_{rw} &= C_i + C_p \\ &= \frac{P(z_i)}{\lambda} \cdot (1 - \exp(-\lambda \cdot t_i)) \cdot \exp(-\lambda \cdot t_p) \\ &\quad + \frac{P(z_p)}{\lambda} \cdot (1 - \exp(-\lambda \cdot t_p)) \end{aligned} \quad (7.2)$$

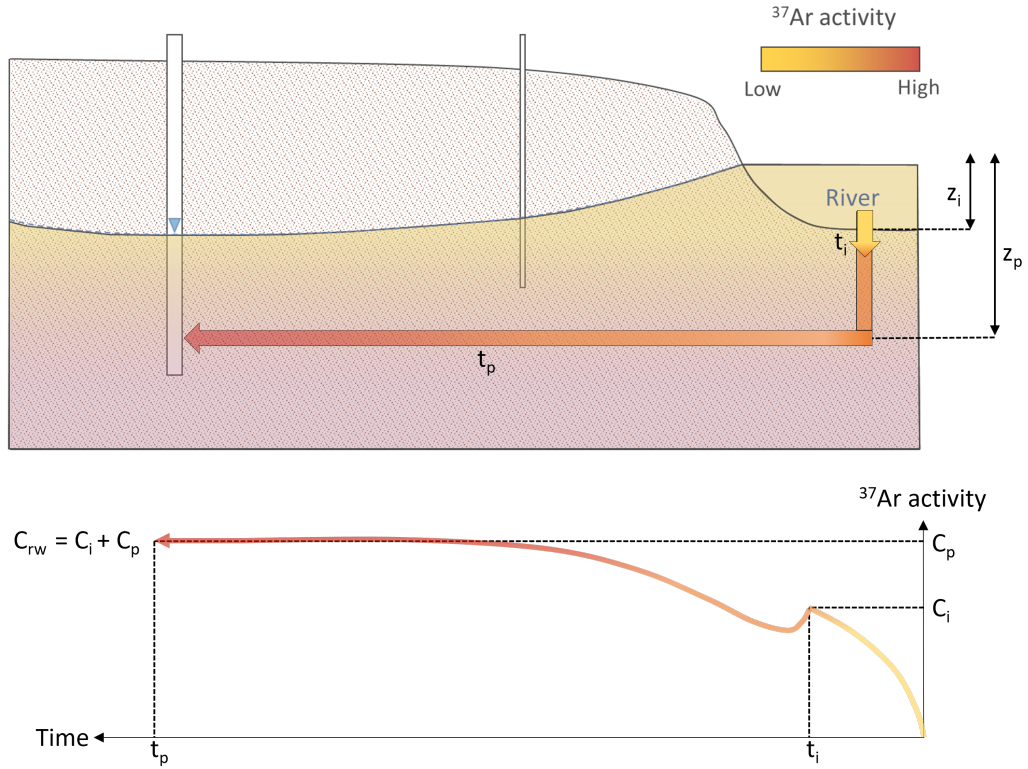


Figure 7.5: Illustration of the building up from the ^{37}Ar activity concentration in the river water C_{rw} . C_i accumulates during the infiltration time t_i at the depth z_i . This activity partially decays during the percolation time t_i . In the same time, ^{37}Ar is produced as function of the percolation depth z_p and time t_p .

The groundwater flow rate v_{aq} was concluded to be in the order of $100 - 150 \text{ m d}^{-1}$ by an artificial tracer test (Popp et al., 2021). Using this value, and assuming a total distance in the flow direction of $\sim 500 \text{ m}$ between the river and VB2 leads to a percolation time of $t_p = 3 - 5$ days. Considering the average total travel time $t_t = 12 - 14$ days concluded from ^{222}Rn activities, leads to an infiltration time $t_i = t_t - t_p$ of ≈ 9 days. The infiltration time is assumed to be the same along the river, whose bottom is situated at $z_i = 2 \text{ m}$. Therefore, the activity produced during the infiltration through the riverbed is $C_i = 4.7 \times 10^{-3} \text{ mBq L}^{-1}$.

Using Eq. 7.1, with C_{rw} from Eq. 7.2 allows for the calculation of the C_{rw} at each depth in the background piezometer A41 :

$$F_{rw}(z) = \frac{C_{meas}(z) - C_{eq}(z)}{C_{rw}(z_p, t_i) - C_{eq}(z)} \quad (7.3)$$

7.3.2.1 Background piezometer A41

At depths between 0 - 30 m, the activity concentrations sampled in the background well are depleted in comparison to the simulated secular equilibrium profile (Figure 7.3 : dashed vs. solid lines). A constant infiltration of fresh river water could be responsible for this dilution of the activity concentrations. The percolation time from the river to A41 is ~ 0.3 days ($d_{rw} = 30$ m), which is negligible for ^{37}Ar production ($C_p = 0$). Therefore, the concentration from the river water infiltration depends solely on the riverbed infiltration process ($C_{rw} = C_i$). Figure 7.6 shows the calculated F_{rw} as a function of depth z in A41. F_{rw} decreases with depth from 43 % at 7 m, up to 23 % at 22 m.

Previous conclusions from Schilling et al. (2017) and Popp et al. (2021) pointed out that the A41 well is not influenced by any seasonal changes and/or the pumping facilities. The concept of a depth-dependent F_{rw} which would be constant over time is not entirely in contraction with these conclusions. A time-serie measurement of ^4He concentrations would be the most appropriate tool to clarify the potential freshwater infiltration patterns in the A41 well.

7.3.3 Effect of the variation of the forcing parameters on ^{37}Ar activities

The detailed steps of the pumping experiment are described in Section 2.2 of Popp et al. (2021). The influence of the changes in the forcing parameters of the system on ^{37}Ar activities is illustrated in Figure 7.7.

7.3.3.1 Monitoring piezometers P48- P52 - RB1

The activities measured in P48 and P52 are not significantly affected by the increased pumping. P48 is expected to have similar behavior to P54 because of their geographical proximity (Figure 7.2). In P54, the fraction of river water was concluded to be constant throughout the experiment ($F_{rw} = 90$ %). The diminution of relative travel times related to the increase of pumping rates was concluded to be ~ 3 days (deduced from ^{222}Rn activities). This timescale is too short to be depicted by a variation of ^{37}Ar activities. P52 is located on the opposite side of the pumping well than the river. Therefore, no variation of the F_{rw} is expected in this piezometer. The decrease in the

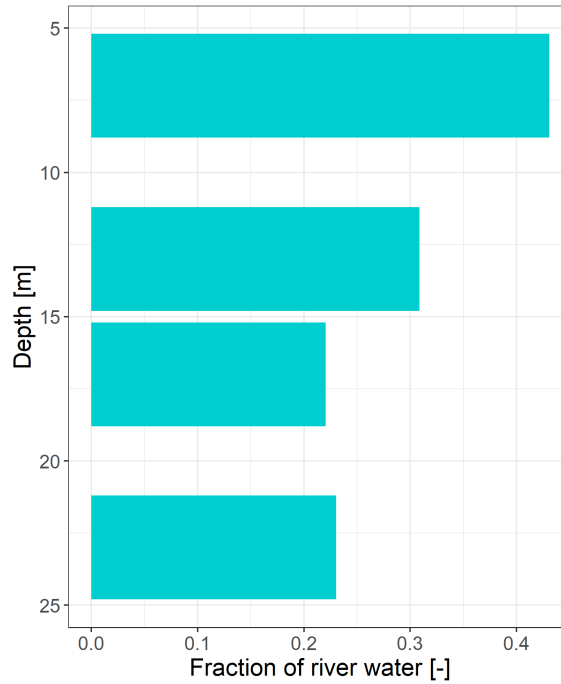


Figure 7.6: Fraction of river water F_{rw} calculated as a function of depth z for the background well.

activities after the pumping experiment might be linked with a complete change in the flow directions that would drain water from a different origin (possibly the hill on the southeastern side). In RB1, the increased pumping resulted in a slight increase of the ^{37}Ar activities, which may be attributed to the preferential drainage of shallower water.

7.3.3.2 Pumping well VB2

In VB2, a significant decrease of the ^{37}Ar activities is observed during the first phase of the increased pumping experiment. When the pump rates are further increased, the ^{37}Ar activities increase again. This pattern might be associated with transient conditions in the catchment before the establishment of a new equilibrium. Note that the conclusions drawn for the water mixture analyzed in the pumping house in Popp et al. (2021) are valid for VB2 until 12/02/2019, since at this point the mixture in the pumping house water incorporated water from the shallower BR4-8 wells, whereas ^{37}Ar was sampled directly at the VB2 wellhead. The decrease of ^{37}Ar activities could thereby be linked with the changes of F_{rw} (from 57 % to 75 %).

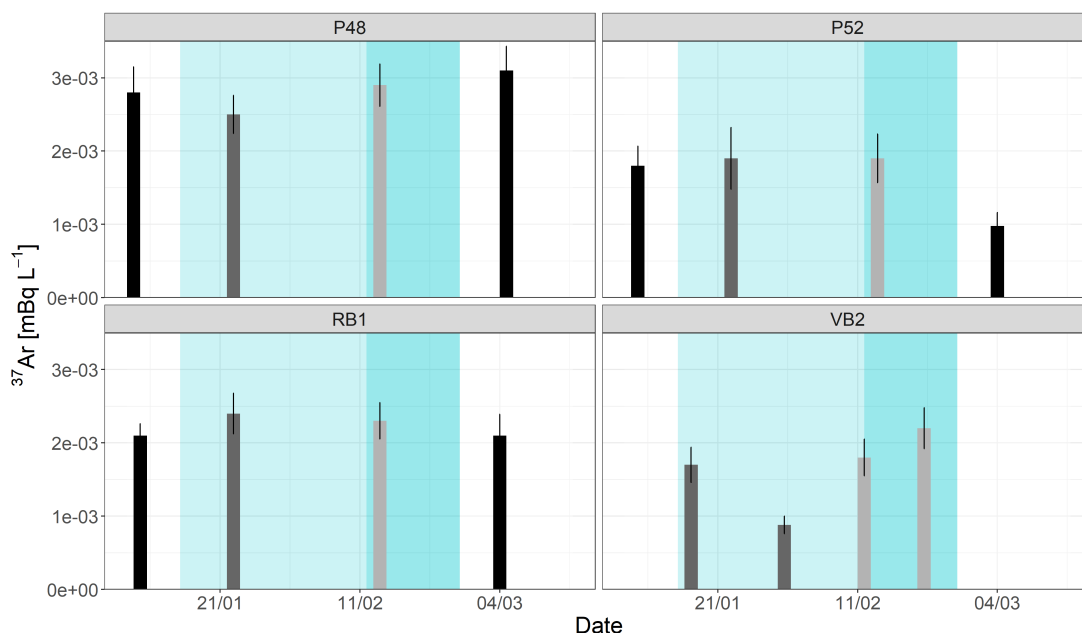


Figure 7.7: ^{37}Ar activities in the monitoring piezometers and pumping well. The blue area represents the increased pumping experiment; Light blue : 2600 min^{-1} pumped in VB1 and VB2; Dark blue : increased pumping up to 3600 min^{-1} with BR4-8.

7.4 Conclusions and outlooks

The strong and very fast coupling between the river water and the groundwater, which is exploited for domestic uses, is exhibited to be more important than previously thought. The important fraction of very young river water emphasizes the vulnerability of the water resource in alluvial aquifers, especially if they are located in areas where Climate Change is projected to profoundly impact the recharge patterns. The important fraction (up to 45 %) of river water in the background well is an indication that a substantial part of the watershed is dominated by surface water.

The combined and continuous monitoring of ^4He and ^{222}Rn demonstrated to be an appropriate tool to untangle transient mixing ratios and travel times in these dynamical conditions. The whole method relies on the different timescale to which the tracers are sensitive: radiogenic ^4He accumulates over decades to centuries, whereas ^{222}Rn is limited to applications ranging from days up to a few weeks. With this regard, ^{37}Ar occupies an intermediate situation and has the advantage of providing integrated-depth information that can be exploited to assess the percolation patterns.

In the frame of this case study, the high permeability of the aquifer and the relatively small area investigated resulted in low sensitivity of ^{37}Ar against hydraulic forcing. The relative variations of travel times are too small to be captured by changes in ^{37}Ar activity concentrations. However, potential applications for ^{37}Ar may be undisclosed due to the remaining unknowns about the flow paths and the origin of the water. In the future, an extensive modeling effort is foreseen with the properly calibrated HGS model used in Schilling et al. (2017) and Popp et al. (2021). Implementing the ^{37}Ar production rate functions, following the methods described in Chapter 6, will likely open new perspectives for the application of cosmogenically produced underground radionuclides for SW-GW interaction studies.

References

- Biaggi, D., Strasser, C., Backman, N., Cholet, N., and Abrecht, J. (2004). Hydrogeologie Seeland Stand 2004.
- Boano, F., Harvey, J. W., Marion, A., Packman, A. I., Revelli, R., Ridolfi, L., and Wörman, A. (2014). Hyporheic flow and transport processes: Mechanisms, models, and biogeochemical implications. *Reviews of Geophysics*, 52(4):603–679. _eprint: <https://onlinelibrary.wiley.com/doi/pdf/10.1002/2012RG000417>.
- Cecil, L. D. and Green, J. R. (2000). Radon-222. In Cook, P. G. and Herczeg, A. L., editors, *Environmental Tracers in Subsurface Hydrology*, pages 175–194. Springer US, Boston, MA.
- Delottier, H., Peel, M., Musy, S., Schilling, O., Purtschert, R., and Brunner, P. (2022). Explicit simulation of environmental gas tracers with integrated surface and subsurface hydrological models. *Frontiers in Water*, 4.
- Gerber, C. (2017). *Groundwater dating with noble gases - from groundwater-surface water interaction and contaminant transport to paleohydrogeology*. PhD thesis, Universität Bern, Bern.
- Harvey, J. and Gooseff, M. (2015). River corridor science: Hydrologic exchange and ecological consequences from bedforms to basins. *Water Resources Research*, 51(9):6893–6922. _eprint: <https://onlinelibrary.wiley.com/doi/pdf/10.1002/2015WR017617>.
- Hoehn, E., Von Gunten, H. R., Stauffer, F., and Dracos, T. (1992). Radon-222 as a groundwater tracer. A laboratory study. *Environmental Science & Technology*, 26(4):734–738.
- Holman, I. P. (2006). Climate change impacts on groundwater recharge- uncertainty, shortcomings, and the way forward? *Hydrogeology Journal*, 14(5):637–647.
- IPCC (2001). *Climate change 2001: impacts, adaptation, and vulnerability: contribution of Working Group II to the third assessment report of the Intergovernmental Panel on Climate Change*. Cambridge University Press, Cambridge, UK ; New York.
- Krause, S., Boano, F., Cuthbert, M. O., Fleckenstein, J. H., and Lewandowski, J. (2014). Understanding process dynamics at aquifer-surface water interfaces: An introduction to the special section on new modeling approaches and novel experimental technologies. *Water Resources Research*, 50(2):1847–1855. _eprint: <https://onlinelibrary.wiley.com/doi/pdf/10.1002/2013WR014755>.
- Käser, D. and Hunkeler, D. (2016). Contribution of alluvial groundwater to the outflow of mountainous catchments. *Water Resources Research*, 52(2):680–697.
- Musy, S., Casolaro, P., Dellepiane, G., Berger, A., Braccini, S., and Purtschert, R. (2022). Quantification of ^{37}Ar emanation fractions from irradiated natural rock samples and field applications. *Journal of Environmental Radioactivity*, 251-252:106966.
- Peel, M., Kipfer, R., Hunkeler, D., and Brunner, P. (2022). Variable ^{222}Rn emanation rates in an alluvial aquifer: Limits on using ^{222}Rn as a tracer of surface water – Groundwater interactions. *Chemical Geology*, 599:120829.
- Popp, A. L., Pardo-Álvarez, , Schilling, O. S., Scheidegger, A., Musy, S., Peel, M., Brunner, P., Purtschert, R., Hunkeler, D., and Kipfer, R. (2021). A Framework for Untangling Transient Groundwater Mixing and Travel Times. *Water Resources Research*, 57(4):e2020WR028362. _eprint: <https://onlinelibrary.wiley.com/doi/pdf/10.1029/2020WR028362>.

- Schilling, O. S., Gerber, C., Partington, D. J., Purtschert, R., Brennwald, M. S., Kipfer, R., Hunkeler, D., and Brunner, P. (2017). Advancing Physically-Based Flow Simulations of Alluvial Systems Through Atmospheric Noble Gases and the Novel Argon-37 Tracer Method: Integrating tracers with models. *Water Resources Research*, 53(12).
- Solomon, D. K., Hunt, A., and Poreda, R. J. (1996). Source of radiogenic helium 4 in shallow aquifers: Implications for dating young groundwater. *Water Resources Research*, 32(6):1805–1813.
- Torgersen, T. and Stute, M. (2013). Helium (and other noble gases) as a tool for understanding long timescale groundwater transport. In *Isotope methods for dating old groundwater*, pages 179–216. International Atomic Energy Agency, Vienna.
- Viviroli, D. and Weingartner, R. (2004). The hydrological significance of mountains: from regional to global scale. *Hydrology and Earth System Sciences*, 8(6):1017–1030. Publisher: Copernicus GmbH.
- Vogt, T., Hoehn, E., Schneider, P., Freund, A., Schirmer, M., and Cirpka, O. A. (2010). Fluctuations of electrical conductivity as a natural tracer for bank filtration in a losing stream. *Advances in Water Resources*, 33(11):1296–1308.

Chapter 8

Conclusions : lessons learned and outlooks about ^{39}Ar and ^{37}Ar underground production

The research about ^{39}Ar and ^{37}Ar underground production processes conducted in the frame of this thesis shed light on the importance and consequences of these processes in the context of groundwater dating applications. At shallow depths (up to a few meters), the radioargon production rate is undoubtedly dominated by the reactions with neutrons from the hadronic component of cosmic rays regardless of the rock composition. Conversely, interactions with neutrons from the natural rock radioactivity prevail at great depth (from 80 - 200 m). The importance of muon-induced processes in the intermediate depth range was highlighted for the first time in the framework of this research. Muon-induced processes include slow negative muon capture reactions and interactions with muon-induced neutrons, which originate either from the capture process or from fast-muon interactions. In the literature, substantial uncertainties remain about muon-induced neutrons and, more specifically, about the yield and energy spectra of neutrons arising from fast-muon interactions. It is, however, commonly accepted that their energy spans up to values in the GeV range, making them the major contributor to radioargon production at intermediate depths. Our calculations are based on the most recent modeled values for conditions as close to the natural aquifer situation as possible. The overall uncertainties were estimated between 30 - 75 % with Monte Carlo iterations, taking unsure values into account transparently. Given these relatively large uncertainties, our calculations should be regarded as robust estimates of the orders of magnitude of ^{39}Ar and ^{37}Ar production rates underground. More simulations of muon-induced neutron fluxes, including various aquifer conditions (saturation, rock chemistry), would be greatly beneficial for a better understanding of these processes.

Emanation remains the most elusive parameter to predict the activities dissolved in the water from subsurface production processes in rocks. The diffusive migration from micro pores to the drainable pore space, which is typically slow, is crucial when dealing with radioactive isotopes. The total emanation depends on the timescale of diffusion, which is inherently dependent on its spatial scale. Therefore, appraising emanation fractions at the field scale requires assessing the fraction of the pore space volume governed by diffusive transport in relation to the one in which advective transport dominates. Such estimations are typically associated with large uncertainties due to the heterogeneity of geology. Additionally, the dependency of the recoil process on the nature and energy of the incident particle is not yet fully understood. Likewise, the influence of the water content on the recoil and diffusion processes, as well as on the energy moderation of the incident particle, are also subject to debate. In these regards, more irradiation experiments, with different rock types, at various scales and saturation conditions would benefit a more comprehensive understanding of emanation processes.

The Denmark field site offered a situation where measurements could be compared with theoretical calculations, which were supported by a sound constraint of recharge patterns thanks to numerical modeling. The significance of muon-induced processes could therefore be unequivocally demonstrated. In addition, underground production substantially biases the ^{39}Ar ages inferred from the activity concentrations in the case where groundwater infiltration is impeded at relatively shallow depths (< 50 m). In contrast, in the case of a fully unconfined porous aquifer, the effect of underground production on dissolved activities is completely negligible. In this regard, numerical modeling is a promising tool to constrain the recharge scenarios in which ^{39}Ar subsurface production might bias the groundwater ages.

Intuitively, groundwater dating with ^{39}Ar can be depicted by a stopwatch, or a clock, that starts when the water infiltrates the underground and is thus theoretically isolated from its source. In light of what is now understood about underground production, this clock needs to be calibrated according to local conditions. First of all, the starting time of the stopwatch may virtually be delayed compared to the actual infiltration time due to high production rates at shallow depths. Indeed, this process postpones the moment the activities start to decrease < 100 % modern. Secondly, in the presence of a constant underground source as in a U/Th-rich rock, the clock's rhythm is slowed to an apparent decay rate, which is lower than the radioactive decay rate. However, if underground production is properly quantified, these elements can be considered, and ^{39}Ar is not only still a reliable method, but the timescale of its applications can even be extended.

Therefore, one should consider the occurrence of cosmogenic underground production processes when using ^{39}Ar for groundwater dating. The often observed disagreement between ^{39}Ar and ^{14}C could be partially explained by cosmogenic ^{39}Ar production during recharge. A suitable indicator of such processes may be ^{37}Ar , whose measurement in a sample foreseen for ^{39}Ar dating is associated with minimal efforts with LLC. Both isotopes are produced by fairly similar nuclear processes and, to some extent, on the same elements in the underground but have very different half-lives. ^{37}Ar reaches its secular equilibrium on the timescales of months, which makes it (i) an indicator of the level of underground production in the aquifer and (ii) a valuable tool for the study of surface water - groundwater interactions. For the latter, the ingrowth from a virtually zero activity concentration in the freshly infiltrating water, as a function of travel time and depth in the aquifer, informs the mixing proportion and residence time of a potentially vulnerable surface water component (in relation to an older regional groundwater component). Finally, the ratio $^{37}\text{Ar}/^{39}\text{Ar}$ is an interesting tool for OSI in the frame of the CTBT since the consideration of a ratio, instead of the absolute ^{37}Ar activity value, could allow for better discrimination the activities from a UNE from the background conditions at shallow depths.

Part II

Development of a new sampling method for ^{85}Kr

Chapter 9

Introduction: ^{85}Kr as a tracer for groundwater dating

Krypton is a noble gas composed of six stable isotopes. The most abundant is ^{84}Kr , which constitutes 57% of natural Kr (Purtschert et al., 2013). ^{81}Kr and ^{85}Kr are two of the eleven unstable isotopes that are commonly used for the investigation of environmental processes. ^{85}Kr [$t_{1/2} = 10.74 \pm 0.01$ yr, Singh and Chen (2014)] is produced by fission of uranium and plutonium in nuclear reactors and released in the atmosphere during reprocessing of spent fuel rods (Ahlsvede et al., 2013). The atmospheric abundance from anthropogenic sources is therefore steadily increasing since the 50s, up to a specific activity of about $1.4 \text{ Bq cm}_{\text{Kr}}^{-3}$ in 2020 (Kersting et al., 2020; Bollhöfer et al., 2019). This is orders of magnitude higher than the natural activity ($\sim 10^{-7} \text{ Bq cm}_{\text{Kr}}^{-3}$) produced by neutron capture on ^{84}Kr (Purtschert et al., 2013; Bollhöfer et al., 2019). ^{81}Kr [$t_{1/2} = 229 \pm 11$ kyr, Baglin (2008)] is one of the few tracers available for dating groundwater on the million years timescale (Matsumoto et al., 2020; Kim et al., 2022; Purtschert et al., 2021; Ling et al., 2019; Buizert et al., 2014; Sturchio and Purtschert, 2013). Although it was identified as a promising dating tracer since the 70s (Lehmann et al., 1985; Loosli and Oeschger, 1969), the absence of effective extraction, separation, and measurement tools limited its applications until the last two decades (Ram et al., 2021). The development of Atoms Trap Trace Analysis (ATTA) methods (Jiang et al., 2012; Yang et al., 2013) improved its accessibility for paleo-groundwater dating (Purtschert et al., 2021; Gerber, 2017; Ram et al., 2021; Zappala et al., 2020). In the following, this thesis focuses only on ^{85}Kr groundwater applications.

^{85}Kr groundwater dating consists in measuring the ratio of ^{85}Kr to stable krypton. Therefore, the results do not depend on recharge temperatures and excess air and are not sensitive to partial sample losses. The detection limit is around $0.05 \text{ Bq m}_{\text{air}}^{-3}$, which corresponds to an upper dating limit of ~ 50 yrs. ^{85}Kr has been measured by low-level proportional counting (LLC) for more than three decades (Smethie Jr et al., 1992; Loosli and Purtschert, 2005).

The recent advent of ATTA methods, and more specifically the rapid-processing procedure (Zappala et al., 2017), contributes to increasing the capacity for ^{85}Kr -dating in the geoscience community. The minimum volume Krypton required for both LLC and ATTA is 2-5 μL at STP, which is extracted from 50 to 100 L of water that needs to be degassed in the field.

Conventionally, degassing is performed by pumping the water from the well to a membrane module at the surface. The active water extraction is associated with two issues : (i) the natural stratification in the aquifer is disturbed, and (ii) pumping inherently weights the sampling towards the most permeable layers of the aquifer. In the frame of this thesis, a new degassing system was developed to extract the gas from the water directly in the borehole. For this purpose, the water is circulated in small diffusion samplers at a scale that minimizes borehole disturbance and avoids preferential drainage in the aquifer. This method was tested in combination with conventional ^{85}Kr sampling, as well as $^3\text{H}/^3\text{He}$ passive and active sampling in a porous aquifer located on the Swiss plateau (Musy et al., 2021). The corresponding article is found in Chapter 10. These quasi-passive samplers were then used in the frame of a multi-tracers study focusing on the depth-sequential investigation of mixing conditions in long-screen wellbores in the St-Lawrence Lowlands (Canada), for which the manuscript is currently in preparation.

References

- Ahlswede, J., Hebel, S., Ross, J. O., Schoetter, R., and Kalinowski, M. B. (2013). Update and improvement of the global Krypton-85 emission inventory. *Journal of Environmental Radioactivity*, 115:34–42.
- Baglin, C. M. (2008). Nuclear Data Sheets for $A = 81$. *Nuclear Data Sheets*, 109(10):2257–2437.
- Bollhöfer, A., Schlosser, C., Schmid, S., Konrad, M., Purtschert, R., and Kraiss, R. (2019). Half a century of Krypton-85 activity concentration measured in air over Central Europe: Trends and relevance for dating young groundwater. *Journal of Environmental Radioactivity*, 205–206:7–16.
- Buizert, C., Baggenstos, D., Jiang, W., Purtschert, R., Petrenko, V. V., Lu, Z.-T., Müller, P., Kuhl, T., Lee, J., Severinghaus, J. P., and Brook, E. J. (2014). Radiometric ^{81}Kr dating identifies 120,000-year-old ice at Taylor Glacier, Antarctica. *Proceedings of the National Academy of Sciences*, 111(19):6876–6881. Publisher: Proceedings of the National Academy of Sciences.
- Gerber, C. (2017). *Groundwater dating with noble gases - from groundwater-surface water interaction and contaminant transport to paleohydrogeology*. PhD thesis, Universität Bern, Bern.
- Jiang, W., Bailey, K., Lu, Z. T., Mueller, P., O'Connor, T. P., Cheng, C. F., Hu, S. M., Purtschert, R., Sturchio, N. C., Sun, Y. R., Williams, W. D., and Yang, G. M. (2012). An atom counter for measuring ^{81}Kr and ^{85}Kr in environmental samples. *Geochimica et Cosmochimica Acta*, 91:1–6.
- Kersting, A., Schlosser, C., Bollhöfer, A., and Suckow, A. (2020). Evaluating 5 decades of atmospheric ^{85}Kr measurements in the southern hemisphere to derive an input function for dating water and ice with implications for interhemispheric circulation and the global ^{85}Kr emission inventory. *Journal of Environmental Radioactivity*, 225:106451.
- Kim, J.-H., Ferguson, G., Person, M. A., Jiang, W., Lu, Z.-T., Ritterbusch, F., Yang, G.-M., Tyne, R. L., Bailey, L., Ballentine, C. J., Reiners, P. W., and McIntosh, J. C. (2022). Krypton-81 dating constrains timing of deep groundwater flow activation. Section: Hydrology.
- Lehmann, B. E., Oeschger, H., Loosli, H. H., Hurst, G. S., Allman, S. L., Chen, C. H., Kramer, S. D., Payne, M. G., Phillips, R. C., Willis, R. D., and Thonnard, N. (1985). Counting ^{81}Kr atoms for analysis of groundwater. *Journal of Geophysical Research: Solid Earth*, 90(B13):11547–11551. _eprint: <https://onlinelibrary.wiley.com/doi/pdf/10.1029/JB090iB13p11547>.
- Ling, X., Chen, P., and Yu, H. (2019). Krypton 81: A New Method of Paleogroundwater Dating. *International Journal of Natural Resource Ecology and Management*, 4(4):96. Number: 4 Publisher: Science Publishing Group.
- Loosli, H. and Purtschert, R. (2005). Rare Gases. In Aggarwal, P. K., Gat, J. R., and Froehlich, K. F., editors, *Isotopes in the Water Cycle: Past, Present and Future of a Developing Science*, pages 91–96. Springer Netherlands, Dordrecht.
- Loosli, H. H. and Oeschger, H. (1969). ^{37}Ar and ^{81}Kr in the atmosphere. *Earth and Planetary Science Letters*, 7(1):67–71.
- Matsumoto, T., Zouari, K., Trabelsi, R., Hillegonds, D., Jiang, W., Lu, Z.-T., Mueller, P., Zappala, J. C., Araguás Araguás, L. J., Romeo, N., and Agoun, A. (2020). Krypton-81 dating of the deep Continental Intercalaire aquifer with implications for chlorine-36 dating. *Earth and Planetary Science Letters*, 535:116120.

- Musy, S., Meyzonnat, G., Barbecot, F., Hunkeler, D., Sültenfuss, J., Solomon, D. K., and Purtschert, R. (2021). In-situ sampling for krypton-85 groundwater dating. *Journal of Hydrology X*, 11:100075.
- Purtschert, R., Yokochi, R., Jiang, W., Lu, Z.-T., Mueller, P., Zappala, J., Van Heerden, E., Cason, E., Lau, M., Kieft, T., Gerber, C., Brennwald, M., and Onstott, T. (2021). Underground production of ^{81}Kr detected in subsurface fluids. *Geochimica et Cosmochimica Acta*, 295:65–79.
- Purtschert, R., Yokochi, R., and Sturchio, N. C. (2013). Krypton-81 dating of old groundwater. In *Isotope methods for dating old groundwater*, pages 91–124. Vienna, i.a.e.a library edition. OCLC: 844871473.
- Ram, R., Purtschert, R., Adar, E. M., Bishof, M., Jiang, W., Lu, Z.-T., Mueller, P., Sy, A., Vockenhuber, C., Yechieli, Y., Yokochi, R., Zappala, J. C., and Burg, A. (2021). Controls on the $^{36}\text{Cl}/\text{Cl}$ input ratio of paleo-groundwater in arid environments: New evidence from $^{81}\text{Kr}/\text{Kr}$ data. *Science of The Total Environment*, 762:144106.
- Singh, B. and Chen, J. (2014). Nuclear Data Sheets for $A=85$. *Nuclear Data Sheets*, 116:1–162.
- Smethie Jr, W. M., Solomon, D. K., Schiff, S. L., and Mathieu, G. G. (1992). Tracing groundwater flow in the Borden aquifer using krypton-85. *Journal of Hydrology*, 130(1-4):279–297.
- Sturchio, N. and Purtschert, R. (2013). Krypton-81 case study: the nubian aquifer, Egypt. *Isotope Methods for Dating Old Groundwater*, pages 319–324.
- Yang, G.-M., Cheng, C.-F., Jiang, W., Lu, Z.-T., Purtschert, R., Sun, Y.-R., Tu, L.-Y., and Hu, S.-M. (2013). Analysis of ^{85}Kr : A comparison at the 10-14 level using micro-liter samples. *Scientific Reports*, 3.
- Zappala, J. C., Baggenstos, D., Gerber, C., Jiang, W., Kennedy, B. M., Lu, Z.-T., Masarik, J., Mueller, P., Purtschert, R., and Visser, A. (2020). Atmospheric ^{81}Kr as an Integrator of Cosmic-Ray Flux on the Hundred-Thousand-Year Time Scale. *Geophysical Research Letters*, 47(3):e2019GL086381. _eprint: <https://onlinelibrary.wiley.com/doi/pdf/10.1029/2019GL086381>.
- Zappala, J. C., Bailey, K., Mueller, P., O'Connor, T. P., and Purtschert, R. (2017). Rapid processing of $^{85}\text{Kr}/\text{Kr}$ ratios using Atom Trap Trace Analysis. *Water Resources Research*, 53(3):2553–2558.

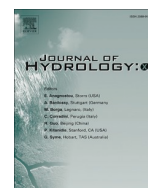
Chapter 10

[Article]In-situ sampling for ^{85}Kr ground-water dating

Stephanie Musy, Guillaume Meyzonnat, Florent Barbecot, Daniel Hunkeler, Jürgen Sültenfuss, D. Kip Solomon and Roland Purtschert

Published in *Journal of Hydrology X*, 11, 100075, 2021
doi: 10.1016/j.hydroa.2021.100075.

Abstract Krypton-85 and other radioactive noble gases are widely used for ground-water dating purposes. ^{85}Kr analysis require large volumes of water to reach the analytical requirements. Conventionally, this water is pumped to the surface to be degassed with a gas extraction system. The large pumping rate may disturb the natural flow field and requires substantial field logistics. Here, we propose a new *in situ* degassing method, in which membrane contactors are used to degas the ground-water directly in the well and collect the gas at the surface. This way, field work is facilitated, the groundwater system disturbance is minimized, and the gas sample is collected at a specific depth. We demonstrate the tightness of the system regarding atmospheric air contamination for a collection times of 24 hours, which is sufficient for both low-level counting and laser-based counting methods for ^{85}Kr . The minimal borehole diameter is 7.5 cm for the prototype presented in this research but can easily be reduced to smaller diameters. In a case study, we compare the results obtained with the new passive method with those from a conventional packer set-up sampling. Additionally, $^3\text{H}/^3\text{He}$ samples were collected for both sampling regimes and the dating results were compared with those from ^{85}Kr . A good agreement between tracer ages is demonstrated and the age stratigraphy is consistent with the expected age distribution for a porous unconfined aquifer. In addition, our study emphasizes the differences between the information sampled with various methods. In conclusion, we demonstrate that the new *in situ* quasi-passive method provides a representative age stratigraphy with depth in most cases.



In-situ sampling for krypton-85 groundwater dating

Stéphanie Musy^{a,*}, Guillaume Meyzonnat^b, Florent Barbecot^b, Daniel Hunkeler^c,
Jürgen Sültenfuss^d, D. Kip Solomon^e, Roland Purtschert^a

^a Climate and Environmental Physics and Oeschger Center for Climate Change Research, University of Bern, Sidlerstrasse 5, 3012 Bern, Switzerland

^b GEOTOP, Université du Québec à Montréal, 201 avenue du Président-Kennedy Montréal, Québec H3C 3P8, Canada

^c Centre d'Hydrogéologie et de Géothermie, University of Neuchâtel, Rue Emile-Argand 11, 2000 Neuchâtel, Switzerland

^d Institut für Umweltphysik, University Bremen, Otto-Hahn-Allee 1, 28355 Bremen, Germany

^e Department of Geology and Geophysics, University of Utah, 115 S 1460 E, Salt Lake City, UT 84112, USA

ARTICLE INFO

Keywords:

Noble gases

Tracers

Groundwater

Dating

Sampling Methodology

ABSTRACT

Krypton-85 and other radioactive noble gases are widely used for groundwater dating purposes. ^{85}Kr analysis require large volumes of water to reach the analytical requirements. Conventionally, this water is pumped to the surface to be degassed with a gas extraction system. The large pumping rate may disturb the natural flow field and requires substantial field logistics. Hence, we propose a new *in-situ* degassing method, in which membrane contactors are used to degas the groundwater directly in the well and gas is collected at the surface. This way, field work is facilitated, groundwater system disturbance is minimized, and the gas sample is collected at a specific depth. We demonstrate the tightness of the system regarding atmospheric air contamination for a collection times of 24 h, which is sufficient for both low-level counting and laser-based counting methods for ^{85}Kr . The minimal borehole diameter is 7.5 cm for the prototype presented in this research but can easily be reduced to smaller diameters. In a case study, we compare the results obtained with the new passive method with those from a conventional packer setup sampling. Additionally, $^3\text{H}/^3\text{He}$ samples were collected for both sampling regimes and the dating results were compared with those from ^{85}Kr . A good agreement between tracer ages is demonstrated and the age stratigraphy is consistent with the expected age distribution for a porous unconfined aquifer. In addition, our study emphasizes the differences between the age information sampled with various methods. In conclusion, we demonstrate that the new *in situ* quasi-passive method provides a more representative age stratigraphy with depth in most cases.

1. Introduction

Groundwater is an essential resource for human societies, as a source of drinking water, but also for agricultural and industrial applications. The anthropogenic stress on groundwater is increasing with the population's growth as well as a consequence of climate change. The deterioration in quality and quantity arising from these changes can be limited by a comprehensive understanding of underground flow patterns, recharge rates, and residence time distributions. These parameters are crucial to appraise the complexity of groundwater systems, especially regarding pollutants transport. Their assessment leads to more effective strategies for sustainable withdrawal.

In this context, groundwater age information is required for two purposes. Firstly, the age stratigraphy is directly linked to water quality and a key information for the estimation of the young water fraction,

which is more vulnerable to anthropic contamination (Bethke and Johnson, 2008; Purtschert, 2008). Secondly, the age information is required for the calibration and validation of numerical hydrodynamic models as well as for groundwater fluxes constrain (Zuber et al., 2011).

Environmental tracers are used to characterize the groundwater travel time along the flow path because they are inherently more integrative than standard methods (i.e., artificial tracers or Darcy Law estimations). They are largely distributed near the earth's surface, and their variations are used to describe environmental processes (Cook and Böhlke, 2000). Dating tracers can be either event markers (Cook and Solomon, 1997), or accumulating in the subsurface (Darling et al., 2012), or decreasing by radioactive decay (Althaus et al., 2009; Collon, Kutscher and Lu, 2004; Lu et al., 2014; Tomonaga et al., 2017). Because different tracers behave differently in case of mixing, additional information is provided when they are applied simultaneously (Kagabu et al.,

* Corresponding author.

E-mail address: stephanie.musy@climate.unibe.ch (S. Musy).

<https://doi.org/10.1016/j.jhydro.2021.100075>

Received 13 November 2020; Received in revised form 7 February 2021; Accepted 10 February 2021

Available online 18 February 2021

2589-9155/© 2021 The Authors. Published by Elsevier B.V. This is an open access article under the CC BY license (<http://creativecommons.org/licenses/by/4.0/>).

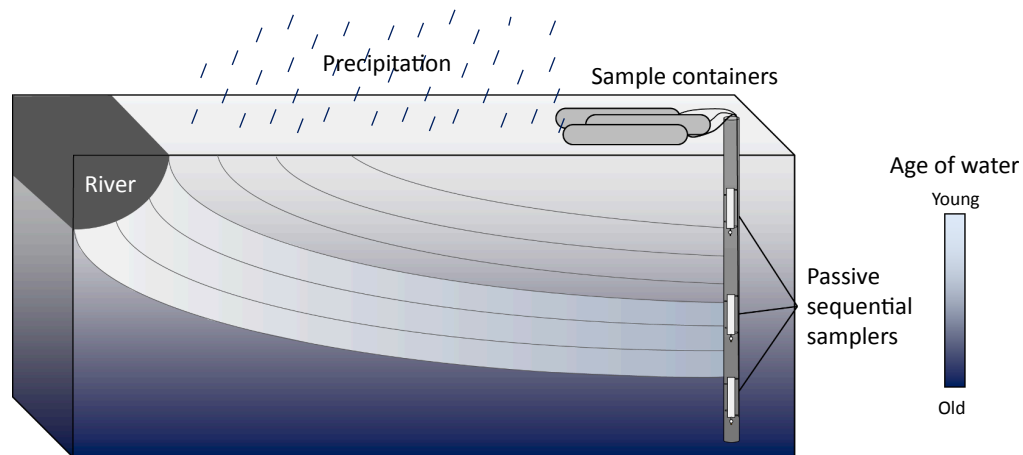


Fig. 1. Depth-dependent sampling in the context of aging with depth in a uniform porous media with an infiltrating river.

2017; McCallum, Cook and Simmons, 2015). Among environmental tracers, noble gas radionuclides are especially interesting because of their inertness and thus, their insensitivity to degradation or retardation processes due to chemical reactions. However, their low abundances in the environment require relatively large volumes of water for analysis.

For this purpose, groundwater degassing in the field is conventionally achieved through either a vacuum extraction chamber or membrane contactors. The water is pumped from the well into the apparatus by a submersible pump and discharged after gas extraction (Gerber, 2012; Ohta et al., 2009; Purtschert and Yokochi, 2013; Yokochi, 2016). These traditional pumping and degassing setups are logistically challenging, and impractical for very low productivity wells with very long sampling times. In addition, active pumping may induce drawdown that disturbs the natural age stratification and, in some cases could even lead to infiltration of gas from the vadose zone.

As an alternative, we propose an approach in which the water is degassed directly in the well for krypton-85 groundwater dating. Membrane modules are placed at a defined depth in the wellbore and

left in place for several hours during which the gas is autonomously extracted, transferred to the surface, and collected in sampling vessels. This method offers several advantages. Firstly, no gas pump, or compressor is required in the field if the gas is extracted in pre-evacuated gas vessels. Secondly, the risk for atmospheric air contamination during prolonged sampling times is minimal since most connections and the membranes are immersed under water. Finally, several samplers can simultaneously be placed at different depths allowing to establish groundwater age profiles without using expensive packers systems (Fig. 1). This way, the sampling procedure is facilitated while the disturbance of the natural flow field is minimized. Its use is especially interesting in porous aquifers with dominant horizontal flow. The application in fractured aquifers is more complex because of localized groundwater inflows that may induce ambient vertical flow in the wellbore. However, if these fluxes are quantified, the method allows for the deconvolution of the activities, and the dating of the water inflows (Meyzonnat et al., 2018).

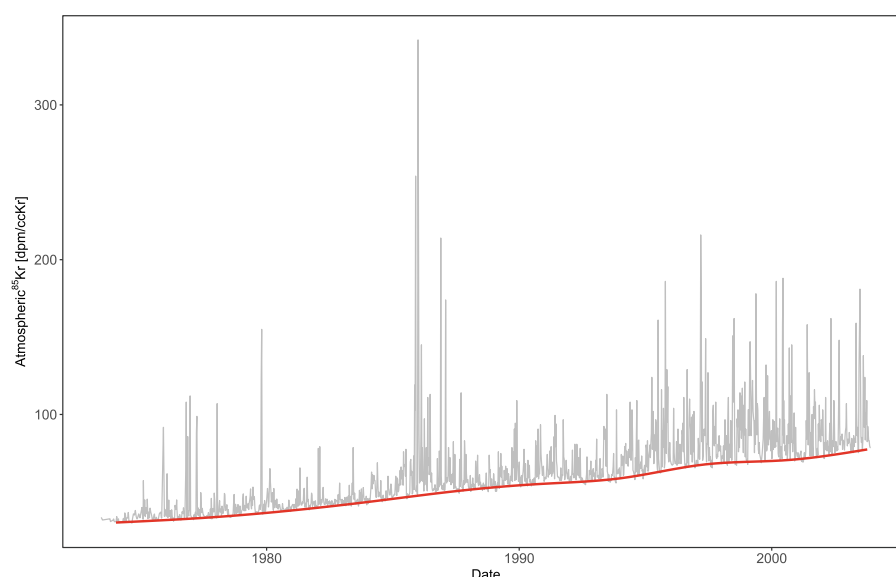


Fig. 2. Atmospheric ^{85}Kr activities [dpm/cc $_{\text{Kr}}$] weekly measured in air in Freiburg by the German Federal Office for Radiation Protection at Freiburg (Source: Bollhöfer et al. 2019). The red line is the baseline calculated with a running average of minima over 15 weeks. The peaks represent pulsed releases from reprocessing plants mainly in La Hague (France). (For interpretation of the references to colour in this figure legend, the reader is referred to the web version of this article).

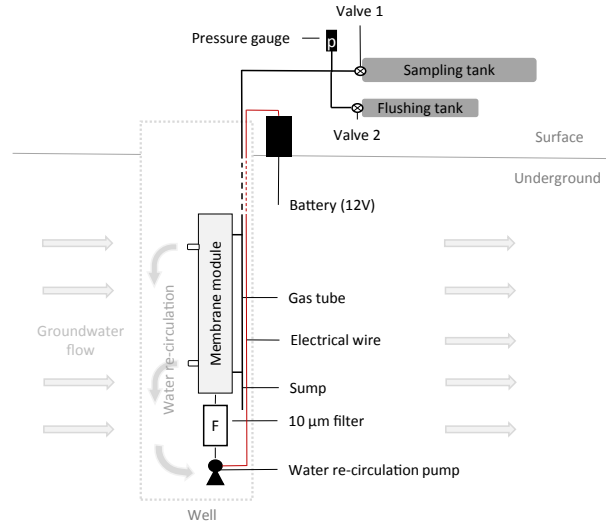


Fig. 3. Degassing setup. The water is circulated through the membrane module between the two outlets of the contactor to the water pump.

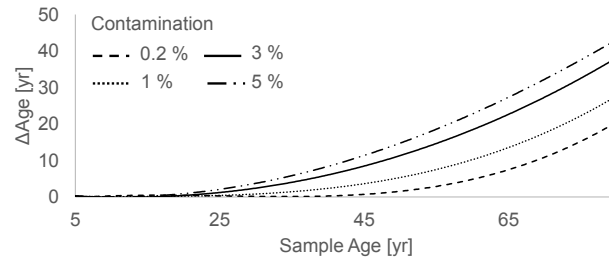


Fig. 4. Age error (ΔAge) induced by modern air contamination as function of the piston flow age for different contamination percentage. We assume a modern activity of 80 dpm/cc_{Kr}.

2. Method

2.1. ⁸⁵Kr groundwater dating

Krypton-85 (⁸⁵Kr) is a noble gas radionuclide with a half-life of 10.74 years used to date young groundwater in the age range from 5 to 50 years (Purtschert, 2008; Singh and Chen, 2014). This radioisotope is naturally produced in the earth atmosphere by cosmic rays (⁸⁴Kr (n,γ)⁸⁵Kr), and fission reactions in the lithosphere. However, the major part of ⁸⁵Kr is anthropogenic as it is produced in nuclear reactors by fission of uranium and plutonium, and released during reprocessing of nuclear spent fuel (Ahlsweide et al., 2013; Bollhöfer et al., 2019). This results in a steadily increasing activity concentration in the atmosphere since 1950 s up to about 80 dpm/cc_{Kr} (decay per minute and cm³_{STP} krypton) in 2019 (Fig. 2). In the proximity of re-processing plants (in Europe: mainly around La Hague, in France), the atmospheric ⁸⁵Kr activity concentration varies temporally due to pulsed releases (Bollhöfer et al., 2019). An interhemispheric exchange time of roughly one year, and the fact that all reprocessing plants are located in the northern hemisphere, lead to a smoother and 15% lower ⁸⁵Kr activity course in the southern hemisphere (Ahlsweide et al., 2013; Lu et al., 2014; Kersting et al., 2020).

Once precipitation reaches the groundwater table, gas and ⁸⁵Kr exchange with the atmosphere is blocked. The ⁸⁵Kr activity decreases

along the groundwater flow path due to radioactive decay. Mixing at variable scales as well as diffusion/dispersion processes lead to a distribution of residence times rather than a single age (Suckow 2014). The probability distribution of ages $g(t)$ (Małoszewski and Zuber, 1982; Suckow, 2014) is commonly described by simple analytical functions. These are combined with the input tracer concentration $C_m(t')$ [dpm/cc_{Kr}] at recharge time t' in the convolution integral (Equation (1))

$$C_{out}(t) = \int_{-\infty}^t C_m(t') \cdot g(t-t') \cdot e^{-\lambda_{85}(t-t')} dt' \quad (1)$$

$C_{out}(t)$ [dpm/cc_{Kr}] is the concentration at observation time t [yr], and λ_{85} [yr⁻¹] is the ⁸⁵Kr decay constant (6.4×10^{-2} /yr). The mean residence time τ , corresponding to the weighted average value of all idealized ages ($t-t'$), is one of the model parameters describing the probability distribution $g(t)$. τ can be determined by an optimisation routine once the functional form of $g(t)$ has been specified.

The dating method is based on the measurement of the specific ⁸⁵Kr activity per volume of total krypton. The concentration of stable krypton isotopes in the atmosphere remains constant at 1.099 ppm(v) (Aoki and Makide, 2005). Transitions between liquid and gas phase, i.e. gas dissolution and degassing, fractionates the ⁸⁵Kr/Kr ratio to <1% for most realistic scenarios (Purtschert, 2008). Dating results are therefore not sensitive to recharge temperatures or excess air (Heaton and Vogel,

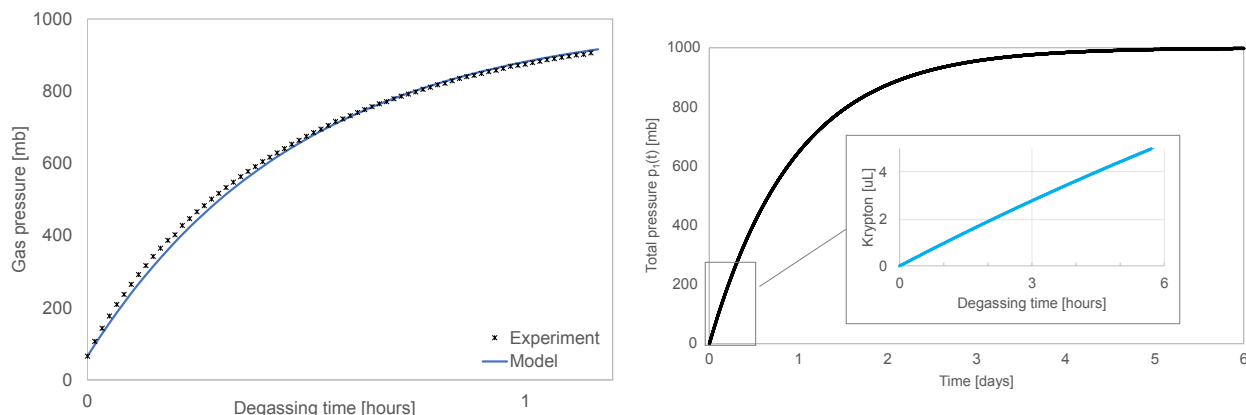


Fig. 5. a) Equilibration experiment (crosses) compared to the fitted values with $K_{\text{air}} = 5.3 \times 10^{-7} \text{ cm}^2/\text{s}$, $V = 420 \text{ cm}^3$; b) Pressure increase in a 20 L tank and corresponding volume of krypton sampled assuming A.E.W at 10°C and a processing efficiency of 50%.

1981), nor to partial degassing prior or during sampling. This is a big advantage compared to other tracers based on absolute concentrations of dissolved gasses.

The composition of gas dissolved in water is determined by solubility, which itself depends on temperature and salinity, and the partial pressure of the gas in the atmosphere. The concentration of krypton in air equilibrated water (A.E.W) at sea level and for a recharge temperature of 10°C is $9.2 \times 10^{-2} \mu\text{L}/\text{L}$ of water. For these conditions, the dissolved gas fraction is 3.93 ppm(v). The minimal amount of krypton required for ^{85}Kr analyses is 1–2 μL for both Low-Level Decay Counting (LLC) and Atom Trap Trace Analysis (ATTA) analyses (Loosli and Purtschert, 2005; Lu et al., 2014; Zappala et al., 2017). Considering a degassing efficiency of $\sim 50\%$, losses during gas purification, and gas transfer into the detection system of another 50% loss, leads to a minimal amount of groundwater of ~ 50 – 200 L that needs to be processed in the field.

2.2. Experimental setup

We present a new sampling system in which small membrane contactors (cells) are inserted directly in the well and the gas is collected at the surface. Fig. 3 illustrates the setup with one degassing unit, composed of a membrane contactor with an internal surface of 2500 cm^2 (PDMSXA-2500; PermSelect®), a water filter, a small water pump (DM212VS; Dynamax Pump Series®) and a sump. The water is locally recirculated through the membrane with a flow rate of $1 \text{ L}/\text{min}$, which brings enough water in contact with the membrane within a sampling time of 24 h, while only minimally disturbing the natural flow field (quasi-passive sampling). The 12 V small water pump is powered by a car battery at the surface. The module is connected by a $1/4$ -inch copper or plastic (PP or PE) tubing to a pre-evacuated sampling tank (20 L) at the surface. The volume of the gas line is $\sim 30 \text{ cm}^3/\text{m}$. To avoid clogging of the membrane, the water is cleaned by a $10 \mu\text{m}$ filter unit. The pressure gradient between both sides of the membrane drives the gas through the membrane and to the sampling bottle. The sample pressure in the tank is continuously monitored during the experiment by a pressure gauge at the surface. The hydrophobic membrane is permeable to some degree to water vapor and a sump ($\sim 10 \text{ cm}^3$) is included in the setup to avoid clogging of the gas line by water. The diameter of our prototype sampler,

without the plastic inserts, is 2.5 cm. The whole prototype setup fits in a 7.5 cm borehole, but future versions will fit in a 5 cm (2 in.) wellbore. Before the sampling starts, the gas lines and connections are evacuated to avoid any contamination by atmospheric air. This can be done by a second pre-evacuated, tank (e.g. 10 L) connected to the degassing line (which has a volume of $0.3 \text{ L}/10 \text{ m}$). Another option for flushing the line is to connect a vacuum pump to valve 2.

For the determination of age-depth profiles, several degassing units are aligned in a serial configuration and individually connected to pre-evacuated flushing and sampling tanks. For a 10 L flushing tank (evacuated $< 0.1 \text{ mb}$), and a tube length of 10 m, the residual pressure in the line is 30 mb. For a 5 L gas sample this residual gas volume of $\sim 9 \text{ cc}/10 \text{ m}$ corresponds to 0.2% air contamination or $\sim 0.14 \text{ dpm}/\text{cc}_{\text{Kr}}$ (Fig. 4). This is below the analytical uncertainty of 0.2–0.5 $\text{dpm}/\text{cc}_{\text{Kr}}$ and could only become relevant for old waters with ^{85}Kr activity levels $< 2 \text{ dpm}/\text{cc}_{\text{Kr}}$. After closing the flushing tanks, the sampling tanks are opened. The setup remains in the well for at least 24 h during which about 5–10 L of gas are collected from A.E.W. After gas collection the pressure in the tank is recorded, the sample bottle is closed, and the line is withdrawn.

The principle of gas sampling based on permeation through a membrane has been previously described and tested by Gardner and Solomon (2009) for stable noble gases and $^3\text{H}/^3\text{He}$ dating. The required total dissolved gas pressure (TDGP) at sampling depth is either measured by a separate probe in the borehole or preserved by closing the gas vial *in situ* and measured afterwards in the laboratory. In contrast, our sampling method does not require the knowledge of the TDGP because the age is determined by the activity ratio $^{85}\text{Kr}/\text{Kr}$.

2.3. Degassing principles

A gas extraction system for groundwater dating purposes must (i) be leak-tight, to avoid sample contamination by modern air (Fig. 4) (Lu, 2014; Purtschert and Yokochi, 2013) (ii) have a high extraction yield to minimize the volume of water required and the extraction time, and (iii) be sufficiently robust, light, and portable for field work. The concepts of our approach are discussed in detail in the following sections.

2.3.1. Phase separation by membranes

A membrane is a selective layer of material for a substance passing

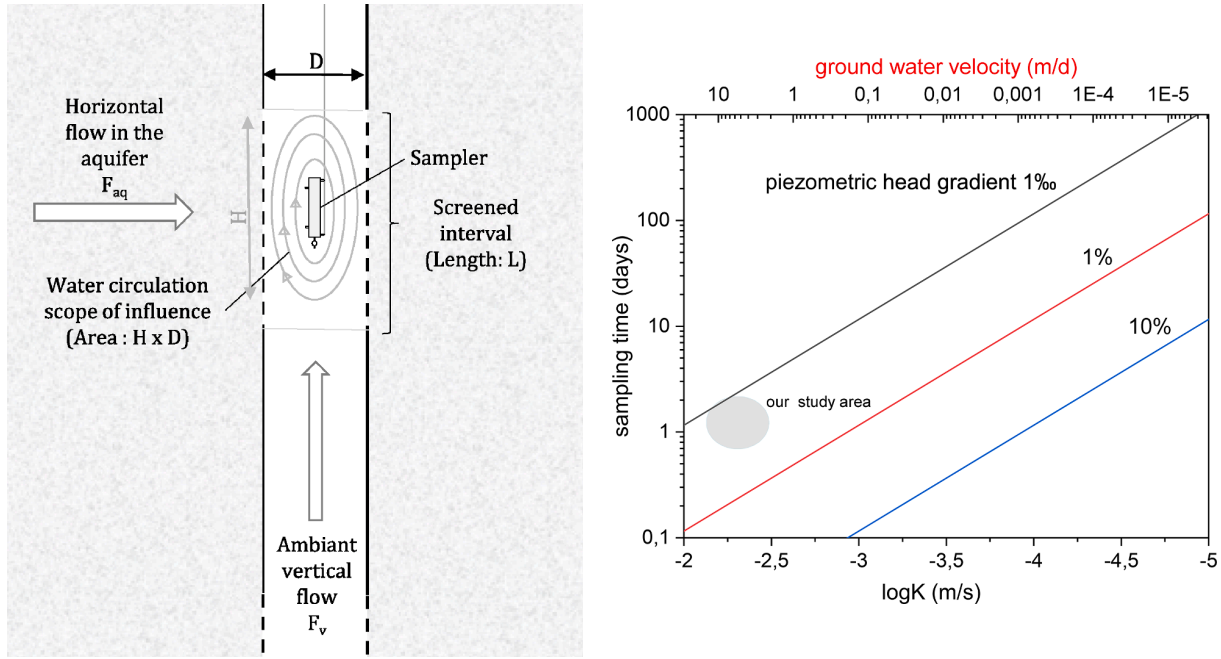


Fig. 6. a) Scheme of water circulation in the aquifer and in the borehole b) Sampling time as function of the aquifer conductivity and piezometric head gradient. For the graph, the following parameters were assumed: minimal sample volume $V_w = 100$ L, borehole diameter $D = 10$ cm, range H of circulation pump: 1 m, $A_{HD} = 0.1$ m² (Equation (5)). The water flow velocity (upper x-axis) refers to $dh/dz = 1\%$ and a porosity of 30%. For a head gradient of 1‰ aquifers with $K < 10^{-4}$ m/s can be sampled within days. Lower conductivities require active pumping in order to increase the head gradient (e.g. to 10%). In the reference aquifer presented in the following, a sampling time of ~ 1 day is sufficient (shaded area).

through it. The gas permeation process is composed of consecutive gas solution on the high pressure side, diffusion through the membrane and evaporation on the low pressure side (Sanders et al., 2013) (Fig. A.1 in Appendix). The dissolution and evaporation processes conform to Henry's Law while diffusion follows Fick's first law (Ahsan and Hussain, 2016; Zhang and Cloud, 2006).

The pressure increase on the gas side (shell side) of the membrane, which includes the volume of the gas lines and the sampling container V [cm³] (Fig. 3), is linked to the gas flow rate through the membrane (i.e. the degassing yield). The resulting pressure increase as function of time $p_1(t)$ [mb] is described by Equation (2) (and derived in Equations (A.1) – (A.4) in Appendix), where p_0 [mb] is the total dissolved gas pressure (TDGP), K [cm²/s] is the diffusion coefficient of gas through the membrane, l [cm] is the membrane thickness, and A [cm²] is the membrane surface area (Gardner and Solomon, 2009). Note that $p_1(t = 0) \cong 0$ mb.

$$p_1(t) = p_0 \cdot (1 - e^{-\frac{KA}{V}t}) \quad (2)$$

2.3.2. Extraction efficiency

The extraction efficiency is defined as the proportion of gas sampled (gas yield or flux) in relation to the dissolved gas content in water, which is maintained constant throughout the experiment thanks to water renewal (Equation (3)).

$$\text{Efficiency} = \frac{\text{Gas flux through the membrane} \left[\frac{\text{cc}}{\text{min}} \right]}{\text{Water flux} \left[\frac{\text{L}_w}{\text{min}} \right] \cdot \text{Gas content} \left[\frac{\text{cc}}{\text{L}_w} \right]} \quad (3)$$

The efficiency is determined by membrane characteristics (surface area, thickness, material, gas dissolution and diffusion coefficients), but also by the solubility and diffusivity of the gas in the water. It further depends on the partial pressure of the gas in the water, and decreases with decreasing contact time with the membrane, which is inversely related to the water flow rate. The efficiency drops from 80% to 40% if

the water flow rate increases from 0.3 L/min to 2 L/min (Fig. B.1 in Appendix). If the gas is collected in a pre-evacuated container, the pressure gradient between both sides of the membrane, and thus the efficiency, decreases over time.

2.3.3. Head loss along the gas tube

The pressure loss along the gas lines between the membranes (in the borehole) and the sample container (at the surface) can be described by the Darcy–Weisbach equation (Brown, 2000) simplified for laminar flow in a circular pipe (Equation (4)).

$$\frac{\Delta P_f}{L} = \frac{128 \mu Q_t}{\pi D^4} \quad (4)$$

where ΔP_f [mb] is the pressure loss in a tube with a length L [m], μ [Pa·s] is the dynamic viscosity of the fluid, i.e. 1.78×10^{-5} Pa·s for air at 10 °C (White, 1988), Q_t [m³/s] is the volumetric flow rate, and D [m] is the tube diameter. A typical gas flux Q_t of 0.4 cc/s is calculated assuming a water flowrate of 1 L/min, a gas content of 23 cc/L, and a degassing efficiency of 50%. For an inner diameter of $\frac{1}{4}$ inches, and a 50 m long tube, the pressure loss is in the order of 10^{-2} mb. This is negligible in comparison to the driving pressure difference in the order of several hundreds of mb.

2.4. Performance and testing

2.4.1. Equilibration experiment

A water degassing experiment was performed in the laboratory to determine the diffusion coefficient for air through the membrane, K_{air} [cm²/s]. For this purpose, tap water (i.e., A.E.W, constantly renewed) is circulated through the membrane with a flow rate of 1 L/min and degassed into a volume of ~ 400 cm³. The pressure increase is recorded as function of time with a pressure gauge (Fig. 5a). These experimental

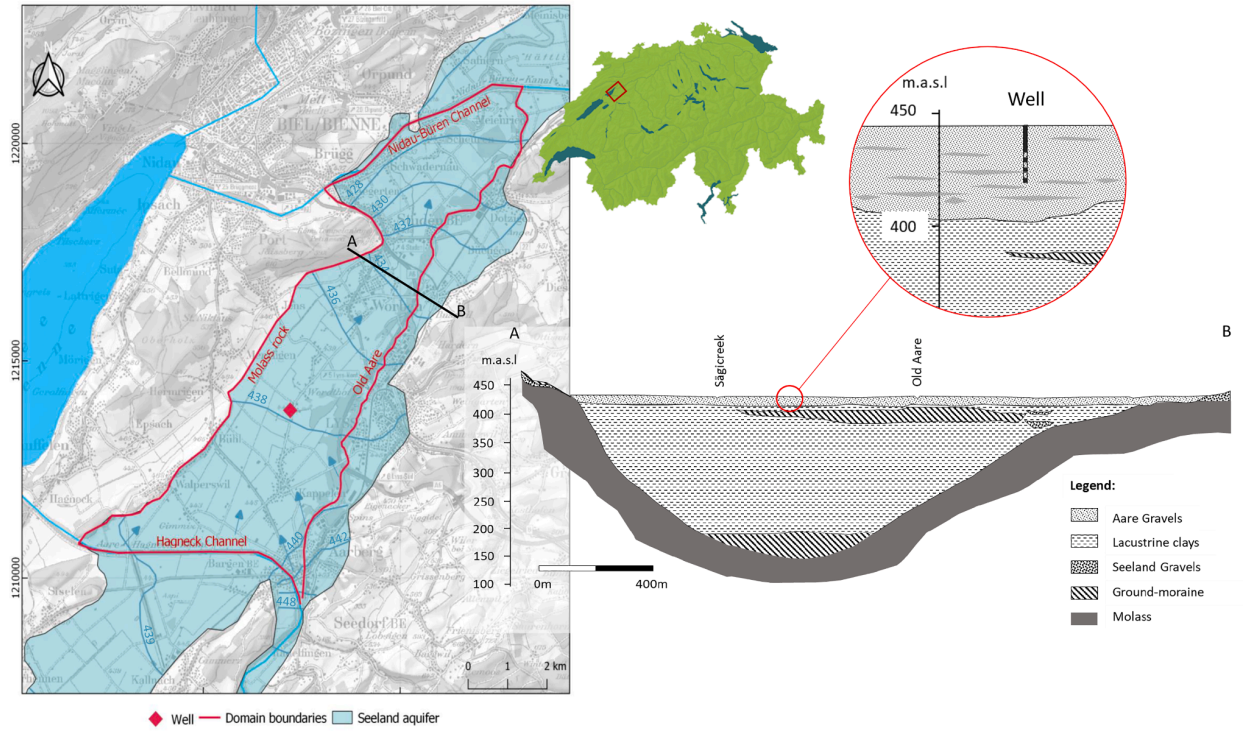


Fig. 7. Field site in the North-Seeland aquifer in Switzerland, and cross section of the area (modified from Biaggi et al., 2004). The well location is projected. The Aare gravel contains silty lenses/layers represented by the grey shapes.

data are then fitted with Equation (2) to extrapolate K_{air} . The resulting diffusion coefficient for air, $K_{air} = 5.3 \times 10^{-7} \text{ cm}^2/\text{s}$, is similar to the diffusion coefficient of argon and krypton through silicone concluded by Gardner and Solomon (2009). Therefore, we use this value to assess the krypton extraction yield in the following.

As discussed earlier, the targeted amount of krypton that needs to be extracted from the water is 2–4 μL (with 50% losses during gas purification and transfers to the counting system). Assuming A.E.W at 10°C , and thus a krypton concentration of 3.93 ppm(v), the collection time is 5 h for 4 μL in a 20 L tank (Equation (2) and Fig. 5b). An equilibration time of 24 h should therefore be sufficient for most scenarios and conditions (partly degassed water, higher recharge elevation or temperature).

This degassing experiment allowed to assess the air degassing efficiency of our samplers. For this purpose, the gas volume sampled is compared with the total gas dissolved in the water circulating around the membrane. The median extraction efficiency observed is 21%, for a final sample pressure of 500 mb, i.e., 10 L of gas in a 20 L sample bottle and A.E.W at 10°C circulated at 1 L/min.

2.4.2. Leak test

The leak rate in operation mode is evaluated by introducing the sampler in stagnant water and degassing it in a known sampling volume of 25 cm^3 . The pressure increase is recorded as a function of time by a pressure gauge. After a few minutes, the water in contact with the membrane is completely degassed and the following pressure increase is interpreted as a maximal leak rate. The experiment was carried out for 5 days. The average leak rate was 0.27 mb/hour, corresponding to a gas flux of $1.1 \times 10^{-4} \text{ cc/min}$. In comparison with the mean degassing rate of 5 cc/min for A.E.W, for a pump rate of 1 L/min and a degassing efficiency of 20%, this leak rate corresponds to an air contamination of 0.03% what is negligible in relation to the analytical uncertainty of ^{85}Kr

analyses (Zappala et al., 2017) and the methodological dating errors.

2.5. Applicability and limitations of the method

A constrain of the method arises from the minimum volume of water that needs to be degassed in the borehole, and therefore needs to be in contact with the degassing unit within a reasonable sampling time. With other words: the natural groundwater flow through the borehole within the targeted sampling time t_s must reach at least the minimum water sample volume of 100 L (V_w) (Equation (5)).

$$t_s = \frac{V_w}{F_{BH}} = \frac{V_w}{v_{Darcy} \cdot A_{HD}} = \frac{V_w}{K \cdot \frac{dh}{dx} \cdot A_{HD}} \quad (5)$$

where $F_{BH} [\text{m}^3/\text{d}]$ is the water flow rate through the effective borehole cross section $A_{HD} [\text{m}^2]$ (Fig. 6a), $v_{Darcy} [\text{m}/\text{d}]$ is the Darcy velocity in the aquifer as function of the aquifer conductivity $K [\text{m}/\text{s}]$ and piezometric head gradient dh/dx (Fig. 6b) (Raja Sekhar and Sano, 2000). In the case where the natural flow rate is too low to allow water renewal within a reasonable sampling time, recirculation of water that was already partly degassed would eventually lead to a standstill of the gas flow (Harrington, Cook and Robinson, 2000).

A potentially limiting factor for any passive sampling method are ambient vertical flows (AVF) in presence of a vertical head gradient along the borehole (Corcho Alvarado, Barbecot and Purtschert, 2009; McMillan et al., 2014). The acceptable threshold for upwelling flow depends on the context, the natural age stratigraphy in the aquifer and the distance that separates the screens or the inflows. Note that this type of limitation is common to all passive sampling methods and generally, it must be clear that almost no vertical flow is acceptable with these methods. AVF are especially common in fractured rocks because of the natural difference in hydraulic heads. In this case, a pump might be

Table 1

Analytical results of ^{85}Kr and $^3\text{H}/^3\text{He}$ measurements, and derived Piston-Flow ages. Passively taken samples are in shaded boxes. Passive $^3\text{He}_{\text{trit}}$ values were calculated for degassing (i) at recharge – (ii) just before sampling.

Mean Depth	Conventional		Passive		Passive	
	⁸⁵ Kr dating					
	April 2019		April 2019		December 2019	
	⁸⁵ Kr [dpm/cc _{Kr}]	Age [yr]	⁸⁵ Kr [dpm/cc _{Kr}]	Age [yr]	⁸⁵ Kr [dpm/cc _{Kr}]	Age [yr]
9	65 ± 2.5	6 ± 0.4	52 ± 1.9	7 ± 0.5	66 ± 3.4	6 ± 0.4
15	63 ± 2.0	6 ± 0.4	54 ± 3.9	7 ± 0.7	57 ± 1.8	7 ± 0.4
22	50 ± 4.3	8 ± 0.8	41 ± 4.2	11 ± 1.3	43 ± 1.9	11 ± 0.7
	³ H / ³ He _{trit} dating					
	April 2019			December 2019		
	³ H [TU]*	³ He _{trit} [TU]*	³ H/ ³ He Age [yr]	³ He _{trit,c} [TU]*	³ H/ ³ He Age [yr]	
	± 1.1	± 0.4		± 0.5		
9	11	6	8 ± 0.8	- 0.7	-1 ± 0.7	
15	10	5	7 ± 0.8	11 – 10	13 – 12 ± 1	
22	8	19	21 ± 1.7	20 – 18	22 – 20 ± 1.7	

*4.0193 10⁻¹⁴ cc/g = 1 TU

*4.0193 10⁻¹⁴ cc/g = 1 TU

placed at the top in order to control the flow direction and intensity in the wellbore. The intensity and location of water inflows in the borehole need then to be quantified by suitable borehole logging techniques (Meyzonnat et al., 2018). The effect of AVF can be reduced by separating depth sections with flow barriers (very simple packers or disks) that impede water exchange between distinct depth levels.

Special attention must be paid in case of high dissolved gas contents (e.g., CO₂, CH₄), which will result in a faster increase of pressure in the sample tank. The size of the tank needs to be adjusted accordingly. In addition, suspended matter in the water may clog the filter and the

membrane. In this case, a series of filters with increasing mesh should be added.

3. Case study in the Seeland aquifer (CH): comparison with conventional sampling and $^3\text{H}/^3\text{He}$ ages

3.1. Field site

The Seeland Region is situated in the Northwestern part of Switzerland between the city of Bern and the lake Biel (Fig. 7). In this

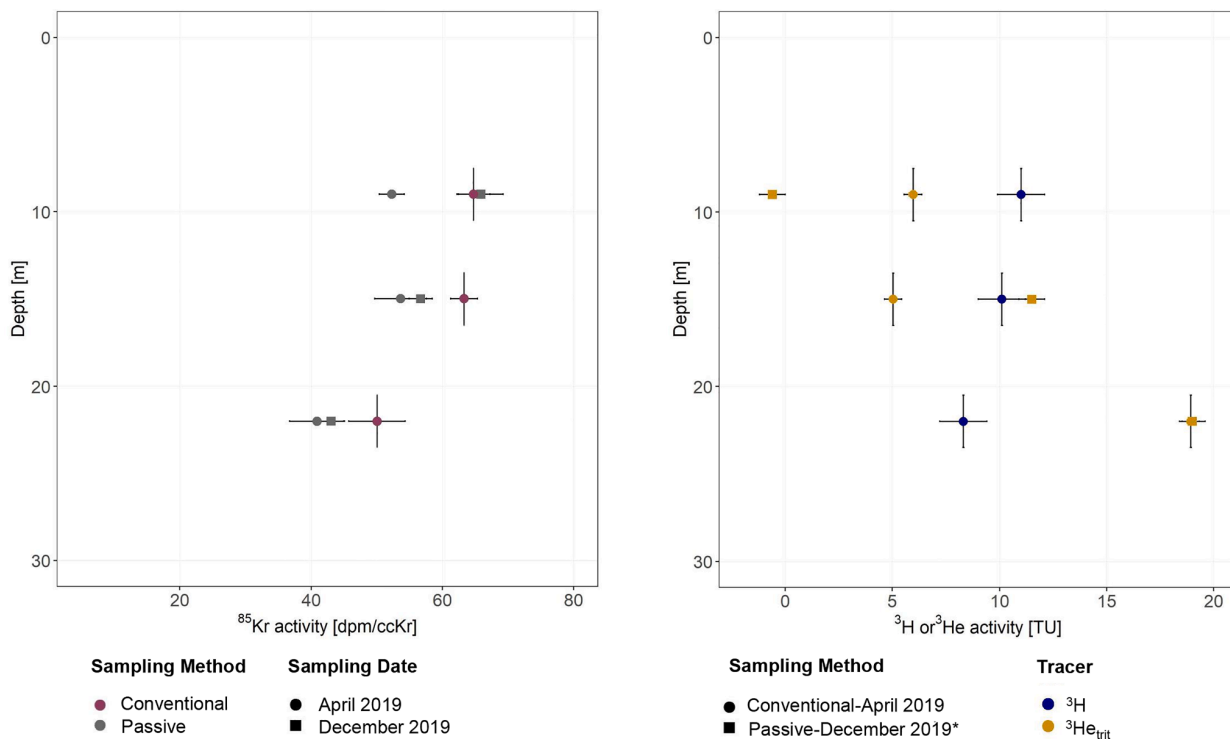


Fig. 8. ^{85}Kr activity concentration, ^3H , and $^3\text{He}_{\text{trit}}$ profiles with depth. The passive $^3\text{He}_{\text{trit}}$ values are an average of the two degassing scenarios discussed before.

Table 2

Concentrations of noble gases for conventional and passive sampling. A solubility equilibrium degassing correction was applied for samples with total dissolved gas pressures (TDGP) < 1. V_g and f_{He} are the volume of the gas phase and the fraction of 3He remaining in solution after degassing (after Visser, Broers and Bierkens (2007)).

	Depth [m]	R/R _a [–]	He ^a [cm ³ _{STP} /g] × 10 ^{−8}	Ne ^b [cm ³ _{STP} /g] × 10 ^{−7}	ΔNe ^y [%]	ΔHe ^y [%]	⁴ He ^y _{atm} [cm ³ _{STP} /g] × 10 ^{−8}	³ He ^y _{atm} [cm ³ _{STP} /g] × 10 ^{−14}	TDGP [atm]	V_g [cm ³ _g /cm ³ _w] × 10 ^{−4}	f_{He}
Conventional	9	1.18	5.2	2.2	13.3	16.5	5.22	7.13			
	15	1.14	5.3	2.2	14.3	18.2	5.27	7.2			
	22	1.58	5.4	2.2	13.7	19.9	5.24	7.15			
Passive	9	0.97	6.2	2.8	48.0	40.0	7.15	9.43	1.5		
	15	1.4	4.1	1.9	−2.0	−7.8	4.37	5.71	0.85	4.8	0.95
	22	1.6	5.0	2.2	17.5	12.5	5.45	7.16	0.95	6.8	0.99

^a±0.05; ^b±0.02; ^yfor a recharge elevation of 500 m and a MAAT of 13 °C.

area, the successive avulsions of meandering Aare River led to a variable lithology that range from well-sorted gravels to clay. Our observation well is situated in the area of Kappelen, where these alluvial gravel deposits are up to 50 m thick. The basement rock is the Tertiary Molasse of the Swiss Plateau covered by ground-moraines and glacio-lacustrine clay sediments up to 200 m deep (Fig. 7). Until the 19th century, this area was a floodplain of the Aare River and its exploitation for human activities was limited. Later, the area was drained by a wide series of hydrological undertakings (e.g., channelization of the rivers) to lower the water table and to protect the area from flooding. Nowadays, the Seeland region is one of the most productive agricultural areas in Switzerland (Baillieux et al., 2014; Biaggi et al., 2004; Gobat, 2015; Kozel, 1992).

Hydrogeological boundaries are delimiting our area (Fig. 7). First, the Seeland aquifer is separated between the northern and southern part by the Hagneck-channel, which acts as a water divide caused by the strong infiltration of channel water (Baillieux et al., 2014). In this case, we are interested in the northern part where the water flows towards the north-eastern direction to the Nidau-Büren channel. The Old Aare river is the south-eastern hydrogeological barrier. The north-western boundary is the outcropping of the Tertiary Molasse (Cochand et al., 2019; Gobat, 2015).

In this area, groundwater recharge occurs by two main processes. Firstly, infiltration of local precipitation, that percolates through soil and thus, drains the minerals and the pesticides applied on the farmlands. The recharge elevation is thus 500–550 m and the mean annual air temperature (MAAT) is ~13 °C. The second recharge process is infiltration from the Hagneck-channel as well as the Old Aare streambed. In contrast to recharge from local precipitation, this water is less mineralized and depleted in heavy isotopes since the catchment area of the river Aare is at higher altitude in the Alps. These two main recharge components are mixed in the aquifer. Previous studies suggested a proportion of Aare river water of up to 50% at our sampling well (Gobat, 2015).

The aquifer conductivity and hydraulic head gradient were estimated to be in the order of 10^{−2} m/s and 2‰ (Gobat, 2015; Kozel, 1992). This results in a water flow velocity of ~10 m/d for a porosity of 20–30%.

The sampling location in Kappelen is a test well with a depth of 25 m and a diameter of 10 cm (Fig. 7). The lithology is mainly composed of permeable sandy gravels (Aare gravels) alternating with an increasing proportion of silty layers with depth (Gobat, 2015). In the borehole casing, three screened intervals are located at 7.5–10.5 m, 14–17 m, and 20.8–23.8 m. Special attention was paid at the time of drilling to avoid leakage between the screened levels via the borehole filling around the casing.

3.2. Sampling and analytical methods

The field site in Kappelen was chosen because of its relatively simple hydrology and the possibility for multi-level sampling. Two field campaigns were conducted in April and December 2019 for ⁸⁵Kr, tritium, stable isotopes of the water molecule, and stable noble gases. The main objectives of this case study were (i) to compare ⁸⁵Kr dating results obtained by passive and active sampling and (ii) to further assess and interpret these results by means of additional dating tracers such as ³H/³He.

In April 2019, three passive degassing units were left in the well for 24 h at the center of each screen (9, 15, and 22 m). The well was undisturbed (i.e., not flushed) prior to sampling. An active sampling was carried out immediately after removing the passive samplers from the well. For this purpose, the three screened intervals were successively isolated by packers, flushed with a submersible pump (MP1; Grundfos®), and sampled for ⁸⁵Kr using a vacuum extraction system (Purtschert and Yokochi, 2013). 600 L of water from each level were degassed with a flow rate of 24 L/min. These samples are denoted “conventional” in the following. Additional samples for ³H, and δ¹⁸O and δ²H were collected, and stable noble gases samples were taken in pinched off copper tubes (Beyerle et al., 2000).

In December 2019, passive ⁸⁵Kr sampling was repeated at the same three levels. Directly afterwards (without purging the well), ³He as well as stable noble gases were collected using the equilibration samplers developed by Gardner and Solomon (2009). These “passive” noble gas samples and ³H values from April were used for ³H/³He dating. The well was undisturbed for more than 6 months before this sampling campaign.

The ⁸⁵Kr activities were measured by LLC (Purtschert and Yokochi, 2013) in the deep laboratory from the University of Bern. Stable isotopes of the water molecule were also measured at the University of Bern (Huber and Leuenberger, 2005). Stable noble gases were measured at the Institute of Environmental Physics of the University of Bremen (Sülfenfuß, Roether and Rhein, 2009) for the conventional samples, resp. at the Department of Geology and Geophysics of the University of Utah for the passive samples (<https://noblegaslab.utah.edu>). ³He, ⁴He, and Ne measurements are used to calculate the ³H/³He ages.

3.3. Results

Table 1 shows the ⁸⁵Kr and ³H/³He_{trit} concentrations with corresponding piston flow ages. ⁸⁵Kr activity concentrations decrease with depth from 65 dpm/cc_{Kr} to 50 dpm/cc_{Kr} for conventional sampling (Fig. 8). Tritium values range from 11 TU to 8 TU with a decreasing trend with depth. ⁸⁵Kr and ³H both suggest the presence of young water (<60 years) at all depths. The samples collected with the new passive samplers for ⁸⁵Kr show a very similar pattern than the conventional samples but with values systematically ~10 dpm/cc_{Kr} lower. This difference between the passive and the conventional activities is discussed

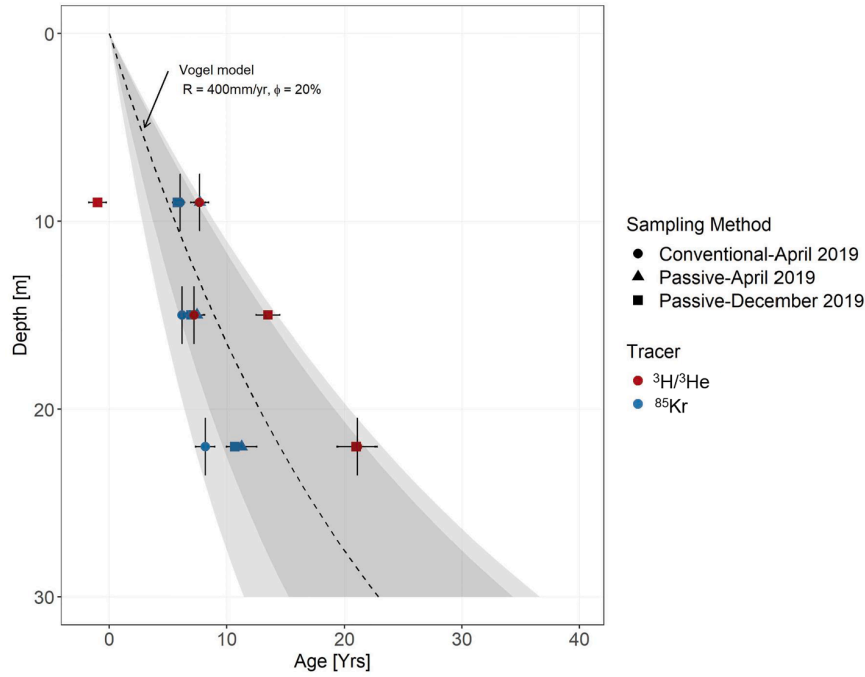


Fig. 9. Age profile with depth for ^{85}Kr and $^3\text{H}/^3\text{He}$ ages with different methods. The dotted line represents the Vogel Model assuming an aquifer thickness of 50 m, a porosity of 20% and a recharge rate of 400 mm/yr; the grey areas show the range of Vogel model for recharge rates between 250 and 600 mm/yr and porosities between 10% and 30%. The passive $^3\text{H}/^3\text{He}$ age are an average of the two degassing scenarios discussed before.

Table 3
Stable isotopes of the water molecule.

	April 2019		December 2019	
	$\delta^{18}\text{O}$ ** (VSMOW) ± 0.1	$\delta^2\text{H}$ (VSMOW) ± 0.5	$\delta^{18}\text{O}$ (VSMOW) ± 0.1	$\delta^2\text{H}$ (VSMOW) ± 0.5
9	−11.2	−81.3	−11.8	−83.2
15	−11.2	−82.2	−11.8	−83.1
22	−11.1	−80.7	−11.9	−83.6

**(VSMOW: Vienna Standard Mean Ocean Water).

in Section 3.4. For the two deeper levels, the repeated ^{85}Kr measurements in April and December agree. The temporal variation observed for the shallow level may indicate changes of the proportion of young water in an active recharge system.

Noble gas samples were collected with pinched off copper tubes in parallel to ^{85}Kr sampling (April 2019) from intervals separated by packers. These samples reveal increasing $^3\text{He}/^4\text{He}$ ratios (R) expressed as relative to the atmospheric $^3\text{He}/^4\text{He}$ ratio (R_a) (Table 2). Excess air (EA), denoted as Ne excess relative to the solubility equilibrium concentration (ΔNe [%]), is similar for all levels (13–14%). In contrast, noble gas data collected with the passive samplers in December 2019 (just after passive ^{85}Kr sampling) show larger scatter in R/R_a , ΔNe values, and total dissolved gas pressures (TDGP) with even negative values (Table 2). These variations are likely related to the passive sampling regime. A better understanding of the underlying processes is required before deriving $^3\text{H}/^3\text{He}$ ages from these data. This is discussed in the following.

For the two deeper passive samples, TDGP below 1 atm indicates the occurrence of degassing. For the calculations of $^3\text{H}/^3\text{He}$ ages, a ^3He degassing correction was applied. For this purpose, gas loss was estimated based on the deficit of ^4He measured in relation to ^4He at solubility equilibrium ($^4\text{He}_{\text{Eq}}$) plus ^4He from excess air ($^4\text{He}_{\text{EA}}$, estimated from ΔNe), and assuming an atmospheric Ne/He ratio (unfractionated

EA). This is a modified version of the correction method proposed by Visser, Broers and Bierkens (2007), where EA was neglected. $^3\text{He}_{\text{trit}}$ is then calculated under the assumptions that (i) degassing occurred at recharge (no loss of $^3\text{He}_{\text{trit}}$) and (ii) degassing occurred shortly prior or during sampling (with $^3\text{He}_{\text{trit}}$ loss) (Equation (6)).

$$(i) \ ^3\text{He}_{\text{trit},c} = ^3\text{He}_m - f_{\text{He}} \cdot \text{He}_{\text{atm}} \quad (ii) \ ^3\text{He}_{\text{trit},c} = \frac{^3\text{He}_m}{f_{\text{He}}} - \text{He}_{\text{atm}} \quad (6)$$

f_{He} is the remaining fraction of He after degassing (Table 2), $^3\text{He}_m$ is the measured concentration and $^3\text{He}_{\text{atm}}$ is the atmospheric concentration before degassing ($^3\text{He}_{\text{Eq}} + ^3\text{He}_{\text{EA}}$). Since the point in time of degassing is unknown, both corrections were applied leading to a (narrow) range of $^3\text{H}/^3\text{He}$ ages (Table 1).

In addition, the slightly depleted $^3\text{He}/^4\text{He}$ ratio ($R/R_a = 0.97$, Table 2) of the shallow passive sample could be caused by (i) non-equilibrium diffusive gas loss, where the lighter ^3He is preferentially lost due to a slightly higher diffusion coefficient compared to ^4He (Nakata et al., 2019) or (ii) a contribution of a significant amount of radiogenic ^4He . The latter would require either an external influx of He from deeper formations (Torgersen et al., 2013) or outgassing of He from the aquifer solids (Solomon, Hunt and Poreda, 1996). In-situ production by the radioactive decay of uranium and thorium naturally present in the aquifer rock would result in a ^4He accumulation rate of $\sim 2.9 \times 10^{-12}$

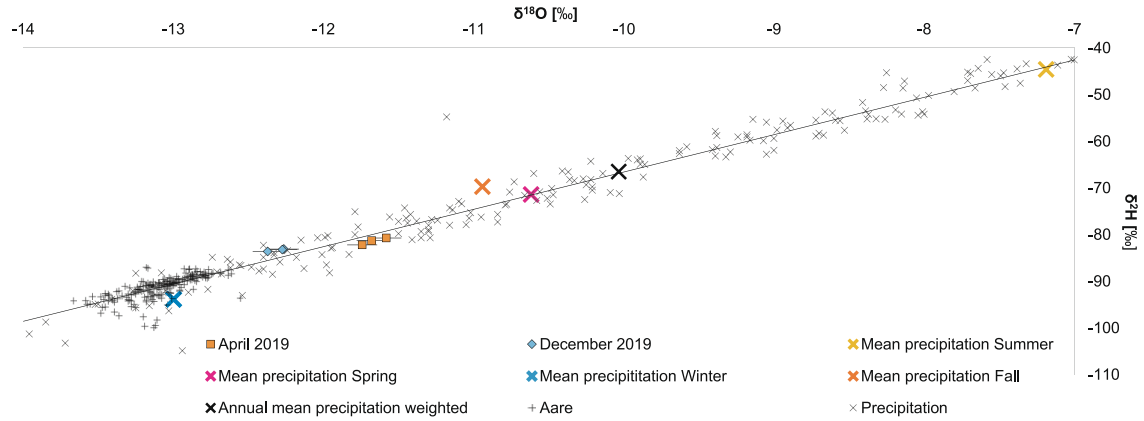


Fig. 10. Stable isotopes of the well in Kappelen (Switzerland), signature in precipitation monthly averaged measured in Bern and Aare water monthly averaged measured in Thun (Source: Global Network of Isotopes in Precipitation (GNIP, AIEA). Winter: December-February; Spring: March-Mai; Summer: June-August; Fall: September-November. The black cross is the average in precipitation weighted by the volume of precipitation.

cc/g/yr (assuming $U = 2$ ppm and $Th = 10$ ppm, Heier, 1965). An accumulation time of >3000 years would then be required to explain a R/R_a of ~ 0.97 . This is unlikely regarding the large conductivity and flow velocity of the aquifer (Gobat and Böhi, 2016). Since the origin of the slightly depleted R/R_a value remains unclear, no correction was applied for the shallow passive sample at 9 m.

^{85}Kr piston flow model ages were calculated by resolving the convolution integral (Equation (1)) and using the mean annual ^{85}Kr input curve for Freiburg i.B., Germany (Fig. 2). $^3\text{H}/^3\text{He}$ ages were calculated by Equation (7)

$$\tau = \frac{T_{1/2}}{\lambda} \ln \left(1 + \frac{^3\text{He}_{\text{trit}}}{^3\text{H}} \right) \quad (7)$$

^{85}Kr and $^3\text{H}/^3\text{He}$ ages are plotted in Fig. 9 as function of depth below the surface. A good agreement is observed between ^{85}Kr ages and $^3\text{H}/^3\text{He}$ ages sampled with the conventional method for the 9 and 15 m levels while the $^3\text{H}/^3\text{He}$ ages are shifted towards older values for the deepest level.

The relationship between $\delta^{18}\text{O}$ and $\delta^2\text{H}$ (Table 3) is shown in Fig. 10 and compared with local precipitation and Aare river values. All samples lay on the local precipitation line and are isotopically lighter than the annual mean precipitation value, indicating that recharge occurs predominately in the cooler season (Jasechko et al., 2014). The values from different depth intervals agree within uncertainties. The April samples have a heavier signature, characteristic for warmer temperatures, while the December samples are more depleted indicating recharge under cooler conditions.

3.4. Discussion

The age stratigraphy of groundwater in a homogeneous unconfined aquifer with temporally and spatially constant recharge rate is described by the Vogel model (Vogel, 1967). Equation (8) expresses the age of groundwater at depth z [m], defined as the time since the parcel entered the saturated zone, in an unconfined aquifer with a constant thickness (Cook and Böhlke, 2000). E [m] is the aquifer thickness, ϕ [-] is the porosity, and R [m/yr] is the recharge rate.

$$t(z) = \frac{E \cdot \phi}{R} \ln \left(\frac{E}{E - z} \right) \quad (8)$$

Assuming realistic values for our study location: a 50 m thick aquifer, a recharge rate of 400 mm/years and a porosity of 20% (Gobat, 2015) results in an age profile which is in reasonable agreement with our tracer ages (Fig. 9).

Potential river water infiltration from the Hagneck channel, as suggested by Gobat and Böhi (2016) and Baillieux et al. (2014), seems to have only a minor effect on the vertical age distribution at the borehole location. However, there are differences and deviations between the individual tracers and the calculated profile that deserve further discussion. One intriguing observation is the systematic shift of ^{85}Kr activities between the passive and the active (conventional) sampling, with lower values for the passive sampling. It is very unlikely that this is related to analytical artefacts or contamination since the conventional method is well established and has been proven contamination free. The lower ^{85}Kr values, and thus older ages, of the passive samples must therefore have an hydrological meaning, which is related to the different sampling regimes. Possible effects to be considered are listed in the following.

First, active pumping from a borehole section drains preferentially water from the most permeable layers. In consequence, the age information from a pumped groundwater sample tends to be biased towards the most active or permeable flow compartments (flow averaged age). In contrast, passive sampling leaves more time for equilibration between the active flow zone and less permeable layers. Passive measurements thus represent the mass or volume averaged age of the entire pore space. On a local scale, even an aquifer considered as homogenous represents a stochastic distribution of permeable, and less permeable zones. In our case, silty layers proportion is increasing with depth (Gobat and Böhi, 2016) and the permeability is consequently decreasing. Pumping drains preferentially water from shallow depths whereas the passive measurements are closer to an undisturbed system. For a polluted aquifer, the arrival time of the contaminants would depend on the fast-flowing pathways while the equilibrium bulk concentration would be related to the water mass in both the permeable and stagnant zones.

Another process that needs to be considered is ambient vertical flow in the open borehole induced by a small head gradient with depth. An upwelling flow of older water would explain why the passive ^{85}Kr ages are older than the conventional one. However, this hypothesis is unlikely as there is no screen below the deepest interval and thus, there is no possibility for an upwelling flow in the borehole up to this level. In addition, special care was taken for the positioning of the packers and the samplers in the center of the screen.

Dispersive admixture of water components that recharged during the time of the bomb peak would explain the apparent shift of $^3\text{H}/^3\text{He}$ ages towards old values (Fig. 9) because the age of mixtures is biased towards the components with highest total tritium ($^3\text{H} + ^3\text{He}$) activity. This is evidenced by total tritium values of 25–27 TU at 22 m (Table 1), which exceeds the input of 6–15 TU from local precipitation (Affolter et al.,

2020; Gerber et al., 2018) at the time of recharge.

Finally, a broad distribution of groundwater ages also explains the occurrence of variations in stable isotope composition despite a mean residence time of many years. The difference between the values from April and December (Fig. 10) is interpreted as a seasonal signal carried by the youngest fraction of water composing the exponential age distribution (Vogel, 1967). The relative amplitude of the observed variations between both groups compared to the seasonal recharge variability (winter/summer) is 10% for $\delta^{18}\text{O}$ and 4% for $\delta^2\text{H}$.

4. Conclusion

In this study, we first demonstrate the use of new *in-situ* quasi-passive degassing samplers for Krypton-85 groundwater dating. These membrane contactors allow water degassing directly in the well and gas collection at the surface with minimal logistic facilities in the field. The gas diffusion coefficient through the membrane and thus, the median degassing efficiency and the minimal equilibration time were assessed by laboratory experiments. In the field, the gas collection time is about one day in order to provide the 100–200 L of water required for the analysis. However, it also depends on the natural groundwater flow velocity in the borehole. In open boreholes, a common limitation to passive (or quasi-passive) sampling methods is ambient vertical flow (AVF).

The goal of passive sampling is to obtain groundwater samples with minimal disturbance of the natural flow system. In our case study, we demonstrated a general consistency of ^{85}Kr age profiles obtained by active and passive sampling methods. $^3\text{H}/^3\text{He}$ ages depict a similar depth systematics than ^{85}Kr but with older ages in the deepest level.

Additionally, this study emphasizes the importance of the choice of sampling and dating method in a multi-screened open borehole. Aquifer heterogeneities on various spatial scales affect the sampling and tracer methods differently. Conventional sampling for radio noble gases (^{85}Kr , ^{39}Ar) implies a larger water volume and pump rate, and these samples are therefore inherently weighted towards the most permeable parts of the aquifer. Thus, ^{85}Kr values collected by the new quasi-passive method show slightly older ages compared to samples collected by active pumping from isolated screen intervals. Completely passive sampling systems, such as $^3\text{H}/^3\text{He}$ diffusion samplers, have a high spatial resolution and are consequently very sensitive to small-scale heterogeneities in the aquifer but also to influences induced by borehole drilling and well

construction methods. Such effects impacted the passive $^3\text{H}/^3\text{He}$ samples collected in our study. Purely passive methods would benefit of a careful borehole characterization before sampling. Our new *in-situ* sampler for ^{85}Kr represents an intermediate resolution with a mixing length of ~ 1 m that smooths out micro-scale variabilities while minimizing flow perturbation and maintaining the age stratigraphy on the meter-scale. This corresponds to sampling strategies proposed earlier with moderate pump rates, i.e. low flow sampling (Puls and Barcelona, 1996; Wang et al., 2019). The combined use of different sampling and tracer methods that depict the dynamics and age of waters from distinct aquifer compartments with different conductivities are a valuable tool for the calibration of hydrological models that aim to assess and predict for example the vulnerability of a groundwater body to contamination.

CRedit authorship contribution statement

Stéphanie Musy: Writing - original draft, Conceptualization, Methodology, Investigation, Data curation, Visualization. **Guillaume Meyzonnat:** Investigation, Writing - review & editing. **Florent Barbecot:** Conceptualization, Resources, Writing - review & editing. **Daniel Hunkeler:** Resources, Validation, Writing - review & editing. **Jürgen Sültenfuss:** Resources, Validation, Writing - review & editing. **D. Kip Solomon:** Resources, Validation, Writing - review & editing. **Roland Purtschert:** Supervision, Conceptualization, Investigation, Writing - review & editing, Project administration, Funding acquisition.

Declaration of Competing Interest

The authors declare that they have no known competing financial interests or personal relationships that could have appeared to influence the work reported in this paper.

Acknowledgments

This work was supported by the Swiss National Science Foundation (no.200020/172550). The authors are grateful to Kurt Grossenbacher, Roberto Costa and Laurent Marguet from the Universities of Bern and Neuchâtel for their precious technical support in the field and in the laboratory. We acknowledge Julien Gobat for his help understanding the hydrology of the Seeland Aquifer area, and the department for Water and Wastes from the Canton of Bern for their support.

Appendix

A. Membrane degassing

Gas separation by membranes offers a number of benefits over other gas separation technologies. They are simple to use, cost effective and robust. In this study a dense membrane made of polydimethylsiloxane (PDMS): $[\text{O-Si}(\text{CH}_3)_2]_n$ was used (Dibrov, 2016). The permeability P_i [$\text{cm}^2/\text{s}/\text{atm}$] of a membrane for a specific gas i depends on the gas atoms/molecule size and/or the solubility and diffusivity of the gas in the membrane material. P_i is defined as the product of diffusivity [cm^2/s] and solubility [$\text{cm}^3_{\text{STP}}/\text{cm}^3/\text{atm}$] (Zhang and Cloud, 2006). The driving force for the gas to pass through the membrane is the difference in partial pressure $\Delta p_i = p_{0,i} - p_{1,i}$ between both sides of the membrane. The gas flow through the membrane, Q_i [$\text{cm}^3_{\text{STP}}/\text{s}$] can then be described as:

$$Q_i = \Delta p_i \cdot \frac{P_i \cdot A}{l} \quad (\text{A.1})$$

where l [cm] is the membrane thickness, and A [cm^2] is the area of the membrane in contact with water (Fig. A.1)

The temporal pressure increase in the sampling bottle with volume V is then:

$$\frac{\partial p_{1,i}(t)}{\partial t} = Q_i(t) \cdot \frac{P_A}{V} = (p_{0,i} - p_{1,i}(t)) \cdot \frac{P_i \cdot A \cdot P_A}{l \cdot V} \quad (\text{A.2})$$

where $P_A = 1 \text{ atm}$. We define then the diffusion parameter for each gas species as $K_i = P_A \cdot P_i \left[\frac{\text{cm}^2}{\text{s}} \right]$.

Solving the resulting differential Equation (A.2), for each gas species i results in the partial pressure increase as function of time, $p_{1,i}(t)$ (Equation

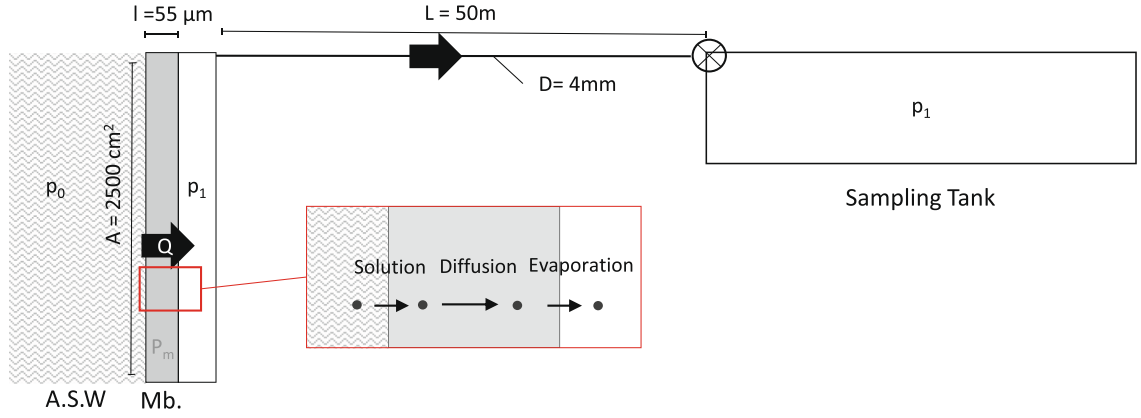


Fig. A.1. Simplified design schematic of a membrane separation process into a sampling tank with volume V . Air equilibrated water (A.E.W) is assumed to be continuously renewed ($p_0 = \text{const.}$). Q is the gas flow through the membrane and through the tubing. Gas permeation through the membrane is composed of a serial solution-diffusion-evaporation process.

(A.3))

$$p_{1,i}(t) = p_{0,i} \left(1 - e^{-\frac{K_i A}{V} t} \right) \quad (\text{A.3})$$

The total pressure in the sampling bottle, $p_1(t)$, is then:

$$p_1(t) = \sum_i p_{1,i}(t) = p_0 \left(1 - e^{-\frac{K A}{V} t} \right) \quad (\text{A.4})$$

where p_0 is the total dissolved gas pressure and K is the total diffusion coefficient for the gas mixture. This equation corresponds to Equation (2). The fractionation that occurs between different gas species i is not affecting the ^{85}Kr dating result because the permeation parameters of ^{85}Kr and ^{84}Kr are almost identical and thus the $^{85}\text{Kr}/\text{Kr}$ ratio is maintained.

B. Gas removal efficiency of the membrane contactor used in this study

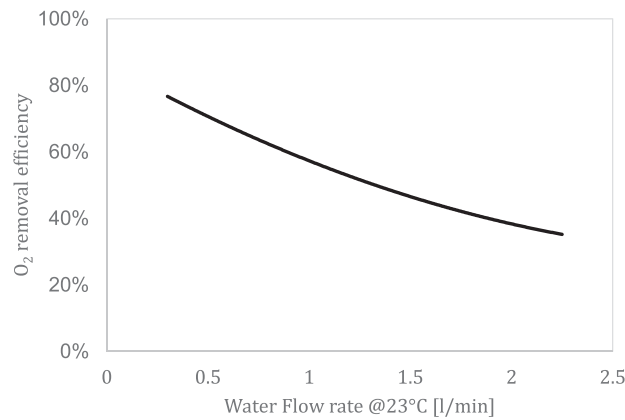


Fig. B.1. Oxygen removal efficiency as function of the water flowrate assuming A.E.W at 10 °C for shell flow and vacuum configuration (Modified from ©Permsselect data sheet). Note: slightly different efficiencies for krypton and other gases do not affect the dating results which depend only on the $^{85}\text{Kr}/\text{Kr}$ ratio.

References

- Affolter, S., et al., 2020. Origin and percolation times of Milandre Cave drip water determined by tritium time series and beryllium-7 data from Switzerland. *J. Environ. Radioact.* 222, 106346 <https://doi.org/10.1016/j.jenvrad.2020.106346>.
- Ahlswede, J., et al., 2013. Update and improvement of the global Krypton-85 emission inventory. *J. Environ. Radioact.* 115, 34–42. <https://doi.org/10.1016/j.jenvrad.2012.07.006>.
- Ahsan, M., Hussain, A., 2016. Mathematical modelling of membrane gas separation using the finite difference method. *Pac. Sci. Rev. A: Nat. Sci. Eng* 18 (1), 47–52. <https://doi.org/10.1016/j.psr.2016.07.001>.
- Althaus, R., et al., 2009. Noble gas tracers for characterisation of flow dynamics and origin of groundwater: a case study in Switzerland. *J. Hydrol.* 370 (1–4), 64–72. <https://doi.org/10.1016/j.jhydrol.2009.02.053>.
- Aoki, N., Makide, Y., 2005. The Concentration of Krypton in the Atmosphere—Its Revision after Half a Century—. *Chem. Lett.* 34 (10), 1396–1397. <https://doi.org/10.1246/cl.2005.1396>.
- Baillieux, A., et al., 2014. Regional water quality patterns in an alluvial aquifer: direct and indirect influences of rivers. *J. Contam. Hydrol.* 169, 123–131. <https://doi.org/10.1016/j.jconhyd.2014.09.002>.
- Bethke, C.M., Johnson, T.M., 2008. Groundwater age and groundwater age dating. *Annu. Rev. Earth Planet. Sci.* 36 (1), 121–152. <https://doi.org/10.1146/annurev.earth.36.031207.124210>.
- Beyle, U., Aeschbach-Hertig, W., Imboden, D.M., Baur, H., Graf, T., Kipfer, R., 2000. A mass spectrometric system for the analysis of noble gases and tritium from water samples. *Environ. Sci. Technol.* 34 (10), 2042–2050.
- Biaggi, D., et al., 2004. 'Hydrogeologie Seeland Stand 2004'. Grundlagen für Schutz und Bewirtschaftung der Grundwasser des Kantons Bern. / Wasserwirtschaftsamt des Kantons Bern (WWA).
- Bollhöfer, A., et al., 2019. Half a century of Krypton-85 activity concentration measured in air over Central Europe: Trends and relevance for dating young groundwater. *J. Environ. Radioact.* 205–206, 7–16. <https://doi.org/10.1016/j.jenvrad.2019.04.014>.
- Brown, G., 2000. 'The Darcy-Weisbach Equation'. Oklahoma State University–Stillwater. Available at: <http://bae.okstate.edu/faculty-sites/Darcy/DarcyWeisbach/Darcy-WeisbachEq.htm>.
- Cochand, F., et al., 2019. 'Groundwater Model of the Seeland Aquifer'. Bernese Office for Water and Wastes.
- Collon, P., Kutschera, W., Lu, Z.-T., 2004. Tracing noble gas radionuclides in the environment. *Annu. Rev. Nucl. Part. Sci.* 54 (1), 39–67. <https://doi.org/10.1146/annurev.nucl.53.041002.110622>.
- Cook, P.G., Böhlke, J.-K., 2000. 'Determining timescales for groundwater flow and solutes transport', in *Environmental Tracers in Subsurface Hydrology*. Springer Science+Business Media, LLC. CSIRO Land and Water, Glen Osmond, Australia: Cook Peter G., Herczeg Andrew L., pp. 1–30. Available at: <https://link.springer.com/content/pdf/bfm%3A978-1-4615-4557-6/1.pdf>.
- Cook, P.G., Solomon, D.K., 1997. Recent advances in dating young groundwater: chlorofluorocarbons, ^3HHe and ^{85}Kr . *J. Hydrol.* 191 (1–4), 245–265.
- Corcho Alvarado, J.A., Barbécot, F., Purtschert, R., 2009. Ambient vertical flow in long-screen wells: a case study in the Fontainebleau Sands Aquifer (France). *Hydrogeol. J.* 17 (2), 425–431. <https://doi.org/10.1007/s10040-008-0383-1>.
- Darling, W.G., et al., 2012. The practicalities of using CFCs and SF6 for groundwater dating and tracing. *Appl. Geochem.* 27 (9), 1688–1697. <https://doi.org/10.1016/j.apgeochem.2012.02.005>.
- Dibrov, G., 2016 'Polydimethylsiloxane Membrane', in Drioli, E. and Giorno, L. (eds) *Encyclopedia of Membranes*. Berlin, Heidelberg: Springer Berlin Heidelberg, pp. 1–2. 10.1007/978-3-642-40872-4_1401-1.
- Gardner, P., Solomon, D.K., 2009. An advanced passive diffusion sampler for the determination of dissolved gas concentrations: passive diffusion samplers. *Water Resour. Res.* 45 (6) <https://doi.org/10.1029/2008WR007399>.
- Gerber, C., 2012 Development of a New Degassing System for Groundwater Dating with Radio-Noble gases and Application of ^{85}Kr in two Case Studies. Master Thesis. Bern: University of Bern.
- Gerber, C., Purtschert, R., Hunkeler, D., Hug, R., Sültenfuss, J., 2018. Using environmental tracers to determine the relative importance of travel times in the unsaturated and saturated zones for the delay of nitrate reduction measures. *J. Hydrol.* 561, 250–266. <https://doi.org/10.1016/j.jhydrol.2018.03.043>.
- Gobat, J., 2015 Vertikale Schichtung der Grundwasserzusammensetzung im Zuströmbereich der Trinkwasserfassung von Kappelen (BE). Master Thesis. University of Neuchâtel, CHYN Institute.
- Gobat, J., Böhi, D., 2016. 'Strengths and weaknesses of groundwater models on the basis of a case study in the Bernese "Seeland"', Swiss bulletin for applied geology 21, 21/1, pp. 53–67.
- Harrington, G.A., Cook, E., Robinson, N.I., 2000. Equilibration Times of Gas-Filled Diffusion Samplers in Slow-Moving Ground Water Systems, Groundwater Monitoring and Remediation, 20(2), pp. 60–65.
- Heaton, T.H.E., Vogel, J.C., 1981. "Excess air" in groundwater. *J. Hydrol.* 50, 201–216.
- Heier, K.S., 1965. Radioactive elements in the continental crust. *Nature* 208 (5009), 479–480.
- Huber, C., Leuenberger, M., 2005. On-line systems for continuous water and gas isotope ratio measurements. *Isot. Environ. Health Stud.* 41 (3), 189–205. <https://doi.org/10.1080/10256100500229942>.
- Jasechko, S., et al., 2014. The pronounced seasonality of global groundwater recharge. *Water Resour. Res.* 50 (11), 8845–8867. <https://doi.org/10.1002/2014WR015809>.
- Kagabu, M., et al., 2017. Groundwater age determination using ^{85}Kr and multiple age tracers (SF 6, CFCs, and 3 H) to elucidate regional groundwater flow systems. *J. Hydrol.: Reg. Stud.* 12, 165–180. <https://doi.org/10.1016/j.ejrh.2017.05.003>.
- Kersting, A., Schlosser, C., Bollhöfer, A., Suckow, A., 2020. Evaluating 5 decades of atmospheric ^{85}Kr measurements in the southern hemisphere to derive an input function for dating water and ice with implications for interhemispheric circulation and the global ^{85}Kr emission inventory. *J. Environ. Radioact.* 225, 106451. <https://doi.org/10.1016/j.jenvrad.2020.106451>.
- Kozel, R., 1992 Erfassung organischer Spurenbelastungen, insbesondere durch Pflanzenbehandlungsmittel, in oberflächennahen Lockergesteins-Grundwässern. PhD Thesis. University of Neuchâtel, CHYN Institute.
- Loosli, H.H., Purtschert, R., 2005. 'Rare gases', in *Isotopes in the Water Cycle: Past, Present and Future of a Developing Science*. I.A.E.A., pp. 91–95.
- Lu, Z.-T., et al., 2014. Tracer applications of noble gas radionuclides in the geosciences. *Earth Sci. Rev.* 138, 196–214. <https://doi.org/10.1016/j.earscirev.2013.09.002>.
- Maloszewski, P., Zuber, A., 1982. Determining the turnover time of groundwater systems with the aid of environmental tracers. *J. Hydrol.* 57 (3–4), 207–231. [https://doi.org/10.1016/0022-1694\(82\)90147-0](https://doi.org/10.1016/0022-1694(82)90147-0).
- McCallum, J.L., Cook, P.G., Simmons, C.T., 2015. Limitations of the use of environmental tracers to infer groundwater age. *Groundwater* 53 (S1), 56–70. <https://doi.org/10.1111/gwat.12237>.
- McMillan, L.A., et al., 2014. Influence of vertical flows in wells on groundwater sampling. *J. Contam. Hydrol.* 169, 50–61. <https://doi.org/10.1016/j.jconhyd.2014.05.005>.
- Mezzonnati, G., et al., 2018. High-resolution wellbore temperature logging combined with a borehole-scale heat budget: conceptual and analytical approaches to characterize hydraulically active fractures and groundwater origin. *Geofluids* 2018, 20.
- Nakata, K., et al., 2019. Degassing behavior of noble gases from groundwater during groundwater sampling. *Appl. Geochem.* 104, 60–70. <https://doi.org/10.1016/j.apgeochem.2019.03.007>.
- Ohta, T., et al., 2009. Separation of dissolved Kr from a water sample by means of a hollow fiber membrane. *J. Hydrol.* 376 (1–2), 152–158. <https://doi.org/10.1016/j.jhydrol.2009.07.022>.
- Puls, R., Barcelona, M., 1996. Ground Water Issue: Low-Flow (Minimal Drawdown) Ground-Water Sampling Procedures, p. 12.
- Purtschert, R., 2008. 'Timescales and tracers', *Natural groundwater quality*, pp. 91–108.
- Purtschert, R., Yokochi, R., 2013. 'Krypton-81 dating of old groundwater', in *Isotope methods for dating old groundwater*. I.A.E.A Library. Vienna, pp. 91–124.
- Raja Sekhar, G.P., Sano, O., 2000. Viscous flow past a circular/spherical void in porous media – an application to measurement of the velocity of groundwater by the single boring method. *J. Phys. Soc. Jpn.* 69 (8), 2479–2484. <https://doi.org/10.1143/JPSJ.69.2479>.
- Sanders, D.F., et al., 2013. Energy-efficient polymeric gas separation membranes for a sustainable future: a review. *Polymer* 54 (18), 4729–4761. <https://doi.org/10.1016/j.polymer.2013.05.075>.
- Singh, B., Chen, J., 2014. Nuclear Data Sheets for A=85. *Nucl. Data Sheets* 116, 1–162. <https://doi.org/10.1016/j.nds.2014.01.001>.
- Solomon, D.K., Hunt, A., Poreda, R.J., 1996. Source of radiogenic helium 4 in shallow aquifers: Implications for dating young groundwater. *Water Resour. Res.* 32 (6), 1805–1813. <https://doi.org/10.1029/96WR00600>.
- Suckow, A., 2014. The age of groundwater – definitions, models and why we do not need this term. *Appl. Geochem.* 50, 222–230. <https://doi.org/10.1016/j.apgeochem.2014.04.016>.
- Sültenfuß, J., Roether, W., Rhein, M., 2009. The Bremen mass spectrometric facility for the measurement of helium isotopes, neon, and tritium in water. *Isot. Environ. Health Stud.* 45 (2), 83–95. <https://doi.org/10.1080/10256100902871929>.
- Tomonaga, Y., Marzocchi, R., Pera, S., Pfeifer, H.-R., Kipfer, R., Decrouy, L., Vennemann, T., 2017. Using noble-gas and stable-isotope data to determine groundwater origin and flow regimes: Application to the Ceneri Base Tunnel (Switzerland). *J. Hydrol.* 545, 395–409. <https://doi.org/10.1016/j.jhydrol.2016.11.043>.
- Torgersen, T., et al., 2013. 'Defining Groundwater Age', in *Isotope methods for dating old groundwater*. I.A.E.A Library. Vienna, pp. 21–32.
- Visser, A., Broers, H.P., Bierkens, M.F.P., 2007. Dating degassed groundwater with $^3\text{H}/^3\text{He}$. *Water Resour. Res.* 43 (10) <https://doi.org/10.1029/2006WR005847>.
- Vogel, J.C., 1967. Investigation of groundwater flow with radiocarbon, Isotopes in Hydrology.
- Wang, Y., Hou, D., Qi, S., O'Connor, D., Luo, J., 2019. High stress low-flow (HSLF) sampling: a newly proposed groundwater purge and sampling approach. *Sci. Total Environ.* 6.
- White, F.M., 1988. Heat and Mass transfer. Addison-Wesley (Addison-Wesley series in mechanical engineering).

- Yokochi, R., 2016. Recent developments on field gas extraction and sample preparation methods for radiokrypton dating of groundwater. *J. Hydrol.* 540, 368–378. <https://doi.org/10.1016/j.jhydrol.2016.06.020>.
- Zappala, J.C., et al., 2017. Rapid processing of $^{85}\text{Kr}/\text{Kr}$ ratios using Atom Trap Trace Analysis. *Water Resour. Res.* 53 (3), 2553–2558. <https://doi.org/10.1002/2016WR020082>.
- Zhang, H., Cloud, A., 2006. 'The permeability characteristics of silicone rubber', Proceedings of 2006 SAMPE Fall Technical Conference.
- Zuber, A., et al., 2011. On some methodological problems in the use of environmental tracers to estimate hydrogeologic parameters and to calibrate flow and transport models. *Hydrogeol. J.* 19 (1), 53–69. <https://doi.org/10.1007/s10040-010-0655-4>.

Appendix

A.1 ^{39}Ar underground production in the context of groundwater dating: importance of muon-induced processes

Stephanie Musy, Klaus Hinsby, Lars Trolldborg, Hugo Delottier, Sophie Guillon, Philip Brunner and Roland Purtschert

Manuscript in preparation for *Geochimica et Cosmochimica Acta*

Abstract ^{39}Ar ($t_{1/2} = 269$ yr) is a well established method for dating groundwater on timescales from 50 to 1000 years. Underground production processes with neutrons from natural radioactivity in rock (U and Th decay chains) as well as with primary cosmogenic neutrons were identified for many decades (Loosli et al., 1989; Andrews et al., 1986; Fabryka-Martin, 1988; Šrámek et al., 2017). More recently, muon-induced reactions, i.e. slow negative muon capture and reactions with muon-induced neutrons, were documented for ^{39}Ar subsurface production in the deep context of WIMP research (Mei et al., 2010). However, the contribution from these particles was never considered for groundwater dating applications.

In the present paper, we first review all relevant production channels for ^{39}Ar production in the underground. Properly accounting for neutron interaction reactions was possible owing to numerical simulations of their energy spectra at depths relevant for groundwater dating with the code FLUKA (Grieger et al., 2020). The activities sampled in the Danish shallow aquifer system were compared to calculations of emanated activities based on (i) the depth-dependent production rates, (ii) the emanation fractions assessed by irradiation experiments (Musy et al., 2021; Johnson et al., 2021), and (iii) the vertical velocity distributions constrained with particle tracking in a numerical model [DK-Model, Henriksen et al. (2003)]. The significance of muon-induced processes for ^{39}Ar dissolved activities was unequivocally demonstrated for the first time. ^{37}Ar ($t_{1/2} = 35$ days) is produced by very similar processes to ^{39}Ar but owing to its shorter half-life, it can be used as an indicator of local underground production in an aquifer.

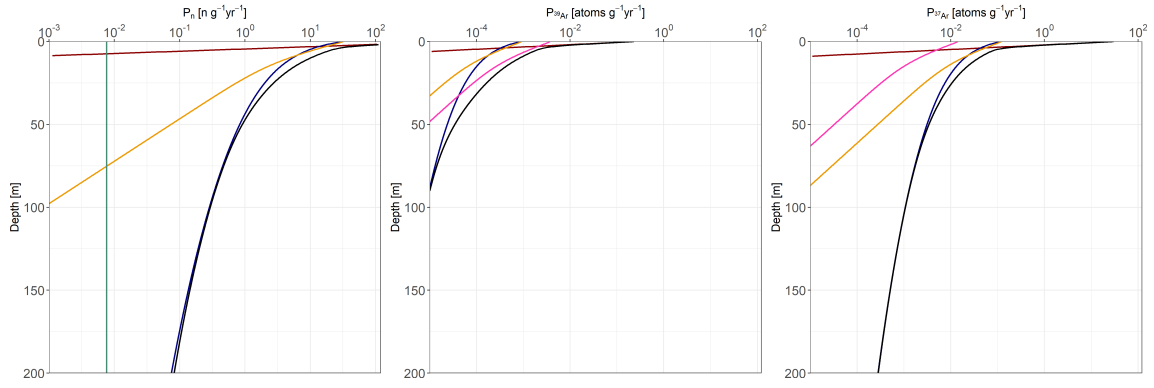
For the purpose of extrapolating these conclusions to a broader range of recharge scenarios, the production rate profiles were implemented in a synthetic numerical model set up in HydroGeoSphere (Aquanty Inc., 2022; Delottier et al., 2022). These simulations demonstrated that underground production is negligible in the case where water infiltrated freely in a porous aquifer. In contrast, the presence of a confining layer impeding the water recharge at shallow – intermediate depths (< 50 m), as is the case in Denmark for instance, leads to over-modern ^{39}Ar activities, and therefore potentially significant age biases. In the future, special attention should be paid to the recharge patterns when using ^{39}Ar for dating groundwater. In doubt, measuring ^{37}Ar activity in the same sample may indicate signs of underground production.

A.2 Radioargon production calculations for typical rock compositions

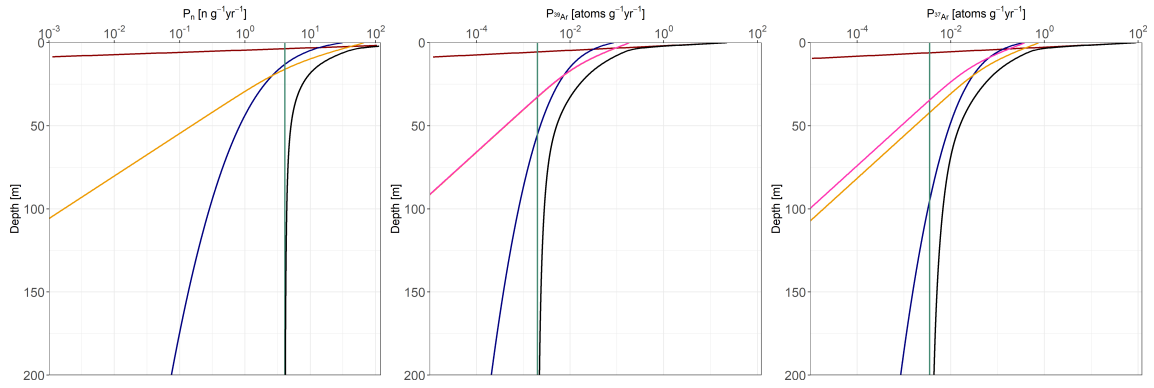
The radioargon $Y_{\mu^-}^{39}$ and $Y_{\mu^-}^{37}$ and neutron $Y_{\mu^-}^n$ production yield per stopped μ^- , as well as neutron production rate from U/Th decay chains ($P_{n,U/Th}$ [$\text{n g}^{-1} \text{yr}^{-1}$]) were calculated following the principle detailed in Chapter 3 for the typical rock compositions computed by Fabryka-Martin (1988). Figure A.2 shows the production profiles calculated with the values summarized in Table A.1.

Table A.1: Elemental weight fractions for the typical rock compositions compiled by (Fabryka-Martin, 1988). Calculated radioargon ($Y_{\mu^-}^{Ar}$) and neutron $Y_{\mu^-}^n$ production yields per stopped muons (Eq. 3.24 and 3.34)

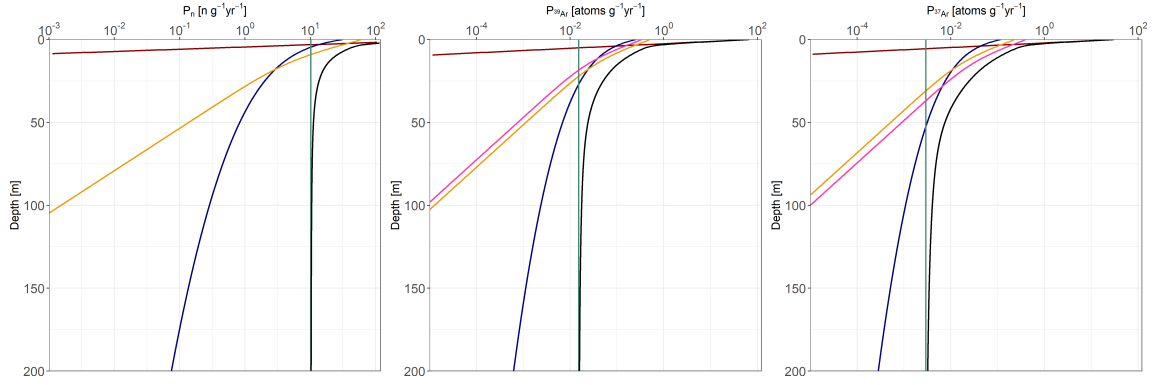
	Ultramafic	Basalt	High-Ca Granite	Low-Ca Granite	Clay, shales	Sandstones	Carbonates
C	1.0E-04	1.0E-04	3.0E-04	3.0E-04	1.0E-02	3.0E-04	1.1E-01
O	4.0E-01	4.0E-01	4.7E-01	4.8E-01	4.9E-01	4.4E-01	4.8E-01
F	1.0E-04	4.0E-04	5.2E-04	8.5E-04	5.0E-04	2.7E-04	3.3E-04
Na	4.2E-03	1.8E-02	2.8E-02	2.6E-02	6.6E-04	3.3E-03	4.0E-04
Mg	2.0E-01	4.6E-02	9.4E-03	1.6E-03	1.3E-02	7.0E-03	4.7E-02
Al	2.0E-02	7.8E-02	8.2E-02	7.2E-02	1.3E-02	2.5E-02	4.2E-03
Si	2.1E-01	2.3E-01	3.1E-01	3.5E-01	2.4E-01	3.7E-01	2.4E-02
K	4.0E-05	8.3E-03	2.5E-02	4.2E-02	2.3E-02	1.1E-02	2.7E-03
Ca	2.5E-02	7.6E-02	2.5E-02	5.1E-03	2.5E-02	3.9E-02	3.0E-01
Ti	3.0E-04	1.4E-02	3.4E-03	1.2E-03	4.5E-03	1.5E-03	4.0E-04
Fe	9.4E-02	8.7E-02	3.0E-02	1.4E-02	3.3E-02	9.8E-03	3.8E-03
Th	4.0E-09	4.0E-06	8.5E-06	1.7E-05	2.2E-05	1.7E-06	1.7E-06
U	1.0E-09	1.0E-06	3.0E-06	3.0E-06	3.2E-06	4.5E-07	2.2E-06
$Y_{\mu^-}^{39}$	2.0E-05	9.6E-04	1.8E-03	2.8E-03	1.6E-03	9.6E-04	1.4E-03
$Y_{\mu^-}^{37}$	7.5E-05	2.0E-03	2.1E-03	2.8E-03	2.0E-03	1.5E-03	4.9E-03
$Y_{\mu^-}^n$	0.17	0.35	0.32	0.32	0.30	0.30	0.29
$P_{n,U/Th}$	7.6E-03	4.07	10.2	14.1	15.1	0.977	2.77



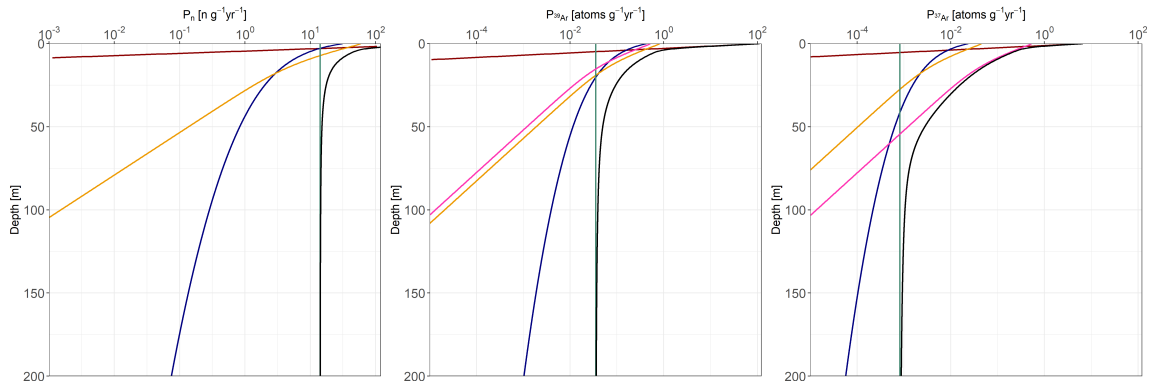
(a) Ultramafic



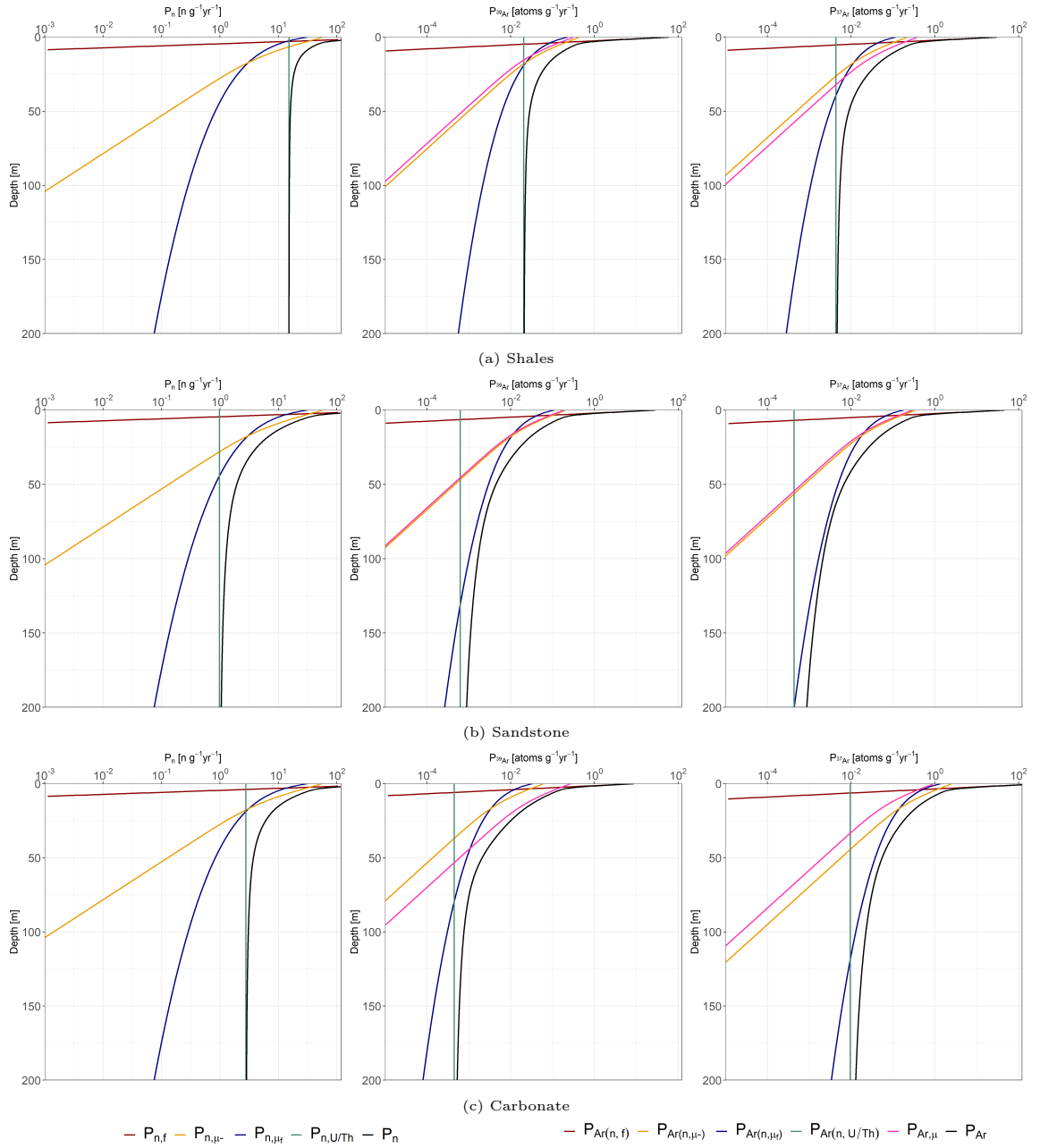
(b) Basalt



(c) High-Ca granite



(d) Low-Ca granite

Figure A.2: Neutron, ^{39}Ar , and ^{37}Ar production rate profiles in typical rocks compiled by (Fabryka-Martin, 1988)

A.3 Neutron energy spectra simulations data

Table A.2: Neutron flux simulated with FLUKA by Grieger et al. (2020)

E [MeV]	ϕ_n [cm ⁻² s ⁻¹]					
	WS		MK1		MK2	
	(α, n)	(μ, n)	(α, n)	(μ, n)	(α, n)	(μ, n)
4.5×10^{-11}	1.9×10^{-10}	3.7×10^{-11}	3.5×10^{-11}	1.3×10^{-11}	0.0	0.0
2.4×10^{-10}	2.4×10^{-9}	5.1×10^{-10}	5.5×10^{-10}	2.6×10^{-10}	0.0	0.0
3.5×10^{-10}	5.7×10^{-9}	4.3×10^{-10}	9.9×10^{-10}	1.6×10^{-10}	3.4×10^{-13}	0.0
5.2×10^{-10}	1.2×10^{-8}	2.3×10^{-9}	2.1×10^{-9}	5.7×10^{-10}	2.1×10^{-12}	0.0
7.6×10^{-10}	2.8×10^{-8}	2.8×10^{-9}	4.5×10^{-9}	1.8×10^{-9}	2.6×10^{-11}	0.0
1.1×10^{-9}	5.8×10^{-8}	3.8×10^{-9}	1.0×10^{-8}	6.9×10^{-9}	4.7×10^{-11}	0.0
1.6×10^{-9}	1.2×10^{-7}	1.3×10^{-8}	2.3×10^{-8}	5.7×10^{-9}	1.1×10^{-10}	4.3×10^{-12}
2.4×10^{-9}	2.7×10^{-7}	4.8×10^{-8}	5.0×10^{-8}	2.0×10^{-8}	2.7×10^{-10}	1.3×10^{-10}
3.5×10^{-9}	5.8×10^{-7}	1.2×10^{-7}	1.1×10^{-7}	7.2×10^{-8}	7.5×10^{-10}	0.0
5.1×10^{-9}	1.2×10^{-6}	1.8×10^{-7}	2.2×10^{-7}	8.1×10^{-8}	1.6×10^{-9}	6.9×10^{-10}
7.5×10^{-9}	2.5×10^{-6}	3.3×10^{-7}	4.6×10^{-7}	1.6×10^{-7}	3.8×10^{-9}	2.0×10^{-9}
1.1×10^{-8}	4.9×10^{-6}	7.0×10^{-7}	9.1×10^{-7}	3.5×10^{-7}	8.4×10^{-9}	1.5×10^{-9}
1.6×10^{-8}	9.0×10^{-6}	1.2×10^{-6}	1.7×10^{-6}	6.6×10^{-7}	1.8×10^{-8}	5.4×10^{-9}
2.4×10^{-8}	1.5×10^{-5}	2.3×10^{-6}	2.9×10^{-6}	1.2×10^{-6}	3.7×10^{-8}	1.2×10^{-8}
3.5×10^{-8}	2.3×10^{-5}	3.3×10^{-6}	4.4×10^{-6}	1.9×10^{-6}	6.4×10^{-8}	2.4×10^{-8}
5.1×10^{-8}	3.0×10^{-5}	4.4×10^{-6}	5.4×10^{-6}	2.4×10^{-6}	9.6×10^{-8}	3.8×10^{-8}
7.4×10^{-8}	3.1×10^{-5}	4.5×10^{-6}	5.2×10^{-6}	2.5×10^{-6}	1.1×10^{-7}	4.0×10^{-8}
1.1×10^{-7}	2.4×10^{-5}	3.7×10^{-6}	3.5×10^{-6}	1.4×10^{-6}	1.1×10^{-7}	3.3×10^{-8}
1.6×10^{-7}	1.8×10^{-5}	3.0×10^{-6}	2.0×10^{-6}	7.8×10^{-7}	1.4×10^{-7}	6.9×10^{-8}
2.3×10^{-7}	1.5×10^{-5}	2.7×10^{-6}	1.3×10^{-6}	4.8×10^{-7}	2.2×10^{-7}	1.1×10^{-7}
3.4×10^{-7}	1.4×10^{-5}	2.4×10^{-6}	1.0×10^{-6}	3.9×10^{-7}	3.1×10^{-7}	1.3×10^{-7}
4.7×10^{-7}	1.3×10^{-5}	2.4×10^{-6}	9.8×10^{-7}	3.7×10^{-7}	4.5×10^{-7}	2.5×10^{-7}
5.8×10^{-7}	1.3×10^{-5}	2.5×10^{-6}	9.5×10^{-7}	3.6×10^{-7}	6.1×10^{-7}	3.9×10^{-7}
6.5×10^{-7}	1.3×10^{-5}	2.7×10^{-6}	9.3×10^{-7}	3.8×10^{-7}	6.9×10^{-7}	7.3×10^{-7}
7.5×10^{-7}	1.3×10^{-5}	2.4×10^{-6}	9.3×10^{-7}	3.6×10^{-7}	8.3×10^{-7}	5.8×10^{-7}
8.5×10^{-7}	1.3×10^{-5}	2.6×10^{-6}	9.2×10^{-7}	3.4×10^{-7}	9.1×10^{-7}	4.2×10^{-7}
9.9×10^{-7}	1.3×10^{-5}	2.5×10^{-6}	9.1×10^{-7}	3.5×10^{-7}	1.0×10^{-6}	7.5×10^{-7}
1.3×10^{-6}	1.3×10^{-5}	2.5×10^{-6}	9.0×10^{-7}	3.1×10^{-7}	1.2×10^{-6}	9.8×10^{-7}
1.6×10^{-6}	1.3×10^{-5}	2.8×10^{-6}	8.8×10^{-7}	3.1×10^{-7}	1.5×10^{-6}	1.1×10^{-6}
2.1×10^{-6}	1.3×10^{-5}	2.5×10^{-6}	8.8×10^{-7}	3.4×10^{-7}	1.8×10^{-6}	1.6×10^{-6}
2.7×10^{-6}	1.3×10^{-5}	2.8×10^{-6}	8.8×10^{-7}	3.2×10^{-7}	2.0×10^{-6}	2.0×10^{-6}

Continued on next page

3.5×10^{-6}	1.3×10^{-5}	2.9×10^{-6}	8.6×10^{-7}	2.9×10^{-7}	2.3×10^{-6}	2.6×10^{-6}
4.5×10^{-6}	1.3×10^{-5}	2.7×10^{-6}	8.5×10^{-7}	4.1×10^{-7}	2.5×10^{-6}	2.2×10^{-6}
5.7×10^{-6}	1.3×10^{-5}	3.2×10^{-6}	8.6×10^{-7}	3.3×10^{-7}	2.8×10^{-6}	2.5×10^{-6}
7.3×10^{-6}	1.3×10^{-5}	3.2×10^{-6}	8.5×10^{-7}	4.0×10^{-7}	3.0×10^{-6}	2.9×10^{-6}
9.4×10^{-6}	1.3×10^{-5}	3.0×10^{-6}	8.6×10^{-7}	3.1×10^{-7}	3.2×10^{-6}	8.3×10^{-6}
1.2×10^{-5}	1.4×10^{-5}	3.2×10^{-6}	8.5×10^{-7}	2.9×10^{-7}	3.4×10^{-6}	3.2×10^{-6}
1.6×10^{-5}	1.4×10^{-5}	3.0×10^{-6}	8.5×10^{-7}	3.1×10^{-7}	3.6×10^{-6}	4.9×10^{-6}
2.0×10^{-5}	1.4×10^{-5}	3.2×10^{-6}	8.5×10^{-7}	3.2×10^{-7}	3.8×10^{-6}	4.4×10^{-6}
2.6×10^{-5}	1.4×10^{-5}	3.4×10^{-6}	8.5×10^{-7}	3.7×10^{-7}	4.0×10^{-6}	4.4×10^{-6}
3.3×10^{-5}	1.4×10^{-5}	3.3×10^{-6}	8.4×10^{-7}	3.1×10^{-7}	4.2×10^{-6}	5.3×10^{-6}
4.2×10^{-5}	1.4×10^{-5}	3.7×10^{-6}	8.3×10^{-7}	3.8×10^{-7}	4.3×10^{-6}	5.4×10^{-6}
5.4×10^{-5}	1.4×10^{-5}	4.3×10^{-6}	8.3×10^{-7}	3.5×10^{-7}	4.4×10^{-6}	5.0×10^{-6}
7.0×10^{-5}	1.4×10^{-5}	3.7×10^{-6}	8.3×10^{-7}	4.8×10^{-7}	4.5×10^{-6}	5.5×10^{-6}
8.9×10^{-5}	1.4×10^{-5}	4.1×10^{-6}	8.2×10^{-7}	3.5×10^{-7}	4.6×10^{-6}	5.6×10^{-6}
1.1×10^{-4}	1.4×10^{-5}	3.5×10^{-6}	8.2×10^{-7}	3.1×10^{-7}	4.7×10^{-6}	5.8×10^{-6}
1.5×10^{-4}	1.4×10^{-5}	3.7×10^{-6}	8.2×10^{-7}	3.1×10^{-7}	4.8×10^{-6}	6.3×10^{-6}
1.9×10^{-4}	1.4×10^{-5}	3.8×10^{-6}	8.0×10^{-7}	3.4×10^{-7}	4.8×10^{-6}	6.0×10^{-6}
2.4×10^{-4}	1.4×10^{-5}	4.4×10^{-6}	8.0×10^{-7}	3.2×10^{-7}	4.9×10^{-6}	6.8×10^{-6}
3.1×10^{-4}	1.4×10^{-5}	4.6×10^{-6}	7.9×10^{-7}	3.2×10^{-7}	5.0×10^{-6}	6.3×10^{-6}
4.0×10^{-4}	1.4×10^{-5}	5.3×10^{-6}	7.8×10^{-7}	3.3×10^{-7}	5.1×10^{-6}	7.3×10^{-6}
5.1×10^{-4}	1.4×10^{-5}	4.8×10^{-6}	7.7×10^{-7}	3.2×10^{-7}	5.2×10^{-6}	7.6×10^{-6}
6.6×10^{-4}	1.4×10^{-5}	4.6×10^{-6}	7.6×10^{-7}	3.4×10^{-7}	5.4×10^{-6}	7.5×10^{-6}
8.5×10^{-4}	1.4×10^{-5}	4.9×10^{-6}	7.4×10^{-7}	4.4×10^{-7}	5.5×10^{-6}	8.6×10^{-6}
1.1×10^{-3}	1.4×10^{-5}	4.9×10^{-6}	7.2×10^{-7}	3.1×10^{-7}	5.7×10^{-6}	9.1×10^{-6}
1.3×10^{-3}	1.5×10^{-5}	4.8×10^{-6}	7.4×10^{-7}	4.0×10^{-7}	7.7×10^{-6}	1.2×10^{-5}
1.4×10^{-3}	1.5×10^{-5}	5.1×10^{-6}	7.4×10^{-7}	5.0×10^{-7}	8.0×10^{-6}	1.2×10^{-5}
1.5×10^{-3}	1.5×10^{-5}	5.1×10^{-6}	7.4×10^{-7}	3.5×10^{-7}	7.9×10^{-6}	1.3×10^{-5}
1.6×10^{-3}	1.5×10^{-5}	5.3×10^{-6}	7.3×10^{-7}	3.6×10^{-7}	7.9×10^{-6}	1.4×10^{-5}
1.8×10^{-3}	1.5×10^{-5}	5.5×10^{-6}	7.3×10^{-7}	3.3×10^{-7}	8.1×10^{-6}	1.2×10^{-5}
1.9×10^{-3}	1.5×10^{-5}	5.1×10^{-6}	7.4×10^{-7}	3.6×10^{-7}	8.4×10^{-6}	1.4×10^{-5}
2.1×10^{-3}	1.5×10^{-5}	5.1×10^{-6}	7.3×10^{-7}	3.6×10^{-7}	8.5×10^{-6}	1.4×10^{-5}
2.4×10^{-3}	1.5×10^{-5}	5.4×10^{-6}	7.4×10^{-7}	3.6×10^{-7}	8.3×10^{-6}	1.6×10^{-5}
2.5×10^{-3}	1.5×10^{-5}	5.5×10^{-6}	7.3×10^{-7}	5.2×10^{-7}	8.4×10^{-6}	1.4×10^{-5}
2.7×10^{-3}	1.5×10^{-5}	5.1×10^{-6}	7.5×10^{-7}	3.9×10^{-7}	8.4×10^{-6}	1.4×10^{-5}
2.8×10^{-3}	1.5×10^{-5}	4.8×10^{-6}	7.4×10^{-7}	2.8×10^{-7}	8.3×10^{-6}	1.4×10^{-5}
2.9×10^{-3}	1.5×10^{-5}	5.3×10^{-6}	7.5×10^{-7}	4.7×10^{-7}	8.2×10^{-6}	1.4×10^{-5}
3.2×10^{-3}	1.5×10^{-5}	5.4×10^{-6}	7.3×10^{-7}	3.9×10^{-7}	8.0×10^{-6}	1.4×10^{-5}

Continued on next page

3.5×10^{-3}	1.5×10^{-5}	5.4×10^{-6}	7.6×10^{-7}	4.5×10^{-7}	7.2×10^{-6}	1.3×10^{-5}
3.9×10^{-3}	1.5×10^{-5}	5.6×10^{-6}	7.6×10^{-7}	3.3×10^{-7}	6.3×10^{-6}	1.2×10^{-5}
4.2×10^{-3}	1.5×10^{-5}	5.3×10^{-6}	7.6×10^{-7}	3.0×10^{-7}	5.6×10^{-6}	1.1×10^{-5}
4.4×10^{-3}	1.5×10^{-5}	5.4×10^{-6}	7.5×10^{-7}	3.6×10^{-7}	5.9×10^{-6}	9.9×10^{-6}
4.8×10^{-3}	1.5×10^{-5}	5.2×10^{-6}	7.6×10^{-7}	3.9×10^{-7}	6.1×10^{-6}	1.1×10^{-5}
5.3×10^{-3}	1.6×10^{-5}	6.1×10^{-6}	8.0×10^{-7}	3.6×10^{-7}	6.6×10^{-6}	1.1×10^{-5}
5.9×10^{-3}	1.4×10^{-5}	5.5×10^{-6}	8.3×10^{-7}	5.2×10^{-7}	5.3×10^{-6}	1.1×10^{-5}
6.7×10^{-3}	1.5×10^{-5}	6.1×10^{-6}	8.3×10^{-7}	3.7×10^{-7}	5.7×10^{-6}	1.1×10^{-5}
7.6×10^{-3}	1.5×10^{-5}	5.9×10^{-6}	8.0×10^{-7}	3.4×10^{-7}	4.9×10^{-6}	1.0×10^{-5}
8.6×10^{-3}	1.5×10^{-5}	5.7×10^{-6}	6.7×10^{-7}	2.8×10^{-7}	4.1×10^{-6}	8.2×10^{-6}
9.7×10^{-3}	1.6×10^{-5}	6.5×10^{-6}	7.2×10^{-7}	3.4×10^{-7}	7.6×10^{-6}	1.5×10^{-5}
1.1×10^{-2}	1.6×10^{-5}	6.5×10^{-6}	7.1×10^{-7}	4.6×10^{-7}	9.6×10^{-6}	1.8×10^{-5}
1.2×10^{-2}	1.6×10^{-5}	7.0×10^{-6}	7.1×10^{-7}	3.8×10^{-7}	8.9×10^{-6}	1.7×10^{-5}
1.4×10^{-2}	1.6×10^{-5}	7.3×10^{-6}	7.1×10^{-7}	3.6×10^{-7}	9.6×10^{-6}	2.0×10^{-5}
1.6×10^{-2}	1.6×10^{-5}	7.2×10^{-6}	7.0×10^{-7}	4.4×10^{-7}	6.2×10^{-6}	1.3×10^{-5}
1.8×10^{-2}	1.6×10^{-5}	7.7×10^{-6}	7.0×10^{-7}	4.3×10^{-7}	1.2×10^{-5}	2.4×10^{-5}
2.0×10^{-2}	1.7×10^{-5}	8.9×10^{-6}	6.9×10^{-7}	3.9×10^{-7}	1.6×10^{-5}	3.2×10^{-5}
2.2×10^{-2}	1.7×10^{-5}	8.3×10^{-6}	6.8×10^{-7}	3.7×10^{-7}	2.1×10^{-5}	4.5×10^{-5}
2.3×10^{-2}	1.7×10^{-5}	8.3×10^{-6}	6.8×10^{-7}	4.0×10^{-7}	2.1×10^{-5}	4.3×10^{-5}
2.4×10^{-2}	1.7×10^{-5}	9.8×10^{-6}	7.0×10^{-7}	4.2×10^{-7}	2.7×10^{-5}	5.9×10^{-5}
2.4×10^{-2}	1.7×10^{-5}	9.4×10^{-6}	8.1×10^{-7}	6.2×10^{-7}	2.9×10^{-5}	5.9×10^{-5}
2.5×10^{-2}	1.9×10^{-5}	1.1×10^{-5}	1.3×10^{-6}	9.1×10^{-7}	2.6×10^{-5}	5.8×10^{-5}
2.7×10^{-2}	1.6×10^{-5}	8.5×10^{-6}	9.3×10^{-7}	4.2×10^{-7}	5.4×10^{-6}	1.5×10^{-5}
3.0×10^{-2}	1.4×10^{-5}	7.0×10^{-6}	5.4×10^{-7}	3.1×10^{-7}	2.3×10^{-6}	7.0×10^{-6}
3.3×10^{-2}	1.3×10^{-5}	7.0×10^{-6}	5.6×10^{-7}	3.7×10^{-7}	7.7×10^{-6}	2.1×10^{-5}
3.5×10^{-2}	9.2×10^{-6}	4.5×10^{-6}	4.7×10^{-7}	4.5×10^{-7}	9.7×10^{-6}	3.0×10^{-5}
3.6×10^{-2}	9.4×10^{-6}	6.7×10^{-6}	5.0×10^{-7}	2.9×10^{-7}	1.1×10^{-5}	2.9×10^{-5}
3.8×10^{-2}	1.2×10^{-5}	7.3×10^{-6}	5.7×10^{-7}	3.9×10^{-7}	1.0×10^{-5}	2.8×10^{-5}
4.4×10^{-2}	1.5×10^{-5}	8.2×10^{-6}	6.8×10^{-7}	4.7×10^{-7}	1.2×10^{-5}	3.1×10^{-5}
4.9×10^{-2}	1.7×10^{-5}	9.2×10^{-6}	7.6×10^{-7}	5.4×10^{-7}	1.5×10^{-5}	4.2×10^{-5}
5.4×10^{-2}	1.2×10^{-5}	7.8×10^{-6}	5.7×10^{-7}	4.0×10^{-7}	1.1×10^{-5}	3.3×10^{-5}
5.8×10^{-2}	1.3×10^{-5}	8.4×10^{-6}	6.4×10^{-7}	5.8×10^{-7}	1.5×10^{-5}	4.6×10^{-5}
6.1×10^{-2}	1.6×10^{-5}	9.1×10^{-6}	6.8×10^{-7}	5.4×10^{-7}	1.7×10^{-5}	5.0×10^{-5}
6.5×10^{-2}	1.6×10^{-5}	9.2×10^{-6}	7.0×10^{-7}	8.7×10^{-7}	1.4×10^{-5}	4.6×10^{-5}
7.2×10^{-2}	1.6×10^{-5}	9.8×10^{-6}	8.6×10^{-7}	2.6×10^{-6}	1.9×10^{-5}	5.6×10^{-5}
8.1×10^{-2}	1.5×10^{-5}	9.4×10^{-6}	7.1×10^{-7}	5.2×10^{-7}	1.7×10^{-5}	4.8×10^{-5}
9.2×10^{-2}	1.1×10^{-5}	8.2×10^{-6}	5.1×10^{-7}	4.6×10^{-7}	1.2×10^{-5}	3.9×10^{-5}

Continued on next page

1.0×10^{-1}	1.5×10^{-5}	1.0×10^{-5}	6.4×10^{-7}	5.6×10^{-7}	1.0×10^{-5}	3.7×10^{-5}
1.1×10^{-1}	1.6×10^{-5}	1.0×10^{-5}	7.0×10^{-7}	1.0×10^{-6}	2.0×10^{-5}	6.7×10^{-5}
1.2×10^{-1}	1.3×10^{-5}	9.8×10^{-6}	6.1×10^{-7}	6.6×10^{-7}	1.8×10^{-5}	5.5×10^{-5}
1.3×10^{-1}	1.7×10^{-5}	1.2×10^{-5}	7.9×10^{-7}	6.8×10^{-7}	1.9×10^{-5}	6.0×10^{-5}
1.3×10^{-1}	1.7×10^{-5}	1.4×10^{-5}	7.8×10^{-7}	7.3×10^{-7}	1.4×10^{-5}	5.4×10^{-5}
1.4×10^{-1}	1.4×10^{-5}	1.0×10^{-5}	6.5×10^{-7}	6.9×10^{-7}	1.0×10^{-5}	3.9×10^{-5}
1.5×10^{-1}	1.2×10^{-5}	9.0×10^{-6}	5.0×10^{-7}	5.8×10^{-7}	7.8×10^{-6}	3.4×10^{-5}
1.5×10^{-1}	1.2×10^{-5}	1.1×10^{-5}	5.4×10^{-7}	7.0×10^{-7}	1.4×10^{-5}	4.9×10^{-5}
1.6×10^{-1}	1.1×10^{-5}	1.1×10^{-5}	5.5×10^{-7}	1.1×10^{-6}	1.7×10^{-5}	6.0×10^{-5}
1.6×10^{-1}	1.3×10^{-5}	1.4×10^{-5}	6.3×10^{-7}	7.4×10^{-7}	1.7×10^{-5}	6.1×10^{-5}
1.7×10^{-1}	1.2×10^{-5}	1.1×10^{-5}	5.8×10^{-7}	1.2×10^{-6}	1.5×10^{-5}	5.6×10^{-5}
1.7×10^{-1}	1.1×10^{-5}	1.0×10^{-5}	4.7×10^{-7}	8.6×10^{-7}	1.2×10^{-5}	4.8×10^{-5}
1.8×10^{-1}	1.0×10^{-5}	1.2×10^{-5}	5.7×10^{-7}	9.0×10^{-7}	2.2×10^{-5}	7.6×10^{-5}
1.9×10^{-1}	8.7×10^{-6}	8.4×10^{-6}	4.3×10^{-7}	5.5×10^{-7}	1.1×10^{-5}	4.4×10^{-5}
2.0×10^{-1}	8.9×10^{-6}	9.0×10^{-6}	4.1×10^{-7}	7.2×10^{-7}	1.1×10^{-5}	4.6×10^{-5}
2.1×10^{-1}	9.2×10^{-6}	9.2×10^{-6}	4.7×10^{-7}	7.3×10^{-7}	1.7×10^{-5}	6.5×10^{-5}
2.2×10^{-1}	9.8×10^{-6}	9.5×10^{-6}	5.1×10^{-7}	1.0×10^{-6}	1.6×10^{-5}	6.1×10^{-5}
2.3×10^{-1}	1.0×10^{-5}	1.0×10^{-5}	4.8×10^{-7}	7.4×10^{-7}	1.7×10^{-5}	6.2×10^{-5}
2.4×10^{-1}	1.1×10^{-5}	1.1×10^{-5}	5.4×10^{-7}	1.0×10^{-6}	1.9×10^{-5}	7.1×10^{-5}
2.5×10^{-1}	1.1×10^{-5}	1.1×10^{-5}	5.4×10^{-7}	8.1×10^{-7}	1.8×10^{-5}	7.1×10^{-5}
2.7×10^{-1}	1.2×10^{-5}	1.3×10^{-5}	5.9×10^{-7}	1.9×10^{-6}	2.6×10^{-5}	9.1×10^{-5}
2.8×10^{-1}	1.1×10^{-5}	1.2×10^{-5}	4.8×10^{-7}	1.4×10^{-6}	1.3×10^{-5}	5.7×10^{-5}
2.8×10^{-1}	9.7×10^{-6}	1.1×10^{-5}	4.5×10^{-7}	1.2×10^{-6}	1.5×10^{-5}	6.6×10^{-5}
2.9×10^{-1}	9.9×10^{-6}	1.1×10^{-5}	4.6×10^{-7}	8.6×10^{-7}	2.1×10^{-5}	8.5×10^{-5}
3.0×10^{-1}	1.1×10^{-5}	1.4×10^{-5}	5.2×10^{-7}	1.3×10^{-6}	3.2×10^{-5}	1.2×10^{-4}
3.1×10^{-1}	1.1×10^{-5}	1.6×10^{-5}	5.7×10^{-7}	2.1×10^{-6}	3.3×10^{-5}	1.2×10^{-4}
3.1×10^{-1}	1.1×10^{-5}	1.3×10^{-5}	5.5×10^{-7}	1.4×10^{-6}	2.6×10^{-5}	1.1×10^{-4}
3.3×10^{-1}	9.8×10^{-6}	1.0×10^{-5}	4.5×10^{-7}	9.5×10^{-7}	1.0×10^{-5}	6.2×10^{-5}
3.4×10^{-1}	1.0×10^{-5}	1.1×10^{-5}	5.3×10^{-7}	1.2×10^{-6}	1.9×10^{-5}	9.3×10^{-5}
3.6×10^{-1}	7.9×10^{-6}	8.1×10^{-6}	4.4×10^{-7}	1.2×10^{-6}	1.4×10^{-5}	6.9×10^{-5}
3.8×10^{-1}	6.9×10^{-6}	8.4×10^{-6}	3.9×10^{-7}	9.1×10^{-7}	1.4×10^{-5}	7.4×10^{-5}
4.0×10^{-1}	6.7×10^{-6}	8.3×10^{-6}	3.5×10^{-7}	8.7×10^{-7}	9.3×10^{-6}	5.5×10^{-5}
4.2×10^{-1}	5.9×10^{-6}	6.8×10^{-6}	3.3×10^{-7}	7.8×10^{-7}	9.1×10^{-6}	5.1×10^{-5}
4.4×10^{-1}	5.7×10^{-6}	7.1×10^{-6}	3.3×10^{-7}	7.5×10^{-7}	1.1×10^{-5}	6.1×10^{-5}
4.6×10^{-1}	8.7×10^{-6}	9.8×10^{-6}	4.8×10^{-7}	1.3×10^{-6}	1.4×10^{-5}	7.5×10^{-5}
4.9×10^{-1}	1.2×10^{-5}	1.2×10^{-5}	5.9×10^{-7}	1.6×10^{-6}	1.2×10^{-5}	6.4×10^{-5}
5.0×10^{-1}	1.3×10^{-5}	1.4×10^{-5}	6.7×10^{-7}	1.3×10^{-6}	1.3×10^{-5}	7.4×10^{-5}

Continued on next page

5.2×10^{-1}	1.3×10^{-5}	1.2×10^{-5}	6.6×10^{-7}	1.1×10^{-6}	1.4×10^{-5}	8.4×10^{-5}
5.3×10^{-1}	1.2×10^{-5}	1.1×10^{-5}	6.5×10^{-7}	1.4×10^{-6}	1.3×10^{-5}	6.8×10^{-5}
5.4×10^{-1}	1.3×10^{-5}	1.3×10^{-5}	6.8×10^{-7}	1.4×10^{-6}	1.2×10^{-5}	6.9×10^{-5}
5.6×10^{-1}	1.2×10^{-5}	1.1×10^{-5}	6.1×10^{-7}	1.7×10^{-6}	1.4×10^{-5}	7.9×10^{-5}
5.9×10^{-1}	1.3×10^{-5}	1.4×10^{-5}	6.8×10^{-7}	2.1×10^{-6}	1.6×10^{-5}	8.7×10^{-5}
6.2×10^{-1}	1.3×10^{-5}	1.2×10^{-5}	7.3×10^{-7}	2.5×10^{-6}	1.2×10^{-5}	8.1×10^{-5}
6.6×10^{-1}	1.2×10^{-5}	1.3×10^{-5}	6.6×10^{-7}	1.7×10^{-6}	9.0×10^{-6}	7.2×10^{-5}
6.9×10^{-1}	1.2×10^{-5}	1.2×10^{-5}	6.6×10^{-7}	2.1×10^{-6}	6.3×10^{-6}	6.2×10^{-5}
7.2×10^{-1}	1.1×10^{-5}	1.1×10^{-5}	6.5×10^{-7}	1.8×10^{-6}	5.2×10^{-6}	5.7×10^{-5}
7.6×10^{-1}	1.1×10^{-5}	1.1×10^{-5}	5.8×10^{-7}	1.8×10^{-6}	3.9×10^{-6}	4.7×10^{-5}
8.0×10^{-1}	8.8×10^{-6}	1.1×10^{-5}	4.7×10^{-7}	1.5×10^{-6}	4.3×10^{-6}	4.8×10^{-5}
8.4×10^{-1}	7.3×10^{-6}	8.4×10^{-6}	3.9×10^{-7}	1.6×10^{-6}	4.3×10^{-6}	4.5×10^{-5}
8.8×10^{-1}	6.3×10^{-6}	7.7×10^{-6}	3.3×10^{-7}	1.4×10^{-6}	4.0×10^{-6}	4.2×10^{-5}
9.3×10^{-1}	4.8×10^{-6}	6.7×10^{-6}	2.6×10^{-7}	1.3×10^{-6}	4.6×10^{-6}	4.7×10^{-5}
9.6×10^{-1}	4.2×10^{-6}	6.6×10^{-6}	2.2×10^{-7}	1.7×10^{-6}	5.7×10^{-6}	5.0×10^{-5}
9.7×10^{-1}	3.8×10^{-6}	5.7×10^{-6}	2.0×10^{-7}	9.1×10^{-7}	2.7×10^{-6}	3.8×10^{-5}
9.9×10^{-1}	3.6×10^{-6}	5.9×10^{-6}	2.1×10^{-7}	1.3×10^{-6}	3.3×10^{-6}	4.1×10^{-5}
1.0	4.0×10^{-6}	5.8×10^{-6}	2.3×10^{-7}	1.4×10^{-6}	3.2×10^{-6}	4.0×10^{-5}
1.1	5.9×10^{-6}	6.8×10^{-6}	3.4×10^{-7}	1.5×10^{-6}	3.0×10^{-6}	3.8×10^{-5}
1.1	7.7×10^{-6}	7.7×10^{-6}	4.3×10^{-7}	1.4×10^{-6}	3.0×10^{-6}	3.9×10^{-5}
1.2	8.4×10^{-6}	8.7×10^{-6}	4.7×10^{-7}	1.6×10^{-6}	2.9×10^{-6}	4.0×10^{-5}
1.2	7.9×10^{-6}	7.6×10^{-6}	4.6×10^{-7}	1.8×10^{-6}	2.6×10^{-6}	4.0×10^{-5}
1.3	7.8×10^{-6}	7.7×10^{-6}	4.3×10^{-7}	1.7×10^{-6}	1.5×10^{-6}	2.9×10^{-5}
1.3	5.4×10^{-6}	5.3×10^{-6}	3.2×10^{-7}	2.0×10^{-6}	1.5×10^{-6}	3.0×10^{-5}
1.4	8.0×10^{-6}	6.7×10^{-6}	4.7×10^{-7}	2.3×10^{-6}	1.5×10^{-6}	2.7×10^{-5}
1.5	8.1×10^{-6}	7.3×10^{-6}	4.5×10^{-7}	1.9×10^{-6}	1.1×10^{-6}	2.5×10^{-5}
1.5	7.4×10^{-6}	5.5×10^{-6}	4.3×10^{-7}	1.9×10^{-6}	1.2×10^{-6}	2.7×10^{-5}
1.6	7.0×10^{-6}	5.6×10^{-6}	3.7×10^{-7}	1.4×10^{-6}	7.8×10^{-7}	2.3×10^{-5}
1.6	6.2×10^{-6}	5.7×10^{-6}	3.5×10^{-7}	1.5×10^{-6}	1.1×10^{-6}	2.6×10^{-5}
1.6	5.3×10^{-6}	4.4×10^{-6}	3.0×10^{-7}	1.6×10^{-6}	8.4×10^{-7}	2.5×10^{-5}
1.7	6.9×10^{-6}	5.7×10^{-6}	4.0×10^{-7}	1.7×10^{-6}	9.0×10^{-7}	2.3×10^{-5}
1.8	8.4×10^{-6}	6.0×10^{-6}	4.5×10^{-7}	1.3×10^{-6}	7.1×10^{-7}	2.0×10^{-5}
1.8	4.6×10^{-6}	3.9×10^{-6}	2.5×10^{-7}	2.2×10^{-6}	5.6×10^{-7}	1.9×10^{-5}
1.9	4.8×10^{-6}	3.9×10^{-6}	3.0×10^{-7}	1.3×10^{-6}	5.5×10^{-7}	1.9×10^{-5}
1.9	5.5×10^{-6}	4.0×10^{-6}	3.2×10^{-7}	1.4×10^{-6}	5.1×10^{-7}	1.7×10^{-5}
2.0	6.3×10^{-6}	5.4×10^{-6}	3.8×10^{-7}	1.2×10^{-6}	6.2×10^{-7}	1.9×10^{-5}
2.1	7.4×10^{-6}	5.3×10^{-6}	4.2×10^{-7}	1.6×10^{-6}	5.3×10^{-7}	1.7×10^{-5}

Continued on next page

2.2	8.4×10^{-6}	5.8×10^{-6}	5.3×10^{-7}	1.5×10^{-6}	5.7×10^{-7}	1.7×10^{-5}
2.3	1.1×10^{-5}	6.3×10^{-6}	6.7×10^{-7}	1.8×10^{-6}	6.4×10^{-7}	1.7×10^{-5}
2.3	1.1×10^{-5}	5.9×10^{-6}	7.0×10^{-7}	1.7×10^{-6}	4.4×10^{-7}	1.5×10^{-5}
2.3	1.5×10^{-5}	7.9×10^{-6}	9.3×10^{-7}	1.6×10^{-6}	4.6×10^{-7}	1.4×10^{-5}
2.4	1.7×10^{-5}	6.2×10^{-6}	1.1×10^{-6}	2.4×10^{-6}	6.0×10^{-7}	1.6×10^{-5}
2.4	1.3×10^{-5}	6.8×10^{-6}	7.3×10^{-7}	2.8×10^{-6}	4.9×10^{-7}	1.7×10^{-5}
2.4	1.1×10^{-5}	6.1×10^{-6}	7.2×10^{-7}	1.4×10^{-6}	3.3×10^{-7}	1.4×10^{-5}
2.4	8.5×10^{-6}	6.1×10^{-6}	4.7×10^{-7}	1.5×10^{-6}	2.6×10^{-7}	1.3×10^{-5}
2.5	5.3×10^{-6}	5.3×10^{-6}	3.1×10^{-7}	1.5×10^{-6}	2.4×10^{-7}	1.2×10^{-5}
2.7	4.7×10^{-6}	4.7×10^{-6}	2.9×10^{-7}	1.4×10^{-6}	2.3×10^{-7}	1.2×10^{-5}
2.8	3.8×10^{-6}	3.5×10^{-6}	2.3×10^{-7}	1.3×10^{-6}	1.7×10^{-7}	9.9×10^{-6}
2.9	3.2×10^{-6}	3.6×10^{-6}	2.1×10^{-7}	1.3×10^{-6}	1.4×10^{-7}	9.0×10^{-6}
3.0	2.6×10^{-6}	3.3×10^{-6}	1.5×10^{-7}	3.0×10^{-6}	1.0×10^{-7}	8.1×10^{-6}
3.1	2.0×10^{-6}	3.1×10^{-6}	1.2×10^{-7}	1.2×10^{-6}	8.7×10^{-8}	7.3×10^{-6}
3.2	1.3×10^{-6}	2.8×10^{-6}	7.9×10^{-8}	1.3×10^{-6}	7.3×10^{-8}	7.4×10^{-6}
3.3	9.8×10^{-7}	1.9×10^{-6}	5.9×10^{-8}	1.2×10^{-6}	5.4×10^{-8}	7.0×10^{-6}
3.4	8.1×10^{-7}	2.2×10^{-6}	5.0×10^{-8}	9.3×10^{-7}	5.4×10^{-8}	5.8×10^{-6}
3.6	7.4×10^{-7}	2.1×10^{-6}	4.1×10^{-8}	1.0×10^{-6}	4.9×10^{-8}	5.4×10^{-6}
3.8	7.0×10^{-7}	1.6×10^{-6}	4.5×10^{-8}	8.8×10^{-7}	3.9×10^{-8}	4.7×10^{-6}
4.0	8.6×10^{-7}	2.0×10^{-6}	5.5×10^{-8}	9.4×10^{-7}	3.7×10^{-8}	4.5×10^{-6}
4.2	8.3×10^{-7}	2.3×10^{-6}	5.3×10^{-8}	9.4×10^{-7}	2.7×10^{-8}	4.0×10^{-6}
4.4	4.8×10^{-7}	1.6×10^{-6}	2.6×10^{-8}	7.7×10^{-7}	2.1×10^{-8}	3.6×10^{-6}
4.5	5.3×10^{-7}	1.7×10^{-6}	3.2×10^{-8}	8.4×10^{-7}	1.7×10^{-8}	3.1×10^{-6}
4.7	5.4×10^{-7}	1.4×10^{-6}	3.4×10^{-8}	9.5×10^{-7}	1.8×10^{-8}	3.2×10^{-6}
4.8	4.9×10^{-7}	1.9×10^{-6}	2.9×10^{-8}	8.4×10^{-7}	1.6×10^{-8}	2.9×10^{-6}
4.9	3.6×10^{-7}	1.7×10^{-6}	2.8×10^{-8}	9.0×10^{-7}	1.5×10^{-8}	2.8×10^{-6}
5.1	3.0×10^{-7}	1.4×10^{-6}	2.2×10^{-8}	1.1×10^{-6}	1.1×10^{-8}	2.7×10^{-6}
5.4	3.3×10^{-7}	1.4×10^{-6}	2.2×10^{-8}	6.4×10^{-7}	1.0×10^{-8}	2.5×10^{-6}
5.6	1.8×10^{-7}	1.2×10^{-6}	1.3×10^{-8}	5.1×10^{-7}	8.8×10^{-9}	2.5×10^{-6}
5.8	1.7×10^{-7}	1.1×10^{-6}	1.1×10^{-8}	5.5×10^{-7}	6.1×10^{-9}	2.7×10^{-6}
6.0	1.5×10^{-7}	1.1×10^{-6}	5.9×10^{-9}	5.7×10^{-7}	5.5×10^{-9}	2.2×10^{-6}
6.1	1.6×10^{-7}	1.1×10^{-6}	1.4×10^{-8}	6.3×10^{-7}	4.3×10^{-9}	1.8×10^{-6}
6.3	1.3×10^{-7}	1.2×10^{-6}	7.5×10^{-9}	6.4×10^{-7}	4.7×10^{-9}	2.0×10^{-6}
6.5	1.2×10^{-7}	1.1×10^{-6}	1.0×10^{-8}	4.7×10^{-7}	4.8×10^{-9}	1.8×10^{-6}
6.6	1.2×10^{-7}	1.0×10^{-6}	1.1×10^{-8}	7.2×10^{-7}	3.8×10^{-9}	2.3×10^{-6}
6.6	1.1×10^{-7}	8.6×10^{-7}	8.4×10^{-9}	5.9×10^{-7}	5.0×10^{-9}	1.8×10^{-6}
6.7	6.1×10^{-8}	5.9×10^{-7}	3.8×10^{-9}	6.7×10^{-7}	3.4×10^{-9}	2.0×10^{-6}

Continued on next page

6.8	7.0×10^{-8}	7.3×10^{-7}	3.7×10^{-9}	1.4×10^{-6}	4.9×10^{-9}	1.9×10^{-6}
7.0	7.9×10^{-8}	1.2×10^{-6}	8.2×10^{-9}	4.7×10^{-7}	3.7×10^{-9}	1.6×10^{-6}
7.1	6.5×10^{-8}	1.4×10^{-6}	4.7×10^{-10}	6.2×10^{-7}	3.1×10^{-9}	1.9×10^{-6}
7.3	3.7×10^{-8}	8.7×10^{-7}	3.2×10^{-9}	4.4×10^{-7}	3.5×10^{-9}	1.8×10^{-6}
7.5	3.9×10^{-8}	6.3×10^{-7}	3.1×10^{-10}	5.1×10^{-7}	1.9×10^{-9}	1.8×10^{-6}
7.7	2.5×10^{-8}	6.4×10^{-7}	3.1×10^{-10}	4.0×10^{-7}	1.2×10^{-9}	1.5×10^{-6}
7.9	1.6×10^{-8}	8.2×10^{-7}	2.5×10^{-9}	6.7×10^{-7}	8.4×10^{-10}	1.7×10^{-6}
8.1	2.8×10^{-8}	7.4×10^{-7}	3.6×10^{-11}	3.7×10^{-7}	2.3×10^{-9}	1.6×10^{-6}
8.3	1.6×10^{-8}	5.6×10^{-7}	7.6×10^{-10}	2.9×10^{-7}	9.0×10^{-10}	1.9×10^{-6}
8.5	8.9×10^{-9}	6.3×10^{-7}	9.3×10^{-10}	4.2×10^{-7}	6.0×10^{-10}	1.5×10^{-6}
8.7	6.8×10^{-9}	6.7×10^{-7}	1.0×10^{-9}	4.1×10^{-7}	0.0	1.6×10^{-6}
8.9	7.4×10^{-9}	8.1×10^{-7}	2.8×10^{-11}	3.6×10^{-7}	2.0×10^{-10}	1.4×10^{-6}
9.2	6.9×10^{-9}	5.7×10^{-7}	8.7×10^{-11}	3.9×10^{-7}	1.0×10^{-11}	1.6×10^{-6}
9.4	2.8×10^{-9}	9.5×10^{-7}	5.8×10^{-10}	3.0×10^{-7}	3.2×10^{-10}	1.6×10^{-6}
9.6	2.7×10^{-9}	5.3×10^{-7}	1.6×10^{-10}	2.5×10^{-7}	7.0×10^{-11}	1.5×10^{-6}
9.9	9.6×10^{-10}	7.5×10^{-7}	3.7×10^{-10}	2.9×10^{-7}	1.4×10^{-10}	1.4×10^{-6}
1.0×10^1	1.9×10^{-10}	4.8×10^{-7}	0.0	3.6×10^{-7}	1.2×10^{-10}	1.5×10^{-6}
1.0×10^1	1.6×10^{-10}	3.8×10^{-7}	0.0	3.3×10^{-7}	0.0	1.3×10^{-6}
1.1×10^1	2.9×10^{-9}	6.7×10^{-7}	0.0	7.7×10^{-7}	0.0	1.3×10^{-6}
1.1×10^1	0.0	4.7×10^{-7}	0.0	2.8×10^{-7}	0.0	1.2×10^{-6}
1.1×10^1	0.0	6.5×10^{-7}	0.0	2.9×10^{-7}	0.0	1.2×10^{-6}
1.1×10^1	0.0	4.2×10^{-7}	0.0	2.2×10^{-7}	0.0	1.3×10^{-6}
1.2×10^1	0.0	4.8×10^{-7}	0.0	3.1×10^{-7}	0.0	1.2×10^{-6}
1.2×10^1	0.0	5.4×10^{-7}	0.0	2.4×10^{-7}	0.0	1.4×10^{-6}
1.2×10^1	0.0	7.8×10^{-7}	0.0	2.4×10^{-7}	0.0	1.1×10^{-6}
1.3×10^1	0.0	6.5×10^{-7}	0.0	3.1×10^{-7}	0.0	1.2×10^{-6}
1.3×10^1	0.0	9.3×10^{-7}	0.0	2.7×10^{-7}	0.0	1.3×10^{-6}
1.3×10^1	0.0	1.1×10^{-6}	0.0	4.0×10^{-7}	0.0	1.1×10^{-6}
1.4×10^1	0.0	5.5×10^{-7}	0.0	4.8×10^{-7}	0.0	1.1×10^{-6}
1.4×10^1	0.0	4.8×10^{-7}	0.0	2.9×10^{-7}	0.0	1.1×10^{-6}
1.4×10^1	0.0	5.0×10^{-7}	0.0	1.0×10^{-6}	0.0	1.1×10^{-6}
1.5×10^1	0.0	4.6×10^{-7}	0.0	4.1×10^{-7}	0.0	9.3×10^{-7}
1.5×10^1	0.0	5.9×10^{-7}	0.0	3.4×10^{-7}	0.0	1.1×10^{-6}
1.5×10^1	0.0	6.7×10^{-7}	0.0	2.4×10^{-7}	0.0	1.4×10^{-6}
1.6×10^1	0.0	4.8×10^{-7}	0.0	3.4×10^{-7}	0.0	9.0×10^{-7}
1.6×10^1	0.0	6.3×10^{-7}	0.0	2.8×10^{-7}	0.0	8.7×10^{-7}
1.7×10^1	0.0	4.7×10^{-7}	0.0	2.6×10^{-7}	0.0	1.0×10^{-6}

Continued on next page

1.7×10^1	0.0	4.1×10^{-7}	0.0	2.9×10^{-7}	0.0	9.4×10^{-7}
1.8×10^1	0.0	4.0×10^{-7}	0.0	3.1×10^{-7}	0.0	9.2×10^{-7}
1.8×10^1	0.0	3.5×10^{-7}	0.0	2.8×10^{-7}	0.0	9.5×10^{-7}
1.8×10^1	0.0	4.6×10^{-7}	0.0	5.4×10^{-7}	0.0	7.8×10^{-7}
1.9×10^1	0.0	3.6×10^{-7}	0.0	3.0×10^{-7}	0.0	8.6×10^{-7}
1.9×10^1	0.0	4.8×10^{-7}	0.0	2.3×10^{-7}	0.0	8.4×10^{-7}
2.0×10^1	0.0	4.0×10^{-7}	0.0	2.5×10^{-7}	0.0	7.7×10^{-7}
2.1×10^1	0.0	4.8×10^{-7}	0.0	3.6×10^{-7}	0.0	6.7×10^{-7}
2.3×10^1	0.0	4.6×10^{-7}	0.0	2.6×10^{-7}	0.0	7.5×10^{-7}
2.5×10^1	0.0	3.8×10^{-7}	0.0	2.7×10^{-7}	0.0	6.9×10^{-7}
2.7×10^1	0.0	5.2×10^{-7}	0.0	2.4×10^{-7}	0.0	6.8×10^{-7}
2.9×10^1	0.0	4.2×10^{-7}	0.0	2.6×10^{-7}	0.0	8.4×10^{-7}
3.2×10^1	0.0	5.2×10^{-7}	0.0	3.4×10^{-7}	0.0	6.0×10^{-7}
3.5×10^1	0.0	5.2×10^{-7}	0.0	3.4×10^{-7}	0.0	6.0×10^{-7}
3.8×10^1	0.0	4.8×10^{-7}	0.0	2.8×10^{-7}	0.0	6.0×10^{-7}
4.2×10^1	0.0	4.4×10^{-7}	0.0	3.1×10^{-7}	0.0	5.6×10^{-7}
4.5×10^1	0.0	6.0×10^{-7}	0.0	2.5×10^{-7}	0.0	5.5×10^{-7}
5.0×10^1	0.0	4.7×10^{-7}	0.0	3.5×10^{-7}	0.0	5.2×10^{-7}
5.4×10^1	0.0	4.1×10^{-7}	0.0	2.7×10^{-7}	0.0	5.8×10^{-7}
5.9×10^1	0.0	4.1×10^{-7}	0.0	3.6×10^{-7}	0.0	4.9×10^{-7}
6.4×10^1	0.0	4.4×10^{-7}	0.0	3.7×10^{-7}	0.0	6.0×10^{-7}
7.0×10^1	0.0	3.8×10^{-7}	0.0	2.9×10^{-7}	0.0	5.5×10^{-7}
7.6×10^1	0.0	3.9×10^{-7}	0.0	2.6×10^{-7}	0.0	5.9×10^{-7}
8.3×10^1	0.0	4.1×10^{-7}	0.0	3.3×10^{-7}	0.0	4.9×10^{-7}
9.1×10^1	0.0	2.9×10^{-7}	0.0	3.6×10^{-7}	0.0	5.3×10^{-7}
9.9×10^1	0.0	4.5×10^{-7}	0.0	2.4×10^{-7}	0.0	5.0×10^{-7}
1.1×10^2	0.0	2.8×10^{-7}	0.0	2.7×10^{-7}	0.0	4.5×10^{-7}
1.2×10^2	0.0	2.7×10^{-7}	0.0	2.4×10^{-7}	0.0	4.3×10^{-7}
1.3×10^2	0.0	2.4×10^{-7}	0.0	2.2×10^{-7}	0.0	3.7×10^{-7}
1.4×10^2	0.0	3.2×10^{-7}	0.0	2.6×10^{-7}	0.0	3.7×10^{-7}
1.5×10^2	0.0	3.2×10^{-7}	0.0	2.1×10^{-7}	0.0	4.1×10^{-7}
1.7×10^2	0.0	3.8×10^{-7}	0.0	2.4×10^{-7}	0.0	3.0×10^{-7}
1.8×10^2	0.0	3.0×10^{-7}	0.0	1.5×10^{-7}	0.0	2.9×10^{-7}
2.0×10^2	0.0	1.9×10^{-7}	0.0	1.7×10^{-7}	0.0	2.2×10^{-7}
2.1×10^2	0.0	4.2×10^{-7}	0.0	1.4×10^{-7}	0.0	2.3×10^{-7}
2.3×10^2	0.0	1.2×10^{-7}	0.0	1.4×10^{-7}	0.0	2.1×10^{-7}
2.6×10^2	0.0	2.1×10^{-7}	0.0	1.4×10^{-7}	0.0	1.6×10^{-7}

Continued on next page

2.8×10^2	0.0	1.3×10^{-7}	0.0	9.8×10^{-8}	0.0	1.3×10^{-7}
3.0×10^2	0.0	1.5×10^{-7}	0.0	9.1×10^{-8}	0.0	1.3×10^{-7}
3.3×10^2	0.0	7.4×10^{-8}	0.0	6.2×10^{-8}	0.0	1.0×10^{-7}
3.6×10^2	0.0	7.3×10^{-8}	0.0	4.6×10^{-8}	0.0	8.2×10^{-8}
3.9×10^2	0.0	4.5×10^{-8}	0.0	6.5×10^{-8}	0.0	7.2×10^{-8}
4.3×10^2	0.0	4.2×10^{-8}	0.0	5.4×10^{-8}	0.0	7.1×10^{-8}
4.7×10^2	0.0	6.1×10^{-8}	0.0	5.4×10^{-8}	0.0	4.4×10^{-8}
5.1×10^2	0.0	3.7×10^{-8}	0.0	3.6×10^{-8}	0.0	3.9×10^{-8}
5.5×10^2	0.0	1.2×10^{-7}	0.0	3.7×10^{-8}	0.0	3.8×10^{-8}
6.0×10^2	0.0	6.2×10^{-8}	0.0	4.0×10^{-8}	0.0	5.2×10^{-8}
6.6×10^2	0.0	2.4×10^{-8}	0.0	2.8×10^{-8}	0.0	2.7×10^{-8}
7.2×10^2	0.0	5.2×10^{-8}	0.0	2.9×10^{-8}	0.0	2.4×10^{-8}
7.8×10^2	0.0	1.6×10^{-8}	0.0	2.0×10^{-8}	0.0	4.6×10^{-8}
8.5×10^2	0.0	3.3×10^{-8}	0.0	1.6×10^{-8}	0.0	1.9×10^{-8}
9.3×10^2	0.0	7.1×10^{-9}	0.0	5.4×10^{-8}	0.0	2.1×10^{-8}
1.0×10^3	0.0	1.1×10^{-8}	0.0	1.2×10^{-8}	0.0	6.9×10^{-9}
1.1×10^3	0.0	3.7×10^{-8}	0.0	1.2×10^{-8}	0.0	1.3×10^{-8}
1.2×10^3	0.0	9.4×10^{-9}	0.0	6.6×10^{-9}	0.0	2.3×10^{-8}
1.3×10^3	0.0	1.1×10^{-8}	0.0	1.2×10^{-8}	0.0	1.1×10^{-8}
1.4×10^3	0.0	7.3×10^{-9}	0.0	6.4×10^{-9}	0.0	2.5×10^{-8}
1.6×10^3	0.0	2.2×10^{-9}	0.0	2.6×10^{-9}	0.0	7.3×10^{-9}
1.7×10^3	0.0	5.8×10^{-10}	0.0	5.2×10^{-9}	0.0	3.2×10^{-9}
1.9×10^3	0.0	3.0×10^{-9}	0.0	3.5×10^{-9}	0.0	6.3×10^{-9}
2.0×10^3	0.0	1.9×10^{-8}	0.0	4.1×10^{-9}	0.0	3.1×10^{-9}
2.2×10^3	0.0	1.9×10^{-9}	0.0	1.8×10^{-9}	0.0	1.5×10^{-9}
2.4×10^3	0.0	2.5×10^{-9}	0.0	2.0×10^{-9}	0.0	3.5×10^{-9}
2.6×10^3	0.0	0.0	0.0	3.6×10^{-9}	0.0	4.0×10^{-9}
2.9×10^3	0.0	7.1×10^{-10}	0.0	5.2×10^{-10}	0.0	1.2×10^{-9}
3.1×10^3	0.0	0.0	0.0	3.0×10^{-9}	0.0	2.4×10^{-9}
3.4×10^3	0.0	4.3×10^{-10}	0.0	2.1×10^{-9}	0.0	4.7×10^{-10}
3.7×10^3	0.0	3.4×10^{-9}	0.0	1.4×10^{-9}	0.0	6.2×10^{-10}
4.0×10^3	0.0	0.0	0.0	1.3×10^{-9}	0.0	9.6×10^{-11}
4.4×10^3	0.0	8.3×10^{-10}	0.0	4.0×10^{-12}	0.0	7.4×10^{-10}
4.8×10^3	0.0	7.5×10^{-10}	0.0	5.6×10^{-10}	0.0	8.6×10^{-10}
5.2×10^3	0.0	0.0	0.0	3.9×10^{-10}	0.0	3.9×10^{-11}
5.7×10^3	0.0	0.0	0.0	2.8×10^{-11}	0.0	0.0
6.2×10^3	0.0	0.0	0.0	0.0	0.0	0.0

Continued on next page

6.8×10^3	0.0	0.0	0.0	1.9×10^{-10}	0.0	0.0
7.4×10^3	0.0	0.0	0.0	0.0	0.0	1.0×10^{-9}
8.1×10^3	0.0	0.0	0.0	1.9×10^{-10}	0.0	0.0
8.8×10^3	0.0	0.0	0.0	1.2×10^{-10}	0.0	0.0
9.6×10^3	0.0	0.0	0.0	3.9×10^{-10}	0.0	0.0

A.4 Tracer database Denmark

Table A.3 compiles the radioactive noble gases data sampled in the Danish shallow aquifers between 2005 and 2021.

Well	DGU	Sampling date	Depth [m]	^{39}Ar [%mod]	^{37}Ar [mBq m $_{\text{air}}^{-3}$]	^{85}Kr [dpm cc $_{\text{Kr}}^{-1}$]	$^3\text{He}/^4\text{He}$	^3H [TU]	$^3\text{He}_{\text{trit}}$ [TU]	$^4\text{He}_{\text{RAD}}$ [cc g $^{-1}$]
Lu251	136.891	25.07.2009	23	4	182	8	1.0	0.1		
Lu253	136.907	24.07.2009	31	5	182	7	1.5	0.7		
BB318	145.274	18.06.2019			64	4	6.5	2.7	1.6	0.2
D4	145.717	19.06.2019			127	16	1.0	1.8	N.A.	
D5	145.746	04.09.2014								
DK08/10	104.2120	04.09.2014	81	6	10	10	0.6			
DK08/3	104.2307	04.09.2014	93	1	30	6	0.8	0.1		
DK08/9	104.2325	04.09.2014	86	2	27	6	15			
DK08/2	105.1565	04.09.2014	125	3	71	4	0.4	0.0		
DK08/4	114.1430	04.09.2014	108	8	11	5	0.9			
DK08/8	114.1618	04.09.2014	105		37	8	0.6	0.3		
DK08/5	114.1857	04.09.2014	110	6	75	4	0.4	0.1	0.3	0.3
DK08/7	114.1861	04.09.2014	125	6	25	6	0.4			
DK08/6	115.1371	04.09.2014	121	6	10	10	0.5		0.3	0.3
DK08/1	115.1474	04.09.2014	133	8	57	8	0.6	0.1		
DK14/13	116.1528	04.09.2014	42	7	120	13	7.5	0.4		
V7 (DK7)	116.153	24.07.2019			37	9	6.3	0.7	2.0	0.8
DK14/24	116.1646	09.09.2014	75	5	45	11	0.7	0.3		
DK14/12	116.1647	04.09.2014	55	3	107	14	1.7	0.2		
DK14/26	116.201	09.09.2014	39	8	70	12		0.5		
DK14/25	116.723	09.09.2014	72	6	61	9		0.6		
S F4	122.1823	16.04.2012	105	5	77	9	0.4	0.1	1.4 $\times 10^{-6}$	-0.1
S F2	122.1823	16.04.2012	159	3	65	5	0.3	0.1	1.1 $\times 10^{-6}$	0.1
B F4	123.1350	15.04.2012	62	4	46	12	0.4	0.1	7.7 $\times 10^{-7}$	0.0
B F2	123.1350	15.04.2012	105	5	5	>	0.3	0.1	7.4 $\times 10^{-7}$	0.0
B F1	123.1350	15.04.2012	141	8	10	>	1.0	0.1	3.3 $\times 10^{-7}$	0.0
V9	124.1019	24.07.2019			59	4	3.5	3.8	1.3 $\times 10^{-6}$	0.0
DK14/17	124.1021	05.09.2014	109	11	45	5	0.6	0.2	0.0	0.2
V8	124.357	24.07.2019			65	8	1.6	0.6	1.9 $\times 10^{-6}$	1.2
								0.3	14.9	3.6 $\times 10^{-9}$

Continued on next page

Well	DGU	Sampling date	Depth [m]	^{39}Ar [%mod]	^{37}Ar [mBq m $^{-3}$]	^{85}Kr [dpm cc $_{\text{Kr}}^{-1}$]	$^3\text{He}/^4\text{He}$	^3H [TU]	$^3\text{He}_{\text{trit}}$ [TU]	$^4\text{He}_{\text{RAD}}$ [cc g $^{-1}$]
F2	125.1713	22.07.2019		64	1.1	1.7	9.8×10^{-7}	0.2	0.1	2.7×10^{-8}
DK14/10	125.2102	04.09.2014	25	6						
DK14/23	125.2210	08.09.2014	90	5						
DK14/11	125.682	04.09.2014	49	4						
F1	125.788	22.07.2019		93	2.1	1.9	9.7×10^{-7}	1.2	0.1	3.0×10^{-8}
B12	133.1107	25.07.2019		51	2.8	1.9	1.1×10^{-6}	0.1	0.0	1.5×10^{-8}
Trudsbro 1	133.1461	20.08.2019		128	7.7	4.0	1.1×10^{-6}	0.2	0.1	2.1×10^{-8}
DK14/16	133.1598	05.09.2014	72	6						
B11	133.1718	25.07.2019		28	4.1	2.6	3.4×10^{-7}	0.0	0.0	2.2×10^{-7}
Trudsbro 2	133.1784	20.08.2019		45	3.0	1.7	1.0×10^{-6}	0.3	0.1	2.5×10^{-8}
DK14/15	133.242	05.09.2014	63	1						
DK14/14	134.1081	05.09.2014	36	6						
DK14/9	135.1232	04.09.2014	31	5						
B10	135.1883	25.07.2019		43	0.4	3.1	4.4×10^{-7}	0.0	0.1	1.7×10^{-7}
DK14/8	135.766	04.09.2014	33	3						
T4	136.218	18.06.2019		95	7.6	2.2	1.7×10^{-6}	3.1	0.3	2.9×10^{-9}
T8	136.285	18.06.2019		107	6.5	1.8	1.1×10^{-6}	0.7	0.1	3.7×10^{-8}
Lunde VV	136.733	25.07.2009	37	3						
Lu 251 Rep	136.891	03.08.2011	23	4	0.4	0.0				
LU251	136.891	19.06.2019		174	5.9	2.1	5.9×10^{-7}	0.6	0.1	1.3×10^{-7}
Lu 253 Rep	136.907	03.08.2011	31	5	0.6	0.0				
LU253	136.907	19.06.2019		164	9.4	2.5	1.0×10^{-6}	1.1	0.2	4.4×10^{-8}
Lu 255	136.914	04.08.2011	25	6	0.7	0.1				
Lu 256	137.884	03.08.2011	29	5	0.6	0.1				
U 190	145.145	06.05.2008	82	14						
Ho 216	145.1515	05.05.2008	92	8	0.5	0.0				
Ho 216	145.1515	05.05.2008	84	8						
Ho 220	145.2022	06.05.2008	66	3						
Br227	145.2026	21.07.2009	63	2	0.6	0.0				

Continued on next page

Well	DGU	Sampling date	Depth [m]	^{39}Ar ± [%mod]	^{37}Ar ± [mBq m $_{\text{air}}^{-3}$]	^{85}Kr ± [dpm cc $_{\text{Kr}}^{-1}$]	$^3\text{He}/^4\text{He}$	^3H ± [TU]	$^3\text{He}_{\text{trit}}$ [TU]	$^4\text{He}_{\text{RAD}}$ [cc g $^{-1}$]
E233	145.2050	23.07.2009	58	5	92	5	0.2			
NS240	145.2097	22.07.2009	37	12	100	10	0.2			
Ho249	145.2212	24.07.2009	66	4	87	4	0.1			
E257	145.2399	24.07.2009	25	3	115	5	0.6			
D338	145.2682	23.07.2009	46	9	94	6	0.4			
BB317	145.2739	26.07.2009	66	7	64	6	0.1			
BB318	145.2740	26.07.2009	59	15	70	8	0.1			
BB318 TNO	145.2740	18.06.2019					0.6			
U310-2	145.2756	25.07.2009	83	7	57.0	3.0	0.3			
U303	145.2814	22.07.2009	24	6	110.0	10.0	0.4			
Mag 1	145.2832	04.05.2008	58	1	85.0	6.0	0.4			
Mag 1	145.2832	04.05.2008	73	1	77.0	4.0	0.5			
U 340	145.2872	06.05.2008	91	12	58.0	7.0	0.5			
U 340	145.2872	07.05.2008	79	12	67.0	7.0				
DK14/BB 346	145.3083	06.09.2014	73	9	33.0	6.0	0.1			
BB346 (m)	145.3083	18.06.2019			30.0	16.0	0.3			
BB346 (b)	145.3083	19.06.2019			45.0	17.0	0.7			
BB346 (t)	145.3083	19.06.2019			65.0	19.0	0.3			
DK14/BB 348	145.3085	06.09.2014	74	9	100.0	10.0	0.3			
Br3	145.384	21.07.2009	34	4	120.0	5.0	0.6			
Br 4	145.471	05.05.2008	60	3	76.0	4.0	1.2			
Ho203	145.668	04.05.2008	96	16	93.0	9.0				
Ho208	145.689	24.07.2009	75	5	66.0	3.0	0.2			
E29	145.718	23.07.2009	41	4	72.0	6.0	0.3			
E30	145.719	24.07.2009	42	6	90.0	5.0	0.2			
D5	145.746	22.07.2009	45		108.0	5.0	0.4			
Ludvigsen	145.879	21.07.2009	55	6	87.0	4.0	0.2			
D231	146.2029	22.07.2009	61	6	107.0	5.0	0.1			
Højby VV	146.2393	25.07.2009	90	6	68.0	6.0	0.1			

Continued on next page

Well	DGU	Sampling date	Depth [m]	^{39}Ar [%mod]	^{37}Ar [mBq m $^{-3}$ air]	^{85}Kr [dpm cc $_{\text{Kr}}^{-1}$]	$^3\text{He}/^4\text{He}$	^3H [TU]	$^3\text{He}_{\text{trit}}$ [TU]	$^4\text{He}_{\text{RAD}}$ [cc g $^{-1}$]
DK14/Boring L345	146.2986	06.09.2014	71	78.0 6.0		0.7 0.2				
DK14/Boring L350	146.3144	08.09.2014	24	3 100.0 10.0		2.9 0.8				
L15	146.483	23.07.2009	66	9 81.0 4.0	4.0 < 0.1	0.3 0.1				
L16	146.487	23.07.2009	61	5 72.0 7.0		1.0 0.2				
Vv	146.490	21.07.2009	82	19 41.0 2.0	1.5 0.1	0.2 0.1				
V5	146.490	17.06.2019		43.0 8.0	12.3 2.0	3.8 1.3	6.9×10^{-7}	0.0 0.0	0.5	7.8×10^{-8}
DK14/Boring V7	146.492	06.09.2014	32	3 100.0 10.0		17.6 0.7				
V7	146.492	17.06.2019		95.0 11.0	9.4 2.0	7.2 0.5	2.0×10^{-6}	2.9 0.3	29.3	1.9×10^{-8}
U321	155.1081	22.07.2009	63	8 103.0 9.0	0.2 < 0.1	0.4 0.1				
DK14/1	159.1033	01.09.2014	20	80.0 10.0		22.0 0.9				
DK14/2	159.1033	01.09.2014	19			26.3 1.4				
DK14/3	159.1033	02.09.2014	17	85.0 9.0		48.0 4.0				
DK14/4	159.1033	02.09.2014	15	94.0 7.0		54.4 2.4				
DK14/5	159.1033	02.09.2014	13			60.4 2.8				
K17	206.900	11.04.2012	18	4 107.0 12.0		6.8 0.6	1.6×10^{-6}	5.8 0.4	10.5	3.2×10^{-9}
K4	206.90B	12.04.2012	36	3 81.0 9.0	0.2 < 0.1	15.3 0.9	1.4×10^{-7}	3.9 0.3	13.8	9.4×10^{-7}
K5	206.90C	12.04.2012	20	2 101.0 14.0		31.4 0.6	1.3×10^{-6}	0.5 0.1	8.7	2.0×10^{-8}
K11	206.90K	11.04.2012	60	37.0 6.0	0.1 < 0.1	4.1 0.3	1.5×10^{-7}	-0.1 0.0	6.1	6.3×10^{-7}
L6A	206.940	12.04.2012	15	1 180.0		5.2 0.9	4.7×10^{-7}		22.6	2.4×10^{-7}
L 1	206.94A	13.04.2012	60	6 53.0 7.0		2.2 0.2	2.6×10^{-7}	0.1 0.1	0.2	3.0×10^{-7}
L2	206.94B	13.04.2012	65	9 49.0 10.0		1.5 0.4	1.9×10^{-7}	0.0 0.1	1.3	4.6×10^{-7}
B25	217.862	13.04.2012	52	27 491.0 71.0			6.5×10^{-7}	0.6 0.1	5.7	1.0×10^{-7}
B24	217.863	13.04.2012	50	25 246.0 15.0		1.5 0.2	9.6×10^{-7}	1.6 0.4	11.6	6.0×10^{-8}
B24	217.863	22.08.2019		198.0 16.0	55.5 3.2	4.4 0.7	9.6×10^{-7}	1.6 0.5	11.6	6.0×10^{-8}
B23	217.913	13.04.2012	53	28 173.0 25.0		1.7 0.3	2.0×10^{-6}	4.0 0.3	30.3	1.7×10^{-8}
T1	242.385	14.09.2021		231.9 23.9	396.1 38.2	0.7 0.5	2.1×10^{-7}	0.0	-5.1	5.2×10^{-7}
DK14/6	8.222	03.09.2014	25	73.0 15.0		1.0				
DK14/7	8.222	03.09.2014	15	79.0 9.0		10.3 1.0				
A4	88.1580	23.07.2019		135.0 30.0	13.4 4.2	3.0 0.2	1.8×10^{-6}	3.1 0.3	19.0	1.2×10^{-8}

Continued on next page

Well	DGU	Sampling date	Depth [m]	^{39}Ar [%mod]	^{37}Ar [mBq m $^{-3}$ air]	^{85}Kr [dpm cc $_{\text{Kr}}^{-1}$]	$^3\text{He}/^4\text{He}$	^3H [TU]	$^3\text{He}_{\text{trit}}$ [TU]	$^4\text{He}_{\text{RAD}}$ [cc g $^{-1}$]
Edslev1	88.1942	21.08.2019		100.0	15.0	29.8	1.5×10^{-6}	4.1	1.1	5.3×10^{-9}
Edslev2	88.1979	21.08.2019		61.0	8.0	5.1	1.9×10^{-6}	3.7	0.4	3.8×10^{-9}
Edslev3	88.1979	21.08.2019		62.0	7.0	4.1	1.8×10^{-6}	3.5	0.4	2.7×10^{-9}
A5	88.969	23.07.2019		77.0	9.0	5.7	1.9×10^{-6}	3.4	0.4	7.5×10^{-9}
A3	89.1421	23.07.2019		62.0	11.0	0.6				
A6	89.1421	23.07.2019		5.0	6.0	3.2		2.0	1.1	
AO3	95.1951	02.08.2011	6	103.0	14.0	45.8				
AO1	95.2730-1	02.08.2011	149	48.0	7.0	1.0				
AO2	95.2730-2	02.08.2011	70	42.0	9.0	1.0				
DK 9b	97.980	29.08.2005	166	65.0	10.0	1.4		0.1	3.1	
PG DK 8a	97.980	29.08.2005	178	65.0	6.0			0.0	3.1	
DK 7b	97.980	30.08.2005	190	62.0	10.0	1.4		0.3	4.8	
DK6a	97.980	30.08.2005	202					0.0	3.4	
DK 5a	97.980	30.08.2005	214	47.0	5.0			0.2	1.0	
DK 4a	97.980	31.08.2005	226	40.0	4.0			0.2	1.0	
DK 3b	97.980	31.08.2005	238					0.2	4.1	
DK 3a	97.980	31.08.2005	238					0.2	3.1	
PG DK2a	97.980	31.08.2005	250	64.0	7.0			0.3	3.7	
DK 1a	97.980	01.09.2005	262	59.0	10.0			0.2	2.4	
Tyrsting 30-50	97.980		40			4.5	0.7			
Tyrsting 71-81	97.980		75			2.5	0.4			
Tyrsting 100-110	97.980		105							
GreviePV5		41013		73.0	7.0	0.5	0.1	0.0	0.1	
Lifa		41013		92.0	9.0		6.1×10^{-7}		-1.3	

A.5 [Article]Explicit simulation of environmental gas tracers with integrated surface and subsurface hydrological models

Hugo Delottier, Morgan Peel, **Stephanie Musy**, Oliver S. Schilling, Roland Purtschert and Philip Brunner

Published in *Frontiers in Water*, Water and Hydrocomplexity, 4:980030, 2022
doi: 10.3389/frwa.2022.980030

Abstract Environmental gas tracers are useful in subsurface hydrology to infer groundwater travel times and mixing ratios. Their concentrations measured in the field, which depend on the partitioning between the liquid and gas phases, are commonly interpreted with simplified and indirect approaches that are conceptually at odds with the high degree of complexity found in natural systems. The direct simulation of tracers through the solution of an advection-dispersion transport equation is needed to enhance data assimilation of this new information type. Integrated surface and subsurface hydrological models are usually variably saturated flow models. These integrated models can be used to explicitly simulate environmental tracers in complex environments. However, the majority of these models do not explicitly simulate gas partitioning with the liquid phase, restricting explicit simulation of environmental gas tracers to fully saturated conditions or to tracers with very low solubility. We propose a simplified mathematical formulation for the production of environmental gas tracers that are emanated in the subsurface. The production is scaled according to water saturation, which is already computed by the flow model. Thus, integrated surface and subsurface hydrological models can now be used for variably saturated simulations of environmental gas tracers without explicitly simulating gas transport. The new formulation has been successfully verified against reference simulations provided with a multiphase flow and transport model. A synthetic river-groundwater model illustrates the capacity of the proposed feature to simultaneously simulate ^{222}Rn and ^{37}Ar isotopes.



OPEN ACCESS

EDITED BY

Giacomo Bertoldi,
Eurac Research, Italy

REVIEWED BY

Reed Maxwell,
Princeton University, United States
Majdi Mansour,
The Lyell Centre, United Kingdom

*CORRESPONDENCE

Hugo Delottier
hugo.delottier@unine.ch

SPECIALTY SECTION

This article was submitted to
Water and Hydrocomplexity,
a section of the journal
Frontiers in Water

RECEIVED 28 June 2022

ACCEPTED 23 August 2022

PUBLISHED 28 September 2022

CITATION

Delottier H, Peel M, Musy S,
Schilling OS, Purtschert R and
Brunner P (2022) Explicit simulation of
environmental gas tracers with
integrated surface and subsurface
hydrological models.
Front. Water 4:980030.
doi: 10.3389/frwa.2022.980030

COPYRIGHT

© 2022 Delottier, Peel, Musy, Schilling,
Purtschert and Brunner. This is an
open-access article distributed under
the terms of the [Creative Commons
Attribution License \(CC BY\)](#). The use,
distribution or reproduction in other
forums is permitted, provided the
original author(s) and the copyright
owner(s) are credited and that the
original publication in this journal is
cited, in accordance with accepted
academic practice. No use, distribution
or reproduction is permitted which
does not comply with these terms.

Explicit simulation of environmental gas tracers with integrated surface and subsurface hydrological models

Hugo Delottier^{1*}, Morgan Peel¹, Stéphanie Musy²,
Oliver S. Schilling^{3,4}, Roland Purtschert² and Philip Brunner¹

¹Centre for Hydrogeology and Geothermics (CHYN), Faculty of Science, University of Neuchâtel, Neuchâtel, Switzerland, ²Climate and Environmental Physics and Oeschger Center for Climate Change Research, Faculty of Science, University of Bern, Bern, Switzerland, ³Hydrogeology, Department of Environmental Sciences, University of Basel, Basel, Switzerland, ⁴Eawag, Swiss Federal Institute of Aquatic Science and Technology, Dübendorf, Switzerland

Environmental gas tracers allow inferring groundwater travel times and mixing ratios. Their concentrations are commonly interpreted with simplified and indirect approaches that are conceptually at odds with the high degree of complexity found in natural systems. However, the information content of the tracers can potentially be fully explored through the explicit simulation of an advection-dispersion transport equation, for example using integrated surface-subsurface hydrological models (ISSHMs). These integrated models can be used to explicitly simulate environmental tracers in complex environments. ISSHMs are usually variably saturated flow models. However, these models do not explicitly simulate gas partitioning with the aqueous phase, restricting explicit simulation of gas tracers to fully saturated conditions or to tracers with very low solubilities. We propose a mathematical formulation for the production of environmental gas tracers that are emanated in the subsurface. The production is scaled according to gas/water partitioning and water saturation, which is already computed by the model. Therefore, ISSHMs can now be used to their full potential to explicitly simulate tracer concentrations under variably saturated and dynamic conditions. The new formulation has been successfully verified against reference simulations provided with a multi-phase flow and transport model. In addition, explicit simulation of ²²²Rn and ³⁷Ar groundwater concentrations in a synthetic alluvial river-groundwater system was demonstrated, for the first time, with an ISSHM.

KEYWORDS

environmental gas tracers, integrated surface and subsurface hydrological models, mass-transport, subsurface hydrology, unsaturated zone processes

Introduction

Hydrologic environmental tracers are widely distributed in the near-surface environment of the Earth, such that their abundance facilitates their consideration for studying a range of subsurface flow processes (Cook and Herczeg, 2012; Partington et al., 2020; Dwivedi et al., 2022). Many environmental tracers (e.g., CFCs, N₂, O₂, Ar, Ne, Kr, He, Xe, CH₄, CO₂, ²²²Rn, and SF₆) are gases that dissolve into water. These environmental gas tracers can be either natural (e.g., ³⁹Ar, ⁸⁵Kr) or anthropogenic (e.g., CFCs, SF₆) and their concentrations can either remain stable, increase (production) and/or decrease (decay) in the subsurface as a function of time.

The residence time of water in the subsurface is the sum of the transit times through the unsaturated and saturated zones. Residence times can be obtained from the decay of radioactive tracers and from tracers that are produced (accumulating tracers) in the subsurface. Therefore, their measured concentrations can be used to determine pathways and timescales (i.e., ages) of groundwater (Kazemi et al., 2006).

Tracer concentrations are usually considered for estimating apparent ages that are then used in the calibration of hydrological models (Van Huijgevoort et al., 2016; Schilling et al., 2017a, 2019, 2022). However, these simplified and indirect approaches are conceptually at odds with the high degree of complexity found in natural systems (McCallum et al., 2015, 2017; Peel et al., 2022). The explicit simulation of tracer mass-transport through the solution of an advection-dispersion equation is a promising pathway that can potentially increase the information contained in the tracers (Goode, 1996; Turnadge and Smerdon, 2014). A zero-order source term (or boundary condition) can be used to consider environmental tracers that are produced in the subsurface.

Gases that are emanated in the unsaturated media will partition between the aqueous and gaseous phases as a function of their solubility in water and water saturation. Therefore, a rigorous way to model accumulating tracers in a numerical flow model requires the consideration of both gas and liquid phases to allow exchanges between the two. For gases with high solubilities (e.g., ²²²Rn), deep unsaturated zones, and for tracers where the concentration is a function of depth (e.g., Ar isotopes), the consideration of a gas phase in the model is a prerequisite for robust tracer simulation.

The consideration of both gas and liquid phases requires the use of multiphase fluid flow and transport models that solve the advection-dispersion equation. HYDRUS, NUFT, and Getflows (Nitao, 1998; Tosaka et al., 2000; Simunek et al., 2016) are examples of multiphase flow and transport models. However, these mechanistic models are computationally demanding and are therefore usually preferred for controlled experiments and to model mass-transport in unsaturated soils (Guillon et al., 2016).

In groundwater hydrology, the simulation of the unsaturated zone along with the groundwater flow domain and the surface water flow domain can be done using integrated surface and subsurface hydrologic models (ISSHM) (Sebben et al., 2013; Paniconi and Putti, 2015). These integrated models are particularly well-suited to study complex hydrodynamic behaviors such as river-groundwater interactions that characterize shallow subsurface environments (Brunner et al., 2017). HydroGeoSphere (Brunner and Simmons, 2012; Aquanty Inc., 2022), ParFlow (Kollet and Maxwell, 2008), or OpenGeoSys (Kolditz et al., 2012) are examples of such integrated models. Some of these models allow the explicit simulation of tracers in the saturated zone of the aquifer. For instance, explicit modeling or a radiogenic tracer such as ²²²Rn has been recently proposed with HydroGeoSphere (Gilfedder et al., 2019). However, most of the integrated models are single-phase flow, preventing the consideration of a gas phase in the unsaturated zone. Thus, the zero-order source, which allows a tracer to be produced in the subsurface, does not consider gas/water partitioning, potentially leading to an overly large concentration in the unsaturated zone, as the produced tracer accumulates in a smaller volume of water compared to what would be the case under full saturation.

To overcome this issue we propose a simplified mathematical formulation for the production of environmental gas tracers that are emanated in the subsurface, which allows the solute mass production rate for variably saturated conditions to be scaled according to the degree of saturation and the gas/water partitioning coefficient. The proposed formulation is designed for single-phase surface and subsurface flow and transport in integrated hydrological models that are capable of simulating variably saturated subsurface flow. In the present study this formulation was implemented in the ISSHM HydroGeoSphere (HGS) and is called *via* the “Zero-order source with partitioning” command (Aquanty Inc., 2022). The new formulation in HGS was validated against an explicit multiphase flow and transport reference case implemented in the software HYDRUS-1D (Simunek et al., 2016). The capability of the new formulation is illustrated for a river-groundwater flow system where ²²²Rn and ³⁷Ar are explicitly simulated.

Mathematical formulation

An instant-equilibration mass balance

The present section introduces the derivation of the proposed instant-equilibration mass-balance to scale the production of dissolved gas tracers according to the degree of water saturation of the subsurface. An underlying assumption is that any produced amount of tracer will partition immediately into both the gas and aqueous phases. In a small test volume V_{test} , we can write:

$$\frac{\delta Q_{tracer,tot}^{prod}}{\delta t} = P_{sat} V_{pore} \quad (1)$$

where, $\delta Q_{tracer,tot}^{prod}$ [M] is the amount of tracer produced in a small time increment δt [T], P_{sat} [$M \cdot L^{-3} \cdot T^{-1}$] is the total tracer production rate (assumed independent of the degree of water saturation), and V_{pore} [L^3] is the pore volume of the matrix (porosity $\times V_{test}$).

If we assume that the amount of tracer δQ_{tracer}^{prod} is partitioned into both gas and aqueous phases, we can write the following mass balance relationship:

$$\delta Q_{tracer}^{prod} = \delta Q_{tracer,water}^{prod} + \delta Q_{tracer,air}^{prod} = \delta C_{tracer,water}^{prod} V_{water} + \delta C_{tracer,air}^{prod} V_{air} \quad (2)$$

where, $\delta Q_{tracer,water}^{prod}$ and $\delta Q_{tracer,air}^{prod}$ are the amounts of produced tracer [M] which go into the liquid and gas phases, respectively. Similarly, $\delta C_{tracer,water}^{prod}$ and $\delta C_{tracer,air}^{prod}$ are changes in tracer concentrations from the zero-order source [$M \cdot L^{-3}$] in the given volumes of water V_{water} [L^3] and air V_{air} [L^3].

Assuming a solubility law of the form $H^{cc} = \frac{C_{water}}{C_{air}}$ with instant equilibration, we can write:

$$\begin{aligned} \delta Q_{tracer}^{prod} &= H^{cc} \delta C_{tracer,air}^{prod} V_{water} + \delta C_{tracer,air}^{prod} V_{air} \\ &= \delta C_{tracer,air}^{prod} (H^{cc} V_{water} + V_{air}) \end{aligned} \quad (3)$$

If we divide both sides by V_{pore} , we get:

$$\begin{aligned} \frac{1}{V_{pore}} \delta Q_{tracer}^{prod} &= \delta C_{tracer,air}^{prod} \frac{H^{cc} V_{water} + V_{air}}{V_{pore}} \\ &= \delta C_{tracer,air}^{prod} (H^{cc} S_w + S_a) \end{aligned} \quad (4)$$

where, S_w and $S_a = 1 - S_w$ are respectively, the degree of water and air saturations [-]. Therefore, by combining Equation (4) with Equation (1) we can write:

$$P_{sat} = \frac{1}{V_{pore}} \frac{\delta Q_{tracer}^{prod}}{\delta t} = \frac{\delta C_{tracer,air}^{prod}}{\delta t} (H^{cc} S_w + [1 - S_w]) \quad (5)$$

Which can also be written as follows:

$$\frac{\delta C_{tracer,air}^{prod}}{\delta t} = \frac{P_{sat}}{H^{cc} S_w + [1 - S_w]} \quad (6)$$

If we define the effective production rate in water P_{eff} [$M \cdot L^{-3} \cdot T^{-1}$] as the amount of tracer input only into the water phase per unit time, we can write:

$$P_{eff} = \frac{\delta C_{tracer,water}^{prod}}{\delta t} = H^{cc} \frac{\delta C_{tracer,air}^{prod}}{\delta t} = \frac{H^{cc} P_{sat}}{H^{cc} S_w + [1 - S_w]} \quad (7)$$

This formulation (Equation 7) is equivalent to the original zero-order source as implemented in HGS (production per unit aquifer volume) in the limit $H^{cc} \rightarrow \infty$ (i.e., no partitioning) and for $S_w = 1$ regardless of H^{cc} . This means that all produced species remain in the aqueous phase. In the case $H^{cc} \rightarrow 0$, the tracer is immediately volatilized. Mean groundwater age, defined with the age-mass concept (Goode, 1996), can be estimated directly by setting $H^{cc} = 1$ with a solute mass production rate equal to the aquifer porosity and with a decay constant of zero (no decay of mean age).

Equation 7 assumes that every produced atom in the unsaturated zone partitions immediately into both gas and aqueous phases according to a fixed partitioning coefficient. Thus, the proposed formulation is equivalent to an equilibrium solute transport model where the mass of volatilized tracer, which in theory would interact with groundwater in case of variations in water saturation, is not considered. The phase-equilibrium partitioning coefficient H^{cc} , is considered constant, synonymous with isothermal conditions. Moreover, H^{cc} is a well-constrained parameter as it strictly depends on water temperature and the considered species. Interested readers should refer to Cook and Herczeg (2012) and Schubert et al. (2012) for default values of H^{cc} for ^{222}Rn and ^{37}Ar , respectively.

The hypothesis of saturation-independent emanation is supported by the fact that ^{222}Rn (and likely ^{37}Ar) emanation has been shown to reach its maximum value at moderate degrees of water saturation, typically between 0.2 and 0.3 (e.g., Sun and Furbish, 1995; Zhuo et al., 2006). Indeed, the presence of a thin moisture film on the surface of mineral grains will prevent produced atoms recoiled into the pore space from embedding into adjacent grains, as recoil ranges of atoms in water are orders of magnitude lower than those in air. Only in very dry conditions and low residual water contents in the porous medium can this hypothesis no longer be justified.

Verification

To verify the proposed instant-equilibration mass balance as newly implemented in HGS, simulations of ^{222}Rn in an unsaturated medium using HGS are compared with explicit multi-phase simulations using HYDRUS-1D. HYDRUS-1D is based on a finite element model that solves Richard's equation for variably-saturated subsurface flow and Fickian-based advection-dispersion equations for heat and mass transport.

In the proposed experiment, HYDRUS-1D was used to solve the advection-dispersion solute transport equations with a linear equilibrium between the aqueous and the gaseous phases.

Diffusion in both aqueous and gas phases were considered to be instantaneous (i.e., equilibrium transport). Moreover, we did not consider the effects of adsorption-desorption and we have assumed no immobile fraction of water. Thus, the advection-dispersion equation can be written in the following form:

$$\frac{\partial \theta c}{\partial t} + \frac{\partial a g}{\partial t} = \frac{\partial}{\partial x} \left(\theta D^w \times \frac{\partial c}{\partial x} \right) + \frac{\partial}{\partial x} \left(a D^g \times \frac{\partial g}{\partial x} \right) - \frac{\partial q c}{\partial x} - (\mu_w \theta c + \mu_g a g) + (\gamma_w \theta + \gamma_g a) \quad (8)$$

where, c and g are solute concentrations in the aqueous [$\text{M} \cdot \text{L}^{-3}$] and gaseous [$\text{M} \cdot \text{L}^{-3}$] phases, respectively; θ [$\text{L}^3 \cdot \text{L}^{-3}$] is the water content, ρ [$\text{M} \cdot \text{L}^{-3}$] is the soil bulk density, a [$\text{L}^3 \cdot \text{L}^{-3}$] is the air content, D^w [$\text{L}^2 \cdot \text{T}^{-1}$] is the dispersion coefficient for the aqueous phase, D^g [$\text{L}^2 \cdot \text{T}^{-1}$] is the diffusion coefficient for the gas phase, q [$\text{L} \cdot \text{T}^{-1}$] is the volumetric fluid flux density, μ_w and μ_g [T^{-1}] are first-order rate (decay) constants for solutes in the aqueous and gas phases, respectively; γ_w and γ_g [$\text{M} \cdot \text{L}^{-3} \cdot \text{T}^{-1}$] are zero-order rate constants (or source) for the aqueous and gas phases, respectively.

Furthermore, equilibrium exchange between water and gas concentrations of the solute in the soil system was assumed. The adsorption isotherm was considered linear. The concentrations in the aqueous and in the gas phases (c and g) are related by a linear expression of the form:

$$g = k_g \times c \quad (9)$$

where, k_g [-] is an empirical constant equal to $(K_H \cdot R_u \cdot T_A)^{-1}$, in which K_H [$\text{M} \cdot \text{T}^2 \cdot \text{M}^{-1} \cdot \text{L}^{-2}$] is Henry's law coefficient, R_u [$\text{M} \cdot \text{L}^2 \cdot \text{T}^{-2} \cdot \text{K}^{-1} \cdot \text{M}^{-1}$] is the universal gas constant and T_A [K] is the absolute temperature. The advection-dispersion equations were solved in the gas and in the aqueous phases, thus permitting the simulation of solute transport simultaneously in both the aqueous and gas phases.

²²²Rn production

²²²Rn is produced as an intermediary product in the ²³⁸U decay chain, and is released into groundwater as a result of the alpha decay of matrix-bound ²²⁶Ra (Cecil and Green, 2000). This radioactive noble gas with a half-life of 3.82 days is commonly used in groundwater hydrology as a tracer of surface water—groundwater interactions, as ²²²Rn activities in groundwater are often orders of magnitude higher than those in surface water (Cecil and Green, 2000). Upon infiltration of surface water with low ²²²Rn activities into the subsurface, ²²²Rn concentrations will gradually increase until they reach secular equilibrium after ~15–20 days (Hoehn and Von Gunten, 1989). Therefore, it has been extensively used

to study very young groundwater dynamics and mixing [i.e., timescales of several hours to a few weeks (Cook et al., 2008; Bourke et al., 2014; Cartwright and Gilfedder, 2015; Peel et al., 2022)]. Assuming spatially homogenous ²²²Rn production, the relationship between production rate per unit pore volume γ_{Rn} [$\text{M} \cdot \text{L}^{-3} \cdot \text{T}^{-1}$] and equilibrium ²²²Rn activity concentration in groundwater $C_{Rn,eq}^{Sat}$ [$\text{M} \cdot \text{L}^{-3}$] is given by the following equation:

$$C_{Rn,eq}^{Sat} = \frac{\gamma_{Rn}}{\lambda_{Rn}} \quad (10)$$

where, λ_{Rn} [T^{-1}] is the ²²²Rn decay constant. The value for $C_{Rn,eq}^{Sat}$, which is site specific since it is closely related to aquifer geochemistry and mineral texture, has been considered homogenous for the present study, and set to 15 Bq·l⁻¹ (e.g., Popp et al., 2021).

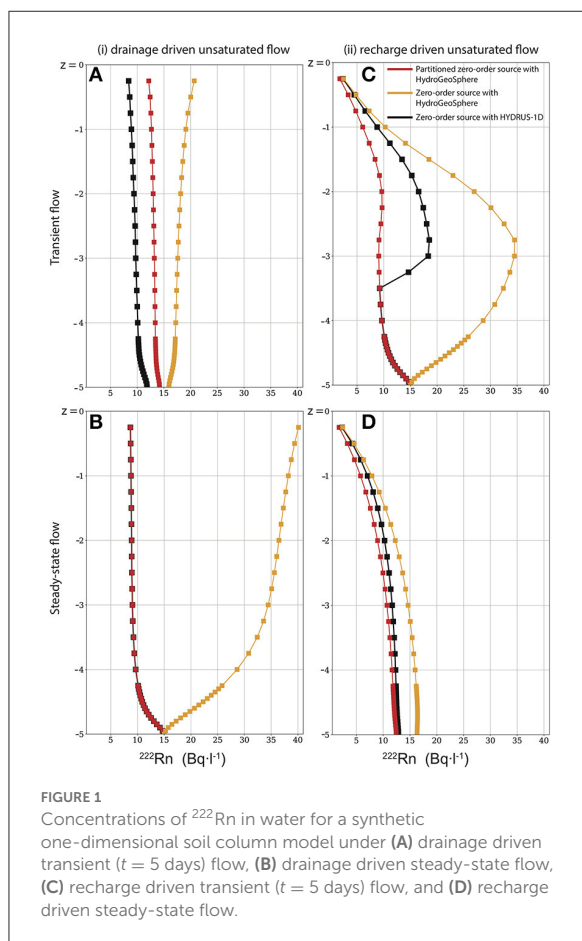
Model set-up

As a verification experiment, a one-dimensional soil column 5-m thick uniformly discretized with 0.05 m vertical intervals is considered for both HYDRUS-1D and HGS.

In both models, the soil column was assumed homogeneous and variably saturated flow was solved using the van Genuchten—Mualem model with the fitting parameters α [L^{-1}] and β [-] set to 3.48 and 1.75, respectively, simulating a typical alluvial gravel (Dann et al., 2009; Schilling et al., 2020). The residual soil water content was set to 0.095 and the porosity to 0.41. A value of 1 m·d⁻¹ was used for the saturated hydraulic conductivity. The tortuosity parameter in the conductivity function was set to 0.5. The longitudinal horizontal dispersivity was set to 0.1 m, while the transverse dispersivities were set to 0.01 m. A pore pressure of 0 was applied to nodes at the bottom ($z = -5\text{m}$) of the column, making the bottom of the soil model a constant water table elevation.

For HYDRUS-1D, the bulk density was set to 1.593 g·cm⁻³. In Equation 9, which controls the interaction between the liquid and the gas concentrations, the empirical constant k_g was set to 2.155 (-), which is the inverse of the partitioning coefficient H^{cc} as defined in Equation 3. The first-order rate (decay) constant for ²²²Rn was set to 0.1814 d⁻¹ for all phases. The γ_w , and γ_g zero-order rate constants were set to 2721 Bq·m⁻³ · d⁻¹, which has been derived from Equation 10, assuming a saturated ²²²Rn activity $C_{Rn,eq}^{Sat}$ of 15 Bq·l⁻¹.

Flow and transport through the soil column were simulated according to two scenarios: (i) drainage conditions and (ii) recharge conditions. The soil column was initially considered fully saturated with water. For scenario (i), the model was run without any infiltration fluxes at the top so that the soil column is progressively drained until a pseudo steady-state condition was reached after 365 days (Figure 1B). We refer to pseudo steady-state as transient simulations that reaches a dynamic equilibrium



state, that is, a point at which there is minimal drift in the model states (similar to actual steady-state conditions). Starting from this new pseudo steady-state condition, for scenario (ii), a constant input flux of $0.1 \text{ m}\cdot\text{d}^{-1}$ was then considered at the top of the column, simulating an extremely high infiltration flux. The model was then run for another 365 days until a new pseudo steady-state condition was reached (Figure 1D). To evaluate the performance of the HGS simulations in transient conditions, snapshots of dissolved ^{222}Rn activities were also taken five days after the beginning of each simulation scenario (Figures 1A,C). For a majority of locations, the simulated saturation profiles of HGS and HYDRUS-1D were nearly identical (Supplementary Figure A1), therefore allowing direct comparisons of the tracer concentrations simulated with the two different software.

Results

Under drainage driven flow and transport (scenario (i); Figures 1A,B), a perfect match of the simulation of ^{222}Rn after

365 days was reached with HYDRUS-1D (under consideration of explicit multi-phase flow) and HGS (under consideration of the new partitioned zero-order source production), demonstrating the consistency of the simplified approach under pseudo steady-state conditions. After five days of drainage (i.e., highly transient conditions), the HGS-based simulations with partitioned zero-order source production slightly overestimated the ^{222}Rn concentrations compared to the multi-phase flow simulations with HYDRUS-1D. This reflects the ability of HYDRUS-1D to explicitly account for ^{222}Rn in both the gas and liquid phases. When the saturation drops, dissolved ^{222}Rn concentrations re-equilibrate with those in the gas phase; in other words, a drop in saturation will lead to the volatilization of some of the dissolved ^{222}Rn to the gas phase and therefore a reduction of the concentration in the aqueous phase. In HGS, the gas phase is not simulated explicitly and the ^{222}Rn concentration in water is therefore not directly affected by changes in saturation; only production is scaled, which leads to an overestimation of ^{222}Rn activities in water after five days of transient simulation of drainage.

Under recharge driven flow (scenario (ii); Figures 1C,D), the opposite mechanism occurs, and ^{222}Rn concentrations in water are slightly underestimated with HGS compared to HYDRUS-1D in highly transient conditions. As in the drainage scenario, the difference is more pronounced under transient conditions compared to the pseudo steady-state, when the simulated concentration profiles of both codes almost match. The reason for the mismatch lies in the fact that once the saturation increases within the soil column because of the constant input flux from the top, dissolved ^{222}Rn concentrations start to increase as a result of soil matrix production, but also because of the dissolution of ^{222}Rn from the gas phase into the water. Again, as in HGS, the gas phase is not explicitly simulated, dissolved ^{222}Rn concentrations in the soil column tend to be underestimated compared to the explicit multi-phase simulations with HYDRUS-1D.

Under both drainage and recharge conditions, more realistic simulations were obtained with HGS when the zero-order source was partitioned with the water saturation (red lines in Figure 1). When the production of ^{222}Rn was not scaled according to water saturation (i.e., unpartitioned zero-order source), the ^{222}Rn concentrations in the unsaturated soil column were significantly overestimated by HGS because the same amount of total produced tracer mass accumulated in a comparatively smaller volume of water (orange lines in Figure 1). Although some discrepancies between HYDRUS-1D and HGS with the proposed partitioned zero-order source along a one-dimensional unsaturated soil column could be identified, the improvement achieved with the partitioned zero-order source implementation is significant, resulting in nearly matching pseudo steady-state conditions under both drainage and recharge conditions. The proposed partitioned zero-order source approach is thus a highly efficient and simplified, yet

TABLE 1 Parameter values involved in the production of ^{37}Ar from fast cosmic ray neutrons.

		Values	Unit
Surface production (SLHL)	P_o	0.00141	$\text{atoms} \cdot \text{cm}^{-3} \cdot \text{yr}^{-1} \cdot \text{mgCa}^{-1} \cdot \text{kg}_{\text{rock}}$
Calcite content	Ca	107,870.83	$\text{mg} \cdot \text{kg}^{-1}$
Potassium content	K	8,365.84	$\text{mg} \cdot \text{kg}^{-1}$
Grain density	ρ_g	3.375	$\text{g} \cdot \text{cm}^{-3}$
Scaling factor	X_{SC}	0.96	–
Emanation	ϵ	1	%
Partitioning coefficient	H^c	0.04182	–
Attenuation length	Λ	94	$\text{g} \cdot \text{cm}^{-2}$

realistic, way to include simulations of environmental gas tracers in the unsaturated zone for applications involving both surface and the subsurface flow processes, especially where the application of computationally demanding and complex two-phase flow models is not desirable or practical.

Illustrative example

The simulation of environmental gas tracer concentrations with a single-phase ISSHM is illustrated below using a more realistic and complex model configuration. For this purpose, a synthetic alluvial plain model was used for the simulation of ^{222}Rn and ^{37}Ar mass-transport. The consideration of both ^{222}Rn and ^{37}Ar was motivated by their short half-lives, making these tracers particularly well-suited to track recently infiltrated surface water in shallow alluvial aquifers (Brunner et al., 2017; Schilling et al., 2017a).

^{37}Ar production

^{37}Ar is a rare radioactive isotope of argon with a half-life of 34.95 ± 0.08 days (Renne and Norman, 2001). A originally ^{37}Ar free water parcel that enters the subsurface reaches 88% of the secular production-decay equilibrium after three half-lives of ^{37}Ar , i.e., after approximately 110 days. In the shallow underground, ^{37}Ar atoms are primarily produced by cosmogenic neutron activation of calcium ($^{40}\text{Ca}(n,\alpha)^{37}\text{Ar}$), and to some extent spallation of potassium ($^{39}\text{K}(n,p2n)^{37}\text{Ar}$) (Fabryka-Martin, 1988; Loosli and Purtschert, 2005; Riedmann and Purtschert, 2011). The flux of fast cosmogenic neutrons is

exponentially attenuated with depth on a length scale, which is proportional to the density of the medium without of its elemental composition (Gosse and Phillips, 2001). Other production reactions, e.g., induced by muons or by neutrons from (α, n) reactions can be neglected in the depth range considered here (Spannagel and Fireman, 1972; Heisinger et al., 2002; Sramek et al., 2017). The depth dependent production rate $^{37}P_{(z)r}$ in ($\text{atoms} \cdot \text{yr}^{-1} \cdot \text{cm}^{-3}$) has been parameterized through a production function equation (Guillon et al., 2016) and can be described as follows:

$$^{37}P_{(z)r} = ([Ca] + 0.38 [K]) \times X_{\text{SC}} \times P_o \times e^{-\frac{z}{\Lambda} [(1-n)\rho_g + n\rho_w S_w]} \quad (11)$$

where, Ca and K are calcite and potassium contents in ($\text{mg} \cdot \text{kg}^{-1}$), X_{SC} (-) is a scaling factor for latitude and altitude, P_o ($\text{atoms} \cdot \text{cm}^{-3} \cdot \text{yr}^{-1} \cdot \text{mgCa}^{-1} \cdot \text{kg}_{\text{rock}}$) is the surface production normalized for sea level and high latitude (SLHL) (Fabryka-Martin, 1988) and for Ca and K content. Λ ($\text{g} \cdot \text{cm}^{-2}$) is the attenuation length for fast neutron in soils/rocks. z ($\text{g} \cdot \text{cm}^{-2}$) is the product of depth below ground surface (cm) and water density ($\text{g} \cdot \text{cm}^{-3}$), n (-) is the porosity. ρ_g ($\text{g} \cdot \text{cm}^{-3}$) is the grain density and S_w (-) is the water saturation.

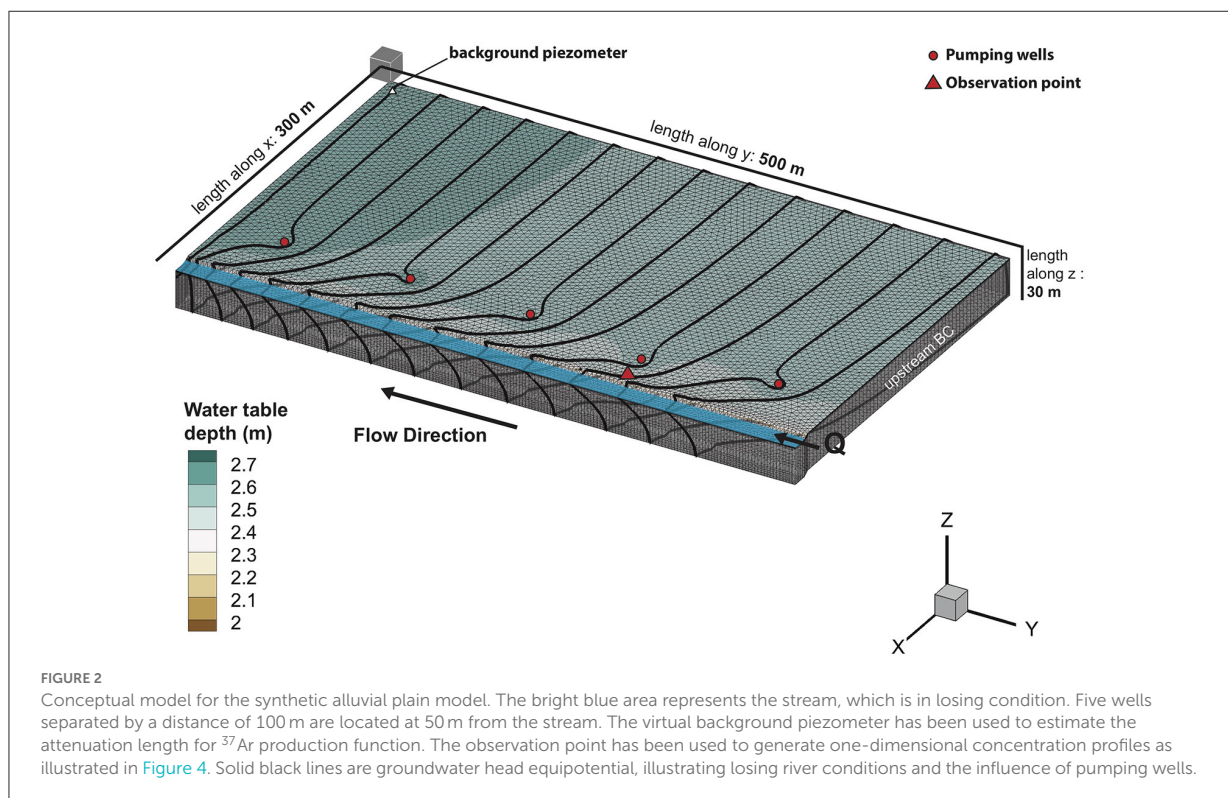
From the above production function, the daily production of ^{37}Ar in water $^{37}P_{(z)w}$ ($\text{atoms} \cdot \text{m}^{-3} \cdot \text{d}^{-1}$) can be computed as follows:

$$^{37}P_{(z)w} = \frac{^{37}P_{(z)r} \times \left[\frac{\epsilon}{n}\right] \times 10^6}{365} \quad (12)$$

where, ϵ (-) is the emanation factor, which was determined by irradiation experiments (Johnson et al., 2021; Musy et al., 2022). The attenuation length of cosmogenic fast neutrons depends on the density of the material crossed. Along a given column of water, the saturation and porosity is 1 in Equation 11, resulting in a lower density and higher attenuation length compared to a same column of rocks. Thus, ^{37}Ar production below a stream ($^{37}P_{\text{stream}}$) is reduced compared to the production in the aquifer at the same depth. The reduction factor depends on the height of the water column h (cm) and the water density ρ_w ($\text{g} \cdot \text{cm}^{-3}$) such that:

$$^{37}P_{\text{stream}} = ^{37}P_{(z)w} \frac{-h \times \rho_w}{\Lambda} \quad (13)$$

Most of the parameters related to the production of ^{37}Ar should be measured in the field so that realistic concentrations of ^{37}Ar can be generated. Therefore, measurements from a pre-alpine alluvial aquifer were here considered to define the values for the parameters introduced in this section (Table 1). As the attenuation length parameter itself cannot be measured directly in the field, for the illustrative model it has been manually



estimated such that the secular equilibrium profile in a virtual background piezometer (Figure 2) reproduces a ^{37}Ar secular equilibrium profile determined from measurements of ^{37}Ar activity concentrations in a sandy-gravel aquifer in the Swiss pre-Alps (Schilling et al., 2017a).

Model set-up

The HGS model for the synthetic alluvial river-groundwater system has a spatial extent of $300 \times 500 \times 30$ m along the x-, y-, and z-directions, respectively (Figure 2). The alluvial plain was gently inclined toward the stream outlet with a slope of 0.003 m/m in the y-direction and discretized with a 2D unstructured triangular mesh with lateral internodal spacing ranging from 4 m along the stream to 7 m on the alluvial plain. The 2D mesh was generated with AlgoMesh (HydroAlgorithmics Pty Ltd, 2016). The model consists of 41 layers of elements used to discretize the alluvial plain in the z-direction, with an exponential range of layer thicknesses varying from 0.05 m at the surface without exceeding more than 1 m at depth (Figure 2). This relatively fine vertical discretization has been chosen to appropriately simulate the vertical and exponential decrease of ^{37}Ar emanation rates. The resulting 3D mesh has a total of 2,87,615 nodes for 5,44,000 elements.

The stream was conceptualized as a 20 m wide and 2 m deep channel (Figure 2). As in all ISSHM, streamflow was simulated explicitly, allowing infiltration of stream water and exfiltration of groundwater to arise naturally, that is, without the need to specify additional internal boundary conditions. Stream water inflow at the upstream end of the model was conceptualized as a second-type (specified flux) boundary condition (BC) with a value of $2 \text{ m}^3 \cdot \text{s}^{-1}$. Surface water outflow was implemented as a critical depth BC to nodes in the stream. Due to very rough surface usually found in alluvial streams, a high value for Manning's n ($1.7 \times 10^{-6} \text{ d} \cdot \text{m}^{-1/3}$) was used. To ensure pressure continuity between the surface and the subsurface, the coupling length (i.e., the first-order exchange coefficient), was set to a low value of 0.001 m (Liggett et al., 2012).

The aquifer was conceptualized as a homogeneous sandy gravel porous medium with a van Genuchten α of 3.40 m^{-1} , a van Genuchten β of 1.71 (-), and a residual water saturation of 0.05 (-). The hydraulic conductivity (K) and porosity (n) of the homogeneous aquifer were set to $500 \text{ m} \cdot \text{d}^{-1}$ and 0.15, respectively, mimicking typical values for sandy-gravel aquifers (Schilling et al., 2017a, 2020). A head-dependent flux (Cauchy-type) BC was used for both the upstream and the downstream groundwater BC. Constant hydraulic heads equal to 99.5 and 93.20 m were considered at the upstream ($y = 0 \text{ m}$) and downstream boundary ($y =$

500 m) of the model, respectively, with a conductance of $5.8 \text{ m}^2 \cdot \text{s}^{-1}$. These boundary conditions were manually adjusted to favor natural losing river conditions. Additionally, five pumping wells were implemented as one-dimensional vertical line elements (along the x -axis = 235 m) screened between 80 and 90 m. From each well, $45 \text{ l} \cdot \text{s}^{-1}$ were abstracted via a nodal flux BC set at an elevation of 82 m (Figure 2). Focusing on losing stream conditions was also preferred to better illustrate the use of these natural gas tracers to track the recent infiltration of surface water into a groundwater body. Note that pumping in the wells was not considered when the attenuation length for the ^{37}Ar production function was manually adjusted to reproduce the secular equilibrium profile of ^{37}Ar . This choice was made to ensure that the ^{37}Ar background piezometer (Figure 2) was in secular equilibrium. The lateral model boundaries ($x = 0 \text{ m}$ and $x = 300 \text{ m}$), and the bottom boundary, were assumed to be impermeable. No riverbed was considered, and it was assumed that the stream is fully connected to the aquifer [see Brunner et al. (2009) and Schilling et al. (2017b) for implications]. A meteoric groundwater recharge BC was applied ($300 \text{ mm} \cdot \text{y}^{-1}$) at the top nodes of the subsurface flow domain to favor vertical flow in the unsaturated zone. The result of this flow model configuration is a shallow water table aquifer ($\approx 2.5 \text{ m}$ thick unsaturated and 27.5 m thick saturated zone) with a losing river all along the model and localized drawdown at the pumping wells (Figure 2). The proposed model design was inspired by the common configuration of bank filtration wells in mountainous river corridors.

The lateral transport BC, at $x = 0 \text{ m}$ and $x = 300 \text{ m}$, and bottom boundaries, were set as zero mass gradients. The upstream boundary of the model, at $y = 500 \text{ m}$, was set as a third-type BC with fixed concentrations at secular equilibrium. Surface nodes act as discharge and/or recharge points regarding the mass gradient between the surface and the subsurface. Due to the negligible atmospheric concentrations as well as the volatility of both ^{222}Rn and ^{37}Ar , a zero concentration BC was specified for the surface nodes. Based on the scaling relationships of Schulze-Makuch (2005), the longitudinal dispersivity of the current transport model was set to 5 m , while the transverse dispersivities were set to 0.5 m . Within the matrix, radiogenic production of ^{222}Rn and ^{37}Ar was set according to the new partitioning zero-order source, while the disintegration was simulated with a first-order decay. The ^{222}Rn aquifer production rate per unit pore volume was computed from Equation 10. The production of ^{37}Ar was computed from Equations 11, 12. For the elements below the stream, the production of ^{37}Ar is slightly attenuated according to Equation 13, assuming a constant water column with a thickness of 1 m . The phase-equilibrium partitioning coefficient H^{cc} was assigned a value of 0.35 for ^{222}Rn and 0.04182 for ^{37}Ar in mole fraction ratio as defined in Equation 3 for 10°C water temperature.

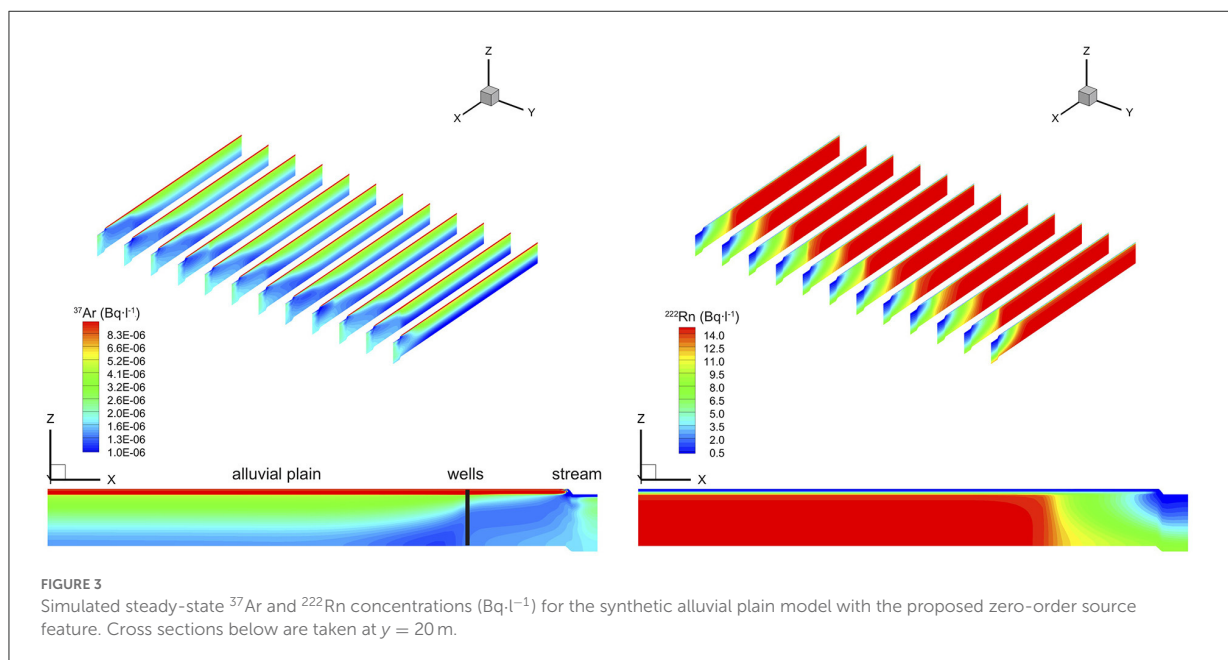
Results

The model was forced with constant boundary conditions and run long enough to reach secular equilibrium for both ^{222}Rn and ^{37}Ar . A comparison of the simulated concentrations of ^{37}Ar at the virtual background piezometer shows that the simulations of ^{37}Ar are in agreement with the secular equilibrium profile estimated from the real-world sandy gravel alluvial aquifer that was used for calibration of the attenuation length parameter (Supplementary Figure A2). The fast neutron attenuation length was estimated at $98 \text{ g} \cdot \text{cm}^{-2}$, which is of the same order as empirically established values (Phillips et al., 2001). Note that the apparent attenuation length observed at the background piezometer is the combined result of depth-dependent production and dispersive smoothing.

The simulated concentrations of ^{222}Rn and ^{37}Ar with the synthetic alluvial plain model under pumping conditions are illustrated in Figure 3. For both gas tracers, for a given depth, groundwater concentrations increase with distance from the stream. This is an expected pattern as the freshly infiltrated water from the stream lowers the groundwater concentrations of ^{222}Rn and ^{37}Ar . Minimum concentrations are located directly underneath the losing stream, corresponding to the location where surface water infiltrates into subsurface. The effect of depth-dependent ^{37}Ar production is clearly visible in the groundwater concentrations.

The pumping at the wells induces faster flow paths from the edge of the riverbank toward the wells (Figure 3). Thus, high groundwater flow velocities are located between the riverbank and the well corridor, where drawdown is induced by the pumping wells. Within these high flow paths or capture zones, recently infiltrated water spends less time in upper layers and is thus less concentrated in ^{37}Ar compared to other stretches along the stream. The low production rates located in the deeper layers are not sufficient to increase the concentrations of ^{37}Ar and the low concentration signals allow tracking the recently infiltrated surface water (Figure 3). In contrast, the production of ^{222}Rn was assumed independent of depth and therefore, concentrations are only related to by residence times in the alluvial aquifer (Figure 3).

Additionally, at the location of the observation point inside the model domain (see Figure 2), vertical one-dimensional profiles of ^{37}Ar and ^{222}Rn tracer concentrations can be drawn across the 27.5 m saturated portion of the aquifer, thus focusing on groundwater tracer concentrations (Figure 4). The main interest is to evaluate the impact of simulating tracer concentrations in the unsaturated zone on tracer concentrations in groundwater, which correspond to measurements usually gathered in the field. In this section, in addition to the standard (non-partitioning) zero-order source and the proposed new zero-order source with partitioning, a (non-partitioning) zero-order source with saturation threshold (which neglects the production of tracers below a given saturation threshold,



assumed here at 99%) is also considered. A saturation threshold fixed at 99% restricts the production of tracers to the saturated zone, essentially neglecting the production of tracers in the unsaturated zone. Groundwater concentration profiles are thus computed for ^{37}Ar and ^{222}Rn with these three approaches.

For both tracers, the one-dimensional profiles show that the standard zero-order source implementation, which doesn't scale the production of tracers in the unsaturated zone, leads to a systematic overestimation of the tracer concentrations in groundwater (Figure 4). This large overestimation (up to one order of magnitude for ^{37}Ar) illustrates the limited capacity of the standard zero-order source implementation to model gas-tracer production in variably saturated conditions, which must usually be considered when studying river-groundwater environments (Brunner et al., 2017).

Alternatively, when the tracer production is completely neglected in the unsaturated zone using the zero-order source with saturation threshold implementation, the concentrations in the groundwater are likely to be underestimated for both ^{222}Rn and ^{37}Ar (Figure 4). These are consistent simulation results since the infiltrated water that reached the water table is less concentrated when the unsaturated zone production of these tracers is ignored, potentially reducing the groundwater concentrations close to the water table. This illustrates the major interest of the proposed zero-order source with partitioning for tracers with high solubility but also for tracers that are heterogeneously emanated in the subsurface and where tracer production in the unsaturated zone cannot be ignored.

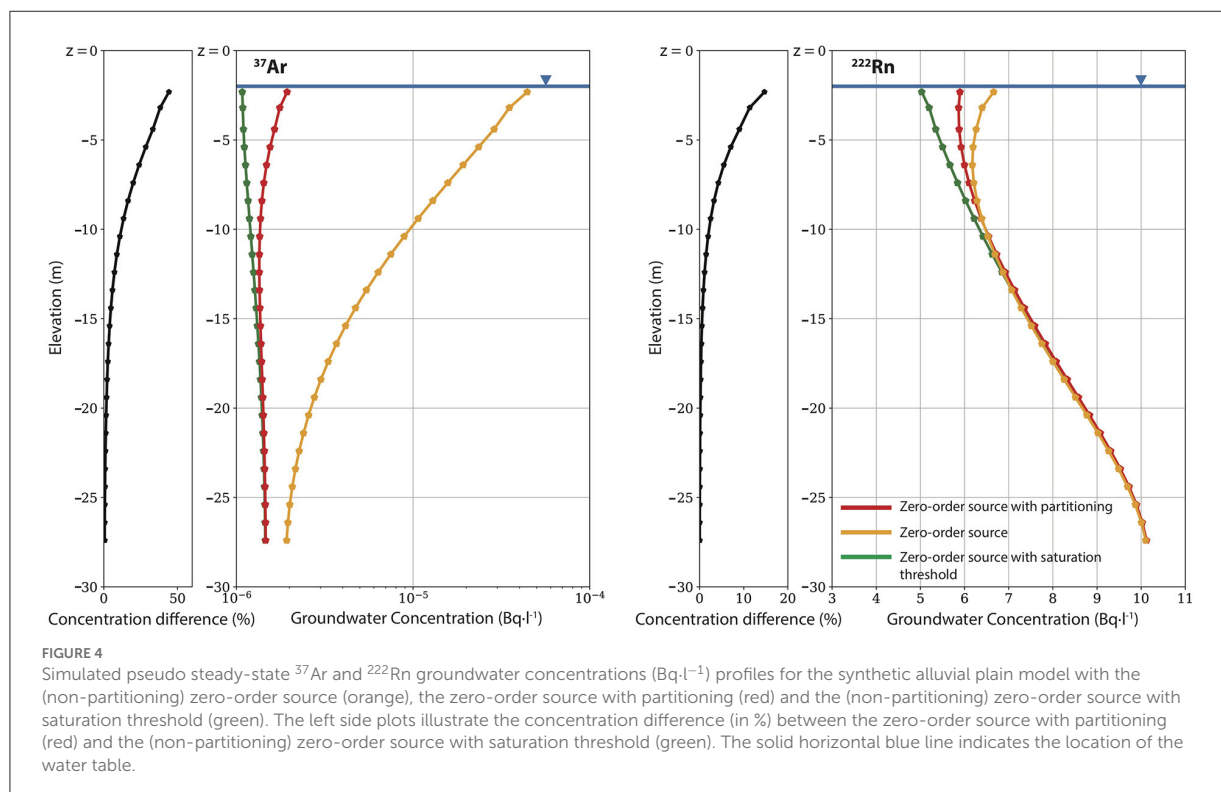
Despite a lower solubility of ^{37}Ar compared to ^{222}Rn , production of ^{37}Ar is exponentially decreasing with depth and a high proportion of the concentration (50% at the observation

point location) is neglected when the tracer is not simulated in the unsaturated zone (Figure 4). This is less significant for ^{222}Rn (difference at about 15% at the observation point location) because production is considered homogeneous and so the impact of not including the larger production in the unsaturated zone is minimized. However, recent studies have shown that ^{222}Rn emanations rates can be highest within the first few meters below the surface (Mullinger et al., 2009; Peel et al., 2022). High ^{222}Rn production rates in the shallow part of the aquifer might have significant effects on measured ^{222}Rn concentrations in groundwater and the proposed zero-order source with partitioning implementation would significantly improve the simulation of ^{222}Rn in such systems. For both tracers, neglecting the production in the unsaturated zone can significantly influence the groundwater concentrations up to 10 m below the ground surface for our river-groundwater alluvial model. Yet more pronounced differences are expected for thick unsaturated zones and highly dynamic transient conditions.

Discussion

Limitation of the partitioning zero-order source production

In the preceding sections, it has been shown that a more consistent simulation of environmental gas tracer concentrations can be achieved with single-phase ISSHMs if the production in the unsaturated zone is considered with the proposed instant-equilibration mass-balance formulation (i.e., the zero-order source with partitioning). However, it



should be noted that the verification section has underlined some limitations under strongly transient conditions since the gas phase is not explicitly simulated. Thus, while the proposed methodology represents a clear and computationally highly efficient improvement of the current capacity of single-phase ISSHMs to explicitly simulate environmental gas tracers, consistent simulation of environmental gas tracer concentrations in the unsaturated zone, should be done with a multi-phase flow and transport model.

Conclusions

A zero-order source implementation that scales the production of environmental gas tracers according to the water saturation and gas/water partitioning has been proposed. The new implementation, labeled as a *zero-order source with partitioning*, is based on an instant-equilibration mass-balance and allows realistic simulations of environmental gas tracers in the unsaturated zone with single-phase, variably saturated hydrologic models. The new feature, which has been implemented in HydroGeoSphere, has been verified against a multi-phase fluid flow and transport model (HYDRUS-1D). As illustrated in the verification and illustration examples, the application of the proposed partitioning of tracer production rates can significantly improve the consistency

of simulations of environmental gas tracer concentrations under variably saturated conditions. The method is particularly well-suited to enhance the capacity of integrated surface and subsurface hydrologic models (ISSHMs) to explicitly simulate environmental gas tracers in steady-state and dynamic conditions, although some limitations has been shown for extremely dynamic contexts. In addition to the presentation of the new zero-order source with partitioning, we demonstrate for the first time the explicit and simultaneous simulation of ^{222}Rn alongside ^{37}Ar under variably-saturated conditions with an ISSHM. These tracers have so far not been jointly simulated.

Data availability statement

Data used for this study are supplied as SI Dataset P2 available for download from HydroShare (<https://www.hydroshare.org/resource/9cee88f43ce6401c92f05c12706308e7/>).

Author contributions

HD: writing—original draft preparation, investigation, software, conceptualization, methodology. MP: writing—review

and editing, conceptualization, and methodology. SM: writing—review and editing, and conceptualization. OS: writing—review and editing. RP: writing—review and editing. PB: writing—review and editing, conceptualization, supervision, and funding acquisition. All authors contributed to the article and approved the submitted version.

Funding

HD and MP acknowledge the funding provided by the Swiss National Science Foundation (SNSF; grant number 200021_179017).

Acknowledgments

The authors acknowledge the Aquanty Inc. scientific team for their support and assistance during the implementation of the zero-order source with partitioning feature into the numerical model code HydroGeoSphere.

References

- Aquanty Inc. (2022). *HydroGeoSphere Theory Manual*. Waterloo, ON. p. 101.
- Bourke, S. A., Cook, P. G., Shanfield, M., Dogramaci, S., and Clark, J. F. (2014). Characterisation of hyporheic exchange in a losing stream using radon-222. *J. Hydrol.* 519, 94–105. doi: 10.1016/j.jhydrol.2014.06.057
- Brunner, P., Cook, P. G., and Simmons, C. T. (2009). Hydrogeologic controls on disconnection between surface water and groundwater. *Water Resour. Res.* 45:W01422. doi: 10.1029/2008WR006953
- Brunner, P., and Simmons, C. T. (2012). HydroGeoSphere: a fully integrated, physically based hydrological model. *Groundwater* 50, 170–176. doi: 10.1111/j.1745-6584.2011.00882.x
- Brunner, P., Therrien, R., Renard, P., Simmons, C. T., and Franssen, H.-J. H. (2017). Advances in understanding river-groundwater interactions. *Rev. Geophys.* 55, 118–129. doi: 10.1002/2017RG000556
- Cartwright, I., and Gilfedder, B. (2015). Mapping and quantifying groundwater inflows to Deep Creek (Maribyrnong catchment, SE Australia) using 222Rn, implications for protecting groundwater-dependant ecosystems. *Appl. Geochem.* 52, 118–129. doi: 10.1016/j.apgeochem.2014.11.020
- Cecil, L. D., and Green, J. R. (2000). “Radon-222,” in *Environmental Tracers in Subsurface Hydrology*, eds P. G. Cook, and A. L. Herczeg (Boston, MA: Springer). doi: 10.1007/978-1-4615-4557-6_6
- Cook, P. G., and Herczeg, A. L. (2012). *Environmental Tracers in Subsurface Hydrology*. New York, NY: Springer Science and Business Media. doi: 10.1007/978-1-4615-4557-6
- Cook, P. G., Wood, C., White, T., Simmons, C. T., Fass, T., and Brunner, P. (2008). Groundwater inflow to a shallow, poorly-mixed wetland estimated from a mass balance of radon. *J. Hydrol.* 354, 213–226. doi: 10.1016/j.jhydrol.2008.03.016
- Dann, R., Close, M., Flintoft, M., Hector, R., Barlow, H., Thomas, S., et al. (2009). Characterization and estimation of hydraulic properties in an alluvial gravel vadose zone. *Vadose Zone J.* 8, 651–663. doi: 10.2136/vzj2008.0174
- Dwivedi, R., Eastoe, C., Knowles, J. F., McIntosh, J., Meixner, T., Minor, R., et al. (2022). Tandem use of multiple tracers and metrics to identify dynamic and slow hydrological flowpaths. *Front. Water*. 4:841144. doi: 10.3389/frwa.2022.841144
- Fabryka-Martin, J. T. (1988). *Production of Radionuclides in the Earth and Their Hydrogeologic Significance, with Emphasis on Chlorine-36 and Iodine-129*. The University of Arizona.
- Gilfedder, B., Cartwright, I., Hofmann, H., and Frei, S. (2019). Explicit modeling of Radon-222 in HydroGeoSphere during steady state and dynamic transient storage. *Groundwater* 57, 36–47. doi: 10.1111/gwat.12847
- Goode, D. J. (1996). Direct simulation of groundwater age. *Water Resour. Res.* 32, 289–296. doi: 10.1029/95WR03401
- Gosse, J. C., and Phillips, F. M. (2001). Terrestrial *in situ* cosmogenic nuclides: theory and application. *Quatern. Sci. Rev.* 20, 1475–1560. doi: 10.1016/S0277-3791(00)00171-2
- Guillon, S., Sun, Y., Purtschert, R., Raghoo, L., Pili, E., and Carrigan, C. R. (2016). Alteration of natural 37Ar activity concentration in the subsurface by gas transport and water infiltration. *J. Environ. Radioact.* 155, 89–96. doi: 10.1016/j.jenvrad.2016.02.021
- Heisinger, B., Lal, D., Jull, A. J. T., Kubik, P., Ivy-Ochs, S., Knie, K., et al. (2002). Production of selected cosmogenic radionuclides by muons: 2. Capture of negative muons. *Earth Planet. Sci. Lett.* 200, 357–369. doi: 10.1016/S0012-821X(02)00640-4
- Hoehn, E., and Von Gunten, H. R. (1989). Radon in groundwater: a tool to assess infiltration from surface waters to aquifers. *Water Resour. Res.* 25, 1795–1803. doi: 10.1029/WR025i008p01795
- HydroAlgorithms Pty Ltd (2016). *AlgoMesh User Guide*. Melbourne, VIC.
- Johnson, C., Lowrey, J. D., Alexander, T., Mace, E., and Prinke, A. (2021). Measurements of the emanation of 37Ar and 39Ar from irradiated rocks and powders. *J. Radioanal. Nucl. Chem.* 329, 969–974. doi: 10.1007/s10967-021-07827-4
- Kazemi, G. A., Lehr, J. H., and Perrochet, P. (2006). *Groundwater Age*. Hoboken, NJ: John Wiley and Sons. doi: 10.1002/0471929514
- Kolditz, O., Bauer, S., Bilke, L., Böttcher, N., Delfs, J. O., Fischer, T., et al. (2012). OpenGeoSys: an open-source initiative for numerical simulation of thermo-hydro-mechanical/chemical (THM/C) processes in porous media. *Environ. Earth Sci.* 67, 589–599. doi: 10.1007/s12665-012-1546-x
- Kollet, S. J., and Maxwell, R. M. (2008). Capturing the influence of groundwater dynamics on land surface processes using an integrated, distributed watershed model. *Water Resour. Res.* 44. doi: 10.1029/2007WR006004
- Liggett, J. E., Werner, A. D., and Simmons, C. T. (2012). Influence of the first-order exchange coefficient on simulation of coupled surface-subsurface flow. *J. Hydrol.* 414–415, 503–515. doi: 10.1016/j.jhydrol.2011.11.028

Conflict of interest

The authors declare that the research was conducted in the absence of any commercial or financial relationships that could be construed as a potential conflict of interest.

Publisher's note

All claims expressed in this article are solely those of the authors and do not necessarily represent those of their affiliated organizations, or those of the publisher, the editors and the reviewers. Any product that may be evaluated in this article, or claim that may be made by its manufacturer, is not guaranteed or endorsed by the publisher.

Supplementary material

The Supplementary Material for this article can be found online at: <https://www.frontiersin.org/articles/10.3389/frwa.2022.980030/full#supplementary-material>

- Loosli, H. H., and Purtschert, R. (2005). "Rare gases", in *Isotopes in the Water Cycle: Past, Present and Future of a Developing Science*, eds P. K. Aggarwal, J. R. Gat, and K. F. Froehlich (Vienna: IAEA), p. 91–95. doi: 10.1007/1-4020-3023-1_7
- McCallum, J. L., Cook, P. G., Dogramaci, S., Purtschert, R., Simmons, C. T., and Burk, L. (2017). Identifying modern and historic recharge events from tracer-derived groundwater age distributions. *Water Resour. Res.* 53, 1039–1056. doi: 10.1002/2016WR019839
- McCallum, J. L., Cook, P. G., and Simmons, C. T. (2015). Limitations of the use of environmental tracers to infer groundwater age. *Groundwater* 53, 56–70. doi: 10.1111/gwat.12237
- Mullinger, N. J., Pates, J. M., Binley, A. M., and Crook, N. P. (2009). Controls on the spatial and temporal variability of ^{222}Rn in riparian groundwater in a lowland chalk catchment. *J. Hydrol.* 376, 58–69. doi: 10.1016/j.jhydrol.2009.07.015
- Musy, S., Casolaro, P., Dellepiane, G., Berger, A., Braccini, S., and Purtschert, R. (2022). Quantification of ^{37}Ar emanation fractions from irradiated natural rock samples and field applications. *J. Environ. Radioact.* 251–252:106966. doi: 10.1016/j.jenvrad.2022.106966
- Nitao, J. J. (1998). *Reference Manual for the NUFT Flow and Transport Code, Version 2.0*. Lawrence Livermore National Laboratory.
- Paniconi, C., and Putti, M. (2015). Physically based modeling in catchment hydrology at 50: survey and outlook. *Water Resour. Res.* 51, 7090–7129. doi: 10.1002/2015WR017780
- Partington, D., Knowing, M. J., Simmons, C. T., Cook, P. G., Xie, Y., Iwanaga, T., et al. (2020). Worth of hydraulic and water chemistry observation data in terms of the reliability of surface water-groundwater exchange flux predictions under varied flow conditions. *J. Hydrol.* 590:125441. doi: 10.1016/j.jhydrol.2020.125441
- Peel, M., Kipfer, R., Hunkeler, D., and Brunner, P. (2022). Variable ^{222}Rn emanation rates in an alluvial aquifer: limits on using ^{222}Rn as a tracer of surface water–Groundwater interactions. *Chem. Geol.* 599:120829. doi: 10.1016/j.chemgeo.2022.120829
- Phillips, F., Stone, W. D., and Fabryka-Martin, J. T. (2001). An improved approach to calculating low-energy cosmic-ray neutron fluxes near the land/atmosphere interface. *Chem. Geol.* 175, 689–701. doi: 10.1016/S0009-2541(00)00329-6
- Popp, A. L., Pardo-Alvarez, A., Schilling, O. S., Scheidegger, A., Musy, S., Peel, M., et al. (2021). A framework for untangling transient groundwater mixing and travel times. *Water Resour. Res.* 57: 2020WR028362. doi: 10.1029/2020WR028362
- Renne, P. R., and Norman, E. C. (2001). Determination of the half-life of ^{37}Ar by mass spectrometry. *Phys. Rev. C.* 63:047302. doi: 10.1103/PhysRevC.63.047302
- Riedmann, R. A., and Purtschert, R. (2011). Natural ^{37}Ar concentrations in soil air: implications for monitoring underground nuclear explosions. *Environ. Sci. Technol.* 45, 8656–8664. doi: 10.1021/es201192u
- Schilling, O. S., Cook, P. G., and Brunner, P. (2019). Beyond classical observations in hydrogeology: the advantages of including exchange flux, temperature, tracer concentration, residence time and soil moisture observations in groundwater model calibration. *Rev. Geophys.* 57, 146–192. doi: 10.1029/2018RG000619
- Schilling, O. S., Cook, P. G., Grierson, P. F., Dogramaci, S., and Simmons, C. T. (2020). Controls on interactions between surface water, groundwater and riverine vegetation along intermittent rivers and ephemeral streams in arid regions. *Water Resour. Res.* 57:e2020WR028429. doi: 10.1029/2020WR028429
- Schilling, O. S., Gerber, C., Purtschert, R., Kipfer, R., Hunkeler, D., and Brunner, P. (2017a). Advancing physically-based flow simulations of alluvial systems through atmospheric noble gases and the novel ^{37}Ar tracer method. *Water Resour. Res.* 53, 10465–10490. doi: 10.1002/2017WR020754
- Schilling, O. S., Irvine, D. J., Hendricks Franssen, H. J., and Brunner, P. (2017b). Estimating the spatial extent of unsaturated zones in heterogeneous river-aquifer systems. *Water Resour. Res.* 53, 10583–10602. doi: 10.1002/2017WR020409
- Schilling, O. S., Partington, D. J., Doherty, J., Kipfer, R., Hunkeler, D., and Brunner, P. (2022). Buried paleo-channel detection with a groundwater model, tracer-based observations and spatially varying, preferred anisotropy pilot point calibration. *Geophys. Res. Lett.* 49, e2022GL098944. doi: 10.1029/2022GL098944
- Schubert, M., Paschke, A., Lieberman, E., and Burnett, W. C. (2012). Air-water partitioning of ^{222}Rn and its dependence on water temperature and salinity. *Environ. Sci. Technol.* 46, 3905–3911. doi: 10.1021/es204680n
- Schulze-Makuch (2005). Longitudinal dispersivity data and implications for scaling behavior. *Groundwater*. 43, 443–456. doi: 10.1111/j.1745-6584.2005.0051.x
- Sebben, M. L., Werner, A. D., Liggett, J. E., Partington, D. J., and Simmons, C. T. (2013). On the testing of fully integrated surface-subsurface hydrological models. *Hydrol. Process.* 27, 1276–1285. doi: 10.1002/hyp.9630
- Simunek, J., Van Genuchten, M. Th., and Sejna, M. (2016). Recent developments and applications of the HYDRUS computer software packages. *Vadose Zone J.* 15, 1–25. doi: 10.2136/vzj2016.04.0033
- Spannagel, G., and Fireman, E. L. (1972). Stopping rate of negative cosmic-ray muons near sea level. *J. Geophys. Res.* 77, 5351–5359. doi: 10.1029/JA077i028p05351
- Sramek, O., Stevens, L., McDonough, W. F., Mukhopadhyay, S., and Peterson, R. J. (2017). Subterranean production of neutrons, ^{39}Ar and ^{21}Ne : Rates and uncertainties. *Geochim. Cosmochim. Acta* 196, 370–387. doi: 10.1016/j.gca.2016.09.040
- Sun, H., and Furbish, D. J. (1995). Moisture content effect on radon emanation in porous media. *J. Contam. Hydrol.* 18, 239–255. doi: 10.1016/0169-7722(95)00002-D
- Tosaka, H., Itoh, K., and Furuno, T. (2000). Fully coupled formulation of surface flow with 2-phase subsurface flow for hydrological simulation. *Hydrol. Process.* 14, 449–464. doi: 10.1002/(SICI)1099-1085(20000228)14:3<449::AID-HYP948>3.0.CO;2-9
- Turnadge, C., and Smerdon, B. D. (2014). A review of methods for modelling environmental tracers in groundwater: advantages of tracer concentration simulation. *J. Hydrol.* 519, 3674–3689. doi: 10.1016/j.jhydrol.2014.10.056
- Van Huijgevoort, M. H. J., Tetzlaff, D., Sutanudjaja, E. H., and Soulsby, C. (2016). Using high resolution tracer data to constrain water storage, flux and age estimates in a spatially distributed rainfall-runoff model. *Hydrol. Process.* 30, 4761–4778. doi: 10.1002/hyp.10902
- Zhuo, W., Lida, T., and Furukawa, M. (2006). Modeling radon flux density from the Earth's Surface. *J. Nucl. Sci. Technol.* 43, 479–482. doi: 10.1080/18811248.2006.9711127

References

- Andrews, J., Fontes, J.-C., Michelot, J.-L., and Elmore, D. (1986). In-situ neutron flux, ^{36}Cl production and groundwater evolution in Crystalline rocks at Stripa, Sweden. *Earth and Planetary Science Letters*, 77.
- Aquanty Inc., H. (2022). Theory Manual. Technical report, Waterloo (CA).
- Delottier, H., Peel, M., Musy, S., Schilling, O., Purtschert, R., and Brunner, P. (2022). Explicit simulation of environmental gas tracers with integrated surface and subsurface hydrological models. *Frontiers in Water*, 4.
- Fabryka-Martin, J. (1988). *Production of radionuclides in the earth and their hydrogeologic significance, with emphasis on chlorine-36 and iodine-129*. PhD Thesis, University of Arizona, Tucson.
- Grieger, M., Hensel, T., Agramunt, J., Bemmerer, D., Degering, D., Dillmann, I., Fraile, L. M., Jordan, D., Köster, U., Marta, M., Müller, S. E., Szücs, T., Taín, J. L., and Zuber, K. (2020). Neutron flux and spectrum in the Dresden Felsenkeller underground facility studied by moderated ^3He counters. *Physical Review D*, 101(12):123027. arXiv: 2006.02696.
- Henriksen, H. J., Trolldborg, L., Nyegaard, P., Sonnenborg, T. O., Refsgaard, J. C., and Madsen, B. (2003). Methodology for construction, calibration and validation of a national hydrological model for Denmark. *Journal of Hydrology*, 280(1):52–71.
- Johnson, C., Lowrey, J. D., Alexander, T., Mace, E., and Prinke, A. (2021). Measurements of the emanation of ^{37}Ar and ^{39}Ar from irradiated rocks and powders. *Journal of Radioanalytical and Nuclear Chemistry*, 329(2):969–974.
- Loosli, H., Lehmann, B., and Balderer, W. (1989). Argon-39, argon-37 and krypton-85 isotopes in Stripa groundwaters. *Geochimica et Cosmochimica Acta*, 53(8):1825–1829.
- Mei, D.-M., Yin, Z.-B., Spaans, J., Koppang, M., Hime, A., Keller, C., and Gehman, V. M. (2010). Prediction of underground argon content for dark matter experiments. *Physical Review C*, 81(5).
- Musy, S., Casolaro, P., Dellepiane, G., Braccini, S., and Purtschert, R. (2021). Argon-37 emanation rates determined for irradiated natural dry and wet rock samples.
- Šrámek, O., Stevens, L., McDonough, W. F., Mukhopadhyay, S., and Peterson, R. (2017). Subterranean production of neutrons, argon-39 and neon-21 : Rates and uncertainties. *Geochimica et Cosmochimica Acta*, 196:370–387.

Declaration of consent

on the basis of Article 18 of the PromR Phil.-nat. 19

Name/First Name: Musy Stéphanie Lisa

Registration Number: 13-511-209

Study program: Graduate School of Climate Sciences

Bachelor ☐ Master ☐ Dissertation ☒

Title of the thesis: Further developments of radio-noble gas groundwater dating: assessment of ^{37}Ar and ^{39}Ar underground production, and developement of a new ^{85}Kr sampling technique

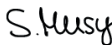
Supervisor: Prof. Markus Leuerberger / Dr. Roland Purtschert

I declare herewith that this thesis is my own work and that I have not used any sources other than those stated. I have indicated the adoption of quotations as well as thoughts taken from other authors as such in the thesis. I am aware that the Senate pursuant to Article 36 paragraph 1 litera r of the University Act of September 5th, 1996 and Article 69 of the University Statute of June 7th, 2011 is authorized to revoke the doctoral degree awarded on the basis of this thesis.

For the purposes of evaluation and verification of compliance with the declaration of originality and the regulations governing plagiarism, I hereby grant the University of Bern the right to process my personal data and to perform the acts of use this requires, in particular, to reproduce the written thesis and to store it permanently in a database, and to use said database, or to make said database available, to enable comparison with theses submitted by others.

Bern, 19.09.2022

Place/Date


Signature